# Modelling local order in organic and metal-organic ferroic materials using the reverse Monte Carlo method and total neutron scattering

H. D. Duncan

*Submitted in partial fulfilment*
*of the requirements of the Degree of*
*Doctor of Philosophy*

12 August 2016

School of Physics and Astronomy
Queen Mary, University of London

Queen Mary
University of London

## Statement of originality

I, H. D. Duncan, confirm that the research included within this thesis is my own work or that where it has been carried out in collaboration with, or supported by others, that this is duly acknowledged below and my contribution indicated. Previously published material is also acknowledged below.

I attest that I have exercised reasonable care to ensure that the work is original, and does not to the best of my knowledge break any UK law, infringe any third party's copyright or other Intellectual Property Right, or contain any confidential material.

I accept that the College has the right to use plagiarism detection software to check the electronic version of the thesis.

I confirm that this thesis has not been previously submitted for the award of a degree by this or any other university.

The copyright of this thesis rests with the author and no quotation from it or information derived from it may be published without the prior written consent of the author.

.....

H. D. Duncan
12 August 2016

Parts of chapter 3 have been previously published [1]

Atomistic configurations were generated by the program `RMCProfile`, using the MidPlus high-performance computing system, provided by the EPSRC (EP/K000233/1, EP/K000128/1).

## Abstract

The ordering processes of ferroelectric and multiferroic materials were investigated via neutron total scattering and the reverse Monte Carlo method.

The results presented in this thesis are from three materials where ferroelectric behaviour is a result of ordering of molecular groups rather than individual atoms. Two of the materials are metal-organic frameworks, three dimensional cage-like structures with guest ions inside the pores; the third material, is a room temperature ferroelectric.

In the high-temperature phase of dimethylammonium manganese formate, the framework distorts around the disordered cation, and the cations form shorter hydrogen bonds with the formate framework than the average structure suggests. Framework deformations became increasingly unfavourable as the material cooled. The cations continue to order as the material was cooled below $T_c$. Analysis of the high-temperature phase atomistic configurations showed that in addition to the three known orientations about the threefold axis, a significant minority of the cations lie mid-way between these positions, a feature which could not have been observed via standard crystallographic techniques.

The mechanisms for thermal expansion of potassium imidazolium hexacyanoferrate change between the intermediate-temperature phase and the high-temperature phase. In the high-temperature phase the framework distorts around the disordered guest, but in the intermediate-temperature phase the framework stiffens. I propose that the temperature of the dielectric transition is dependent of the volume inside the framework, but that the temperature range of the intermediate-temperature phase is dependent on the rate of contraction of the framework around the guest cation..

For triglycine sulfate no correlation was observed between the orientation of the polar molecules and the motion of the intermediate deuterium. Furthermore, in the high temperature phase the atomistic configurations produced models with macroscopic polarisation. I propose that this material forms domains of aligned polar molecules above $T_c$ and that these domains are larger than the atomistic configurations.

# Contents

## Acknowledgements

This thesis is the result of four years work, many gallons of coffee and quite a few sleepless nights. I am very proud of it, and I would like to thank everybody who has helped and supported me while I have been at Queen Mary. I would especially like to thank my two supervisors, **Anthony Phillips** and **Martin Dove**, who have been both infuriatingly enthusiastic and calm (at different points), and who have challenged and supported me. I would also like to extend my gratitude to **Dave Keen**, **Matt Tucker** and **Helen Playford** who assisted with the neutron scattering experiments, and helped me deal with a somewhat temperamental `GUDRUN`.

On a more personal note, I would like to thank my parents, **Dot Richards** and **James Richards** for their love and support, and for continuing to show such interest in what I can appreciate is quite a niche subject. I would also like to thank **William Little** for his understanding, his love, and for spending weekends listening to me practice presentations. I would finally like to extend special thanks to my fellow PhD students **Dave Holford** and **Asmi Barot** who have commiserated with me when things have gone poorly, and have enthusiastically celebrated successes.

# Chapter 1

# Background

## 1.1 Materials and functionality

The work in this thesis is an attempt to use neutron total scattering with the reverse Monte Carlo (RMC) method to understand how changes in the local structure of three different materials cause them to display interesting and useful bulk properties. Although the RMC method is now well established, the systems I have studied are far more complex than have previously been investigated with this method. This has meant that some aspects of the work have required a lot of care, and it has been necessary to create a number of bespoke setup and analysis programs. Because each system shows a high degree of disorder over a range of temperatures, the work has highlighted how the average structure can sometimes overlook crucial features associated with disorder and ordering processes.

In the first part of this chapter I will discuss the link between atomic structure and the macroscopic properties, such as ferroelectricity, that are observed in my systems and which make certain materials so useful to modern technology. In the second part of this chapter I will discuss how, when we know that a material possesses a desirable or interesting bulk property, we can go about extracting information about how the phenomena arises.

Most investigations into functional material properties stem from the desire to improve on the current generation of materials. For example, if we have materials that have a coupling between magnetic and electric ordering, we need to understand the underpinning mechanisms, which may then lead to opportunities to increase the strength of the coupling, or increase the temperature at which the coupling occurs. In order to do this it is necessary to understand how the materials behave and respond to changes in temperature at the atomic scale

There are many ways to probe atomic structure, such as traditional Bragg diffraction, NMR and Raman spectroscopy, but these methods do not allow for direct access to the local structure. Neutron total scattering, coupled with computer modelling using the RMC algorithm allows the local structure of materials to be modelled via atomistic configurations which can then be directly analysed.

### 1.1.1 Ferroelectrics

Ferroelectric materials display spontaneous polarisation, which upon application of an external field, can be reversed. The ferroelectric phase transition usually occurs upon cooling and

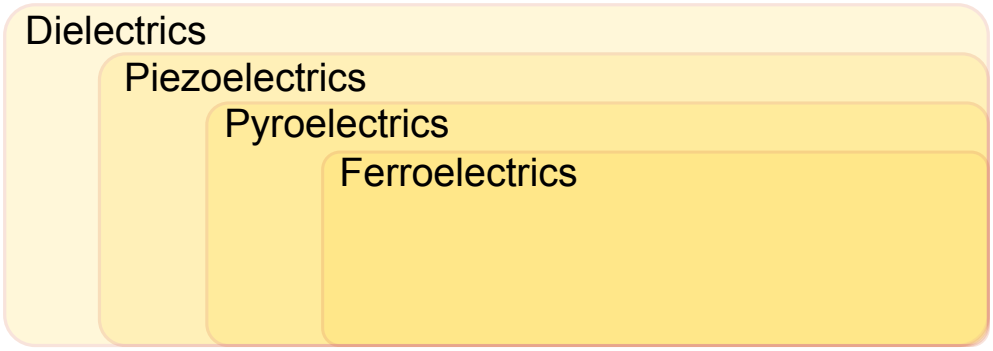


**Figure 1.1:** The relationship between ferroelectrics and dielectrics. All ferroelectric materials are dielectric, piezoelectric, and pyroelectric.

involves a reduction in symmetry.

Figure 1.1 is a diagram outlining the relationship between dielectrics, piezoelectrics, pyroelectrics, and ferroelectrics. Materials which contain polar groups, that can be polarised via application of an electric field are called dielectrics. Of these dielectrics, 20 out of the 21 non-centrosymmetric point groups are piezoelectric, that is a dipole moment can be induced by a mechanical stress. Piezoelectrics with a unique polar axis which display spontaneous polarisation which varies with temperature are defined as pyroelectrics. If the spontaneous polarisation observed in a pyroelectric material can be reversed upon application of an electric field, then the material is ferroelectric.

Above the transition temperature ferroelectrics behave as normal dielectrics; a field is applied and the electric dipoles align relative to it, if no field is applied, the material is paraelectric (electrically disordered). Below the transition temperature the material displays a reversible spontaneous polarisation.

The first confirmed ferroelectric was an organic structure, Rochelle Salt ($KNaC_4H_4O_6{\cdot}4\,H_2O$) which was reported in 1920 [2]. Its spontaneous polarisation is due to rotation of tartrate OH between two equilibrium positions [3].

Since Rochelle salt, there have been few reported organic ferroelectrics [4]. In 1935 ferroelectricity was reported in potassium dihydrogen phosphate, $KH_2PO_4$, (KDP) [5], and then there were very few reports of new ferroelectric materials until the 1940's. In the 1940's there was a boom in reports of ferroelectric materials, but these ferroelectrics were inorganic materials with a perovskite architecture (general formula $ABX_3$). In 1945/6 ferroelectricity was reported in $BaTiO_3$ followed by reports of ferroelectricity in $PbTiO_3$, $KNbO_3$ [5] and lead zirconate titanate (PZT), $Pb[Zr_xTi_{1-x}]O_3$, [6]. With the exception of Rochelle salt, KDP and triglycine sulfate (which is examined in this thesis), the search for ferroelectric materials was focussed on the inorganic perovskites [7], and as such most ferroelectrics today with practical applications are transition metal oxides [8].

The emergence of metal organic frameworks (MOFs), with perovskite-like architecture allows for an expansion of the range of possible ferroelectrics. Metal centres linked via multiatom bridges form a charged framework in which a cation can rotate and order with its neighbours. Longer atomic linkers provide a larger pore volume in which a molecular polar guest can move and align. These MOFs allow for a much wider variety of structures and

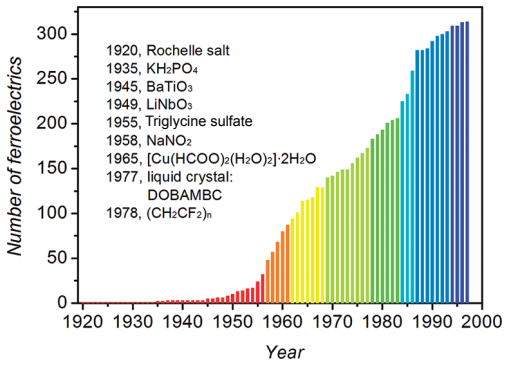


**Figure 1.2:** The number of reported ferroelectrics with years, taken from [9]

therefore functionalities than would be observed in purely inorganic perovskites. Two such materials, dimethylammonium formate and potassium imidazolium hexacyanoferrate (III) are the focus of chapters 3 and 5.

Ferroelectric materials have many applications, they're used as capacitors due to their high dielectric permittivity; their piezoelectricity means they are used in transducers and actuators [10]. Ferroelectrics with broad hysteresis loops allow for two stable states with opposite polarisation [10] and can be used for ferroelectric RAM which has been realised with PZT [11].

Given the range of realised and potential applications of ferroelectrics, it is understandable that there is a search for ferroelectrics with steeper hysteresis loops, larger dielectric permittivities, and a stronger physical response to an applied electric field, so investigating the mechanisms behind ferroelectrics is a valuable endeavour.

In addition to the possibility of magnifying the desirable properties of ferroelectrics, there is also significant interest in coupling electric ordering with magnetic ordering, producing multiferroics. So in order to lead the way for designer materials, we need to understand the mechanisms behind the current generation of ferroelectrics.

### 1.1.2 Multiferroics

Multiferroic materials are ones which contain two or more of the so-called ferroic orders which include ferromagnetism, ferroelectricity, ferroelasticity and potentially ferrotoroidicity. For the work presented in this thesis, we describe a multiferroic as a material with two or more ferroic orders present, the ferroic orders may or may not be coupled.

Perhaps one of the most useful types of multiferroics are the ones which combine magnetic and electric ordering. They have potential uses in either 4-state magnetic memory (if the magnetic and electric orders are independent [14]) or RAM written electrically and read magnetically [15]. However finding such materials is difficult, especially when we search within the transition metal oxide family to first find the ferroelectric material (that's not to say they haven't been found - $BiFeO_3$ is multiferroic [16]).

In inorganic perovskites the electric dipole arises from small displacements of metal ions (see 1.1.3). For example in $PbTiO_3$ where in the paraelectric phase Ti ions are in the centre of $TiO_6$ octahedra, but move away from the centre in the ferroelectric phase. In order to have a

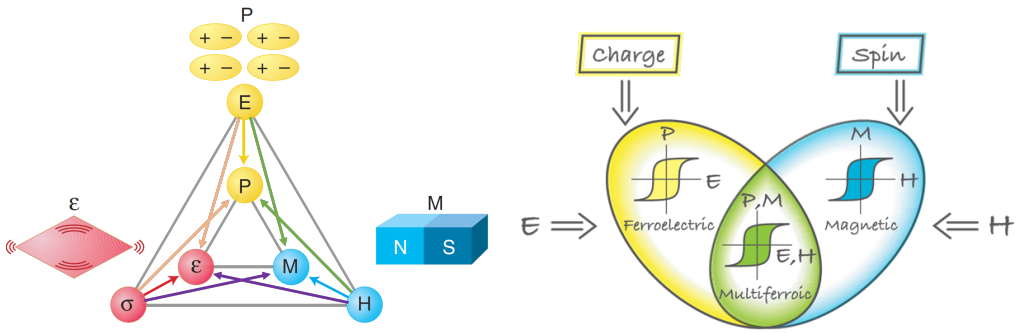


**Figure 1.3:** Left: Three ferroic orders, Ferroelectric -magnetic, -elastic adapted from [12]. The electric field, $E$, controls the polarisation, $P$; the magnetic field $H$, the magnetisation, $M$, and the stress $\sigma$ controls the strain $\epsilon$. Right: Overlap between between classes of material that display magnetic and electric ordering [13].

magnetic moment transition metals with partially filled $d$ orbitals are required. However the electrons in the $d$ orbitals reduce the likelihood that the metal ions are displaced. It appears that the requirements for ferroelectricity and magnetic ordering are mutually exclusive.

MOFs with perovskite-like architecture can circumvent the restrictions observed for inorganic perovskites, by separating the origin of magnetic and electric ordering. For these MOFs the magnetic moment can reside on the metal sites, and be mediated by the multiatom bridges, and the dipole moment can reside on the guest cations on the A sites.

### 1.1.3 Different types of disorder

Ferroelectricity is the result of relative shifts of positive and negative charges in a material, which induce a macrosopic polarisation [8]. These shifts can originate from small displacements of metal ions, by ordering of large polar groups, or by the hopping motion of a hydrogen atom between two different sites. For all ferroelectric materials, there are contributions from short-range repulsions of nearby polar groups, and long-range Coulomb forces [17].

The mechanisms behind the ferroelectric phase transition can be broken into two types.[4]
1. Order-disorder: eg $NaNO_2$
2. Displacive: eg $PbTiO_3$

However these two categories can all be thought of as different extremes of the same spectrum when considered using a simple model and Landau theory [18].

In the Landau model, shown at the top of figure 1.4, neighbouring atoms are joined via harmonic forces. The atoms are placed in a potential double well. The "depth" of this well is given by $V_0$ and the strength of the harmonic forces by $W$.

Well below the transition temperature the atoms will settle on the same side of the potential well as all of their neighbours. However it is the behaviour at $T \gg T_c$ which distinguishes the order disorder ferroelectrics from the displacive. The discussion below follows the outline of [18].

If we denote the ratio of the depth of the potential well, and the strength of the harmonic interactions as

$$s = \frac{|V_0|}{W}, \tag{1.1}$$

then, well above $T_c$, it is the value of $s$ which dictates how the atoms orient themselves.

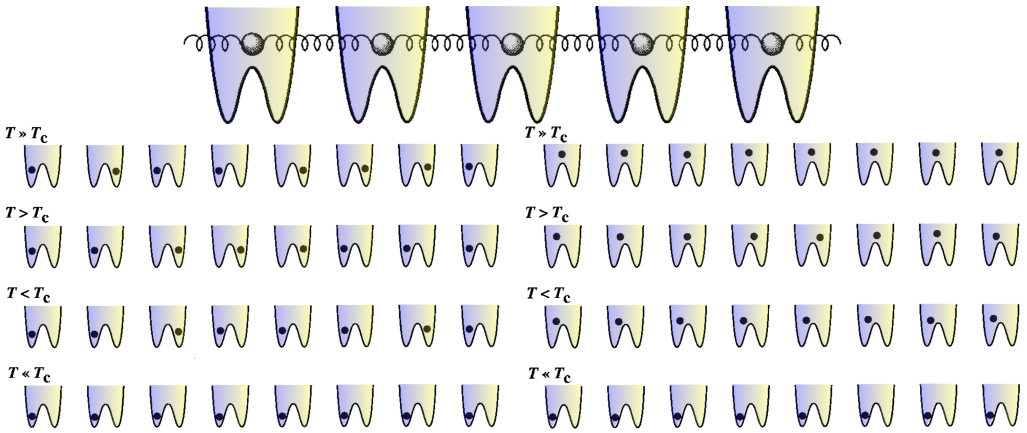


**Figure 1.4:** Top: Outline of a 1D model with neigbouring atoms interact via harmonic forces (springs) experience a double well potential (lines) which represents the rest of the crystal structure. Left: Order-disorder limit. Right Dispacive limit. Adapted from [18]

The order-disorder limit occurs when $s \gg 1$. When $s \gg 1$ the depth of the potential well is significantly greater than the strength of the harmonic interactions. At $T \gg T_c$, the atoms will be found in one of the two potential wells (shown left in figure 1.4). However the occupancy of the wells will be random. As the material cools and approaches $T_c$ the harmonic potential becomes more important, and short-range ordering is observed, where nearest neighbours have a propensity to fall to the same side of the potential well. Below $T_c$ there is a greater likelihood of finding the atom in one side of the potential well than the other. This probability increases on cooling until the material is fully ordered.

When $s \ll 1$, the strength of the interatomic potentials is significantly greater than the depth of the potential well. This is the displacive limit. At $T \gg T_c$ the atoms vibrate about the centre of the double well. As the material is cooled and approaches $T_c$ the effect of the potential well increases, with the atoms spending more time either side of the origin. The strength of the harmonic interaction means that neighbouring atoms are displaced from the origin by similar amounts [18]. Below $T_c$ the atoms will continue to vibrate about their origin, however this is now shifted away from the initial point. As with the order-disorder limit, at $T \ll T_c$, the atoms are almost exclusively found on one side of the potential well.

$NaNO_2$ (figure 1.5a) undergoes an order-disorder phase transition. The nitrogen is disordered over two sites above $T_c$ and $NaNO_2$ displays no net electric dipole. Below $T_c$ neighbouring nitrogen align and the material is polarised.

Conversely $PbTiO_3$ (figure 1.5b) undergoes a displacive phase transition, where below $T_c$, the oxygen are displaced from their equilibrium position in one direction, and the titanium in the other, giving the material a net polarisation.

Proton transfer can be thought of as an extension of the order-disorder model. The phase transition for KDP, (figure 1.5c) occurs when protons mid-way between adjacent $PO_4$ tetrahedra move into one of two energy minima, closer to one $PO_4$ unit producing a structure where spontaneous polarisation is observed.

The order-disorder/displacive narrative when thinking about ferroelectric phase transitions is a very useful tool, however they are idealised versions of a complex mechanism, and we

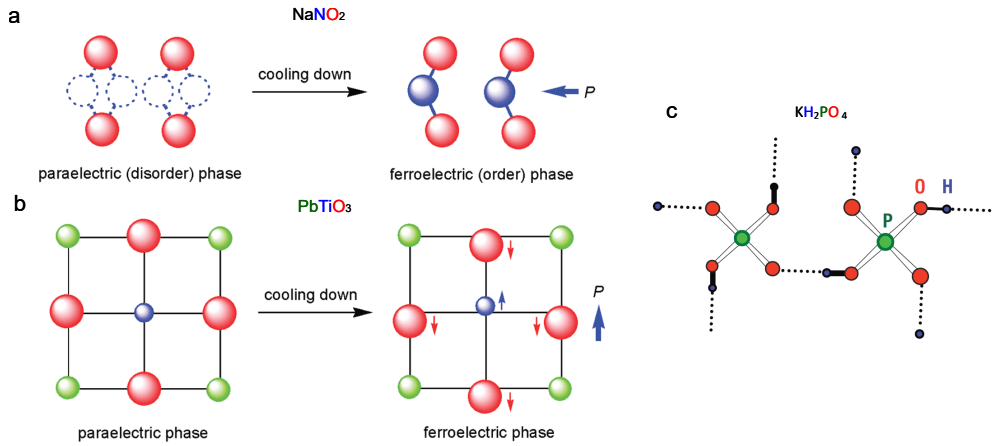


**Figure 1.5:** Three different mechanisms behind the ferroelectric phase transition in inorganic ferroelectrics. a: Order disorder, as shown with $NaNO_2$. b: Displacive, as shown with $PbTiO_3$. c: Proton hopping, as shown with KDP. Images adapted from [9] and [4].

shouldn't be surprised to see contributions from both when examining the onset of ferroelectric ordering.

In this thesis I attempt to understand the behaviour of the polar groups in three ferroelectrics as they approach the dielectric transition. It is necessary to consider how the disorder in the paraelectric phase is defined. Is the paraelectric phase truly disordered, is there evidence for short-lived local order? Or is the paraelectric phase a mix of random ordered domains which give the appearance of disorder? Do the polar groups continue to order below $T_c$? We must also consider if using the techniques available to us, we can identify these different features. As will be discussed in the analysis on triglycine sulfate (TGS), it isn't as straightforward as perhaps we could hope for.

### 1.1.4 Deuteration

Total neutron scattering experiments require perdeuterated materials (see 2.1.1), therefore it is necessary to mention that, for some ferroelectrics, substitution of the hydrogen with deuterium has a significant effect on the temperature of the phase transition and in at least one case cause an additional transition [16].

A significant change in transition temperature is observed in KDP where an substitution of hydrogen for deuterium increases $T_c$ by $\approx 90\,K$ [16]. This is perhaps expected as the mechanism behind the phase transition relies upon hydrogen motion, and effectively doubling the mass of the mobile species is a significant change to make. This does mean that we need to be careful about the effect that deuteration has on the transition temperatures of the materials that I am focussing on. The change in $T_c$ for triglycine sulfate upon deuteration is well-documented, and $T_c$ for the deuterated analogue is $\approx 10\,K$ higher than it is for the undeuterated sample. For the other two materials which I am investigating, their change in $T_c$ upon deuteration is less than 10 K. It is hoped that these relatively small changes in $T_c$, mean that structral changes deduced from analysis of the deuterated analogue should still be true for the undeuterted material.

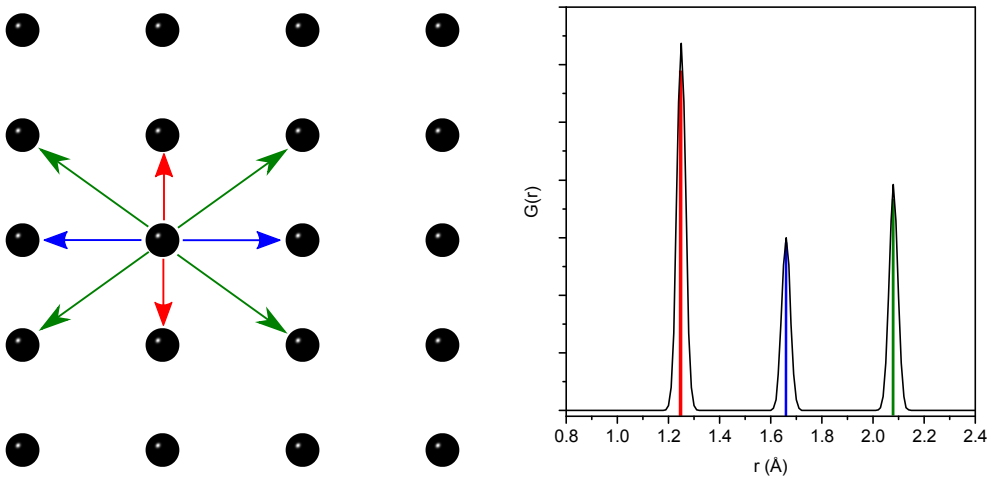


**Figure 1.6:** Left: A 2D assembly of atoms with the three nearest neighbour distances highlighted. Right; the corresponding PDF for such an assembly

## 1.2 Ways to analyse atomic structure

### 1.2.1 Accessing the pair distribution function via scattering experiments

If we want to understand the changes in materials as they approach the ferroelectric phase transition, it is necessary to understand and be able to identify both the short range and long range ordering.

The pair distribution function (PDF) is a way of modelling such features. The PDF is a histogram of interatomic separations, where the number of atoms of type $j$ in a shell of radius $r$ and thickness d$r$ around an atom of type $i$ is $n_{ij}(r) = 4\pi r^2 \rho_j g_{ij}(r)\mathrm{d}r$. The relationship between $g_{ij}(r)$ and scattering data will be discussed in section 2.1.2. The left of figure 1.6 shows a 2D assembly of atoms, with the three nearest neighbours of one of the atoms highlighted and the corresponding distances highlighted on the PDF. The atom search is repeated for all atoms in the assembly to produce a pair distribution function as shown on the right of figure 1.6.

From the PDF, it is possible to extract information about the local atomic environment, in the example in figure 1.6, the coordination number of the first shell could be found from the area under the first peak. It is also possible to extract information on the angles between atoms based on the atomic separation. The PDF is extracted by application of a Fourier transform to a diffraction scattering function, therefore in order to access the PDF, we have to perform scattering experiments.

Diffraction is a widely used method of structural determination. Analysis of a diffraction pattern yields the materials average crystal structure, composition, lattice parameters, and symmetry. From the structural determination information on the chemical bonding and reactivity of a material can also be derived. The two most widely used types of radiation for diffraction are x-ray and neutron.

In a diffraction experiment, the structure factor $S(\mathbf{Q})$ is measured, and it is from this that the PDF can be generated. For radiation incident on a system containing $N$ atoms, the change in wavevector after scattering, $\mathbf{Q}$ is given by $\mathbf{Q} = \mathbf{k}_i - \mathbf{k}_s$ where $\mathbf{k}_i$ and $\mathbf{k}_s$ are the initial and scattered wavevectors. The structure factor has the form

$$S(\mathbf{Q}) = \frac{1}{N}\sum_{ij} b_i b_j \left\langle \exp\left(i\mathbf{Q}(\mathbf{r_i} - \mathbf{r_j})\right)\right\rangle, \tag{1.2}$$

where $\mathbf{r_i}$ is the instantaneous position of atom type $i$, and $b_i$ is its scattering length [19].

In addition to using the PDF to ascertain how the deviations in the local structures change as materials approach their dielectric transitions, it is necessary to be aware that the types of materials we are looking at are crystalline, and as such will have some long range order which we need to accurately model.

This long range order can also include cooperative motion of the polar species which can tell us if the material is completely ordered just below the transition temperature, or if the ordering process continues as the material is cooled further. Therefore the scattering data need to include information on both the short and long-range order.

### 1.2.2 Diffuse and Bragg scattering and the local and long range structure

The scattering function can be broken into two distinct parts [20], the Bragg and diffuse scattering contributions such that

$$S(\mathbf{Q}) = S_{\text{Bragg}}(\mathbf{Q}) + S_{\text{Diffuse}}(\mathbf{Q}) \tag{1.3a}$$

$$S_{\text{Bragg}}(\mathbf{Q}) = \frac{1}{N}\left\langle \left| \sum_i b_i \exp(i\mathbf{Q}\cdot\mathbf{r_i}) \right| \right\rangle^2 \tag{1.3b}$$

$$S_{\text{Diffuse}}(\mathbf{Q}) = S(\mathbf{Q}) - S_{\text{Bragg}}(\mathbf{Q}). \tag{1.3c}$$

The Bragg component gives average one-body structural information [21] and does not contain any pair correlation information, only the spatial average position of each atom type is derived. Atoms which move away from the average position diminish the intensity of the Bragg peak, which is corrected for with atomic displacement parameters (ADPs).

The diffuse scattering is everything other than the contribution from the perfect crystalline order. Diffuse scattering is much weaker than Bragg and arises from a breakdown of space group symmetry [22] and from it information on the deviations from the average structure can be found. The difference between the structural information from Bragg and diffuse scattering is that for Bragg scattering $\langle r_i\rangle - \langle r_j\rangle$ is extracted, whereas $\langle r_i - r_j\rangle$ is extracted from the diffuse scattering. This can be seen in equation (1.2), where structure factor is defined we can get information about $r_i - r_j$ whereas in equation (1.3b), which only deals with the Bragg scattering, we only get information about the average distribution of one particular species.

The method of collecting and analysing both the Bragg and the diffuse component of the scattering simultaneously is called total scattering. Scattering from a perfect crystal would give only Bragg scattering, whereas the scattering from an amorphous material with no long range order is diffuse [23]. For materials that, while not perfectly crystalline do display some long-range order, total scattering is an ideal method to gather information on both short and long range correlations.

### 1.2.3 The partial pair distribution function

However, the PDF as extracted from scattering experiments does not differentiate which atomic pairs contribute to it at any point. For simple materials such as the example in figure 1.6 it

is straightforward to see the contribution each pair has to the PDF, but for complex systems, especially organic molecules it is not unusual for one peak to contain information from several different scattering pairs. Furthermore the PDF becomes increasing complex with increasing $r$ as there are more atomic pairs to contribute to the peaks. It is useful to deconstruct the PDF into contributions from each atomic pair, the partial PDFs.

The partial PDF is simply the part of the PDF which only has contributions from two different atom pairs. It is not possible to directly extract the partial PDFs from the PDF derived from scattering data, however computer models of the structure can be generated and the PDFs compared to experimental data, and the partial PDFs can be extracted from these models.

### 1.2.4 Computer models and the partial PDF

Computer models can be split into two groups, small-box models and big-box models.

Small box models such as `PDFFIT` [24, 25] / `PDFFIT2`[26] use configurations consisting of only one or two unit cells and perform "real-space Rietveld refinements". The PDF of the model is calculated and compared to the experimentally derived PDF. Atomic displacement parameters and peak-sharpening functions are utilised to account for short-range correlations within the model [25]. The limitation of small-box modelling is that it is assumed that the structure can be described using relatively few atoms [26], however using small box models means that it is not possible to see long range correlations. When fluctuations in a structure are being investigated, larger structural models are required.

Big-box models such as the reverse Monte Carlo (RMC) method typically span tens of thousands of atoms, with length scales such that cooperative ordering can be reproduced in the model. Additionally the RMC method incorporates contributions from diffuse scattering, and as such can produce models which include information about short-range correlations. Details of the RMC algorithm and the program `RMCProfile` will be given in section 2.5, now however it is is sufficient to state that a supercell, an initial configuration of atoms, is generated from the average unit cell. Atoms in the configuration are moved at random, by a random amount in an iterative process until the model PDF and scattering function are in agreement with the experimentally observed functions.

In big-box modelling such as RMC, the final model comprises a list of thousands of atomic species and their coordinates, from these it is straightforward to extract the partial PDFs, and thus the local structure. Multiple examples of the same site, say C in a formate group - are accumulated and provide information on the atomic displacement parameters.

### 1.2.5 Example of total scattering and the RMC Method

A key result highlighting how the average structure is not necessarily representative of the "true" instantaneous structure, and how computer methods were used to solve the problem is given by a study by Tucker et al. [27] into the structure of $\beta$-cristobalite. In $\beta$-cristobalite the average bond structure implies that the Si$-$O$-$Si bond is linear with a shorter than expected Si$-$O bond. However when the diffuse scattering is considered, information about the atomic pair distribution functions (not just the distribution of positions of individual atoms) is made available. Analysis of RMC models which included the diffuse scattering found that the

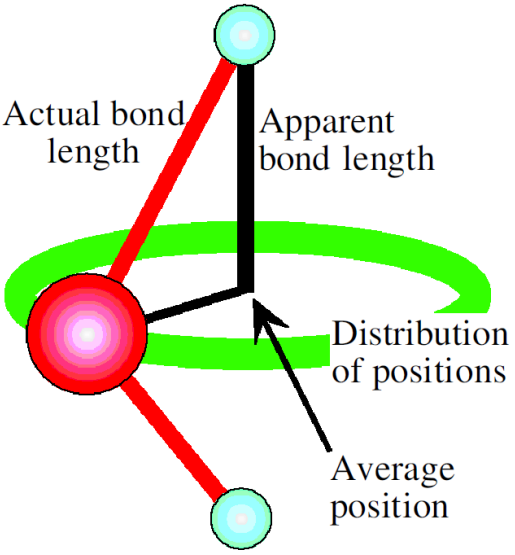


**Figure 1.7:** The local structure of Si—O—Si in $\beta$-cristobalite highlighting the difference between the average and instantaneous structure. The red oxygen is distributed around the green silicon, the average structure implies linear Si—O—Si bonding, however RMC modelling of diffuse scattering indicated otherwise. Image taken from [28].

distribution of the O about the Si···Si axis which had given the impression of a short, linear bond, was in fact a result of a longer, angled bond (figure 1.7).

The work of this thesis can be thought of as a continuation of this type of analysis. In this thesis I am asking if it is possible, through total scattering and RMC refinement, to perform similar analysis on significantly more complicated structures such as organic and metal-organic ferroic materials, and can the mechanisms behind their phase transitions be explained through improved understanding of the local structure?

## 1.3 Overview of the thesis

In this thesis I will describe the processing and analysis methods applied to total scattering data of three ferroelectric materials as they undergo phase transitions. Chapter 2 details the experimental techniques and programs used to produce the atomistic configurations. Chapter 3 details the analysis into the onset of electric ordering in dimethylammonium manganese formate (DMMnF), while chapter 4 describes the magnetic structure of it. Potassium imidazolium hexacyanoferrate (III) (PIH) is discussed in chapter 5 and triglycine sulfate (TGS) in chapter 6. Finally the broad conclusions and overarching themes of my work, along with possible future analysis are provided in chapter 7.

Analysis and processing programs written in `Fortran` and in `MATLAB` are provided in the electronic appendix, and data collection run numbers, RMC restraints, and lattice parameters are found in appendices A B, and C.

# Chapter 2

# Methods

In this thesis the structural origin of the ordering mechanisms of three materials have been investigated. While each material had its own unique features which needed to be accounted for, all analysis followed the same broad pattern, outlined in the flowchart in figure 2.1. Firstly, neutron total scattering data were collected at the `ISIS` neutron spallation facility. From these scattering data the pair distribution functions were derived, and Rietveld refinement was performed. From the Rietveld refinement, perfectly crystalline atomistic configurations consistent with the scattering data were found and used as a starting point for reverse Monte Carlo (RMC) refinement. The program `RMCProfile` was used to generate atomistic models consistent with the real and reciprocal-space data and Bragg profiles. Finally, bespoke analysis programs were written to derive features such as molecular rotation, bond angles and relationships between neighbouring magnetic moments. In this section I will discuss the data collection and correction methods, along with the RMC algorithm and `RMCProfile`.

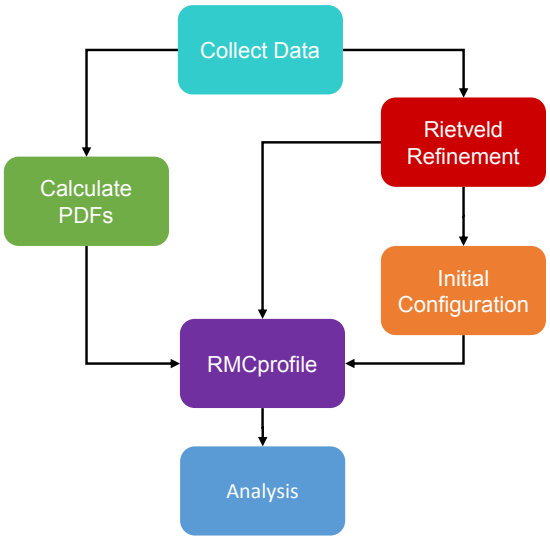


**Figure 2.1:** Flowchart showing the work pattern carried out on the three materials in this thesis.

## 2.1 Diffraction

For all materials presented neutron total scattering was used rather than x-rays; neutrons were the preferred source for three reasons. Firstly, for neutrons the scattering power of a species is independent of the atomic number $Z$. Secondly neutrons have a magnetic moment, which can interact with the material and be used to collect information on its magnetic structure. Finally with neutrons it is possible to collect data over a very large $Q$ range.
When discussing neutron scattering abilities two quantities are used to quantify the scattering ability of a particular atom. The scattering length, $b$ which has units of length, and the scattering cross section, $\sigma$, where $\sigma = 4\pi b^2$ and has units of area.

### 2.1.1 Neutrons vs x-rays

The suitability of neutrons over x-rays for the materials studied in this thesis can be broken down into three points.

Firstly, all three of the materials presented in this thesis possess a significant organic component, where the making and breaking of hydrogen bonds influences the structural changes accompanying the phase transition. Therefore the radiation source chosen must be sensitive to light atoms. When x-rays scatter from matter they are interacting with the electron cloud of each atom. This means that x-ray scattering is dominated by elements with high atomic numbers, making scattering from hydrogen very difficult to identify. Conversely, neutrons interact with the nucleus of the atom via the strong nuclear force, and there is no correlation between atomic number and scattering length. The change in coherent neutron scattering lengths with respect to atomic number is given in figure 2.2 and we see no obvious $Z$ dependence.

Neutrons also have spin which interacts with the spin of the nucleus and affects the resultant diffraction pattern. The scattering from the sample can be broken into two distinct parts, coherent and incoherent. For coherent scattering the scattering from each atom type can be thought of as independent of the spin state (based on its isotope), whereas there are two sources of incoherent scattering, different isotopes and different spin states. Atoms with only one isotope and zero spin will have no incoherent scattering, and for atoms where the natural abundance of one particular isotope is significantly greater than any other, the expected incoherent contribution from the other isotopes is small. For the work presented in this thesis the incoherent scattering is unwanted and limits the accuracy of the information that can be taken from the diffraction pattern, therefore every effort is taken to reduce its contribution.

For most atoms the coherent scattering cross section is significantly larger than the incoherent cross section, however there are a few a notable exceptions, most important for this work is $^1$H. The coherent scattering length for $^1$H is $-3.74$ fm, the incoherent scattering length is 25.27 fm [29]. Diffraction patterns taken from materials containing $^1$H will have a significant unwanted contribution over all values of $Q$ from the hydrogen incoherent scattering. In order to avoid this incoherent scattering, isotopic substitution is applied. The spin state of the $^2$H (deuterium) nucleus is 1 and it has an incoherent scattering length of 4.04 fm[29], much smaller than the incoherent scattering length for $^1$H. Therefore replacing hydrogen with deuterium results in a chemically identical sample with a significantly reduced incoherent contribution.

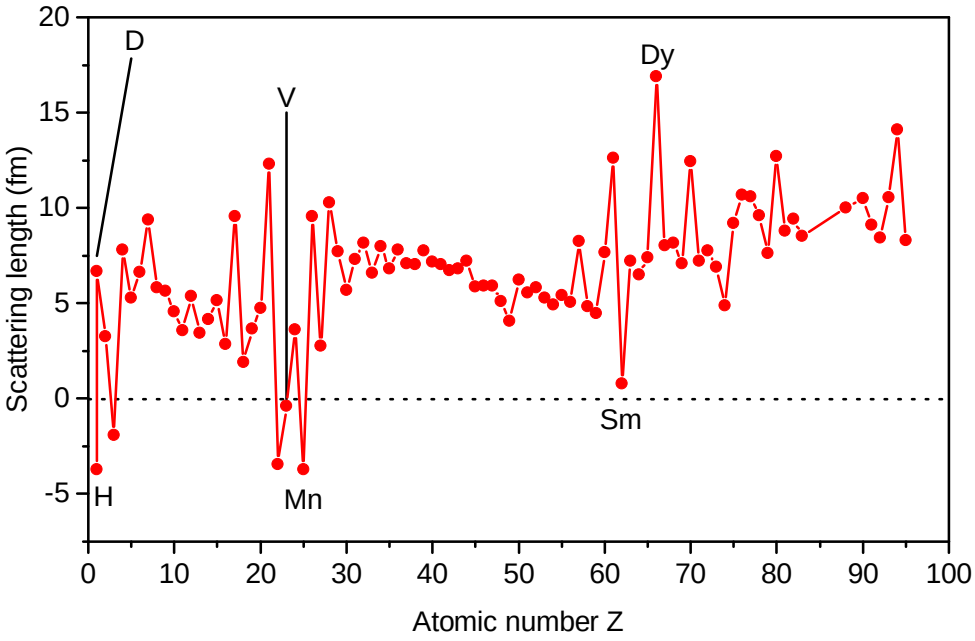


**Figure 2.2:** The change in the coherent neutron scattering lengths with increasing atomic number, $Z$. Unlike with x-rays, no correlation between scattering length and atomic number is observed. The difference in scattering length of hydrogen and deuterium can be seen. Data are from [29]

A final point in favour of deuteration is that the magnitude of the coherent scattering length of deuterium is greater than the magnitude of that of hydrogen (6.67 fm vs. $-3.74$ fm - see figure 2.2) , meaning deuterium will contribute more significantly to the neutron diffraction pattern than hydrogen would have.

In addition to interacting via the strong nuclear force, neutrons can also interact with the magnetic moment of the atom. One of the materials reported in this thesis, DMMnF, is known to display magnetic ordering below 8.5 K [30], therefore a radiation source which is sensitive to magnetic moments as well as to atomic position allows the onset of magnetic ordering to be observed. Magnetisation arises from unpaired electrons in the electron cloud, so when the neutrons undergo magnetic scattering they are interacting with the electron cloud as x-rays would (length scales of $\approx 10^{-10}$m). Due to the relative length scales of the radiation wavelength and the electron cloud, there is a reduction in scattering intensity at high $Q$ values for magnetic neutron diffraction.

The final difference between neutron and x-ray diffraction is the range of $Q$ values obtainable. In order to produce a useful PDF, the structure factor must be measured to high $Q$ values, and with a high statistical accuracy [31]. The limit on the resolution, $\Delta r$, of the real-space pair distribution functions is given by

$$\Delta r = \frac{2\pi}{Q_{\text{max}}}. \tag{2.1}$$

Neutron scattering lengths do not decay with increasing $Q$ as x-ray form factors do and so the data can readily be collected to high $Q$ values, where the higher the $Q_{\text{max}}$ the higher resolution of the resultant PDFs. For the work carried out in this thesis, `ISIS` instruments `GEM` and `POLARIS` were used to collect scattering data. Both can readily collect up to $Q_{\text{max}}$

values of $\approx 50\,\text{Å}^{-1}$. In practice the $Q_{max}$ value was chosen, during derivation of the PDF, to be between $30\,\text{Å}^{-1}$ and $46\,\text{Å}^{-1}$ depending on the noise observed in the scattering data. Construction of XPDF, an instrument designed to produce high quality PDFs from x-ray scattering, is underway at the Diamond light source. With optimal settings, the highest $Q_{max}$ which is achievable is $41.2\,\text{Å}^{-1}$ to $45.1\,\text{Å}^{-1}$, using a 76.6 keV beam with a wavelength of 0.16 Å [32], a value which has been exceeded by the two neutron instruments used.

Neutron scattering is not without its downsides however. Due to the low flux of the beam, data collection times are significantly longer than they would be for an x-ray source. Neutrons must be produced at central facilities, and as such there is a lag between formulation of an experiment and being able to carry it out. Finally the cost of producing samples for neutron experiments is usually greater than it is for x-rays. Neutron experiments such as the ones performed for the three materials presented in this thesis used 1 g to 4 g of sample, significantly more than would be used in an x-ray experiment. Another additional cost associated with neutron scattering is the need to fully deuterate the samples, which for the three materials presented here meant starting with fully deuterated precursors.

### 2.1.2 Diffraction formalism

Different communities of crystallographers define scattering functions differently, the work in this thesis follows the nomenclature outlined by Keen [33]. This section will discuss deriving the pair distribution functions from scattering data, and dealing with total scattering data.

Any given sample can be described as an assembly of atoms whose positions can be approximated by a Dirac delta function, and their ability to scatter neutrons given by the scattering length, $b$. The scattering function, $F(\mathbf{Q})$, is the Fourier transform of the sample's density, $\rho(\mathbf{r})$ over all space where, for a monatomic material

$$\rho(\mathbf{r}) = \sum_j b_j \delta(\mathbf{r_j} - \mathbf{r}). \tag{2.2}$$

Application of the standard Fourier transform $\int \delta(\mathbf{r_j} - \mathbf{r}) \exp(i\mathbf{Q} \cdot \mathbf{r}) d\mathbf{r} = \exp(i\mathbf{Q} \cdot \mathbf{r_j})$ gives:

$$\begin{aligned} F(\mathbf{Q}) &= \int \rho(\mathbf{r}) \exp(i\mathbf{Q} \cdot \mathbf{r}) d\mathbf{r} \\ &= \sum_j b_j \exp(i\mathbf{Q} \cdot \mathbf{r_j}), \end{aligned} \tag{2.3}$$

where the integral is taken over all space.

Neutron scattering experiments measure the scattered intensity per unit atom - $\left|F(\mathbf{Q})\right|^2$, which we will call the structure factor $S(\mathbf{Q})$, and is given in equation 2.4

$$\begin{aligned} S(\mathbf{Q}) &= \frac{1}{N} \left|F(\mathbf{Q})\right|^2 \\ &= \frac{1}{N} \left| \sum_j b_j \exp(i\mathbf{Q} \cdot \mathbf{r_j}) \right|^2 \\ &= \frac{1}{N} \sum_{i,j} b_i b_j \exp[i\mathbf{Q} \cdot (\mathbf{r_i} - \mathbf{r_j})] \\ &= \frac{1}{N} \sum_{i,j} b_i b_j \exp(i\mathbf{Q} \cdot \mathbf{r_{ij}}), \end{aligned} \tag{2.4}$$

where $\mathbf{r_{ij}}$ is the separation between pairs of atoms and $N$ is the total number of atoms in the sample.

In total scattering experiments, the dynamic structure factor, $S(\mathbf{Q},\omega)$ is measured, where

$$S(\mathbf{Q},\omega) = \frac{1}{N}\sum_{i,j} b_i b_j \int \exp(i\mathbf{Q}\cdot\mathbf{r_{ij}}(t))\exp(-i\omega t)\mathrm{d}t. \tag{2.5}$$

Here, $\mathbf{r_{ij}}(t)$ is $\mathbf{r_i}(0) - \mathbf{r_j}(t)$, and $\omega$ corresponds to the frequency of dynamic processes between atoms $\mathbf{r_i}$ and $\mathbf{r_j}$, and is related to the change in energy of the neutron beam by $\Delta E = \hbar\omega$. From equation (2.5), we see that $S(\mathbf{Q},\omega)$ is the time average of all instantaneous pair correlations and that it we can extract information on the average instantaneous structure, rather than the average structure (see $\beta$-cristobalite example in 1.2.5). The total scattering experiments performed for this thesis collected data over all energies with no record of the change in energy. Therefore when $S(\mathbf{Q},\omega)$ is integrated over all $\omega$ – equation (2.6) – the distinction between the different types of diffuse scattering are lost [22] and we only see snapshots of the instantaneous structure.

$$S(\mathbf{Q}) = \int S(\mathbf{Q},\omega)\mathrm{d}\omega \tag{2.6}$$

The structure factor can also be expressed in terms of $\mathbf{Q}$ and time, $t$, by:

$$S(\mathbf{Q},t) = \int S(\mathbf{Q},\omega)\exp(i\omega t)\mathrm{d}\omega, \tag{2.7}$$

which will equal $S(\mathbf{Q})$ at $t = 0$. Therefore, we see that collecting data over all energies removes information about interatomic separations at $t \neq 0$, meaning the collected scattering data only corresponds to the sum of instantaneous separations, rather than the time average of $\mathbf{r_i}(0) - \mathbf{r_j}(t)$.

In this thesis, all total scattering experiments were performed on powder (polycrystalline) samples, and so the collected scattering data is averaged over all orientations of $\mathbf{Q}$ and $\mathbf{r_{ij}}$, to give $\langle\exp(i\mathbf{Q}\cdot\mathbf{r_{ij}})\rangle$

$$\langle\exp(i\mathbf{Q}\cdot\mathbf{r_{ij}})\rangle = \frac{1}{4\pi}\int_0^{2\pi} d\phi \int_0^{\pi} \exp(iQr_{ij}\cos\theta)\sin\theta d\theta, \tag{2.8}$$

where $Q = |\mathbf{Q}|$, $r_{ij} = |\mathbf{r_{ij}}|$, $\theta$ is the polar angle between $\mathbf{Q}$ and $r_{ij}$ ranging between 0 and $\pi$, and $\phi$ is the azimuthal angle ranging from 0 to $2\pi$. If $\cos\theta$ is substituted by $x$ then $-\sin\theta\mathrm{d}\theta = \mathrm{d}x$, with $x$ ranging from $-1$ ($\cos\pi$) to $+1$ ($\cos 0$), accounting for the minus sign of $\sin\theta\mathrm{d}\theta$ gives:

$$\begin{aligned}
\langle\exp(i\mathbf{Q}\cdot\mathbf{r_{ij}})\rangle =& \frac{1}{4\pi}\int_0^{2\pi} d\phi \int_{-1}^{+1} \exp(iQr_{ij}x)\mathrm{d}x \\
=& \frac{1}{2}\int_{-1}^{+1} \exp(iQr_{ij}x)\mathrm{d}x \\
=& \frac{1}{2}\frac{1}{Qr_{ij}}\left[-i\exp(iQr_{ij}x)\right]_{x=-1}^{x=+1} \\
=& \frac{\sin(Qr_{ij})}{Qr_{ij}}
\end{aligned} \tag{2.9}$$

where the final step utilised Euler's formula $e^{ix} = \cos x + i\sin x$. Substituting $\left\langle\exp(i\mathbf{Q}\cdot\mathbf{r_{ij}})\right\rangle$ into equation 2.4 gives us a way to calculate the experimentally observed structure factor, $S(Q)$, averaged over all orientations, from an atomic configuration.

$$S(Q) = \frac{1}{N}\sum_{i,j} b_i b_j \frac{\sin(Qr_{ij})}{Qr_{ij}}, \tag{2.10}$$

which can be broken down into two parts, one involving scattering between the same atoms ($i = j$), and the scattering between pairs where $i \neq j$

$$S(Q) = \frac{1}{N}\sum_i b_i^2 + \frac{1}{N}\sum_{i\neq j} b_i b_j \frac{\sin(Qr_{ij})}{Qr_{ij}}. \tag{2.11}$$

For a sample with a known concentration of species $i$, $\frac{1}{N}\sum_i b_i^2$ can be readily substituted for $\sum_i c_i b_i^2$, where $c_i$ is the concentration of species $i$.

The second part of equation (2.11) can be described as the number of atoms of type $j$ in a shell of radius $r$ and thickness d$r$ around an atom of type $i$, $n_{ij}(r)$ which is given by

$$n_{ij}(r) = 4\pi r^2 \rho_j g_{ij}(r)\mathrm{d}r \tag{2.12}$$

where $g_{ij}(r)$ is the partial radial distribution function. In a sample with number density $\rho$ and where the fraction of atom type $i$ and $j$ is $c_i$ and $c_j$ respectively, $\rho_j = \rho \cdot c_j$ and the second part of equation (2.11) can be redefined using $g_{ij}(r)$ according to

$$\frac{1}{N}\sum_{i\neq j} b_i b_j \frac{\sin(Qr_{ij})}{Qr_{ij}} = 4\pi\rho \int \sum_{i\neq j} c_i c_j b_i b_j r^2 g_{ij}(r)\frac{\sin(Qr)}{Qr}\mathrm{d}r. \tag{2.13}$$

Therefore, the scattering function $S(Q)$, equation (2.11), can be expressed as:

$$S(Q) = \sum_i c_i b_i^2 + 4\pi\rho \int \sum_{i\neq j} c_i c_j b_i b_j r^2 g_{ij}(r)\frac{\sin(Qr)}{Qr}\mathrm{d}r. \tag{2.14}$$

In the high $r$ limit of equation (2.12), $g_{ij}(r) \to 1$ as the thin shell of radius $r$ is sampling a more uniform distribution of the atoms. The integral in (2.14) diverges at $Q = 0$ since $g_{ij}(r) \to 1$ as $r \to \infty$ . For this reason, we define a function $i(Q)$ such that

$$i(Q) = 4\pi\rho \int \sum_{i\neq j} c_i c_j b_i b_j r^2 (g_{ij}(r) - 1)\frac{\sin(Qr)}{Qr}\mathrm{d}r, \tag{2.15}$$

then $i(Q)$ can be expressed in terms of the scattering function $S(Q)$ according to

$$i(Q) = S(Q) - \sum_i c_i b_i^2 - 4\pi\rho \int \sum_{i\neq j} c_i c_j b_i b_j r^2 g_{ij}(r)\frac{\sin(Qr)}{Qr}\mathrm{d}r. \tag{2.16}$$

The real-space pair distribution function $D(r)$ is defined as

$$D(r) = 4\pi\rho r \sum_{i,j} c_i c_j b_i b_j (g_{ij}(r) - 1), \tag{2.17}$$

which can be expressed in terms of $i(Q)$ by

$$\begin{aligned} i(Q) =& 4\pi\rho \int \sum_{i\neq j} c_i c_j b_i b_j r^2 (g_{ij}(r) - 1)\frac{\sin(Qr)}{Qr}\mathrm{d}r \\ Qi(Q) =& 4\pi\rho \int \sum_{i\neq j} c_i c_j b_i b_j r (g_{ij}(r) - 1)\sin(Qr)\mathrm{d}r \\ Qi(Q) =& \int D(r)\sin(Qr)\mathrm{d}r, \end{aligned} \tag{2.18}$$

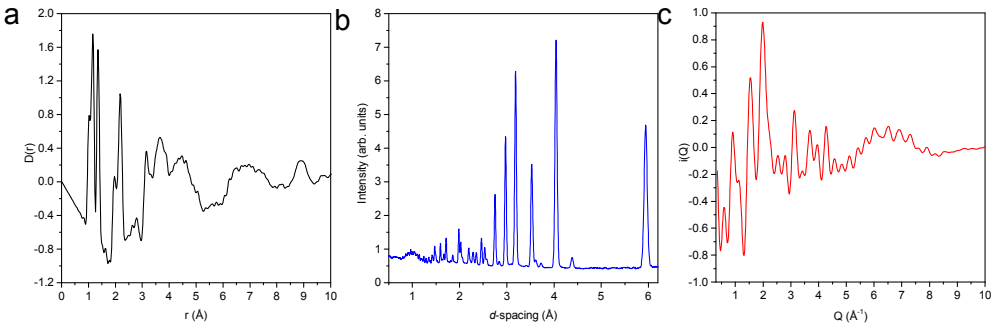


**Figure 2.3:** Three functions all derived from the same neutron scattering data: (a) $D(r)$; (b) Bragg profile; and (c) $i(Q)$

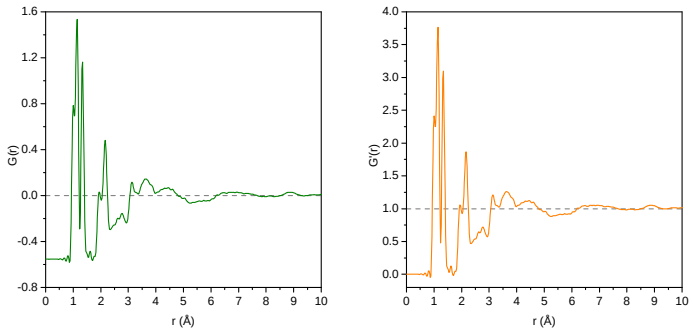


**Figure 2.4:** Left: $G(r)$ with a high $r$ limit of 0. Right: $G'(r)$ with a high $r$ limit of 1. Both functions are derived from the same scattering data as shown in figure 2.3. For both $G(r)$ and $G'(r)$ the peaks at high $r$ are less pronounced than they are in $D(r)$

with the corresponding reverse Fourier transform giving

$$D(r) = \frac{1}{(2\pi)^3} \int Qi(Q)\sin(Qr)\mathrm{d}r. \tag{2.19}$$

Figure 2.3 shows $D(r)$, the Bragg profile and $i(Q)$ all derived from the same neutron scattering data. The PDF $D(r)$ was calculated up to $r = 40$ Å, and $i(Q)$ was collected up to a $Q$ value of 40 Å$^{-1}$. The full $d$-spacing range of the Bragg profile is shown.

Two other real-space functions will be mentioned in this thesis $G(r)$ and $G'(r)$. These two functions are related to $D(r)$ by

$$G(r) = D(r) - 4\pi r\rho \tag{2.20a}$$

$$G'(r) = \frac{G(r)}{\left(\sum_i c_i b_i\right)^2} + 1$$

$$G'(r) = \frac{D(r) - 4\pi r\rho}{\left(\sum_i c_i b_i\right)^2} + 1 \tag{2.20b}$$

It is sometimes useful to use $G(r)$ or $G'(r)$ instead of $D(r)$, for example when calculating areas under peaks $G(r)$ has a flat baseline at low $r$ as seen in figure 2.4.

$G'(r)$ is a normalised version of $G(r)$ where the low $r$ limit which was previously material specific is now constant at 0, therefore $G(r)$ and $G'(r)$ have different limiting values at high $r$

too;

$$G(r < r^0) = -\left(\sum_i c_i b_i\right)^2 \qquad G(r \to \infty) = 0 \tag{2.21a}$$

$$G'(r < r^0) = 0 \qquad G'(r \to \infty) = 1. \tag{2.21b}$$

In equation (2.21) $r^0$ is the shortest distance between $r_{ij}$ [33], that is the point on the PDF where there is no atomic pair density.

In this thesis information on the real-space structures of the materials has been stated in terms of $D(r)$. When $D(r)$ and $G(r)$ are compared (figures 2.3a and 2.4) it can be seen that the peak intensity in $D(r)$ falls off much slower at high $r$ than it does in either $G(r)$ or $G'(r)$ which means that $D(r)$ is more sensitive to changes in the structure at high $r$ than $G(r)$ is.

## 2.2 Instruments

All neutron scattering data in this thesis were collected at ISIS, the pulsed neutron (and muon) source at the Rutherford Appleton Laboratory. ISIS is a spallation source where $H^-$ ions are accelerated along a 70 MeV linac before having the electrons stripped and being introduced to an 800 MeV synchrotron, as shown in figure 2.5. The protons are extracted from the synchrotron and collide with a tungsten target. This collision knocks out neutrons from the tungsten which are ejected radially. Target station 1 at ISIS produces 50 pulses of neutrons a second during optimal operation, this corresponds to a proton current of approximately 160 µA. The neutrons exiting the target have a wide range of energies, and hence wavelengths. The shorter the wavelength of the neutrons, the smaller the time-of-flight. The energies of the exiting neutrons are too high to perform diffraction experiments on and so the neutrons are cooled via a moderator. A moderator is a volume of material, usually containing a significant fraction of hydrogen or other light atoms (and so with a comparable mass to neutrons) which slow the neutrons via collisions to energies more suitable for diffraction. Figure 2.5 shows the layout of instruments around target station one, the two instruments which are used in this thesis, GEM and POLARIS have been highlighted. ISIS is a time-of-flight source which means the length of time the neutrons take to reach the detectors after scattering from the sample is recorded, and related back to the incident wavelengths. The flight path from the target to the detector is only tens of meters and while the neutrons have been slowed, there is not a lot of travel time for the different speed neutrons to separate before they impinge on the sample. For high time-resolution diffraction, instruments can be placed at greater distances from the target, this allows the pulse of neutrons to spread out and gives better time-resolution of the resultant scattering pattern.

### 2.2.1 GEM

Scattering data for DMMnF were collected on the GEneral Materials diffractometer (GEM). The distribution of the detector banks is shown in figure 2.6, these detector banks cover a $2\theta$ range of 1.7° to 171.4°. Neutrons received by GEM have been cooled by a liquid methane moderator with a temperature of 100 K to 110 K [35], and the distance between the moderator and the sample is 17 m.

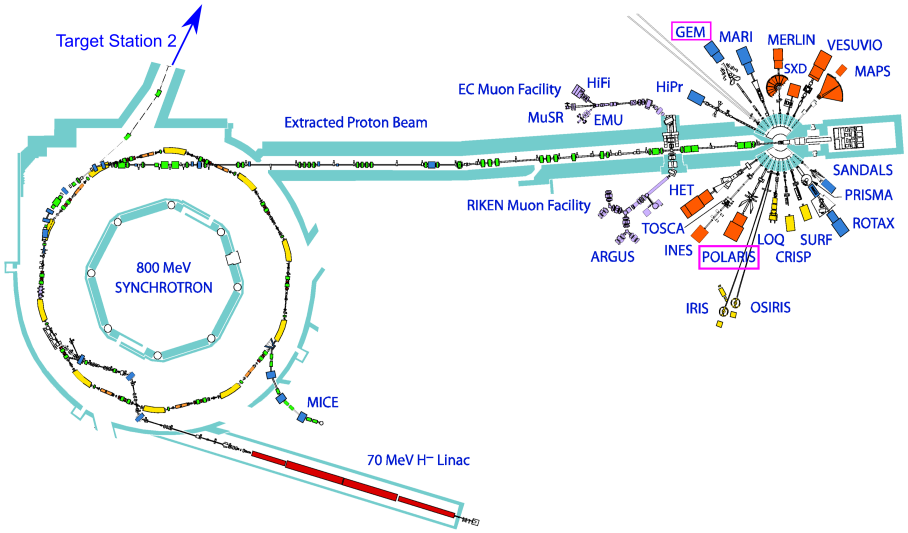


**Figure 2.5:** ISIS target station 1, with the closest instruments surrounding it [34]. The positions of GEM and POLARIS have been highlighted.

For both GEM and POLARIS the incident beam enters the diffractometer, and impinges upon the sample, and anything else in it's path, such as the sample environment. The beam is scattered by $2\theta$ and makes contact with a detector.

### 2.2.2 POLARIS

Scattering data for PIH and TGS were collected on POLARIS, shown in figure 2.7. The neutrons received by POLARIS have been cooled by a $H_2O$ moderator at 316 K [36]. The distance between the moderator and the sample is 12 m, slightly less than GEM, and as such POLARIS has a slightly poorer reciprocal space resolution than GEM due to poorer distinction of neutron flight times. POLARIS covers a $2\theta$ range of approximately 6° to 168° [37].

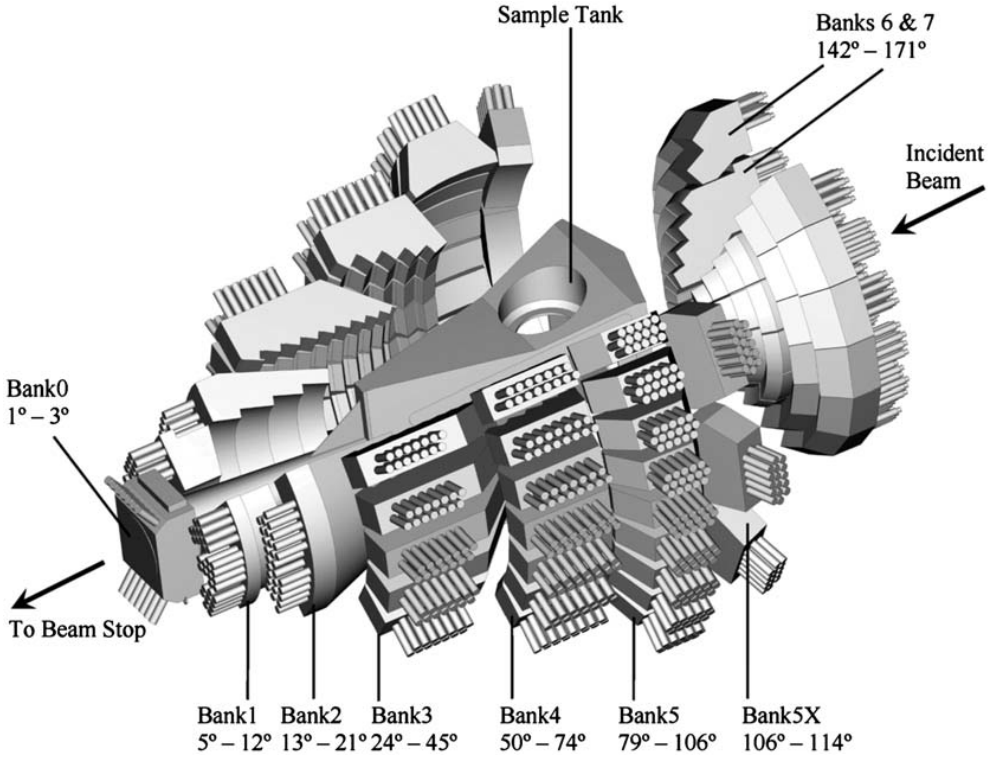


**Figure 2.6:** View of the GEM diffractometer, showing the individual detector banks from [35].

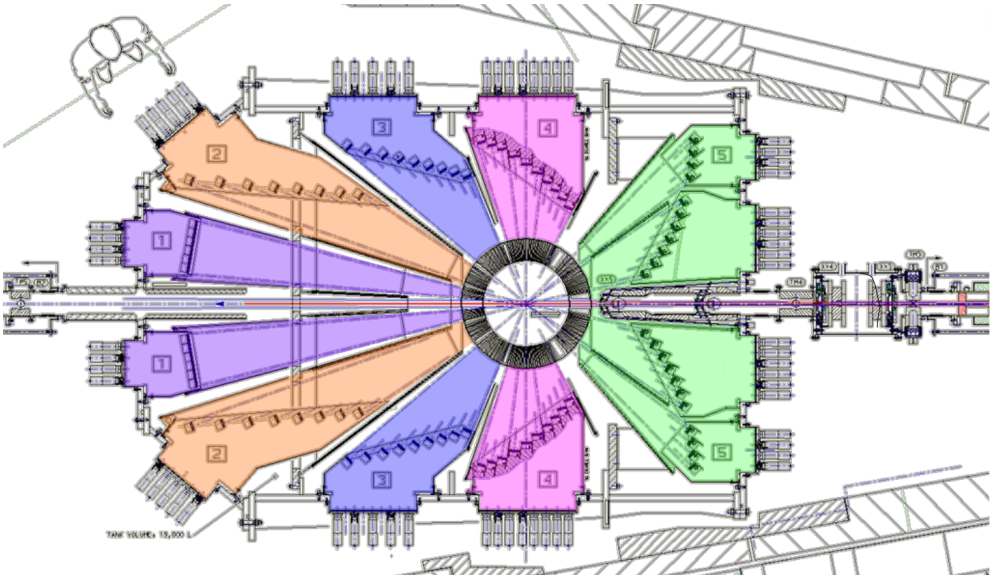

**Figure 2.7:** Schematic view of POLARIS adapted from [37] with detector banks 1–5 shaded with different colours

## 2.3 Data collection and correction

There are few programs available for extracting the differential cross section from raw neutron scattering data, PDFgetN [38] is one, and GUDRUN is another. The data presented in this thesis were corrected using GUDRUN [39]. GUDRUN was written and is maintained by Alan Soper, and is used to analyse diffraction data from several ISIS instruments, including POLARIS and GEM. In addition to extracting the cross section, GUDRUN also calculates the scattering function $i(Q)$ from which real-space PDFs can be derived. Both $i(Q)$ and the PDFs are used for RMC refinement

In order to fully correct the data, five different scattering measurements need to be made. The procedure is outlined in detail in [22] and [39], and will briefly be discussed below with respect to the data collected for this thesis.

**1 Sample measurement.** For all data presented in this thesis, total scattering measurements were performed on powder samples in 8 mm thin-walled vanadium cans. The length of time the data at each temperature were collected for corresponded to a total proton beam charge of 900 µA h to 1200 µA h. 150 µA h corresponds to approximately one hour of collection time when ISIS is running optimally, so total scattering measurements typically take 6 to 8 hours. Due to the relatively slow collection time, and to allow periodic checks of the data while being recorded, the sample collection data were broken into multiple scans corresponding to $\approx$ 150 µA h runs. The first step in the GUDRUN program is to combine the multiple measurements into one spectrum. Vanadium cans are used because vanadium has a low coherent scattering length (figure 2.2) and vanadium Bragg reflections will be significantly weaker than those from the sample.

**2 Empty diffractometer.** This is the background measurement. For total scattering measurements in GEM and POLARIS data were collected for approximately 150 µA h.

**3 Empty sample environment.** Background data were collected in furnaces, CCRs and cryostats. Despite being optimised for use in a neutron environment, each sample environment attenuates and scatters the beam which needs to be corrected for. The amount of data required for a sample environment correction depended on not only the type of environment (i.e. furnace or cryostat) but also the particular model. Typically empty sample environment data were collected for 200 µA h to 600 µA h as different environments attenuate the bean differently.

**4 Empty container.** A container with the same composition and dimensions as the one used for the sample was placed into the environment and the instrument response recorded. Because the scattering from the empty container is weak, it is not necessary to collect for a long time, typically data are collected for half as long as a sample measurement. The contribution to the scattering from the empty container is subtracted from the scattering from the sample measurement.

**5 Vanadium standard.** The response of the instrument to a vanadium rod with the same dimensions as the sample container in an empty diffractometer was recorded and used for normalisation. The vanadium standard experiment is performed because beam attenuation and multiple scattering events for vanadium can be readily calculated and used to compare attenuation and multiple scattering estimates for non-ideal materials such as the samples [39].

At the start of each cycle, a standard sample was placed into the instrument, the response

was used to calibrate the instrument geometry and identify inactive detectors. The incident beam is monitored by a monitor placed in the beam before the instrument, which collects for the same amount of time as a data collection. The monitor is designed such that any attenuation of the beam due to its presence is minimal.

Figure 2.8 - adapted from [40] - shows the workflow performed by `GUDRUN` to generate the differential scattering cross section, and hence the scattering functions of the sample. In figure 2.8 the blue boxes detail the processes performed by `GUDRUN`. The orange box is information generated at the start of each cycle, such as the detector geometry and a table of neutron scattering lengths. The green boxes are for input provided by the user, such as the raw scattering files, sample composition, a "tweak factor" (described later) and smoothing functions applied to the Fourier transform of the scattering data.

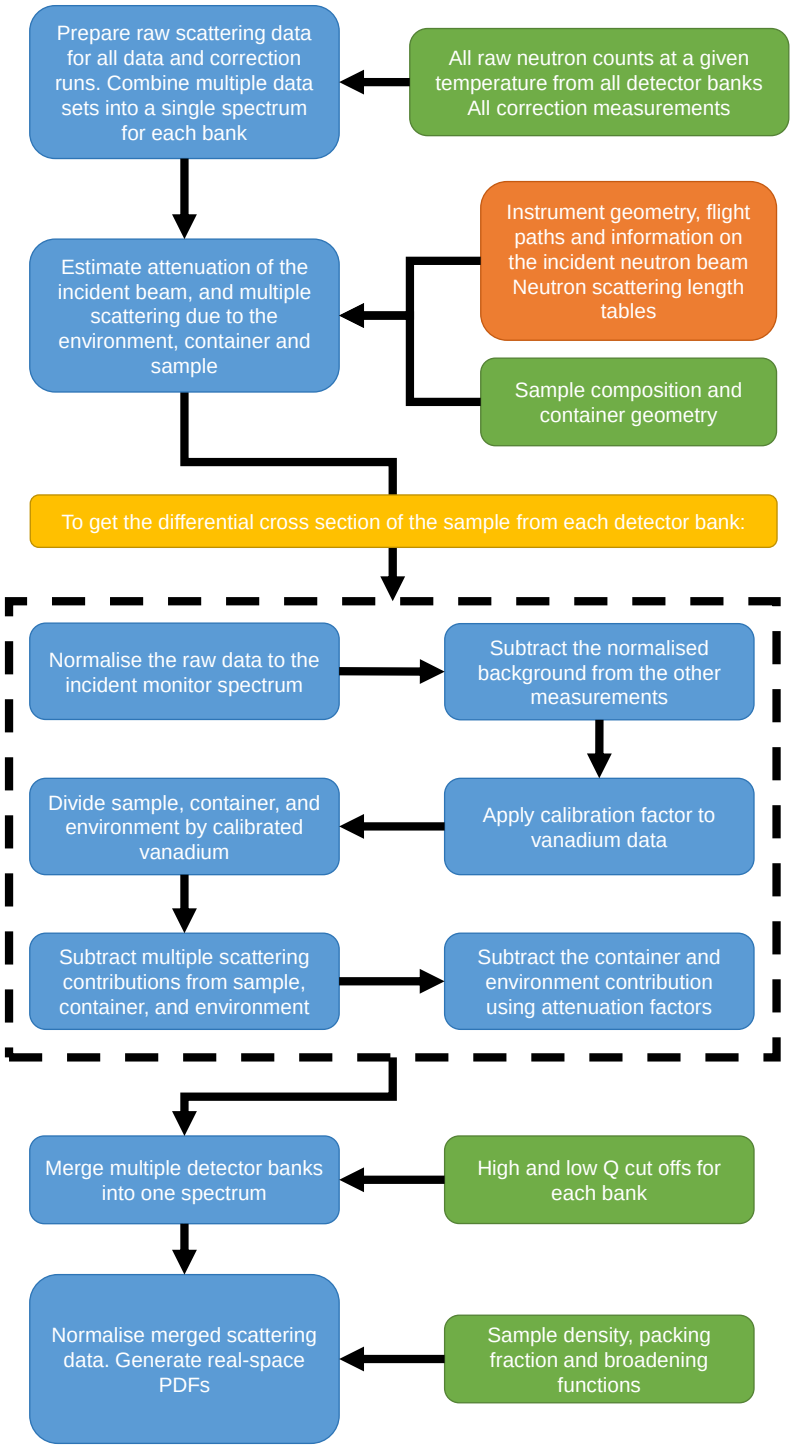


**Figure 2.8:** Flowchart highlighting the procedure of extracting the differential scattering cross section and scattering functions from raw neutron counts using GUDRUN. Blue boxes show the processes performed by the program, orange instrument parameters, and green user input.

The "tweak factor" is, in theory, the inverse of the packing efficiency. As the mass of material placed into the beam, container dimensions and height of the material within the

container are known this is a calculable value. In practice the tweak factor is adjusted to ensure that at high $Q$, the differential cross section of the merged data is consistent with the expected limit of $\sum c_i b_i$ where $c_i$ is the concentration of each atom type in the material and $b_i$ the corresponding neutron scattering length. Once an estimate for the tweak factor (based on the packing fraction) is input into GUDRUN it can be corrected so that the current high $Q$ DCS limit matches the expected limit according to

$$Tweak_{\mathrm{N}} = \frac{Tweak_{\mathrm{C}} \times DCS_{\mathrm{E}}}{\mathrm{DCS_C}}, \tag{2.22}$$

where $Tweak_{\mathrm{N}}$ and $Tweak_{\mathrm{C}}$ are the new and current tweak factors respectively, $DCS_{\mathrm{E}}$ is the expected DCS at high $Q$, and $DCS_{\mathrm{C}}$ is the current DCS at high $Q$. The process of refining the tweak factor may require several iterations before the expected and current DCS levels match.

GEM and POLARIS have several different detector banks, each bank is at a different angle, and hence has a different $Q$ range, but due to the distribution of incident neutron velocities, there is overlap of $Q$ ranges for neighbouring banks. GUDRUN merges the contribution from each bank into a single spectrum. The choice of where to cut off each detector bank was made on a material by material basis, remembering that scattering from high $Q$ contributes to fine detail in the real-space PDFs. Low-angle banks are cut off at low $Q$ as inelastic scattering means that their measured structure factor at high $Q$ is too low. Higher angle banks are used to contribute to the high $Q$ scattering data which limits the effects of inelastic scattering on the scattering data and their associated PDFs due to the inelastic scattering cross sections falling off at high $Q$. The choice of maximum and minimum $Q$ ranges per detector bank is a balance between maximising the amount of information available while minimising the noise in the scattering data. Figure 2.9 shows the differential cross section for PIH at 293 K for individual banks, and the merged cross section used for generation of the PDFs. We see that the low angle banks have a shorter $Q$ range than their high angle counterparts, and only contribute to the low $Q$ part of the merged DCS.

Due to the finite range of $Q$ values measurable, when the scattering data are Fourier transformed into real-space PDFs, regular termination ripples are produced in the PDF. These ripples can be suppressed by application of a Lorch function. In GUDRUN, this function is given by (2.23a), which can be rearranged into a form useful for suppressing observed ripples, (2.23b).

$$\Delta(r) = \Delta_0 \left(1 + r^{\beta}\right) \tag{2.23a}$$

$$\beta = \frac{\log\left(\frac{\Delta(r)}{\Delta_0} - 1\right)}{\log r}. \tag{2.23b}$$

Here $\Delta(r)$ is the degree of broadening in the PDF required at point $r$, $\Delta_0$ is the broadening required at $r = 1.0$ Å, and $\beta$ is the power of the broadening function.

At high $r$ values, the truncation ripples are evident as small repeating ripples on much larger, broader peaks, as shown in the left of figure 2.10. In order to calculate the power of the broadening function, $\beta$, two small peaks are identified and the distance between them measured to give $\Delta(r)$, the point at which the calculated $\beta$ is applied. The point at which the broadening function is applied, $r$, is simply the average of the two peak positions. The

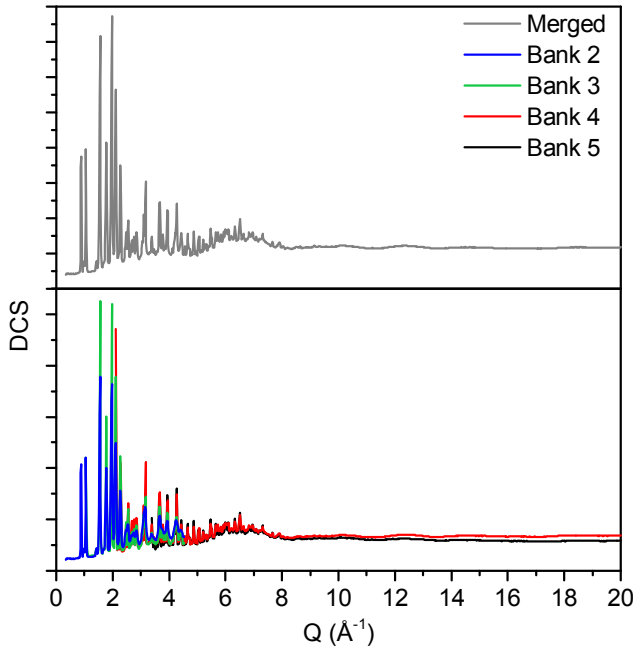


**Figure 2.9:** The merged differential cross section (grey) and the individual bank contributions (colour) for PIH at 293 K. Lower angle banks are used for the low $Q$ region, banks 4 and 5 extend up to 46 $\text{Å}^{-1}$.

broadening at 1.0 Å, $\Delta_0$, is kept small and constant as at low $r$, it is not unusual for there to be several peaks within a short range, and over-zealous broadening could cause them to merge into one another.

From these values, $\beta$ can be calculated such that the truncation ripples in the PDF at high $r$ are effectively suppressed and the features at low $r$ are retained. On the right of figure 2.10 the $r$ region 20 Å to 30 Å for $D(r)$ of PIH after the application of the broadening function is shown. We see that the termination ripples have been suppressed with minimal broadening of the structural peaks. The values $\Delta_0 = 0.02$ Å and $\Delta(r) = 0.15$ Å at $r = 27.75$ Å were chosen by inspection of the unsuppressed $D(r)$ at high $r$, and give $\beta = 0.57$.

When performing a `GUDRUN` refinement, the raw data files for the sample, empty diffractometer, vanadium standard, empty container, and empty environment are first read in. The container dimensions, sample composition (including isotope substitution) and sample height in the container are provided. The $Q$-range for each bank is selected such that the merged DCS (grey in figure 2.9) is smooth. An estimate for the tweak factor is provided and `GUDRUN` initiated. If necessary, the tweak factor is re-calculated according to equation (2.22). The maximum and minimum radius for the Fourier transform are supplied (the real-space range of the PDFs) and the scattering data transformed into PDFs. Termination ripples in the PDFs are smoothed via equation (2.23). Normalisation, setting the high and low limits of $D(r)$ and $G(r)$, as shown in with $G(r)$ and $G'(r)$ in figure 2.4 is then be applied.

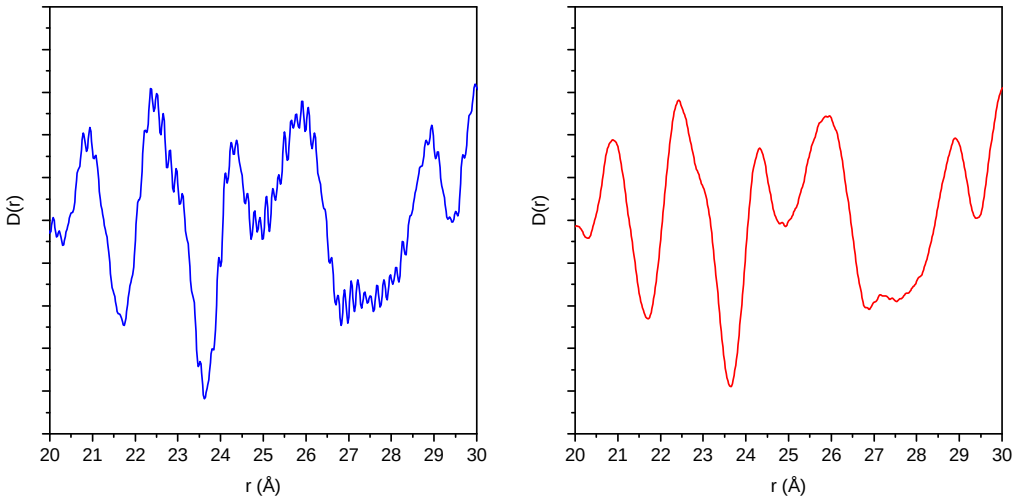


**Figure 2.10:** Left: $D(r)$ for $r = 20\,\text{Å}$ to $30\,\text{Å}$ of PIH at $293\,\text{K}$ with no suppression of the termination ripples. Right: $D(r)$ after application of the broadening function. The periodic ripples are suppressed with minimal broadening of the peaks.

## 2.4 Rietveld refinement

Rietveld refinement was developed when a method was required to solve the structure of powder samples from diffraction data [41]. With single crystal diffraction the Bragg profile contains distinct sharp peaks, where the area under each peak can readily be calculated and used to produce the structure factor. However in powder samples peaks overlap and contributions from particular reflections are difficult to isolate, the structure factors could not be extracted. The Rietveld method was novel in that instead of attempting to extract individual Bragg peaks, the whole data set is fit at once.

Several programs exist which can perform Rietveld refinement, including `FULLPROF` and `TOPAS`. For the work presented herein, the program `GSAS` (General Structure Analysis System) [42] with the `EXPGUI` interface [43] was used. `GSAS` allows stereochemical restraints such as bond lengths and angles to be applied to the model.

The theoretical diffraction pattern for a given structural model is fit to the observed data via the method of least squares. Successful Rietveld refinement generates a structural model based on the Bragg profile. In `GSAS`, the minimisation function, $M$ (that is the function which is to be minimised), consists of several components:

$$M = f_{\mathrm{h}} \sum_{h} M_{\mathrm{h}} \tag{2.24}$$

where $M_{\mathrm{h}}$ is the minimisation function of a particular histogram – say a particular detector bank or set of bond restraints – and $f_{\mathrm{h}}$ is the weighting factor for each histogram. The "goodness of fit", the reduced $\chi^2$, is given by

$$\chi^2 = \frac{M}{N_{\mathrm{obs}} - N_{\mathrm{var}}} \tag{2.25}$$

where $N_{\mathrm{obs}}$ is the number of observations in all histograms, and $N_{\mathrm{var}}$ is the number of variables in the least-squares refinement. For powder diffraction data, the minimisation function $M_{\mathrm{p}}$ is defined as:

$$M_{\mathrm{p}} = f_{\mathrm{p}} \sum_{i} \left( I_{\mathrm{obs},i} - I_{\mathrm{calc},i} \right)^2, \tag{2.26}$$

where $I_{\mathrm{obs,i}}$ is the observed intensity at each data point (either time, $d-$spacing or scattering angle) and $I_{calc,i}$ is the corresponding calculated intensity for the model [44]. If bond length restraints are applied, an additional term, $M_d$, is added to the minimisation function such that

$$M_{\mathrm{d}} = \sum_{i=1}^{N_{\mathrm{d}}} w_{\mathrm{d}} \left( d_{\mathrm{obs},i} - d_{\mathrm{calc},i} \right)^2, \tag{2.27}$$

where the observed and calculated distances are $d_{\mathrm{obs}}$ and $d_{\mathrm{calc}}$ respectively, and $w_{\mathrm{d}}$ is a weighting factor.

### 2.4.1 Steps in `GSAS` refinement

Here I will outline the key steps in processing scattering data from `ISIS` instruments.

**Initial structures:** In a standard `GSAS` refinement an initial structural model is provided to the program. For the work presented, proposed structures in at least one of the phases for each material had been published, although several were from x-ray data where the hydrogen

positions were often omitted. Estimates for $U_{iso}$, the isotropic atomic displacement parameter which models the thermal motion of atoms about their coordinates, is also included with the atomic coordinates and can be refined along with the atomic coordinates.

**Scattering data:** The profiles from multiple detector banks were provided. Each detector bank covers a different scattering angle range, the high and low $2\theta$ cut off is specified. Each bank would correspond to an individual $M_p$ histogram in equation (2.24).

**Instrument information:** An instrument parameter file is also required. This supplies information on the diffractometer constants, the geometry and distance of the detector from the moderator, and the profile parameters [45] which calculate the shape of the Bragg reflections based on the diffractometers response to a standard sample. Neutrons with shorter flight times experience less absorption during scattering than those with longer flight times. A parameter `DiffA` applies a correction to account for this, and can be refined along with the profile. The relationship between flight time, $t$, and $d$-spacing is

$$t = \text{DiffC} \cdot d + \text{DiffA} \cdot d^2 + \text{Zero}. \tag{2.28}$$

In equation (2.28) "DiffC" is a diffractometer – and detector bank – specific constant which is proportional to the total flight path of the detected neutron from the moderator to the detector via the sample, and is also dependent on $\theta$, half the scattering angle. "Zero" corrects for differences in timing signals, and along with "DiffC" is not refined.

**Additional restraints:** Bond length and bond angle restraints are applied, the bond length restraints are modified using the `EXPGUI` interface, and the weightings on them are manually edited. Bond angle restraints are modified in the command line. The $U_{iso}$ for each type of atom, or even specific atoms, can also set to be consistent with one another.

**Background:** The background contribution from both `GEM` and `POLARIS` is best modelled as a 10-term shifted Chebyshev polynomial.

**Peak shape:** The shape of the peaks is dependent on the instruments, the moderator and hence the profile of the incident neutron beam. Full descriptions of the peak-shape functions are found in [42] and [46]. `GSAS` has 4 built-in time-of-flight peak shape profiles. The profiles from `GEM` are best described by the second profile, `GSAS2`, which incorporates the Ikeda-Carpenter function with an exponential decay. `POLARIS` profiles are best described by function `GSAS3`, which is based on two back-to-back exponential functions with an additional Lorentzian contribution. In practice the peak shape can be varied in `GSAS` by adjusting the variables $\sigma_1$, $\sigma_2$, $\gamma_1$ and $\gamma_2$, which are coefficients in the `GSAS2` and `GSAS3` peak shape profiles. Figure 2.11 is the observed profile for DMMnF as recorded by `POLARIS` in blue, which is best described using the `GSAS` type 3 profile, and `GEM` in red, which is best described using the `GSAS` type 2 profile. The profiles have been scaled to allow for a direct comparison, and it can be seen that the `GEM` peak has a sharper increase than the `POLARIS` peak, but both have a similar decay.

**Refinement:** During Rietveld refinement, the lattice parameters, atomic coordinates, and fractional site occupancy are all refined, as are scale factors, backgrounds and peak profile parametes. The resultant unit cell is then used as a basis for RMC refinement.

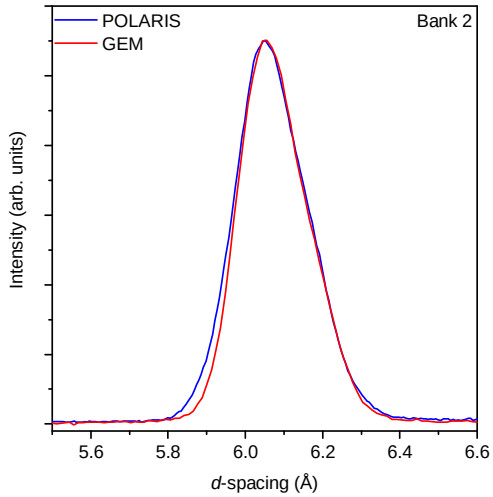


**Figure 2.11:** Observed background-subtracted Bragg profile for DMMnF from GEM bank 2 (T = 150 K) and POLARIS bank 2 (T = 140 K). GEM data has been scaled and offset for direct comparison of the peak shape profiles.

## 2.5 Reverse Monte Carlo method

So far in this chapter, we have discussed how we can extract the average structure of a material by Rietveld refinement of neutron scattering data. How the total scattering function can also be transformed into a real-space PDF which provides information on interatomic separations. Total scattering data also contains information about the short range correlations between atoms including hydrogen-bonding, which, for the materials presented herein mediate the onset of ferroelectric ordering and which the RMC method can be used to model.

The RMC method was developed by McGreevy and Pusztai [47] and is an extension of the Metropolis Monte Carlo (MMC) method [48]. RMC differs from usual application of Monte Carlo methods in that while the standard method attempts to generate a configuration of atoms which has a Boltzmann distribution of energies [48], the RMC method produces atomistic configurations which are consistent with observed scattering data. In the RMC method only selected energies are calculated, typically for well-characterised molecules via interatomic potentials. The RMC method was initially developed for structural determination of disordered systems, such as liquids and amorphous materials, without using interatomic potentials to guide the refinement. The "reverse" in the name can come from several origins, one possibility is that as the program can be applied without the use of interatomic potentials, the resultant configuration could be used to determine previously unknown potentials [22] (rather than using the potentials to guide the models).

### 2.5.1 RMC algorithm

The RMC method produces atomistic configurations consistent with observed scattering data via comparison of the observed data, say $D(r)$, to the same function which would be produced by the model. The agreement between the calculated function for the model and the observed

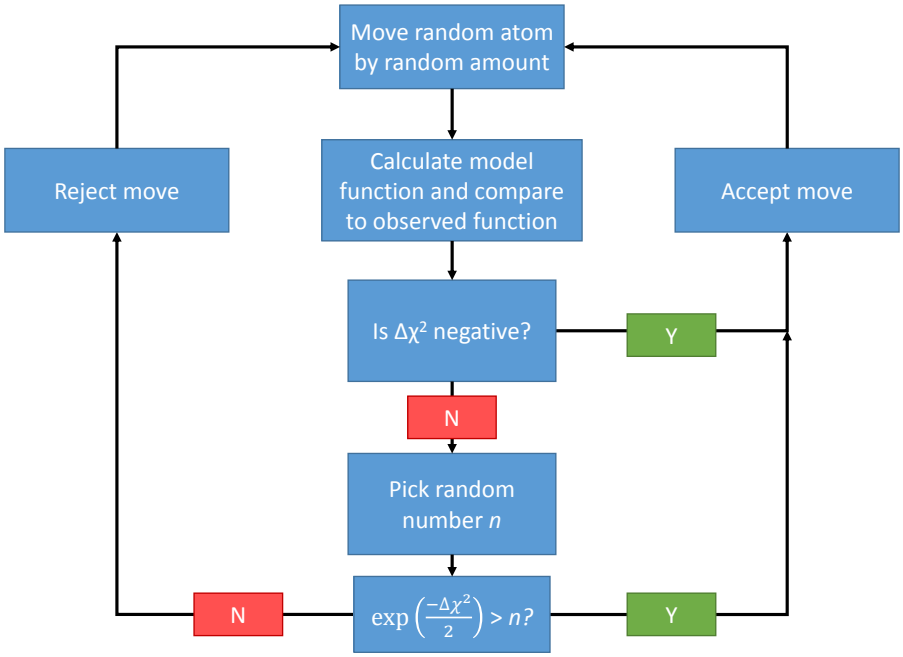


**Figure 2.12:** Flowchart detailing the reverse Monte Carlo algorithm. $\Delta\chi^2$ corresponds to the change in the goodness of fit between the current model, and the model with the moved atom. A negative $\Delta\chi^2$ is always accepted as the modified model shows better agreement with the data than the current model. Moves which worsen agreement are accepted subject to a probability distribution [22] which reduces the likelihood of the final model being stuck in a local minimum.

data is $\chi^2$ (the penalty function [20]), which for any function is defined by

$$\chi^2 = \sum_j \frac{\left(f_{j,\text{calc}} - f_{j,\text{obs}}\right)^2}{\sigma_j^2} \tag{2.29}$$

where $\sigma_j$ is the estimated noise at a given point $j$, in the data. For RMC the data sets which are compared against are typically a real-space PDF and $i(Q)$.

After $\chi^2$ for the initial model is calculated, a random atom is moved by a random amount (or swapped with another atom), and the agreement between the model and observed functions is calculated. If the move improves agreement ($\Delta\chi^2 < 0$) then the atomic move is accepted and another atom is moved at random and the process repeated.

The RMC method also allows for moves which worsen the agreement between model and data to be accepted. The flowchart describing the process is given in figure 2.12. If an atomic move worsens the agreement ($\Delta\chi^2 > 0$) then a random number $n$ is calculated from a uniform distribution with $0 < n < 1$. If $\exp(-\Delta\chi^2/2) < n$ then the move is rejected, otherwise the move is accepted. The process of allowing unfavourable moves ensures that the model does not get stuck in a local minimum, where any one move will not improve the fit, but a few unfavourable moves could be followed by more good moves.

### 2.5.2 Comments about the RMC method

There are a few potential drawbacks to the RMC method. When using traditional refinement techniques to model diffuse scattering data, Paściak and Welberry note that, to ensure good agreement between the model and the data, the amount of data must be significantly greater than the number of free parameters [49]. In a simulation box containing approximately 10 000 atoms, each with an $x$, $y$, and $z$ fractional coordinate, each model has 30 000 parameters. The range of allowed values of these parameters is significantly reduced however, by application of distance window restraints on an initial model which is already chemically "sensible" as it is supercell of the Rietveld-derived unit cell. The intensity of the PDF at low $r$ is a further restraint; for example in figures 2.3a and 2.4, below $r = 0.8\,\text{Å}$, there is no pair density in the PDF and this marks the minimum distance of approach between neighbouring atoms. Similarly application of interatomic potentials means that the effective number of data points is increased. However the data to parameter ratio is still poor.

These issue can be addressed when discussing the "uniqueness problem" that is often cited as a limitation of the RMC method [48]. No converged RMC configuration is unique. Even if the algorithm is applied to multiple copies of the same initial configuration, as has happened in this thesis, the converged configurations will all differ. Hopefully not in the overall trends, but the random moves and move acceptance criteria ensure that each configuration is unique. This allows us to produce multiple models of a material which are all consistent with the data and look for trends in the behaviour. It is this analysis of multiple unique configurations which means that the premise that a high data to parameter ratio is required, is incorrect.

A final comment regarding RMC is that if a material is known to have a specific coordination number, say 4, there is no impetus for the RMC algorithm to produce a model with each species 4-coordinated. Without additional information a model with half of the sites with 5 coordinate and half with 3 is no different than a model with all sites 4 coordinate. Again, a sensible initial configuration and distance window constraints or interatomic potentials will alleviate this problem.

### 2.5.3 `RMCProfile`

The program `RMCProfile` [50] expands upon the general RMC method by inclusion of the Bragg profile in addition to the scattering function and PDF, and by inclusion of interatomic potentials. `RMCProfile` also allows multiple data sets to be fit simultaneously, including the Bragg profile as a distinct data set from the scattering function $i(Q)$ which contains both Bragg and diffuse scattering. The inclusion of the Bragg profile is important as while the focus of the work presented in this thesis is on local order, we must be sensitive to the fact that these are crystalline materials, which do still have some long range order. $i(Q)$ for the model is calculated from the supercell, and so the longest-range information which can be gathered from it is approximately 25 Å, half the supercell size. The Bragg profile provides the information on the long range order.

As the PDFs are derived from the scattering functions it may appear that refining atomistic configurations against both PDFs and $i(Q)$ is unnecessary, however the PDF is the Fourier transform of $Q$ times $i(Q)$ rather than the scattering function on its own, and as such the $i(Q)$

and PDF intrinsically favour different length scales. The PDFs contain more information on the local structure than would be found in the scattering function.

The inclusion of interatomic potentials within `RMCProfile`, with equations which will be given later in this section, adds another term to the penalty function, which is now the sum of the contributions from the scattering function, the PDF, the Bragg and the energy term, such that

$$\chi^2_{\mathrm{RMC}} = \chi^2_{i(Q)} + \chi^2_{\mathrm{PDF}} + \chi^2_{\mathrm{Bragg}} + \frac{\Delta E}{k_{\mathrm{B}}T}, \tag{2.30}$$

where the change in energy is calculated via the applied interatomic potentials, and $T$ is the temperature at which the data were collected. In equation (2.29), the noise ($\sigma$) of the data can be specified on a point by point basis, however for `RMCProfile` a single value is given as the estimate for the noise, which represents the average noise within the data. For `RMCProfile`, the weight assigned to each data set is estimated using $\frac{1}{\sigma}$, so smaller uncertainties lead to higher weightings of the data.

As outlined in section 2.1.2, the PDFs have precise definitions and their behaviour at low and high $r$ are consistent, therefore when the model PDF is calculated, it can be directly compared to the observed PDF. The scattering function $i(Q)$ however cannot be directly compared. The model $i(Q)$ is derived from the Fourier transform of the model's PDF which has a significantly smaller $r$ range than that of the collected data. This means that the peaks in the $i(Q)$ generated from the model will be broader than the observed $i(Q)$. To allow comparison between the observed and the model's scattering function the observed $i(Q)$ is convolved with a box function with size $L/2$ [28], where $L$ is the shortest length of the RMC configuration, according to

$$i_{\mathrm{con}}(Q) = \frac{1}{\pi}\int_{-\infty}^{+\infty} i_{\mathrm{obs}}(Q')\frac{\sin\left(L(Q-Q')/2\right)}{Q-Q'}\mathrm{d}Q'. \tag{2.31}$$

Therefore the cost function for $\chi^2_{i(Q)}$ is calculated according to,

$$\chi^2_{i(Q)} = \sum_j \frac{\left(i(Q_j)_{\mathrm{calc}} - i(Q_j)_{\mathrm{con}}\right)^2}{\sigma^2_{i(Q)}}, \tag{2.32}$$

whereas the cost function for $\chi^2_{D(r)}$ is simply

$$\chi^2_{D(r)} = \sum_j \frac{\left(D(r_j)_{\mathrm{calc}} - D(r_j)_{\mathrm{obs}}\right)^2}{\sigma^2_{D(r)}}. \tag{2.33}$$

Using the expanded definition of the penalty function from (2.30), the contribution from the Bragg profile is

$$\chi^2_{\mathrm{Bragg}} = \sum_j \frac{\left(I(t_j)_{\mathrm{calc}} - sI(t_j)_{\mathrm{obs}}\right)^2}{\sigma^2_{\mathrm{Bragg}}}. \tag{2.34}$$

In equation 2.34, $I(t)_{\mathrm{obs}}$ is the intensity of the observed Bragg profile for a given neutron flight time, where the contribution from all detectors banks have been merged in `GSAS` or a similar program into one profile. `GSAS` includes information on the background, and peak shapes which is provided to `RMCProfile` and included in the calculation of $I(t)_{\mathrm{calc}}$. Unlike the

penalty functions for $D(r)$ and $i(Q)$, equation 2.34 includes a scaling term, $s$, for the calculated profile, as there is no definite scale as there is for $D(r)$ and the observed data is not corrected to account for the size of the model as with $i(Q)$.

RMCProfile also includes interatomic potentials to guide the refinements. As shown in equation (2.30) the change in energy $\Delta E$ after an atomic move is incorporated into the penalty function $\chi^2_{\mathrm{RMC}}$ which guides the probability of unfavourable moves being accepted [20]. The interatomic potentials are given in the form of Morse stretch potentials, and harmonic cosine bending potentials. The energy from Morse potentials is given by

$$E = D\left[1 - \exp\left\{\alpha(r_{ij} - r_0)\right\}\right]^2, \tag{2.35}$$

where $D$ is the energy prefactor in eV and $\alpha$ is set at $2.55\,\text{Å}^{-1}$ in accordance with the MM3 force field potential sets [51]. The ideal bond length is given by $r_0$, and the distance between atoms $i$, and $j$ is $r_{ij}$.

The energy from harmonic bond bending potentials are given by

$$E = \frac{K}{2}\left(\cos\theta - \cos\theta_0\right)^2, \tag{2.36}$$

where $\theta$ is the measured angle between atoms, $\theta_0$ is the ideal angle, and $K$ is the energy prefactor in eV. Both $D$, and $K$ are taken from experimentally derived values tabulated in [52] unless otherwise stated.

In addition to bond stretching and bending potentials, RMCProfile also incorporates a planarity potential [53], where atoms within planar molecules are identified, and their deviation from planarity calculated. As with the stretching and bending interatomic potentials, an additional penalty term is added to the total $\chi^2$ if the material deviates from planarity. The energy associated with the planarity potential is given by

$$E = L\sum_i d_i^2, \tag{2.37}$$

where $L$, with units $\text{eVÅ}^{-2}$, is a user-defined constant and $d_i$ are the distances between the atoms in the planar molecule, and the plane of best-fit of the molecule.

Finally RMCProfile can refine the magnetic structure of a material. If information on the magnetic form factor and the magnetic species in a material is provided then the magnetic contribution to $i(Q)$ and the Bragg profile can be calculated. No information on the magnetic structure of the material can be extracted from the real-space PDFs.
As with the structural refinements, random magnetic spin moves are performed. These moves are generated by treating the magnetic moment as a point on a sphere, adding a random move vector to that point and then projecting the resultant vector back onto the sphere, to give the new orientation. The probability distribution for whether moves are accepted or not is based on a user-defined maximum move size. A full description of the algorithm for magnetic moves is given in [52], but the key point is that random changes can be applied to either the position of atoms in a configuration or to the direction of the magnetic moments in a structure.

### 2.5.4 Running RMCProfile

RMCProfile requires several input files in order to run, firstly are the functions which the program will fit against, $D(r)$, $i(Q)$, and $I(t)$ which are given in the form of files with two or

three columns where the first column is the variable, either $r$, $Q$, or $t$, the second is the intensity at that point and the third – if present – is the associated uncertainty. The coefficients of the polynomial which describe the background of the Bragg profile are provided in a separate file. It is also possible to supply `RMCProfile` with information about the chemical environment of the material through interatomic potentials and through restricting some of the motion of the atoms. They main keywords are presented below:

**Number density:** The number density of the atomistic configuration. This information is provided to the program, but is also calculated and is given in the data file containing the Bragg profile. The value given in the *.dat* file should be consistent with both the calculated and Bragg value. If they are not the program will give a warning, however it will continue to run.

**Maximum moves:** The RMC algorithm moves atoms by a random amount, with smaller displacements being more likely than larger ones, however it may be undesirable to have atoms move a significant amount, especially as the initial configuration is usually a "best guess" based on the average structure. The maximum moves keyword allows users to limit the size of the atomic moves – which would likely be rejected – and waste computational time. For the work presented here the maximum displacement for any one move was set to 0.05 Å.

**Minimum distances:** In addition to supplying information about interatomic potentials which should in theory prevent atoms moving unphysically close together, it is possible to set a minimum distance of approach. If a proposed move would cause two atoms to come too close together, then that move is automatically rejected, before it can be subject to the probability distribution. The choice of minimum distance values can be decided by observation of the PDF, for all materials in this thesis no atoms were allowed to move closer than 0.88 Å. The minimum distances of approach for different pairs of atoms can be specified separately.

**Distance windows:** Distance windows are used to ensure that atoms which start within a given range, say in a molecule bonded to one another, don't get torn away during refinement. The distance windows contain a minimum and a maximum approach and much like the Minimum distances constraint if they are broken by a proposed move, the move is rejected. When selecting distance windows it is necessary to make them wide enough that the partial PDF will have a "sensible" shape. When the distance window cut off is too tight the partial PDF displays a sharp, unphysical cut off, as shown in figure 2.13. Distance windows prohibit moves into clearly unphysical regions of the structure, whereas interatomic potentials apply a penalty to the $\chi^2$ for even small deviations from ideal geometry. Therefore interatomic potentials are only applied to regions of the structure which are well-understood, but distance window restraints can be applied to all atomic pairs.

**Peak shape:** Gives the program the information on the peak shape (see section 2.4.1) so the model Bragg profile can be compared to the observed Bragg profile.

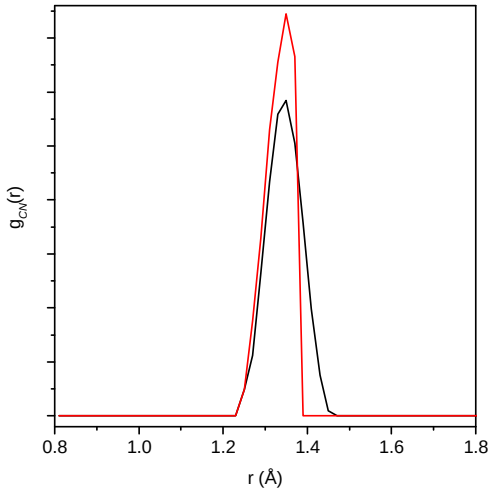


**Figure 2.13:** The effect of distance window restraints on the partial pair distribution function $g_{CN}(r)$. Black: Adequate distance windows range ($1.21$ Å to $1.48$ Å), distribution is approximately Gaussian. Red: The maximum distance window is not high enough, ($1.21$ Å to $1.39$ Å) causing an unphysical sharp drop in the partial PDF.

# Chapter 3

# Dimethylammonium Manganese Formate

## 3.1 Introduction

In section 1.1.1 MOFs with a perovskite-like architecture were introduced. In MOFs, multiatom linkers replace the X site, which in turn increases the pore volume and allows for polyatomic guest cations to reside on the A site. Using larger and more flexible unit cells, means there are more interactions available between the framework and the guest cation, and a much larger variety of structures.

From this range of MOFs with perovskite-like architecture, one family, with the X linker replaced by the formate anion $HCO_2^-$, has been subject to several systematic studies. These MOFs, with general formula $A[M(HCO_2)_3]$, have a range of possible A site cations including imidazolium [54], azetidium [55], formamidinium [56], guanidinium [57–60], ammonium [61–64], methylammonium [65], ethylammonium [66] and dimethylammonium which this chapter will focus on.

The first reported dimethylammonium (DMA) metal formate was $(CH_3)_2NH_2[Cu(HCO_2)_3]$ [67] whose crystal structure was reported in 1973, after that there was a 30 year break in interest until systematic studies of the DMA metal formate family were performed. Structural studies have been performed on $(CH_3)_2NH_2[M(HCO_2)_3]$ where the divalent metal M = Zn [68, 69], Fe [70, 71], Ni [72], Mg [73, 74], Co [16, 75], and Cu [76]. In addition to single metal sites, alternating $Fe^{3+}/M^{2+}$ formates (M = Mn,Co [77], and Fe [77, 78]), $Mn^{2+}/Cr^{3+}$ [79], and $Na^+/Fe^{3+}$ [80] have also been reported.

To highlight the breadth of the study on DMA metal formates, there have been several papers systematically investigating one or more properties on two or more different structures including thermal expansion [81], enthalpy of formation [82], unit cell size with changing metal site [83], Young's modulus [84], elastic relaxation [85], multiferroicity [86] and magnetic ordering [30, 87, 88] and the dielectric transition. [89]

In this chapter I will be focussing on dimethylammonium manganese formate, DMMnF, $(CH_3)_2NH_2[Mn(HCO_2)_3]$ [90–93] which displays both electric and magnetic ordering. As I have shown the scope of potential features to investigate with DMMnF is as wide as the variation of the composition. But it is necessary to focus the analysis onto one or two features of interest. In chapter 4, the magnetic ordering is investigated, in this chapter RMC modelling has been used to understand dynamics of the DMA cation upon cooling and the interaction the cation has with the formate framework.

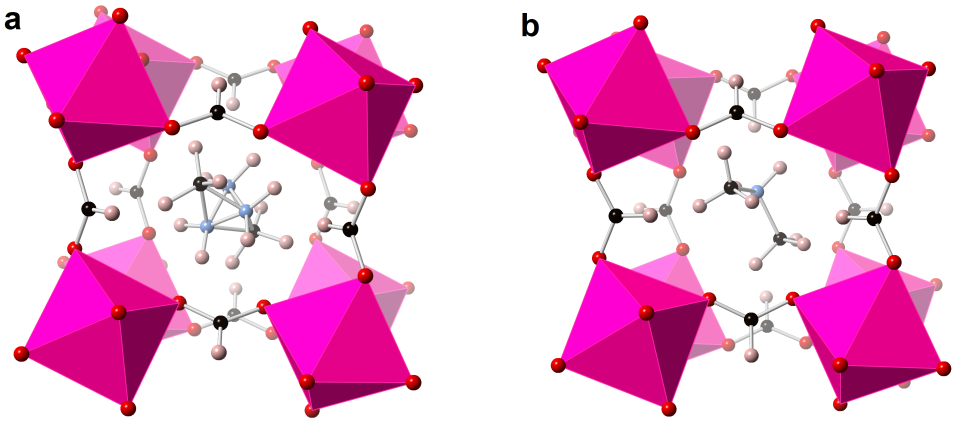


**Figure 3.1:** DMMnF in the high (a) and low (b) temperature phase with pink $MnO_6$ octahedra surrounding the $(CD_3)_2ND_2$ cation with blue nitrogen, pale pink deuterium and black carbon. In the high temperature phase the disorder of the $ND_2$ cation is represented by partially occupied sites about the three-fold axis.

## 3.2 The material

DMMnF, was first reported by Wang et al. in 2004 [30] where the magnetic ordering of the system was investigated (discussed in chapter 4). In 2009 the multiferroic nature of DMMnF was reported [86]. DMMnF has a perovskite-like structure with $Mn^{2+}$ occupying the B site, linked by formate anions. Within the pore is a DMA cation on the A site. At room temperature DMMnF crysatallises in space group $R\bar{3}c$; the DMA cation is dynamically disordered with the $NH_2$ group rotating about the three-fold C···C axis of the cation. The high temperature structure is shown in figure 3.1a. Much like other dimethylammonium metal formates, DMMnF undergoes a dielectric transition at 183 K, where the previously disordered DMA cation orders antiferroelectrically in a first-order phase transition to space group $Cc$ [89] shown in figure 3.1b.

There are two principal aims for this study. First is to investigate the strength and geometry of the hydrogen bonding between the DMA cation and the framework. Reported crystal structures from the high temperature phase show the $NH_2$ of the DMA cation forming hydrogen bonds of equal length with the formate framework with N···O separations of $\approx$ 2.9 Å [86, 89, 91] at room temperature, and $\approx$ 2.8 Å at 100 K [91]. The making and breaking of these hydrogen bonds dictate the freedom of motion of the DMA cation and mediate the interactions between cation and the framework during electric ordering. However the N−H···O distances were derived from analysis of single crystal x-ray scattering data, therefore only the average positions have been reported, and due to the small x-ray scattering length of H, the positions of the H are either hard to determine or in some instances have been omitted. As the position of the hydrogen is not well defined, the geometry of N−H···O cannot be defined. In the work reported here, total neutron scattering studies were performed on the fully deuterated analogue and analysis of the resultant atomistic configurations allows the bond geometries to be probed.

Raman studies performed on DMMnF show that the nitrogen of the DMA cation interacts with the formate framework via medium strength N−H···O hydrogen bonds [89], that the strength of the hydrogen bonds increases as DMMnF is cooled, and that just below $T_c$ the

ordering of the $NH_2$ group is incomplete. The relative strength of these hydrogen bonds can be extracted from the atomistic configurations through measuring the atomic separations via partial pair distribution functions of the DMA nitrogen and deuterium and formate oxygen.

The reported transition temperature for fully hydrogenated DMMnF is only 0.5 K below that of the deuterated analogue [89]. The weak effect that isotropic substitution has on the transition temperature of DMMnF means that motion of the hydrogen (or deuterium) along the N−H···O bond does not have a significant contribution to the ordering of the DMA cations during the phase transition.

The second aim of this study is to determine the change in entropy, $\Delta S$, between the ordered and disordered phases. If the phase transition is simply an order-disorder transition, then the change in entropy can be calculated according to $\Delta S = R\ln(N) - 9.1$ $JK^{-1}mol^{-1}$, where $N$ is the number of sites in the disordered phase and so for DMMnF is 3. Heat capacity measurements performed on hydrogenated DMMnF found that the change in entropy ranges from 0.9 $JK^{-1}mol^{-1}$ to 8.83 $JK^{-1}mol^{-1}$ [86, 92]. In the upper limit, the change in entropy was found to be dependent on the heating rate, but suggested that the phase transition was largely order-disorder. The lower limit suggests that ordering of the DMA cations takes place over a large temperature range, and that just below $T_c$ the DMA cations are not fully ordered. Analysis of atomistic configurations provide an independent method for calculating $\Delta S$ by assigning the orientations of the DMA cations into several microstates.

The neutron total scattering, atomistic configurations and analysis presented herein have been used to propose a new mechanism for the ferroelectric phase transition which sees orientational ordering of the DMA cation with respect to the framework, and framework deformations with respect to the DMA cation.

## 3.3 Experimental

In this section the data collection and processing prior to application of the RMC method will be discussed. Full details of collection numbers can be found appendix A.1.

### 3.3.1 Synthesis

Synthesis of DMMnF for the total scattering experiment was carried out by Dr. A. E. Phillips, according to the published procedure [30]. 1.42 g of $MnCl_2{\cdot}H_2O$ - obtained by heating the tetrahydrate - was dissolved in 10.69 g $D_2O$, and 10 g of $CDON(CD_3)_2$ was added. This was held in a heated pressure vessel at 140 °C for three days before being cooled to room temperature where crystals of DMMnF had formed. The crystals were filtered and washed with with $CD_3OD$ and dried under suction, producing a yield of 1.67 g (70%). The $^1H$ from $MnCl_2{\cdot}H_2O$ was calculated to be no greater than 1% of the total hydrogen content in the system, and was undetectable during subsequent neutron analysis.

### 3.3.2 Data collection

Variable temperature total neutron scattering data were collected at the ISIS facility using the `GEM` diffractometer. The data were collected on cooling the sample from room temperature to 7 K. Total scattering measurements – consisting of a minimum of eight hour collection

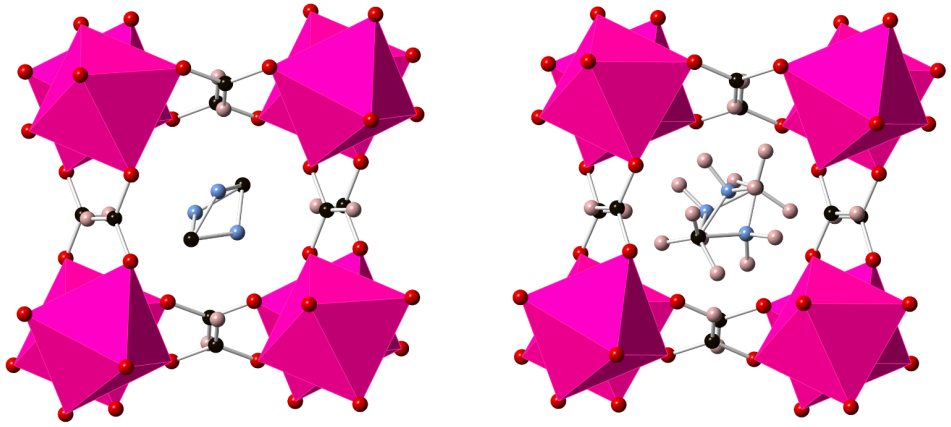

**Figure 3.2:** The pseudo-cubic perovskite unit cell of DMMnF in the high temperature phase of DMMnF showing 3-fold disorder of the (blue) nitrogen. *Left:* The published structure, derived from x-ray sources where only the formate hydrogen position has been given. *Right:* The edited structure when the methyl and ammonium deuterium have been introduced. N−C−D angles optimise during RMC refinement.

times – were carried out at room temperature, 250 K, 200 K, 150 K, 100 K, 20 K and 7 K. Each eight-hour collection corresponded to a total proton beam charge ranging from 900 µA h to 1200 µA h. Room temperature measurements were taken in the diffractometer with no additional sample environment, all measurements taken below room temperature were taken in a closed cycle refrigerator (CCR). In addition to the total scattering data collections, shorter runs with one hour collection times (150 µA h) were also taken in 10 K intervals between 200 K and 150 K, which covered the phase transition. These shorter "diffraction-only" runs were used to calculate lattice parameters around the phase transition but were not used for RMC refinement. A mid-length run of 500 µA h was also recorded at 225 K. Details of the run numbers along with the measured sample temperature can be found in table A.1

### 3.3.3 Rietveld refinement

The diffraction data were analysed by the Rietveld method [41], carried out using the `GSAS` program [42] and the `EXPGUI` interface [43]. Starting configurations for the high and low temperature phases were taken from published x-ray structure determinations [92] (CSD identifiers *DADTOS04* and *DADTOS03* respectively). The high temperature phase unit cell was modified to include deuterium in the DMA cation, whose positions had not been reported in *DADTOS04*. As the DMA cation lay along the 3-fold axis, the N−C−D angles were unrealistic, but RMC refinement where no space group limitations were applied, allowed the methyl hydrogen to re-orient. The published and modified structures of the high temperature phase are shown in figure 3.2. The reported low temperature phase structure had all hydrogen (deuterium) present, although the N−D and C−D lengths (0.9198 Å to 0.9803 Å) were shorter than analysis of the PDF (section 3.3.4) indicated, it was decided to allow the bond lengths in the unit cell to optimise during refinement. During refinement, `GEM` detector banks 2–5 were refined simultaneously. The bank 2 ($13° \leq 2\theta \leq 21°$) profile was chosen to be used for subsequent RMC modelling. The observed Bragg profiles from bank 2 are shown in figure

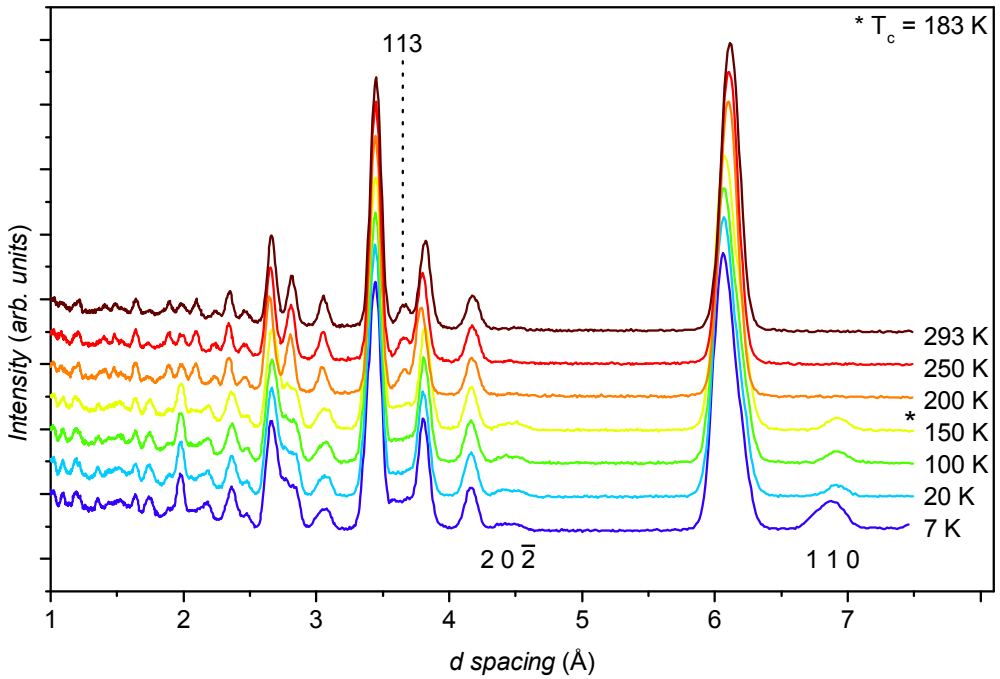


**Figure 3.3:** Observed Bragg profiles in the $R\bar{3}c$ ($T > 183\,\mathrm{K}$) disordered phase and in the $Cc$ ($T < 183\,\mathrm{K}$) ordered phase, emergence of the $(110)$ and $(20\bar{2})$ peaks along with the loss of the $(113)$ peak accompany the phase transition

3.3. The phase transition is clearly visible, as below $T_c$ we see the emergence of two peaks with $d$-spacing of 6.90 Å $(110)$, and 4.39 Å $(20\bar{2})$, and the $(113)$ peak of the high temperature phase, with $d$-spacing of 3.66 Å is lost.

The background for each bank was modelled as a ten-term shifted Chebyshev polynomial, and the peak profiles were fit using the `GSAS` type 2 profile (see section 2.4.1). Least squares refinement was carried out by varying the parameters in the following order: cell parameters, diffractometer constant `DiffA` (see section 2.4.1), peak-shape parameters $\sigma_1$ and $\sigma_2$, the deuterium coordinates of the DMA cation, deuterium $U_{\mathrm{iso}}$s and all atomic coordinates. Bond length restraints as outlined in table 3.1 were applied at the beginning of the refinement and given a weighting such that the $\chi^2$ of the bond restraints histogram was of the same order of magnitude as the $\chi^2$ of individual detector banks. The thermal parameters $U_{\mathrm{iso}}$ were also constrained to ensure the atomic displacement parameters of the deuterium and carbon (and oxygen in the low temperature phase) were consistent. Throughout refinement, it was assumed that the sample was fully deuterated. Trial analyses with a partial hydrogenation worsened the agreement between the model and the observed data, which confirmed that the sample had undergone negligible hydrogen exchange between synthesis and measurement.

Representative fits of the high and low temperature refinements are shown in figure 3.4. The poorer fit of the high temperature phase model is attributed to the restriction of the N−C−D angles due to C···C being along the 3-fold axis. Subsequent analysis of RMC configurations where the methyl group is not restricted by symmetry constraints display better agreement with the observed Bragg profile.

| Bond type | Restraint length /Å |
|---|---|
| C−D (DMA) | 1.050 |
| C−D (formate) | 1.050 |
| N−D | 1.050 |
| Mn−O | 2.180 |
| C−O (formate)* | 1.250 |

**Table 3.1:** Bond types and restraints applied to them during GSAS refinement. **applied to the low-temperature phase only*

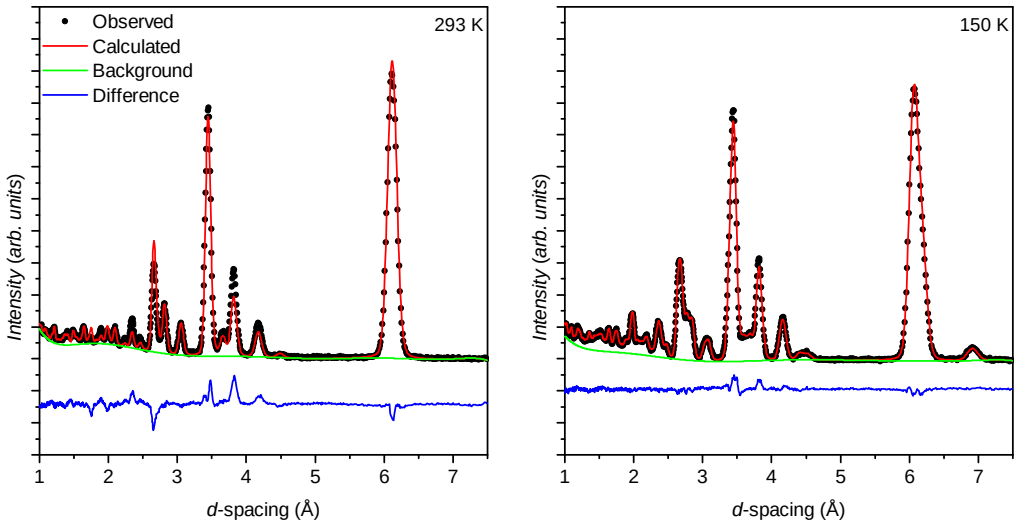


**Figure 3.4:** Representative GSAS fits after refinement for the high (left) and low temperature phase (right). The poorer fit of the high temperature phase is thought to be a function of symmetry restrictions affecting the methyl group of the DMA cation.

### 3.3.4 Data processing

The scattering function $i(Q)$ and pair distribution functions $D(r)$ and $G(r)$ were extracted from the scattering data using GUDRUN. Details of the correction run numbers can be found in table A.2.

| Bank # | $Q_{min}$ | $Q_{max}$ | Bank # | $Q_{min}$ | $Q_{max}$ |
|---|---|---|---|---|---|
| 1 | 0.50 | 2.00 | 5 | 2.50 | 13.00 |
| 2 | 0.50 | 3.00 | 6 | 3.40 | 42.00 |
| 3 | 0.90 | 4.00 | 7 | 12.50 | 42.00 |
| 4 | 1.80 | 7.50 | 8 | 12.50 | 42.00 |

**Table 3.2:** Bank cut offs used in GUDRUN.

After the bank cut offs had been chosen the tweak factor was adjusted so the high $Q$ value of the merged differential cross section matched the the expected level, $S_{Q\to\infty} = \sum_i c_i b_i$. The data were then normalised to $\sum_i c_i b_i$. The tweak factors for each temperature are given in table 3.3.

Termination ripples were suppressed using equation (2.23b), with the broadening at 1.0 Å

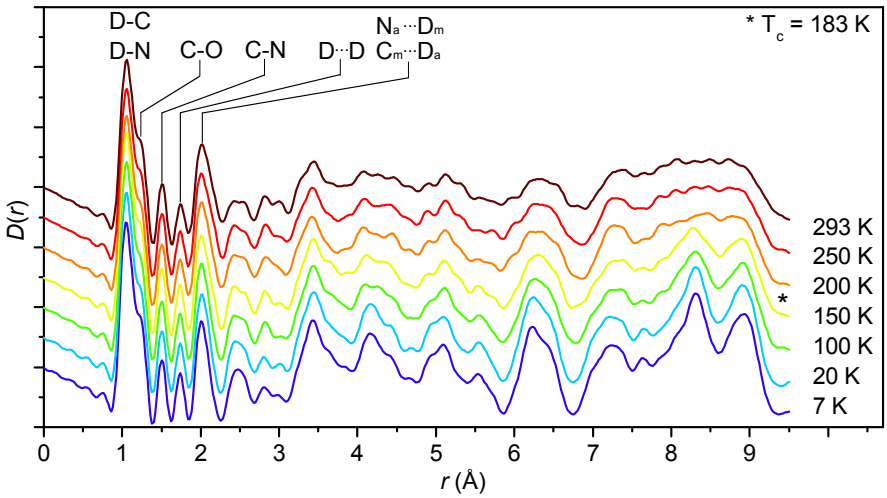


**Figure 3.5:** The $D(r)$ for $r < 9.5$ Å with intramolecular pair separations identified. The difference between the high and low temperature phase $D(r)$ at $r > 8.3$ Å indicates the phase transition is first-order

held constant at $\Delta_0 = 0.01$ Å and the power of the function, $\beta$, calculated for each temperature and given in table 3.3.

| Temperature /K | Tweak Factor | $\beta$ |
|---|---|---|
| 293 | 2.4320 | 0.8312 |
| 250 | 2.5207 | 0.8927 |
| 200 | 2.5232 | 0.9601 |
| 150 | 2.5292 | 0.7731 |
| 100 | 2.5122 | 0.8968 |
| 20 | 2.5503 | 0.8967 |
| 7 | 2.5384 | 0.9299 |

**Table 3.3:** Parameters used in GUDRUN to extract the $i(Q)$ and PDFs.

The Q range 0.8 Å$^{-1}$ to 40 Å$^{-1}$ was transformed to give the pair distribution function $D(r)$ (section 2.1.2). The derived $D(r)$ up to 9.5 Å are given in figure 3.5, with low $r$ peaks identified. Below 4.00 Å the peaks of the high and low temperature phase are very similar. These peaks largely correspond to bonding pairs of atoms in the DMA cation and formate framework and are expected to be the same over the phase transition. Above 8.00 Å the difference between the two phases are more apparent, with peaks at 8.34 Å and 8.96 Å emerging below $T_c$. This discontinuity between the high and low temperature phase $D(r)$ suggests a first-order phase transition. The scattering lengths and relative concentrations of each atomic pair are given in table 3.4

### 3.3.5 Initial RMC configurations

Initial configurations were generated from supercells of the refined crystal structure. For the high temperature phase a $6 \times 6 \times 2$ supercell was generated, with approximate dimensions 50 Å $\times$ 50 Å $\times$ 45 Å and volume $\approx 99 \times 10^3$ Å$^3$ and containing 10 368 atoms. For the low

| Atom pair $i$, $j$ | $b_i b_j c_i c_j$ (fm$^2$) | Atom pair $i$, $j$ | $b_i b_j c_i c_j$ (fm$^2$) |
|---|---|---|---|
| D, D | 9.349 | C, N | 1.08 |
| D, O | 8.871 | N, N | 0.152 |
| D, C | 8.567 | Mn, Mn | 0.024 |
| C, O | 4.017 | Mn, N | −0.121 |
| D, N | 2.385 | C, Mn | −0.430 |
| O, O | 2.105 | O, Mn | −0.451 |
| C, C | 1.917 | D, Mn | −0.950 |
| O, N | 1.132 | | |

**Table 3.4:** Faber-Ziman weighting factors for the partial pair distribution functions' contribution to the total PDF.

temperature phase a $4 \times 6 \times 6$ supercell with approximate dimensions 57 Å $\times$ 50 Å $\times$ 53 Å, volume $\approx 130 \times 10^3$ Å$^3$, and containing 13 842 atoms was generated.

To simulate the disorder of the DMA cations, the rotation of the $ND_2$ group about the centre of the molecule, a program was written (provided in the electronic appendix) to randomly orient the $ND_2$ of the DMA cation about the C···C axis, a flowchart describing the process is given in figure 3.6.

Figure 3.7 shows the angle of rotation of the $ND_2$ group for the high temperature phase initial configurations. Each distribution was constructed from 30 different configurations at each temperature. No disorder was introduced into the starting configurations of the low temperature phase. Attempts to fit the low temperature data using disordered initial configurations resulted in a significantly larger final $\chi^2$ than configurations where no disorder was introduced (average total $\chi^2 = 235$ vs. 28). It was not possible to produce an ordered configuration from a disordered starting configuration and so the models derived from an initially disordered configuration were considered implausible.

### 3.3.6 RMC restraints

For each configuration `RMCProfile` refined against $D(r)$, $i(Q)$ and the Bragg profile $I(d)$, where the relative weightings of the functions were 1 : 2 : 1

To ensure the atoms within the DMA and formate molecules were chemically sensible, bond stretching and bending potentials as outlined in tables 3.5 and 3.6 were applied. The energy prefactors $D$ and $k$ (equations (2.35) and (2.36)) for the bending and stretching potentials, and the equilibrium angle $\theta_0$ for the bending potentials were taken from the standard MM3 data set. The atomic separations $r_0$ were chosen to be consistent with pair separations derived from the $D(r)$.

| Atomic pair | $D$/eV | $r_0$/Å |
|---|---|---|
| C−N | 2.051 | 1.50 |
| C=O | 3.376 | 1.24 |
| C−D | 2.275 | 1.06 |
| N−D | 2.947 | 1.06 |

**Table 3.5:** Morse bond stretch potentials used to constrain RMC refinement.

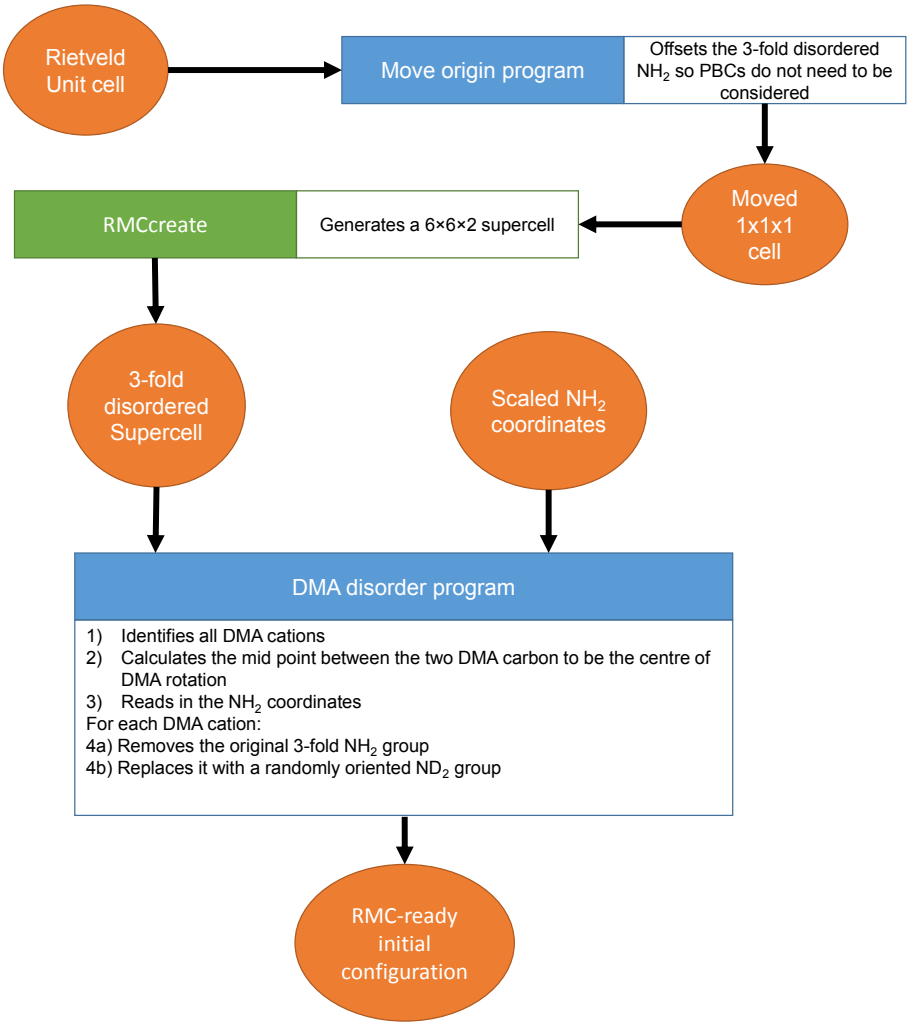


**Figure 3.6:** Scheme used to generate the disordered initial configurations of the high-temperature phase of DMMnF.

| Atoms | $k$/eV | $\theta_0$/° |
|---|---|---|
| O=C=O | 17.876 | 129.800 |
| C−N−C | 7.864 | 108.600 |
| D−C−D | 8.976 | 107.114 |
| C−N−D | 7.602 | 106.376 |
| D−C−O | 7.403 | 114.900 |
| N−C−D | 11.235 | 104.700 |
| C−N−D | 6.504 | 105.949 |

**Table 3.6:** Angle potentials used to constrain RMC refinement.

In addition to the interatomic potentials, distance window constraints (outlined in table 3.7) were applied to ensure atomic pairs which were bonded in the crystal structure remained within bonding distance during the refinement. The maximum ($d_{\max}$) and minimum ($d_{\min}$) distances in the Rietveld-derived unit cell were found, and the distance windows calculated

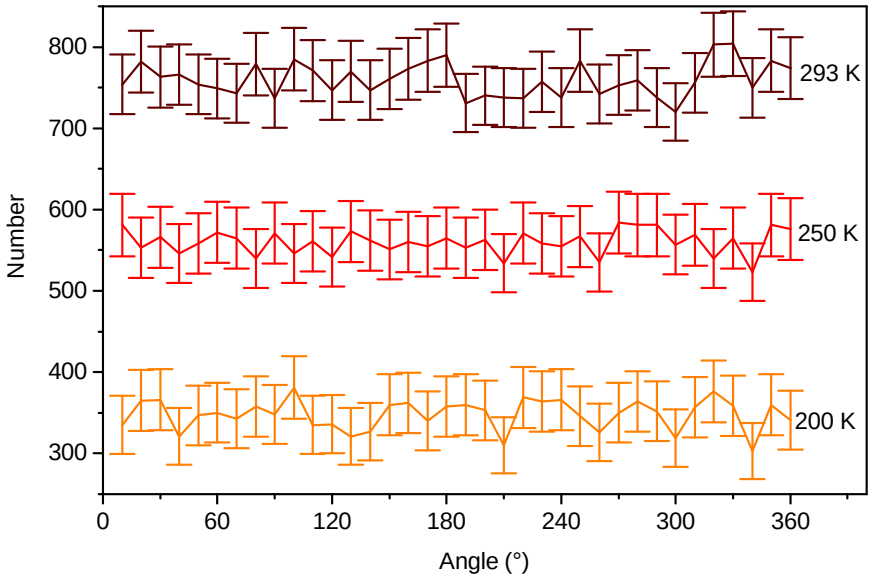


**Figure 3.7:** Graph of the initial distribution of nitrogen angles - offset by 200 - for 30 individual configurations at each temperature after application of the disorder program. The flat distribution confirms that the initial configurations have randomly oriented $ND_2$.

according to equation (3.1) where for all pairs bar Mn−O $x$ and $y = 10$ and for Mn−O $x = 7.5$ and $y = 5$.

$$\begin{aligned} dw_{\max} &= d_{\max} + x\% \\ dw_{\min} &= d_{\min} - y\% \end{aligned} \tag{3.1}$$

| $T$/K | D−C | D−N | C−O | C−N | O−Mn |
|---|---|---|---|---|---|
| 300 | 0.91-1.13 | 0.95-1.17 | 1.12-1.38 | 1.33-1.64 | 2.08-2.36 |
| 243 | 0.92-1.14 | 0.95-1.17 | 1.12-1.38 | 1.33-1.64 | 2.07-2.36 |
| 194 | 0.95-1.17 | 0.95-1.17 | 1.12-1.38 | 1.32-1.63 | 2.07-2.36 |
| 146 | 0.92-1.23 | 0.93-1.21 | 1.14-1.35 | 1.37-1.70 | 2.02-2.38 |
| 97 | 0.93-1.24 | 0.93-1.22 | 1.16-1.36 | 1.36-1.72 | 2.02-2.32 |
| 22 | 0.93-1.26 | 0.93-1.23 | 1.16-1.36 | 1.37-1.74 | 2.03-2.32 |
| 7 | 0.93-1.24 | 0.93-1.23 | 1.16-1.38 | 1.37-1.72 | 2.00-2.35 |

**Table 3.7:** Distance windows applied to RMC refinements

When several atomic pairs in $D(r)$ all contribute to the same peak, it is possible for RMC to generate a skewed distribution of bond separations within that peak, so it is useful to apply artificial PDFs to ensure a chemically sensible distribution. For DMMnF there were three overlapping peaks at low $r$ in $D(r)$ corresponding to C−D, N−D and C−O bonding pairs. Therefore three artificial pair distribution functions were applied for $r \leq 1.7$ Å; $g_{\mathrm{CD}}(r)$, $g_{\mathrm{ND}}(r)$, and $g_{\mathrm{CO}}(r)$. Each artificial pair distribution had a Gaussian distribution and was scaled to the expected scattering length and atomic concentration. The weighting of the artificial functions was $\frac{1}{25}$ of the weighting of $D(r)$. Figure 3.8 shows the $g_{\mathrm{ND}}(r)$ from two different refined 293 K configurations, one where no artificial PDF was applied and one where it was. Before the

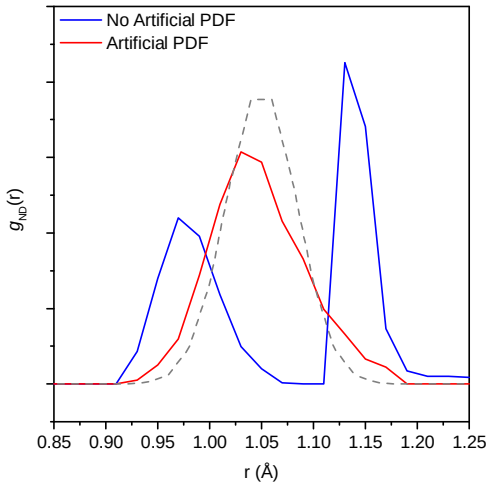


**Figure 3.8:** The $g_{\mathrm{ND}}(r)$ for DMMnF at $293\,\mathrm{K}$ for converged models where no artificial PDF was used in the model (blue) and where an artificial PDF was applied (red). The grey dashed line shows the artificial distribution used in the second instance. The distribution of the red $g_{\mathrm{ND}}(r)$ is closer to the expected Gaussian distribution of peaks than the blue.

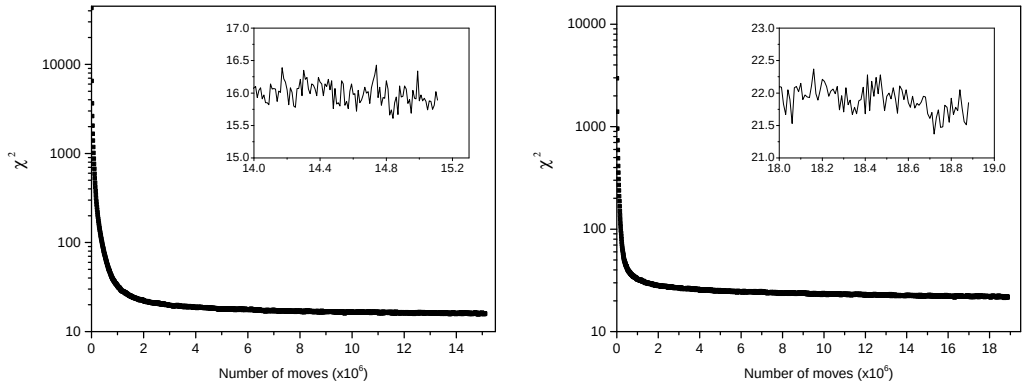


**Figure 3.9:** The "goodness of fit" $\chi^2$ as a function of number of atomic moves for the $D(r)$ in the high temperature phase (left) and the low temperature phase (right). Inset is the change in $\chi^2$ during the final $\approx 1 \times 10^6$ moves

artificial PDF is applied, the $g_{\mathrm{ND}}(r)$ distribution splits to accommodate the pair density of the C−D peak. In the configuration generated after application of the artificial PDF the $g_{\mathrm{ND}}(r)$ and $g_{\mathrm{CD}}(r)$ peaks have a more Gaussian shape, as is expected. The fit between the overall $D(r)$ at $r \leq 1.7\,\text{Å}$ is equally good for both models, however the second model represents a more chemically sensible structure.

### 3.3.7 Completion criteria

The high temperature phase configurations were refined for approximately $15 \times 10^6$ atomic moves, and the low-temperature phase configurations were refined for approximately $18 \times 10^6$ atomic moves, this took four days of computing time. Observation of $\chi^2$ for the $D(r)$, $i(Q)$ and $I(d)$ configurations show no significant improvement during the final $1 \times 10^6$ moves, (figure 3.9) indicating that the models had converged.

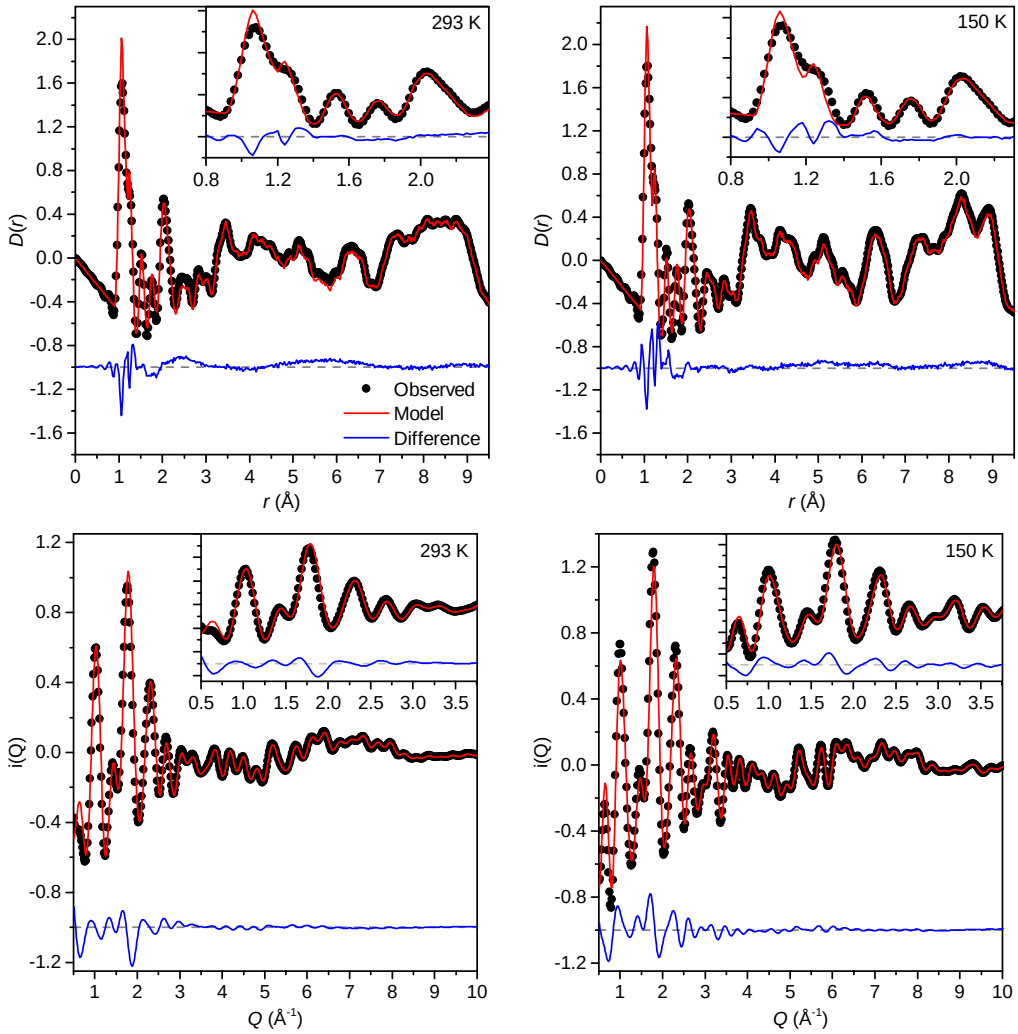


**Figure 3.10:** Top row: The observed (black dots) and calculated (red line) $D(r)$ for a high (left) and low (right) temperature phase refinement. Bottom row: The observed and calculated $i(Q)$ for a high and low temperature phase refinement. Differences are shown in blue.

### 3.3.8 Representative fits

Representative fits of the $D(r)$ and $i(Q)$ to one high and one low temperature converged configuration are shown in figure 3.10. In section 3.3.3 the poor agreement in the Bragg profile between the $R\bar{3}c$ crystal structure and the observed data was attributed to the symmetry restrictions acting on the $CD_3$ group of the DMA cation. When such restrictions are removed during RMC modelling, a significant improvement in agreement between the converged configurations and the observed data when compared to the symmetry-restricted crystal structure is observed. Figure 3.11 shows the observed Bragg profile and the profile as calculated by `RMCProfile` and `GSAS`, and it can be seen that the RMC configuration has better agreement with the observed profile.

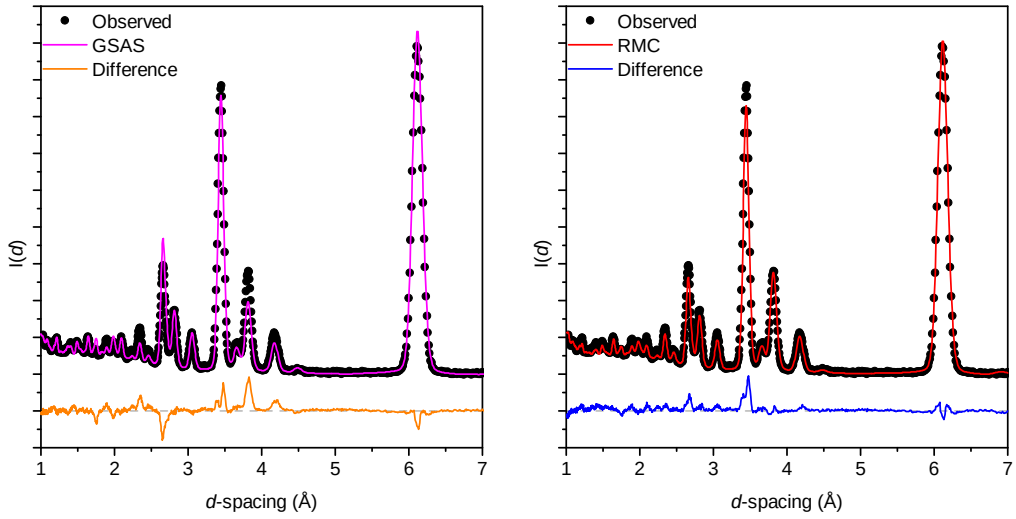


**Figure 3.11:** The observed Bragg profile for DMMnF in the high temperature phase (black dots) compared to the profiles derived from GSAS (left) with $R\bar{3}m$ symmetry restrictions and `RMCProfile` (right) with no symmetry restriction.

## 3.4 Analysis

The primary focus of the investigation into DMMnF was to look for indications of cooperative ordering of DMA cations above the transition temperature. However during the course of the investigation, the N−D···O hydrogen bonding between the dimethylammonium cation and the formate framework was investigated, and strain analysis was performed to infer the DMA cation behaviour below $T_c$.

### 3.4.1 Lattice paramters

In order to directly compare the lattice parameters from the high and low temperature phases, and to calculate the spontaneous strain across the phase transition, the lattice parameters of the high temperature phase were expressed in terms of the low temperature phase by application of equation (3.2), [92], where $\mathbf{a}_h, \mathbf{b}_h, \mathbf{c}_h$ correspond to the $R\bar{3}c$ lattice parameters, and $\mathbf{a}_m, \mathbf{b}_m, \mathbf{c}_m$ to the $Cc$ parameters.

$$\begin{aligned} \mathbf{a}_m &= -\mathbf{a}_h - 2\mathbf{b}_h \\ \mathbf{b}_m &= -\mathbf{a}_h \\ \mathbf{c}_m &= \frac{1}{3}\mathbf{a}_h + \frac{2}{3}\mathbf{b}_h - \frac{1}{3}\mathbf{c}_h \end{aligned} \tag{3.2}$$

The angle $\beta$ was calculated taking the cross product of $\mathbf{a}_m$ and $\mathbf{c}_m$ according to

$$\sin\beta = \frac{|\mathbf{a}_m \times \mathbf{c}_m|}{|\mathbf{a}_m||\mathbf{c}_m|}. \tag{3.3}$$

The lattice parameters calculated for both total scattering and shorter collections are given in table B.1, and the parameters as a function of their ambient temperature values are shown in figure 3.12.

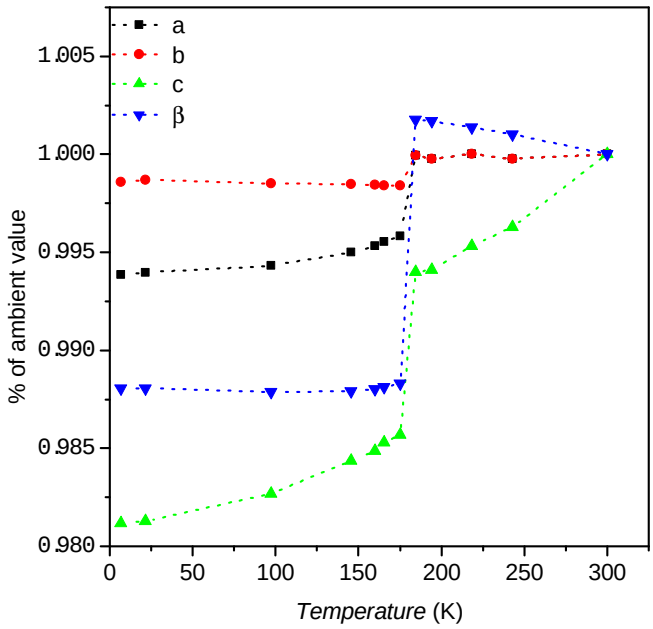


**Figure 3.12:** Lattice parameters $\mathbf{a}_m$, $\mathbf{b}_m$, $\mathbf{c}_m$ and $\beta$ as fractions of their values at 293 K. The sharp discontinuity between 190 K and 180 K is indicative of a first-order phase transition

Observation of $D(r)$ across $T_c$ indicated that the transition was first order, and the sharp discontinuity between the lattice parameters at 190 K and 180 K is consistent with this observation. Furthermore, the temperatures between which the discontinuity falls are consistent with the reported transition temperatures of the fully hydrogenated [86] and partially deuterated [89] analogues, confirming that full deuteration of this material does not significantly alter the phase transition temperature.

### 3.4.2 Strain tensor analysis

The linear Eulerin strain tensor, $e_{ij}$, represents the magnitude and direction of the spontaneous strain on the unit cell as the material cools below $T_c$.

$e_{ij}$ is defined in [94] and is given as

$$e_{ij} = \begin{bmatrix} e_{11} & e_{12} & e_{13} \\ e_{21} & e_{22} & e_{23} \\ e_{31} & e_{32} & e_{33} \end{bmatrix} \tag{3.4}$$

where the diagonal terms $e_{11}, e_{22}$ and $e_{33}$ are given by:

$$e_{11} = 1 - \frac{a_0 \sin\beta_0 \sin\gamma_0^*}{a_1 \sin\beta_1 \sin\gamma_1^*} \tag{3.5a}$$

$$e_{22} = 1 - \frac{b_0 \sin\alpha_0}{b_1 \sin\alpha_1} \tag{3.5b}$$

$$e_{33} = 1 - \frac{c_0}{c_1} \tag{3.5c}$$

and the off-diagonal terms by:

$$e_{12} = e_{21} = \frac{1}{2}\left[\frac{a_0 \sin\beta_0 \cos\gamma_0^*}{a_1 \sin\beta_1 \cos\gamma_1^*} - \frac{b_0 \sin\alpha_0 \cos\gamma_1^*}{b_1 \sin\alpha_1 \cos\gamma_1^*}\right] \tag{3.6a}$$

$$e_{13} = e_{31} = \frac{1}{2}\left[\frac{c_0 \cos\beta_1}{c_0 \sin\beta_1 \sin\gamma_1^*} + \frac{\cos\gamma_1^*}{\sin\gamma_1^*}\left(\frac{c_0 \cos\alpha_1}{c_1 \sin\alpha_1} - \frac{b_0 \cos\alpha_0}{b_1 \sin\alpha_1}\right) - \frac{a_0 \cos\beta_0}{a_1 \sin\beta_1 \sin\gamma_1^*}\right] \tag{3.6b}$$

$$e_{23} = e_{32} = \frac{1}{2}\left[\frac{c_0 \cos\alpha_1}{c_1 \sin\alpha_1} - \frac{b_0 \cos\alpha_0}{b_1 \sin\alpha_1}\right] \tag{3.6c}$$

In these equations $a_0, b_0, c_0, \alpha_0, \beta_0, \gamma_0$ are the lattice parameters before deformation (in the high temperature phase), $a_1, b_1, c_1, \alpha_1, \beta_1, \gamma_1$ are the lattice parameters after deformation (in the low temperature phase) where both are expressed in terms of the same space group. $\gamma_1*$ is 180° - $\gamma_1$ and so on.

The principal components $e'_1$, $e'_2$ and $e'_3$ were calculated by diagonalising $e_{ij}$ using `MATLAB` code given in the electronic appendix.

The principal components as a function of temperature are shown in the left of figure 3.13. The directions in which each component acts with respect to the perovskite pseudo-cubic cell were also calculated and are shown to the right. From the graph we see that below $T_c$ the components become non-zero, as is expected, and in the case of $e'_3$, continue to change upon cooling.

Based on Landau theory, the strains will be proportional to the square of an order parameter $\eta^2$, which for DMMnF is a measure of orientational disorder of the guest cations [95].

If it is assumed that at 7 K the DMA cations are fully ordered, then an estimation of the disorder of the DMA cation at 180 K, just below $T_c$, can be made using equation (3.7).

$$\begin{aligned}\eta_{180\,\mathrm{K}} &= \sqrt{\frac{e'_{3(180\,\mathrm{K})}}{e'_{3(7\,\mathrm{K})}}} \\ &= \sqrt{\frac{20.3890 \times 10^3}{27.0384 \times 10^3}} \\ &= 0.8684\end{aligned} \tag{3.7}$$

From this it can be seen that just below $T_c$ approximately 13% of the disorder found in the high-temperature phase is already present. This result is consistent with Raman studies of DMMnF [89] which found that below $T_c$, the N···O hydrogen-bond strength continued to increase on cooling, indicating that just below $T_c$, dimethylammonium had more freedom to move than at lower temperatures. In subsequent analysis of the N···O distances, (section 3.4.5) there is indication that there is a change in the bonding pairs between the DMA cation and the framework from just below $T_c$ to 20 K, but there is no obvious indication of a change in hydrogen bonding strength.

The direction of the eigenvector of the most positive strain $e'_3$ (blue arrow in figure 3.13) is approximately 20° away from the DMA C···C axis about which the $ND_2$ rotates, and the direction of the most negative strain ($e'_1$) lies approximately 20° from the normal to $e'_3$. The directions along which these vectors lie suggest that during the phase transition, the framework contracts around dimethylammonium, a conclusion which is supported by analysis of the atomistic configurations (section 3.4.5) and by Raman studies [89].

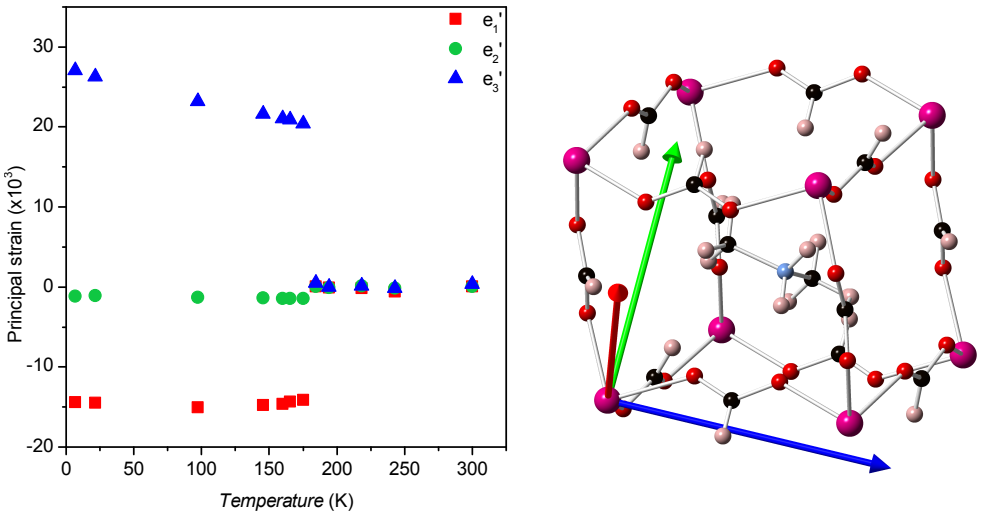


**Figure 3.13:** Left: The principal components $e'_1$ (red), $e'_2$ (green) and $e'_3$ (blue) of DMMnF across the phase transition. Right: The corresponding eigenvectors of each component applied to the $Cc$ cell

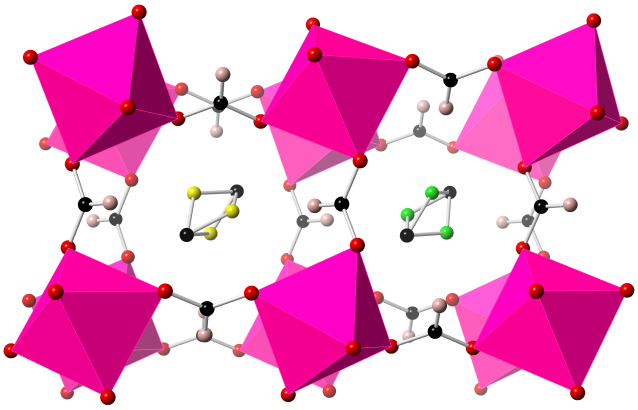

**Figure 3.14:** The two DMA cation sites in neighbouring pores are related by the $c-$glide plane, and are shown in green and yellow to distinguish. Deuterium of the DMA cation have been removed for clarity

### 3.4.3 Rotation of the dimethylammonium cation

Above 183 K the DMA cations are 3-fold disordered, with $\frac{1}{3}$ occupancy of the $ND_2$ group of each DMA cation about the rotation axis. Due to the $c$-glide plane of the $R\bar{3}c$ crystal structure, neighbouring framework pores have their corresponding DMA cation reflected through 180° as shown in figure 3.14. This means that in the average structure there are six different orientations of the DMA cation relative to its C···C axis. Figure 3.14 shows two different DMA cation sites inside neighbouring pores coloured green and yellow. The six orientations observed correspond to the threefold disorder on the "yellow" and "green" sites. For the rest of this chapter "green" and "yellow" will be used to differentiate between these two sites.

The orientational distribution of the DMA cations was calculated for the final configurations of the high temperature phase refinements and compared to the random initial configurations (figure 3.7). When the distribution of DMA orientations in the final configurations was observed, six large maxima were seen. When the distributions were split into those from DMA

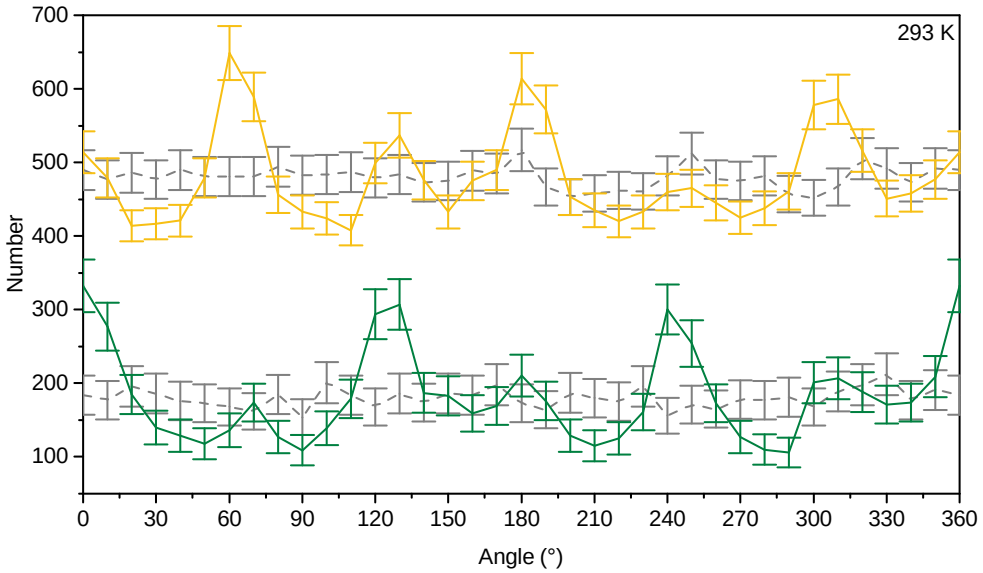


**Figure 3.15:** The distribution of $ND_2$ orientations about the centre of the DMA cation from 12 960 DMA cations. The plots have been coloured to correspond with the two different orientations of the three-fold disordered DMA cation has in the crystal structure. The grey lines are the initial orientations for the corresponding sites.

on the yellow sites and those on the green sites, the orientations of the yellow DMA were preferentially observed at 60°, 180°, and 300°, and the preferential orientations of the green sites offset from the yellow sites by 180°. Figure 3.15 shows the distribution of $ND_2$ angles for DMMnF at 293 K from 30 unique initial configurations, each with 432 DMA cations. From this figure we see that the $ND_2$ groups become more ordered during refinement, moving away from the random initial orientations.

These distributions shown in figure 3.15 correspond to the disordered model of the average structure with the DMA cation forming two N···O hydrogen bonds with two distinct formate ions as shown on the left in figure 3.16. In addition to the large maxima, small maxima are between the main peaks are observed in both the green and yellow sites. The small maxima correspond to the DMA cation being in a non preferred orientation, forming two (chemically plausible) hydrogen bonds with the same formate (right in figure 3.16).

In order to test the sensitivity of the DMA orientational disorder to the initial configurations, two different initial configurations were also investigated. 30 RMC configurations were generated each using one of two different starting models, and the distribution of the final DMA orientations was calculated. Model **1** refers to the previously reported configurations with randomly oriented DMA in the initial structure. Model **2** had the green and yellow DMA cations distributed randomly on one of the three sites in the published rhombohedral crystal structure, this produced 30 unique initial configurations, and model **3** where the cations were forced onto only one of these three sites, which necessarily produced only one unique configuration. The $\chi^2$ for the model **2** and model **3** trials were calculated and are shown in figure 3.17. The Bragg contribution to $\chi^2$ from models **2** and **3** were comparable to, but smaller than the Bragg contribution to $\chi^2$ for model **1**. The $\chi^2$ for the $D(r)$ and $i(Q)$ fits for models **1**, **2**, and **3** are comparable.

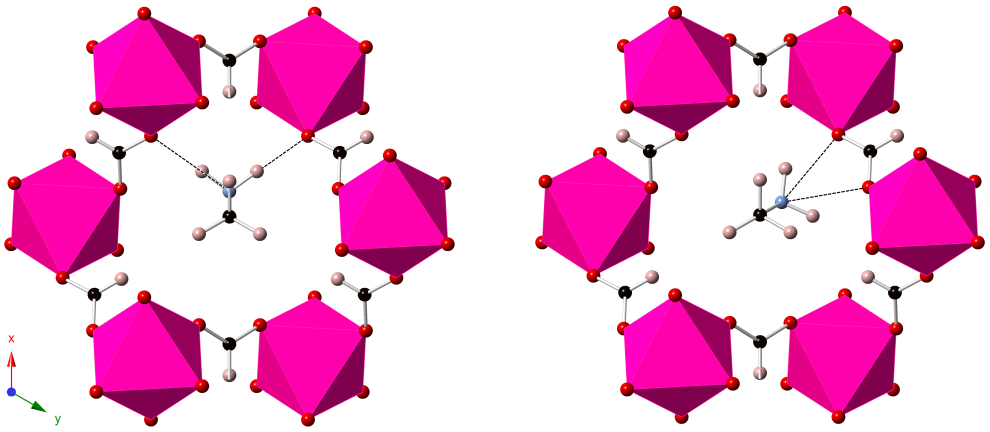


**Figure 3.16:** Average structure of DMMnF. Left: Orientation of the DMA cation corresponding to the average structure, and one of the large maxima and the DMA cation hydrogen bonds (dashed lines) with two different formate groups. Right: Orientation of the DMA cation corresponding to the small maxima where DMA forms two hydrogen bonds with the same formate group.

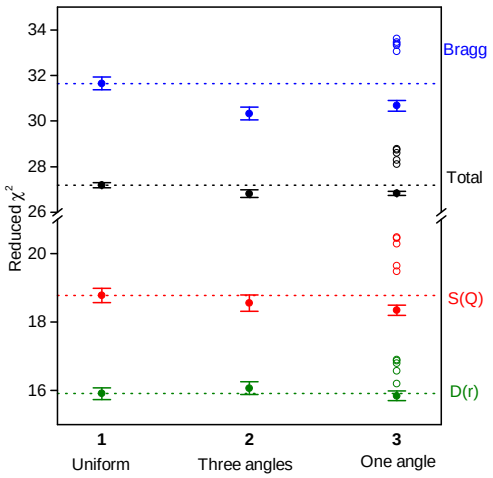


**Figure 3.17:** The $\chi^2$ for 30 RMC configurations of DMMnF at 293 K when the distribution of DMA orientations in the initial configuration is **1**. uniform. **2**. one of three angles, and **3**. one angle. Model **3**. had 5 configurations with significantly higher $\chi^2$ than the others, which have been shown as open circles. Error bars are the standard deviations for the multiple runs.

Figure 3.18 shows the initial (grey) and final (coloured) distributions for each model. From this we see in model **2** the small minima at 60°, 180°, and 300° on the green sites, and the corresponding peaks in the yellow sites are absent. In model **3** the other two major peaks for the green and yellow sites are absent.

Despite the significant difference in the orientational order of the DMA cation, the $\chi^2$ for all three models are comparable. This indicates that the experimental data has limited sensitivity to the orientations of the DMA cations. This result also shows, that while in theory RMC models are independent of their initial configuration [48] as moves which worsen the agreement between the experimental and the model may be accepted, in practice there is a limit to this independence.

Furthermore, for configurations which started with a uniform distribution of DMA orien-

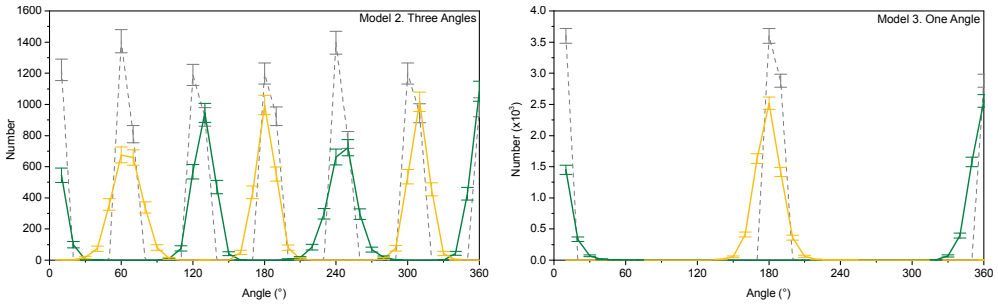


**Figure 3.18:** Initial (grey) and final (colours) distribution of DMA orientations for two different models.

tations (model **1**), there was no change in the preferred orientations as DMMnF approached $T_c$.

Unless otherwise stated, all analysis presented in this chapter has been performed on structures where the initial configurations were generated according to model **1**. Model **1** was chosen as the focus of this work is on the short range interactions between guest cations and frameworks, and $D(r)$ contains more information on the local structure. The $\chi^2$ of $D(r)$ for model **1** had the lowest value and the smallest variation, and so would likely allow for a more consistent and accurate description of the local order in DMMnF.

### 3.4.4 Entropy calculations

The most recent published calculation for the change of entropy $\Delta S$ across the phase transition, of DMMnF was consistent with freezing in of three-fold disorder [92] ($\Delta S/R \approx \ln(3)$), this result has also been observed in the Mg analogue [73].

In order to compare the distribution of DMA orientations observed in the atomistic configurations, the entropy of each phase, due to DMA orientation, was estimated using the relationship from statistical mechanics:

$$S_{\text{molar}} = -R \sum_i p_i \ln(p_i) \tag{3.8}$$

where the sum is over all microstates $i$, with corresponding probabilities $p_i$. The rotation angles were divided into equal sized bins and each bin was taken to be one microstate.

For model **1** where there was a uniform distribution of initial angles, the change in entropy between the low and high-temperature phases, $\Delta S/R \approx \ln(6.4)$, significantly higher than that of a simple three-fold order-disorder transition. The difference between the atomistic estimation and the DSC-derived calculation is likely to be due to the atomistic configuration estimate only considering DMA orientation as contributing to the change in entropy and not accounting for correlations between the DMA orientation and the framework. If correlations between the cation and the framework were accounted for, then the entropy of the high temperature phase would be reduced, and hence reduce $\Delta S$. The discrepancy between the orientational estimate and the experimentally derived $\Delta S$ indicates that correlations between the DMA motion and the framework are important.

Similar entropy calculations were performed on model **2** and **3** with the initial angles distributed on three and one site respectively. For model **2** $\Delta S/R \approx \ln(2.1)$ which indicates that when the distribution of the angles is taken into account, the rotational entropy of the

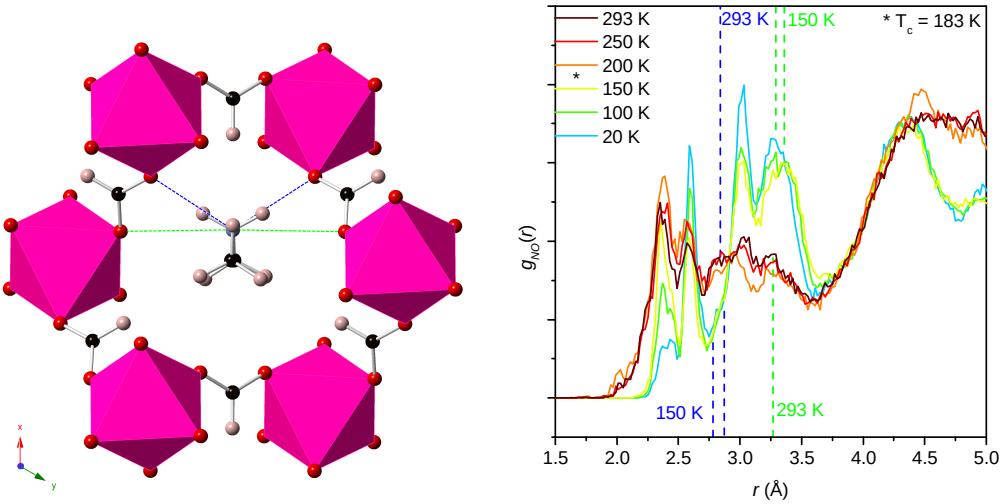


**Figure 3.19:** Left: Average crystal structure for DMMnF highlighting the N···O bonding for the nearest (blue) and second nearest pairs (green). Right: $g_{\mathrm{NO}}(r)$ for DMMnF at six different temperatures with the positions of the N···O nearest and second nearest pairs from the average crystal structure at both 293 K and 150 K shown as dashed lines.

DMA cation is insufficient to account for the observed change in entropy. Model **3** produced a negative change in entropy, indicating that the rigidly ordered initial configuration is not representative of the DMA orientations in the high temperature phase and that `RMCProfile` cannot rotate the DMA cations out of this particular local minimum.

### 3.4.5 N...O hydrogen bonding

Analysis of the DMA orientation and entropy calculations had indicated that correlations between the guest cation and the framework were important to understanding the mechanism behind the phase transition of DMMnF. So with this in mind, changes in the hydrogen bonding between the dimethylammonium cation and the formate framework (N−D···O) as the dielectric transition was approached were investigated.

Raman studies performed on DMMnF [89] suggested that the strength of N···O hydrogen-bonding between the guest cation and the framework (dashed lines on the structure in figure 3.16) increases as the material cools, and that the ordering process was likely mediated by the making and breaking of these bonds. These vibrational studies had ruled out the possibility of the hydrogen moving along the N−H···O bond as the origin of the phase transition. Atomistic configurations allow for partial pair distribution functions for all pairs of atoms in the model to be investigated, which meant that the $g_{\mathrm{NO}}(r)$ partial pair distribution function could be examined.

Figure 3.19 shows the average $g_{\mathrm{NO}}(r)$ from 30 distinct configurations at six different temperatures. In the high temperature phase, a large peak at 2.4 Å and a smaller peak at 2.6 Å are observed. Below $T_c$, the intensity of the 2.4 Å peak decreases on cooling, and the intensity of the 2.6 Å peak increases. The peaks in $g_{\mathrm{NO}}(r)$ at 2.4 Å and 2.6 Å differ from the average crystal structure in that the shortest N···O distances are not the same length.

Another significant result of analysis of $g_{\mathrm{NO}}(r)$, is that in both the high and the low

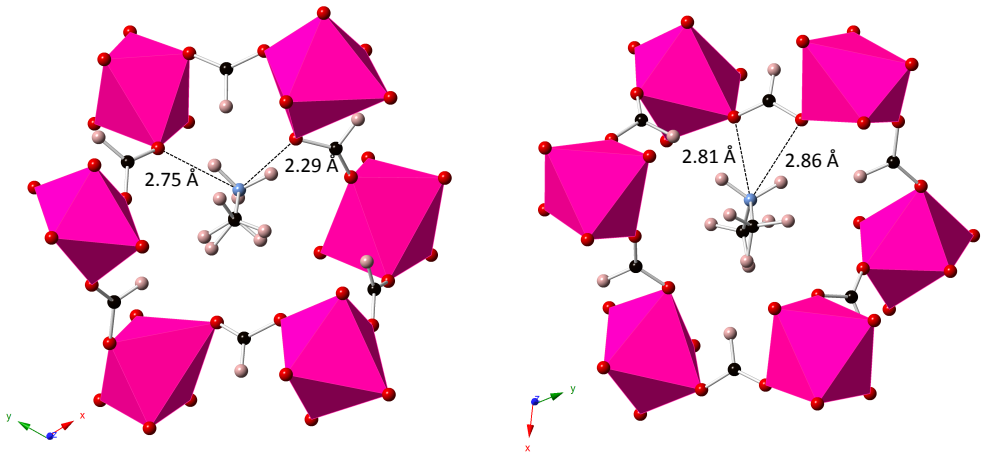


**Figure 3.20:** Representative final configurations of DMMnF in the high temperature phase with closest N···O distances highlighted. Left: DMA is bonded to two adjacent formates producing two different bond lengths, but with the same topology of the average structure (left in fig 3.16). Right: DMA cation bound to two oxygen of the same formate ion (right in fig 3.16) with similar bond lengths to those in the average structure, but a different topology.

temperature phase, the N···O separations are significantly shorter than those indicated in the average structure, shown as dashed lines on the graph in figure 3.19. This difference in the instantaneous and average N···O distances is attributed to short-lived distortions of the framework to accommodate the position of the dimethylammonium cation. Figure 3.20 shows two representative configurations of the dimethylammonium cation within the pore in the high temperature phase. On the left we see the cation hydrogen bonding with the framework with the same topology as in the average unit cell, but with two different N···O bond lengths. On the right of figure 3.20 we see two similar N···O bond lengths but the dimethylammonium cation is only forming bonds with one formate, in a "pincer-like" configuration.

The relative changes in intensity of the 2.4 Å and 2.6 Å peaks imply that as the DMA cations begin to order, it becomes increasingly unfavourable to distort the framework to accommodate the very short N···O bonds.

The position of these short N···O bonding peaks are constant through the phase transition indicating that these N···O separations are due to favourable local geometry and are independent of the onset of long-range interactions. Conversely when the second-nearest N···O separations are investigated (green dashed lines in figure 3.19) we see that in the low temperature phase, $g_{\mathrm{NO}}(r)$ is more structured, which is attributed to more distant formate ions freezing into longer hydrogen bonds as the framework contracts about the dimethylammonium cation below $T_c$

When the interactions between a DMA cation in one pore and the formate of the framework nearest to it are investigated, it becomes clear why the framework is seen to distort in such a way. Figure 3.21 shows two adjacent DMMnF pores, with the formate's oxygen with which the DMA can interact with shown in yellow and green based on the designations earlier in the chapter. We see that even though the DMA cations are neighbours, the formate linkers which they interact with are completely separate, meaning that the distortion of the framework around one DMA cation does not hinder the ability of the formates around the neighbouring

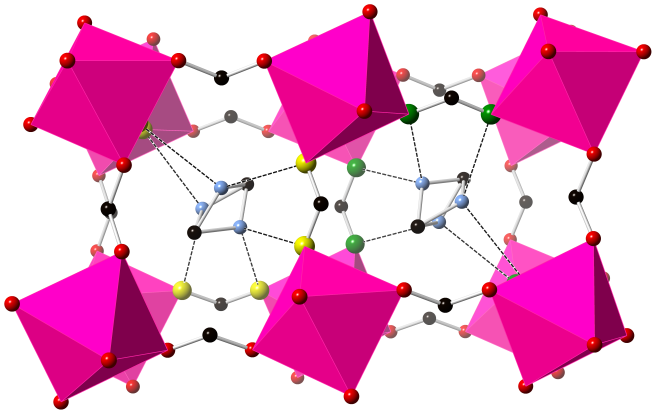

**Figure 3.21:** Two adjacent pores of DMMnF with the 3-fold disordered DMA cations in the centre. N···O bonds are shown as dashed lines. The oxygen with which the DMA cation bonds have been coloured yellow and green in accordance with earlier DMA site designations (figure 3.14). Despite the fact that the DMA cations are in neighbouring pores, they do not form hydrogen bonds with any of the same oxygen.

DMA cation to deform around it.

As with all partial PDFs reported in this thesis, the contribution from any one atomic pair, (such as N and O) is dependent on their relative concentrations and their scattering lengths (table 3.4). The contribution of $g_{\mathrm{NO}}(r)$ to the overall PDF $D(r)$ or $G(r)$ is small. The RMC algorithm moves atoms individually and without regard for the effect on any single partial PDF. In addition, the application of interatomic potentials (table 3.5) which are applied to $g_{\mathrm{NO}}(r)$ via the N−D stretching potential, and multiple configurations producing the same distribution give confidence to any results obtained via analysis of the partial PDFs.

Given that the orientation of the DMA cation was found to be dependent on the initial configurations, the partial PDF $g_{\mathrm{NO}}(r)$ was generated for 10 configurations from each of the three different high temperature phase configurations. Figure 3.22 shows $g_{\mathrm{NO}}(r)$ generated from high temperature phase configurations generated with model **1** a uniform random distribution of DMA cations, model **2** where in the initial configuration DMA cations were distributed randomly on one of the three sites in the rhombohedral crystal structure, and model **3** where the cations were forced onto only one of these three sites. From this we see that formation of short 2.4 Å and 2.6 Å N···O hydrogen bonds are independent of the initial configurations, which is an encouraging sign that the results obtained by partial PDF analysis are robust.

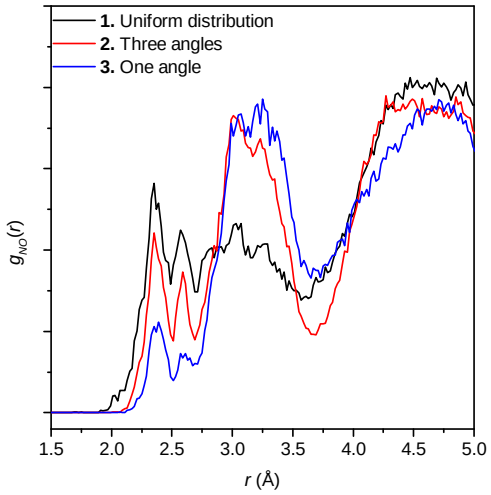


**Figure 3.22:** $g_{\mathrm{NO}}(r)$ from three different initial configurations. Each $g_{\mathrm{NO}}(r)$ is averaged from 10 different converged configurations. We see that the short N···O peaks at 2.4 Å and 2.6 Å are observed in all models, although the relative magnitude of the peaks differ.

## 3.5 Summary

This chapter reports the total scattering and RMC study on the behaviour of guest DMA cations in the multiferroic MOF DMMnF. Scattering data were collected above and below the dielectric phase transition and the interactions of the DMA cations with the framework analysed.

Analysis of the atomistic configurations found that the DMA cations form significantly shorter hydrogen bonds with the formate framework than the average structure suggests. The shortest of these bonds correspond to short-lived deformations of the framework with respect to the cation; these deformations become increasingly unfavourable at low temperatures. Strain tensor analysis shows that the framework contracts around DMA at the phase transition, and that the guest cations continue to order as DMMnF is cooled further below $T_{\mathrm{c}}$.

The threefold disorder of the DMA cation present in the high-temperature average structure was reproduced in high-temperature phase atomistic configurations generated from initial configurations where the DMA cation is randomly oriented around the C···C axis. In addition to the orientations consistent with the average structure, subsidiary orientational maxima, which could not have been seen via standard crystallography were observed. The change in entropy between the high and the low-temperature phase configurations is higher than can be accounted for by a simple threefold disorder model which indicates that there are important correlations between the guest cation and the framework in the high temperature phase.

# Chapter 4

# Magnetic Analysis of Dimethylammonium Manganese Formate

## 4.1 Introduction

Inorganic perovskites such as $Pb_2CoWO_6$ and $Pb_2FeTaO_6$ [96] display multiferroicity, the coexistence of two or more ferroic orders in one material. These materials also display magnetoelectric coupling, where electric polarisation responds to applied magnetic fields and the magnetisation responds to applied electric fields. The coexistence of magnetic and electrical ordering, and their potential to be coupled are of particular interest for data storage applications. In addition to displaying electric ordering, DMMnF orders magnetically below 8.5 K [30].

Unlike many inorganic perovskites, in MOFs the magnetism and electric ordering have different origins and are not mutually exclusive. For MOFs such as DMMnF, and others in the dimethylammonium formate family, the origin of electric ordering is the cooperative behaviour of the polar guest cations. Magnetism can then arise from the divalent metal ions on the perovskite B site, where the exchange interactions are mediated by the formate bridge. For DMMnF, the magnetic moment is found on the $Mn^{2+}$ ions.

Bulk measurements have been performed DMMnF in an attempt to understand the local magnetic environment. Neutron diffraction is important as it allows for information on the magnetic structure of DMMnF to be collected via the Bragg profile and $i(Q)$. Application of the RMC method using the neutron scattering data allows the magnetic moments of multiple $Mn^{2+}$ to be modelled. Analysis of the magnetic moments on multiple $Mn^{2+}$ from converged models allow the nearest and second-nearest neighbour interactions to be probed, and for these interactions to be compared against observations of the bulk behaviour found via susceptibility measurements.

## 4.2 The material

In addition to the DMA formate family, the guanidinium formate family with general formula $C(NH_2)_3M(HCO_2)_3$ also display magnetic ordering, with M = Mn, Fe, Co, Ni and Cu [57] and magnetic transition temperatures ranging from 4.6 K to 34.2 K.

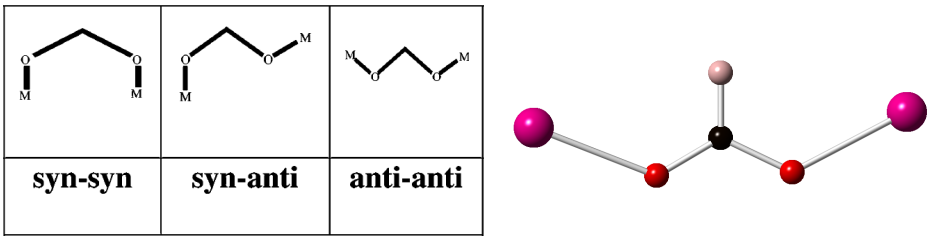


**Figure 4.1:** Left: Three possible bridging modes of the formate group with metal (M) ions on either side (taken from [30]). Right: The anti-anti bridging mode for all formate groups in DMMnF which, for some $Cu^{2+}$ complexes mediates antiferromagnetic interattions.

There is an isostructural range of materials with general formula $M_3(HCO_2)_6S$ where M is a paramagnetic or diamagnetic metal, and S one of over 40 solvents which are also magnetic [97].

Other linkers can also be used to mediate magnetic exchange between metal sites, including OH [64], $N_3$ [30, 64], and CN [30, 64, 97]. Cyanide will allow for stronger interactions than the formate bridges [97] because as a rule, the shorter and more conjugated the bridge, the more efficient the transmission of the magnetic coupling [64], this comes at the expense of bridging modes however.

Therefore, the three-atom formate linker (called three-atom as the formate H isn't involved in magnetic coupling [64]) allows a compromise, a short enough distance that the magnetic exchange can be mediated, and the possibility of several different bridging modes as shown in figure 4.1. The magnetic properties are closely linked with the different bridging modes for the formate, where either ferro or antiferromagnetic exchange is mediated in different situations [30, 98]. All $Mn^{2+}$ within DMMnF are connected via formate bridges in the anti-anti bridging mode [30] (see figure 4.1). Magnetic studies on formate-bridged $Cu^{2+}$ complexes have found that the anti-anti bridging mode mediates strong antiferromagnetic interactions [99].

Magnetic susceptibility measurements have been performed on DMMnF, and the data $\chi_M$ were fit to the Curie-Weiss law

$$\chi_M = \frac{C}{T-\theta}, \tag{4.1}$$

where $C$ is the Curie constant, $T$ is the temperature, and $\theta$ is the Weiss constant. A negative Weiss constant ($-14.6\,\mathrm{K}$ [88] and $-16.3\,\mathrm{K}$ [30]) indicative of antiferromagnetic ordering, was found. In addition to the susceptibility measurements, muon spin relaxation measurements on DMMnF found antiferromagnetic coupling between neighbouring $Mn^{2+}$. [87]

A particularly useful feature of multiferroics would be if there was coupling between the magnetic and electric order parameters. The significant difference between the electric and magnetic ordering temperatures in DMMnF indicates that if there is any coupling between the two order parameters then it is weak, [87]. However there have been reports with evidence that DMMnF both does [93, 100] and doesn't display magnetoelectric coupling [90]. But weak magnetoelastic coupling in DMMnF has been reported, [85] so even if there is not direct coupling between the magnetic and electric order parameters, they could still interact via the strain in the unit cell.

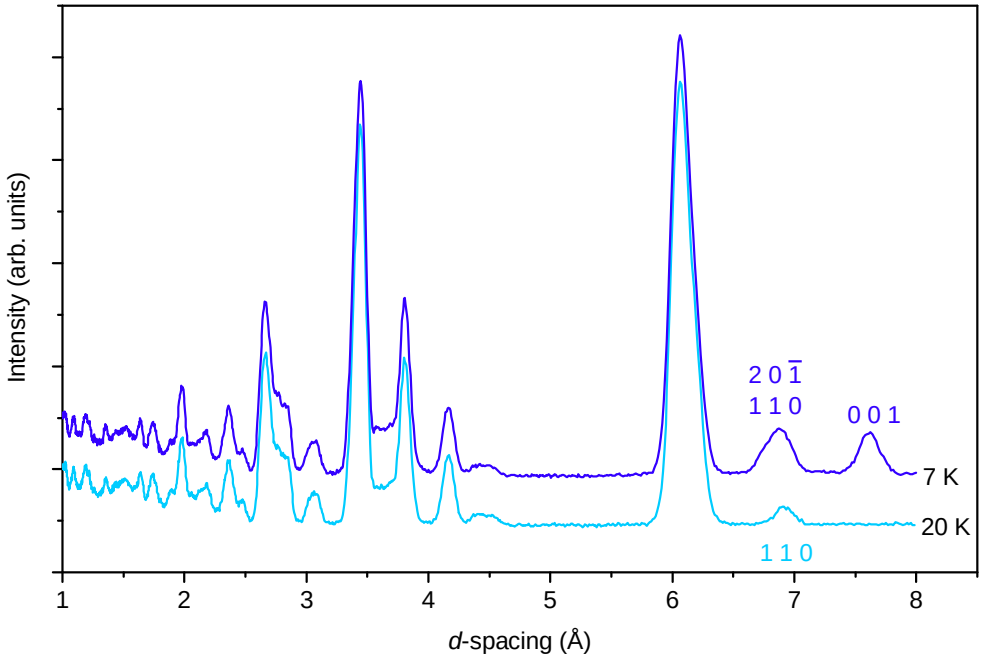


**Figure 4.2:** The observed Bragg profile for DMMnF at 20 K and 7 K. The magnetic profile has an additional peak at 7.60 Å and the $(110)$ peak at 6.90 Å present at 20 K is joined by a $(20\bar{1})$ peak at 6.77 Å which is not fully resolved for bank 2.

## 4.3 Experimental

Scattering data was collected as outlined in 3.3.2 below the magnetic transition temperature 8.5 K. Processing and analysing the magnetic data for DMMnF had its own particular set of issues that had to be overcome. Most notably was getting a stable Rietveld refinement (discussed in section 4.3.1) and deciding the most appropriate way to apply the RMC algorithm to ensure that the Bragg and $i(Q)$ data - containing magnetic information were correctly weighted.

### 4.3.1 Magnetic rietveld refinement

Figure 4.2 shows the observed Bragg profile for DMMnF at 20 K and 7 K. The magnetic phase has a $(001)$ peak with $d$-spacing of 7.60 Å. In addition to the magnetic only peak, below 8.5 K a peak with $d$-spacing 6.77 Å $(20\bar{1})$, shown in figure 4.2 emerges.

For the purposes of the magnetic structure refinement, the primary peak of interest was the purely magnetic $(001)$ peak, as there was no possibility of intensity from the structural peak affecting the refinement as there would be if the $(20\bar{1})$ peak was investigated. Neutrons are sensitive to the magnetic moments perpendicular to the **Q** direction, therefore the $(001)$ peak will contain information about the $a$ and $b$ component of the magnetic moment but not the $c*$ as it lies along the $c*$-direction.

As the magnetic peaks can be indexed in the structural unit cell, there is no magnetic cell doubling, therefore there are two possible magnetic space groups which could be applied to the DMMnF refinement, $Cc$ and $Cc'$ [101]. For $Cc$, there is no time reversal operations, and so the

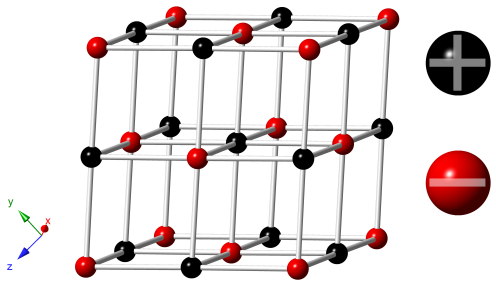

**Figure 4.3:** G-type structure where the spins on atoms in a cubic framework are shown pointing either $+$ (black) or $-$ (red) along an arbitrary direction. The nearest neighbours of each spin are pointing in opposite directions.

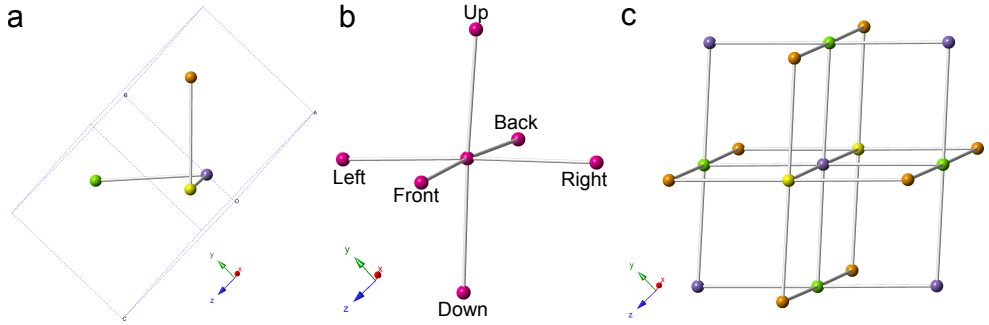


**Figure 4.4:** The relative positions of $Mn^{2+}$ in the Rietveld unit cell and for subsequent analysis where for all three images formate linkers have been drawn as straight lines to highlight the cubic network topology. a) The four $Mn^{2+}$ with respect to the unit cell (dashed lines) $Mn_1$ (purple) at $(0, \frac{1}{4}+x, 0)$, $Mn_2$ (orange) at $(\frac{1}{2}, \frac{3}{4}+x, 0)$, $Mn_3$ (green) at $(0, \frac{3}{4}-x, \frac{1}{2})$, and $Mn_4$ (yellow) at $(\frac{1}{2}, \frac{1}{4}-x, \frac{1}{2})$, with $x = 0.00159$. b) The 6 nearest neighbours of Mn in the initial RMC supercell with all other atoms removed for clarity and their designations "Up" "Down", "Left", "Right", "Front" and "Back" which are based on their positions in the RMC supercell relative to the target atom. The distance between the "up" and "down" Mn is $12.14\,\text{Å}$. c) The first and second nearest neighbouring $Mn^{2+}$ in the RMC supercell coloured to highlight their origin in the unit cell.

magnetic moment is manipulated in the same way the atoms would be by symmetry operators, for DMMnF this means a checkerboard (G-type - figure 4.3) antiferromagnet with the moment parallel to the $b$ axis. For $Cc'$, magnetic moments subject to time-reversal operations, but still produce a checkerboard antiferromagnetic arrangement, now with moments in the $ac$ plane. As the $(001)$ peak is insensitive to the component parallel to $c^*$ component, then the moments in the $Cc'$ refinement have a substantial $a$ component.

Figure 4.4a shows the positions of the four magnetic $Mn^{2+}$ ions within the unit cell, the formate linkers have been shown as lines to highlight the cubic topology.

An alternative to the space group analysis presented in the previous paragraphs is shown in figure 4.5. Atomistic configurations of approximate dimensions $60\,\text{Å} \times 50\,\text{Å} \times 53\,\text{Å}$ were generated and the magnetic moments on $Mn^{2+}$ aligned in a checkerboard pattern (so the nearest neighbours of each moment are pointing in opposite directions). The direction of the magnetic moments were changed and the Bragg profile for the configurations calculated. In figure 4.5 the black dots show the observed profile, and the lines the different directions of the moments. We see that for the model with the moment along $c^*$ (red), the $(001)$ peak is

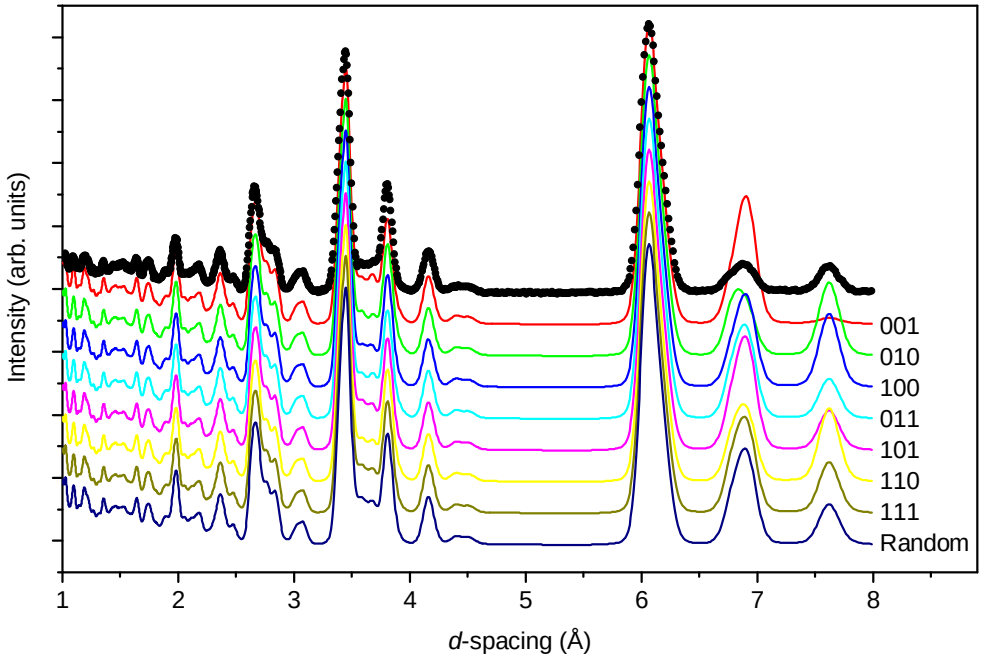


**Figure 4.5:** The observed Bragg profile (black dots) compared to the calculated profile for several G-type antiferromagnetic arrangements of Mn spins where $\pm$ the spin direction is given. "Random" moment $= \pm$ $(-0.63, -0.34, -0.61)$

absent, as expected. However models with an $a$ or $b$ component all produce a peak at 7.60 Å. Furthermore, in the models where the moments which lie solely on the $a$ or $b$ axis (green and blue) the $(20\bar{1})$ and (110), and (001) peaks at high $d$-spacing are approximately equal in height, as observed in the scattering data. For the models shown in figure 4.5, the 010 model (green) is consistent with the $Cc$ model, and the red, blue and pink lines are consistent with the $Cc'$ model.

The initial set-up of the Rietveld refinement for the $Cc$ and $Cc'$ models was performed as described in section 3.3.3 using the `GSAS EXPGUI` interface. Instead of a purely structural refinement, a combined magnetic and structural refinement was chosen for the $Cc$ model. A magnetic moment of $5.92\,\mu_B$ pointing along (100) was placed on the $Mn^{2+}$ and allowed to refine. Another refinement using the $Cc'$ model with a magnetic moment $5.92\,\mu_B$ pointing along 010 direction was also allowed to refine. The top of figure 4.6 shows the `GSAS` fit with the peak positions for the $Cc$ refinement, and the bottom shows the $Cc'$ refinement. The magnetic moment was allowed to refine, as was the background, unit cell and atomic coordinates. The refined lattice parameters and unit cell volume for both refinements were the same within experimental uncertainty. The magnitude of the magnetic moment on $Mn^{2+}$ did not remain constant at $5.92\,\mu_B$ however, for the $Cc$ model the moment was refined to $3.55\,\mu_B$ and for the $Cc'$ model, $3.73\,\mu_B$ shown in table 4.1. Introduction of a component along $c*$ to the magnetic moment did not improve agreement in the $Cc'$ model.

Both models fit the data well, with the $Cc'$ model, with spins aligning along the $b$ axis fitting the $(20\bar{1})$ and (110) peaks better than the $Cc$ model. Therefore it was concluded that $Cc'$ model gave the best description of the Bragg profile.

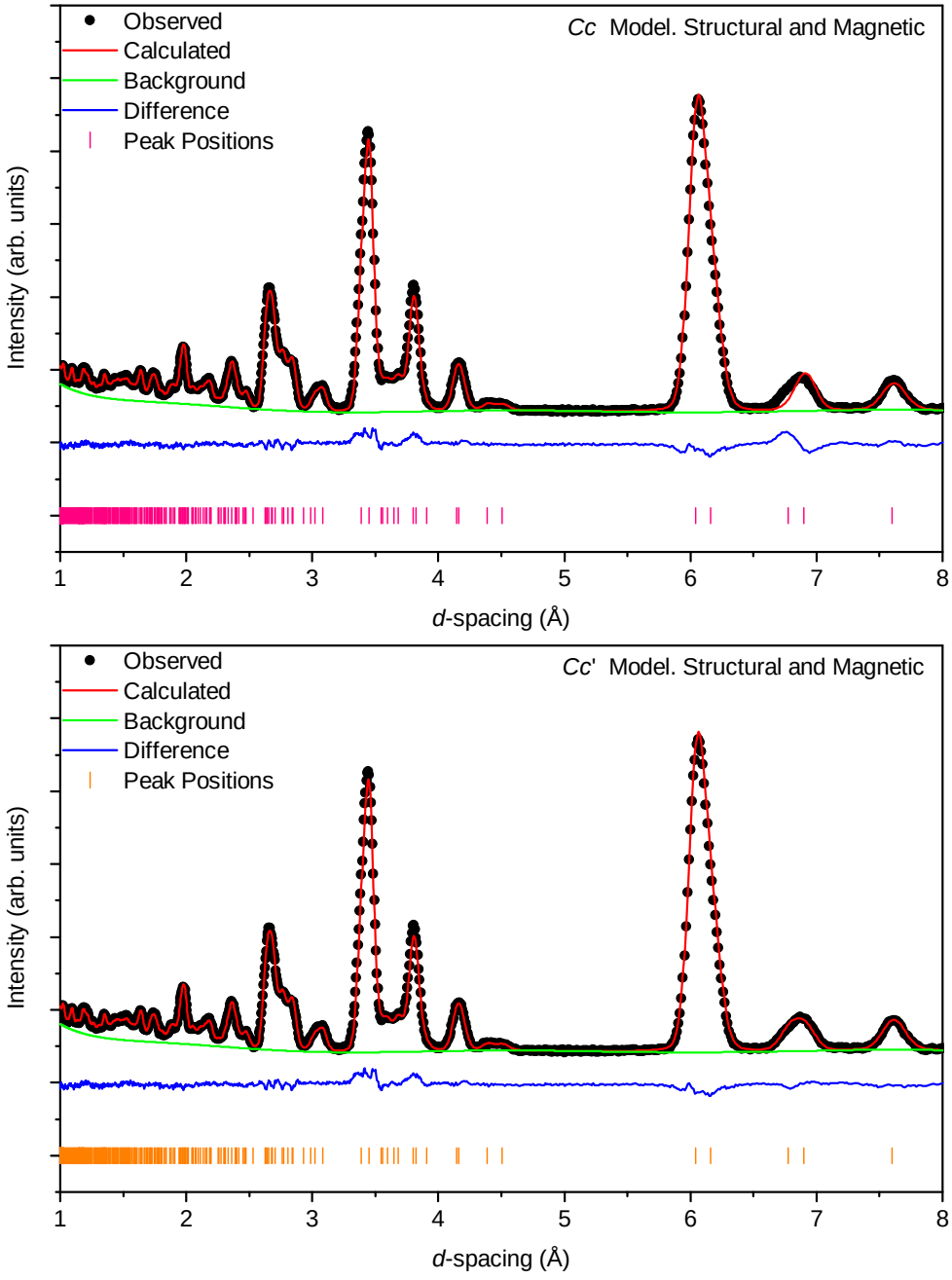


**Figure 4.6:** Top: Refinement for the $Cc$ model with magnetic moment on $Mn^{2+}$ along the $a$ axis. Peak positions shown in pink. Bottom: Refinement for the $Cc'$ model with magnetic moment on $Mn^{2+}$ along the $b$ axis. Peak positions shown in orange.

| Space Group | Reduced $\chi^2$ | Bank 2 $R(F^2)$ | Magnetic Moment / $\mu_B$ |
|---|---|---|---|
| $Cc$ | 14.51 | 0.0835 | 3.546, 0 , 0 |
| $Cc'$ | 13.63 | 0.0715 | 0 , 3.725, 0 |

**Table 4.1:** Comparison of selected fitting parameters for the $Cc$ and $Cc'$ magnetic refinements

**Difference refinement:**

In order to investigate how different arrangements of the 4 moments on $Mn^{2+}$ contributed to the profile, a magnetic-only refinement was performed. In order to isolate the magnetic component of the profile from the structural, a "difference" profile was generated by taking the difference between the 20 K and the 7 K profiles. The peak positions for both profiles are the same as there is little thermal expansion between 7 K and 20 K, with the largest difference in lattice parameters being 0.012% along the *a* axis. Therefore a direct subtraction yielded the magnetic only contributions. The refinement focussed on the low-$Q$ region (high $d$-spacing) of the profile as there was a lower density of peaks, a magnetic-only peak and the magnetic form factor falls off quickly with increasing $Q$. The symmetry of the magnetic-only unit cell was discarded and the cell had dimensions equal to those in the $Cc$ and $Cc'$ refinements. Figure 4.4a shows the positions of the Mn as used for the difference refinement with respect to the unit cell.

The magnetic moment on $Mn_1$ (see fiure 4.4a) was held constant pointing along the *b* axis with magnitude 5.92 $\mu_B$, while the eight possible configurations with spins of the three other $Mn^{2+}$ pointing either *up*, $\uparrow$ or *down*, $\downarrow$ were investigated (configurations 2–5 are equivalent). Table 4.2 lists the configurations, and if they successfully reproduced the $(20\bar{1})$ and (110), and (001) peaks.

The scale factor is the one used by GSAS to scale the calculated Bragg profile to the scattering data. As will be shown in figure 4.7, there are very few data points describing the magnetic-only structure, and there is one point, with $d$-spacing of approximately 6.1 Å which is noise, but almost half the height of the magnetic peak. A high GSAS scale factor as seen in configurations **1** and **6** indicates that the model is - incorrectly - putting high weighting on what is likely noise. Given that the data are noisy, these refinements with a high scale factor can be considered unsuccessful. Geometry optimised DFT calculations, using PBE+TS, were performed by Dr. A. E. Phillips on the eight configurations the relative energy of the configurations (with respect to the lowest energy configuration **7**) are given in the "Energy" column.

| Configuration # | Energy /meV | Scale | Peaks? |
|---|---|---|---|
| 1 ↑↑↑↑ | 62.20 | 25816 | None |
| 2 ↑↓↑↑ | 30.80 | 9.77 | All |
| 3 ↑↑↓↑ | 30.80 | 9.77 | All |
| 4 ↑↑↑↓ | 30.80 | 9.77 | All |
| 5 ↑↓↓↓ | 30.80 | 9.77 | All |
| 6 ↑↓↑↓ | 39.50 | 39140 | None |
| 7 ↑↑↓↓ | 0.00 | 2.44 | All |
| 8 ↑↓↓↑ | 21.30 | 3.91 | None |

**Table 4.2:** The orientations of the moments $Mn_1$ to $Mn_4$, the DFT calculated energy of such a configuration, the scale factor GSAS used and the presence oor absence of the magnetic peaks.

Configuration **7** (↑↑↓↓) has the lowest GSAS scale factor, and fits both peaks, in addition it has the lowest DFT energy. Figure 4.7 shows the fit of configuration **7**, we see that there is

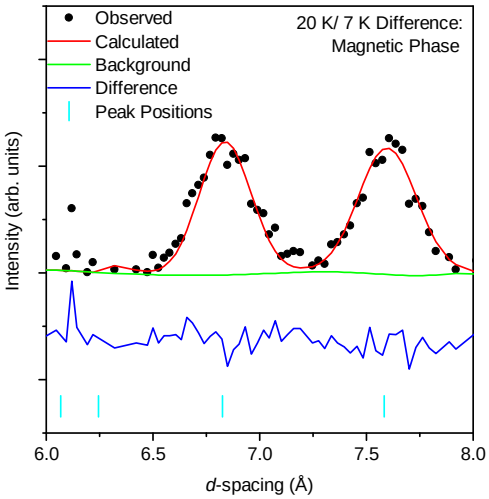


**Figure 4.7:** The refined "difference" GSAS fit for configuration **7**, corresponding to G-type antiferromagnetism, where both peaks are fit.

good agreement between the "difference" data and the model. When the orientations of the moments on the difference model are placed on the pseudo-cubic axis in figure 4.4a, we see that the lowest energy configuration again corresponds to checkerboard antiferromagnetism.

The DFT results, "difference" refinement, and the structural and magnetic Rietveld refinements all describe the magnetic structure of DMMnF as one with G-type antiferromagnetism. The $Cc'$ model, shows that the best fit to the data is when the magnetic moments point along the $b$ axis. Analysis of the unit cell has shown that, as with select $Cu^{2+}$ complexes, the anti-anti bridging modes seen in DMMnF also mediate antiferromagnetic interactions. This is the best description for the average magnetic structure, and so will be the basis for the initial magnetic structure for the RMC configurations.

### 4.3.2 RMC magnetic set up

Combined magnetic and structural refinements in `RMCProfile` require 4 additional pieces of information to those used for structural refinements alone (section 2.5). A *cfg* file, which is a list of 3-component normalised vectors, representing the magnetic moment on each $Mn^{2+}$ and which is subsequently refined, much like the atomic coordinates. In addition to the *cfg* file information about the magnetic form factor, information about the $d$-spacing range of interest, and the fraction of `RMCProfile` moves which will be magnetic (randomly changing the direction of the magnetic moments) rather than structural are also required.

**1:** The magnitude and shape of the magnetic form factor (section 2.1) are atom and oxidation-state dependent, and need to be provided in the main *dat* file. `RMCProfile` calculates the magnetic form factor, $f(Q)$, according to equation (4.2), where the coefficients are taken from [102] and given in table 4.3. The magnitude of the $Mn^{2+}$ magnetic moment was 5.92.

$$f(Q) = A\exp\left(\frac{-aQ^2}{16\pi^2}\right) + B\exp\left(\frac{-bQ^2}{16\pi^2}\right) + C\exp\left(\frac{-cQ^2}{16\pi^2}\right) + D. \tag{4.2}$$

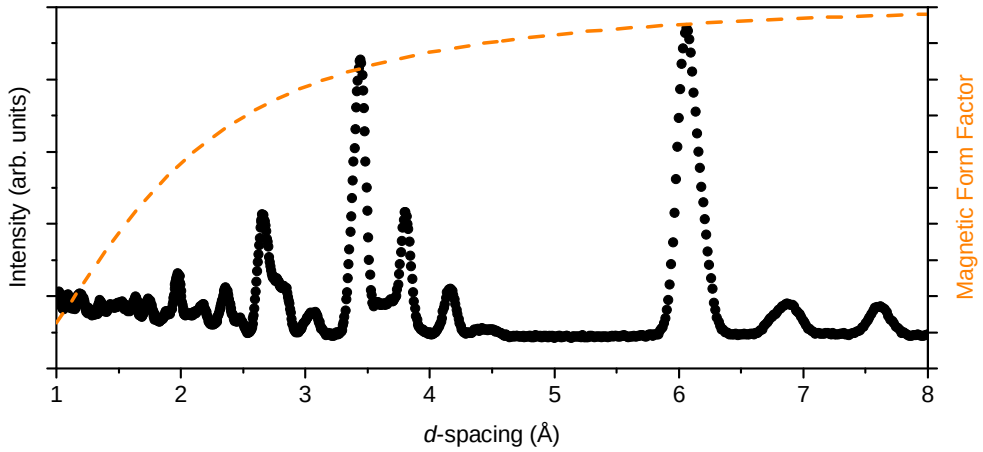


**Figure 4.8:** The observed magnetic Bragg profile for DMMnF with the magnetic form factor as a function of $d$-spacing overlayed. The form factor is highest for high $d$-spacing values.

| Coefficient | Value | Coefficient | Value / Å$^2$ |
|---|---|---|---|
| A | 0.4420 | a | 17.6840 |
| B | 0.5948 | b | 6.0050 |
| C | 0.0043 | c | -0.6090 |
| D | -0.0219 | | |

**Table 4.3:** Coefficients of the $Mn^{2+}$ magnetic form factor given in equation (4.2)

**2:** A minimum $d$-spacing of 0.9 Å was used for all magnetic refinements, to be consistent with the ranges used for structural DMMnF refinement, and because the magnetic form factor drops off with decreasing $d$ (see figure 4.8), and so the substantial magnetic scattering is expected at higher $d$-spacings.

**3:** The optimal magnetic spin move rate had to be established. As approximately 4% of the number of atoms were magnetic, it was first decided to try refining the magnetic structure so that 4% of the moves were random re-orientations of magnetic spins, and 96% atom translations. Refinements used the same Bragg, $i(Q)$, and $D(r)$ (with a 1:2:1 weighting ratio such that the $i(Q)$ was twice as heavily weighed as the Bragg and $D(r)$) as applied in the structural refinements in section 3.3.6. However the refinements continually failed to reproduce the characteristic $(001)$ magnetic Bragg peak at 7.60 Å. The $(001)$ peak is relatively small, and the inability of `RMCProfile` to fit is is likely due to the program being able to more significantly improve the $\chi^2$ though changing more intense peaks, and the weighting of the Bragg profile being low enough that there was not a significant enough penalty for the magnetic peak not being fit. The optimal spin move rate is discussed in section 4.3.3.

**4:** Finally, the *cfg* file had to be produced. As the analysis on the unit cell had found the spins of $Mn^{2+}$ to be aligned antiferromagnetically the 6 nearest Mn neighbours of each Mn were established and used to generate *cfg* files with either perfectly antiferromagnetic or ferromagnetic spin orientations, or random spin orientations. The Rietveld refinement had indicated that the system was a G-type antiferromagnetic, however short magnetic `RMCProfile`

trials had shown that the final magnetic configuration was heavily influenced by the starting configuration. Based on the Rietveld results, the initial configuration was chosen to have G-type antiferromagnetism based on a randomly oriented initial spin.

### 4.3.3 Magnetic RMC

It was decided, after several trial refinements, to break the refinement of the magnetic structure into four steps. Firstly a $5 \times 10^6$-move (two-day) purely structural refinement as with the higher-temperature configurations where the relative weightings of the Bragg, $i(Q)$ and $D(r)$ were $1 : 2 : 1$. There were two reasons to start with a structural only refinement. First it is known what the atomic configuration of DMMnF should look like and so it is easy to see if the refinement has failed at this first stage. Secondly the contributions to the Bragg profile and $i(Q)$ from the $Mn^{2+}$ ions are dependent on not only the magnetic form factor, but their relative positions. Allowing the atomic coordinates to refine first would ensure that the magnetic moves were refining against the magnetic peaks, and not a result of poorly fit structural features.

In the second stage the relative weighting of the Bragg profile was increased so the weightings of the Bragg, $i(Q)$ and $D(r)$ were $10 : 2 : 1$ and an $11 \times 10^6$-move (two-day) magnetic-only refinement performed. Given that Rietveld refinement had indicated DMMnF displayed antiferromagnetic ordering, and that initial configurations with anitferromagnetic orientations had reproduced the magnetic-only peak at 7.60 Å, it was decided to start the magnetic refinement with a purely G-type antiferromagnetic arrangement, where the first spin was chosen at random, and the others aligned to produce the desired magnetic configuration. When trial runs with a lower relative weighting of the Bragg profile were performed, the intensity of the magnetic 001 peak fell to zero.

After the magnetic refinement, a $5 \times 10^6$-move two-day structural only refinement (relative Bragg:$i(Q)$:$D(r)$ weightings = $1 : 2 : 1$) was performed, to allow $D(r)$ again to refine, this time with magnetic moments on $Mn^{2+}$ which were consistent with the Bragg profile.

Finally a $1.5 \times 10^6$-move two-day mixed refinement with a Bragg:$i(Q)$:$D(r)$ weighting of $1 : 2 : 1$, and 4% magnetic moves was performed. 4% corresponds to the percentage of $Mn^{2+}$ in DMMnF. Trials performing the mixed refinement before an individual structural or magnetic refinement resulted in either the loss of the magnetic 001 peak, or very poor agreement between the model and the observed $D(r)$.

Bond bending and stretching potentials as given in tables 3.5 and 3.6 were applied, and the distance window constraint, given (for the 7 K sample) is given in table 3.7. Throughout the four-stage refinement, three artificial partial pair distribution functions were used, they were for $g_{CD}(r)$, $g_{ND}(r)$, and $g_{CO}(r)$ for $r \leq 1.7$ Å. The weightings of all the artificial functions were $\frac{1}{25}$ of the weighting of $D(r)$.

### 4.3.4 Representative fits

The representative Bragg and $i(Q)$ fits for each of the four stages of refinement are shown in figure 4.9. In the first step, `RMCProfile` only performs atomic moves. The contribution from the initially magnetically ordered *cfg* file means the intensity of the two Bragg peaks with the

highest $d$-spacing is too high. There is also poor agreement between the model $i(Q)$ and the scattering data at low $Q$ values.

In step 2; where the weighting of the Bragg profile has been increased, and `RMCProfile` is performing purely magnetic moves, the intensities of the final two peaks in the Bragg profile show significant improvement. The agreement between the model and the experimental $i(Q)$ at low $Q$ is improved, but still poor.

The step 3; structural-only refinement improved agreement between the model $D(r)$ and the observed $D(r)$ (not shown), but there was no such improvement in $i(Q)$.

Step 4; with it's mixed magnetic and structural refinement significantly improved the agreement between the experimental and model $i(Q)$, at the expense of the Bragg profile.

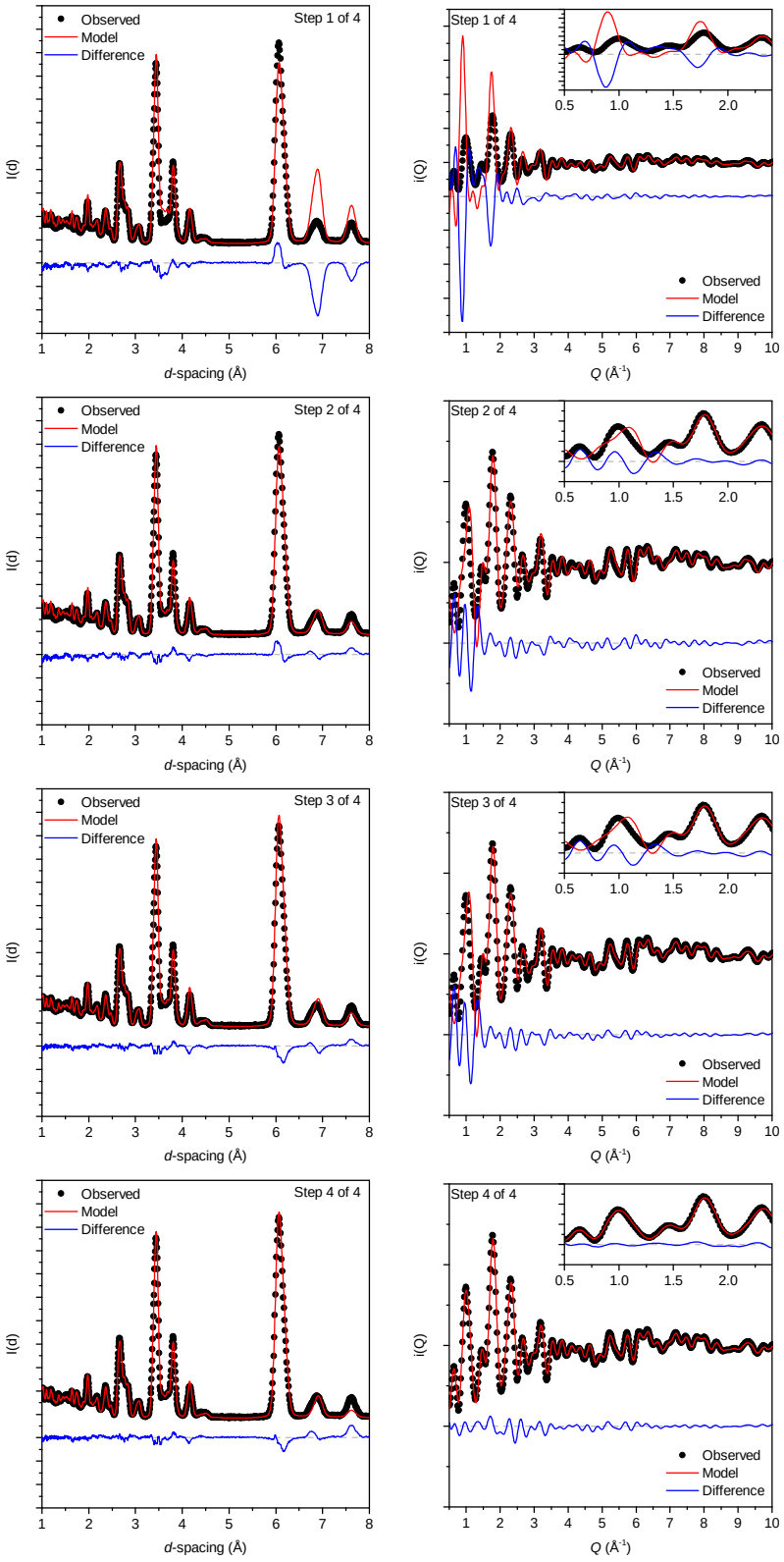


**Figure 4.9:** Representative fits over the four stages of refining the magnetically ordered phase of DMMnF for the Bragg profile (left) and $i(Q)$ (right). There is poor agreement between the model and the $i(Q)$ data up until the final step, however the improvement in the fit of $i(Q)$ is at the expense of the fit of the Bragg profile.

## 4.4 Analysis

Figure 4.10a shows $g_{\mathrm{NO}}(r)$ for DMMnF with the data for the magnetic phase included, the dashed lines indicate the first and second nearest Mn distances in the 150 K unit cell (shown in 4.10c). At 7 K, the short N···O bonds observed at higher temperatures are now absent and that there are 4 sharp peaks below 4 Å. Figure 4.10b shows just the 7 K partial PDF, with the areas under the two peaks shaded to indicate the contributions from the first (blue) and second (green) nearest pairs. The first three peaks correspond to the nearest N···O pairs, where DMA nitrogen bonds exclusively with two separate formate groups as described by the average unit cell. Representative structures and their corresponding N···O distances are shown in figure 4.10d and 4.10e. At 7 K there is little movement of the DMA cation away from the initial ordered configuration and there is no distortion of the framework which lead to the "pincer-like" configuration observed in the high-temperature phase.

### 4.4.1 Competing magnetic information

Information on the magnetic structure is contained in both the Bragg profile and $i(Q)$. The initial RMC magnetic configurations were generated based on the Rietveld refinements and so were only based on the Bragg profile information. When the evolution of the Bragg and $i(Q)$ fits are examined over the 4 stages (figure 4.9), it can be seen that the Bragg and $i(Q)$ appear to work against one another.

In the first step, where a structural refinement was performed on the initial perfectly antiferromagnetically ordered system, we see that the positions of the magnetic Bragg peaks are correct, but the intensity is not. For $i(Q)$, we see that at low $Q$ both the peak position and intensity is incorrect.

The second stage of refinement was purely magnetic, and the intensity of the magnetic Bragg peaks in the model decreases to match the data. There is an improvement in $i(Q)$ but the low $Q$ fit is still poor.

The third stage was again a structural refinement, and there is little improvement in either the Bragg or $i(Q)$.

In the final stage where both the magnetic moment and atomic coordinates were varied, a marked improvement in the $i(Q)$ is observed, but this is at the expense of the magnetic 001 peak.

The current weighting scheme and number of atomic moves were selected through trial and error. The final step shown in figure 4.9 was the best compromise of agreement between both sets of data. As the $\chi^2$ is dependent on relative weightings a direct comparison of $\chi^2$ for the Bragg profile and $i(Q)$ is not useful.

### 4.4.2 Spin orientations: nearest neighbours

When looking for signs of cooperative behaviour between the spins of $Mn^{2+}$, the first interaction investigated was that between nearest neighbours.

Figures 4.4b and 4.4c show the Mn from the Rietveld refinement, and the relationship between any target Mn and its 6 nearest neighbours, designated up, down, left, right, front, and back. From this we see that the up, down, left, and right Mn are equivalent by the

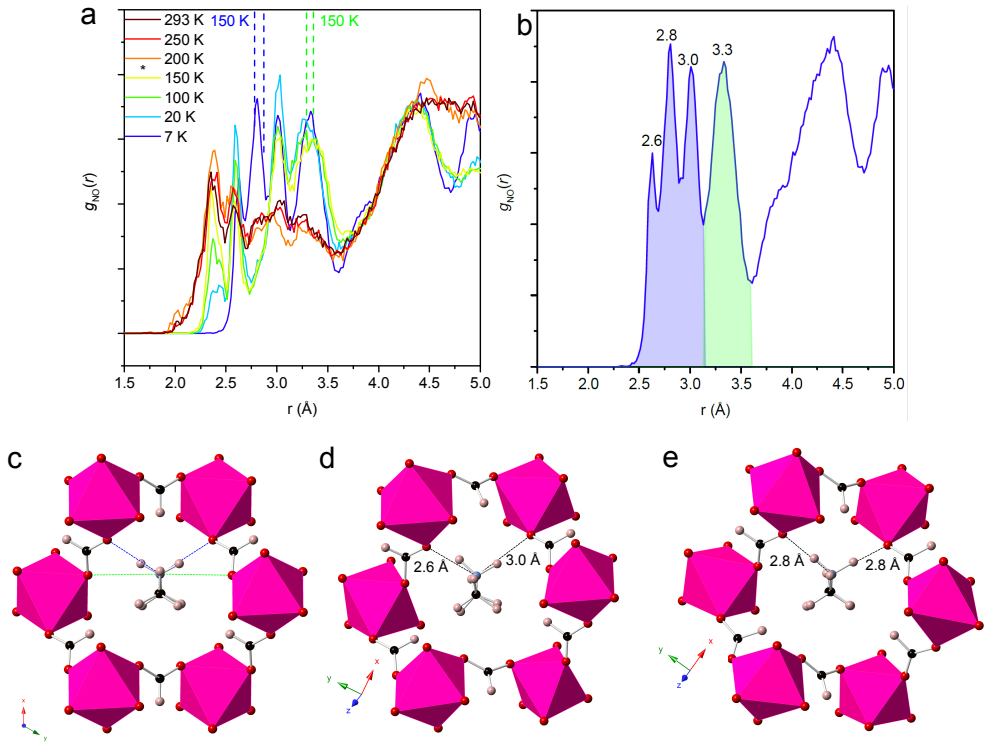


**Figure 4.10:** a) $g_{\mathrm{NO}}(r)$ for DMMnF including the 7 K partial PDF, the short N···O bond is now absent and there are four distinct peaks. b) The 7 K $g_{\mathrm{NO}}(r)$ with shading to indicate contributions from the first (blue) and second (green) nearest neighbours. c) Average crystal structure for DMMnF highlighting the N···O bonding for the nearest (blue) and second nearest pairs (green). d) and e) Representative final configurations for the 7 K structures with N···O distances shown.

symmetry of the average structure. The distances between the 6 nearest neighbours in the RMC supercell are given in table 4.4.

| Relative Position | Distance /Å |
|---|---|
| Up | 5.9596 |
| Down | 6.1873 |
| Left | 5.9596 |
| Right | 6.1873 |
| Front | 6.2090 |
| Back | 6.2090 |

**Table 4.4:** Distances between the 6 nearest Mn neighbours

The `RMCProfile` supercell is $(4 \times 6 \times 6)$ the unit cell, with dimensions 57.38 Å, 49.93 Å, and 53.07 Å. As the supercell is subject to periodic boundary conditions, the maximum range that can be explored from any site is approximately 25 Å in any direction before the boundary conditions mean that the same atom is interacting with itself. Therefore any analysis of magnetic moments made from this size of system, must limit the range of investigation to $r \leq 25$ Å. This analysis will not stretch past the third neighbour $r \approx 12$ Å. First the angle $\theta$ that the

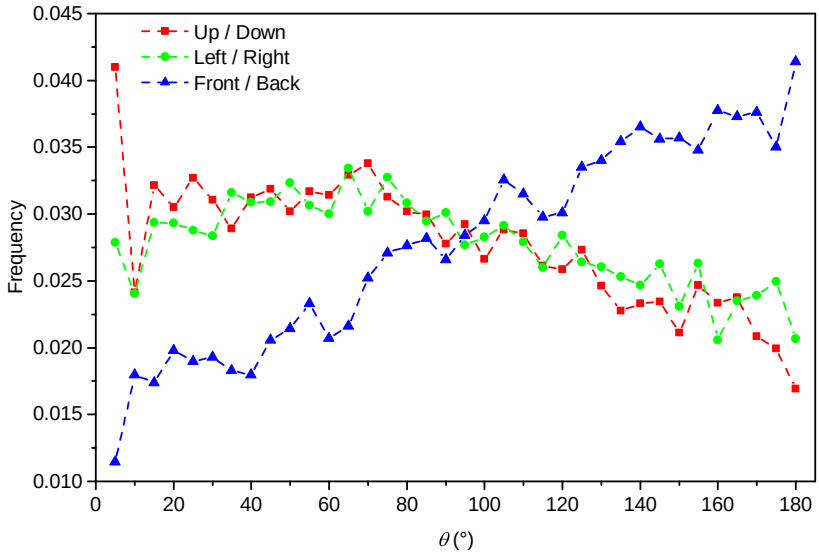


**Figure 4.11:** The angles between the magnetic moment on neighbouring Mn. We see that the up/down and left/right distributions are similar, in agreement with the symmetry of the unit cell, and there is a preference for the moments to align ferromagnetically (unlike the Rietveld). We also see that the front/back moments are likely to align antiferromagnetically.

6 nearest neighbouring spins made with each Mn was calculated. In a purely ferromagnetic configuration, all $\theta = 0°$. Similarly in a purely G-type antiferromagnetic configuration all $\theta$ =180°.

For all Mn in the sample, the 6 nearest neighbours were identified, and the angle between the spin of the central Mn and the neighbouring spins (figure 4.4b) were calculated.

Figure 4.11 shows the normalised frequency distribution of the angle $\theta$ which is made between neighbouring spins. Data presented in figure 4.11 are from 29 different refinements, all with unique antiferromagnetic initial *cfg* files. From this we see that the relative orientations of the up/down and left/right spins are similar. This is consistent with the symmetry of the unit cell (figure 4.4c). We also see that the up/down left/right spins are more likely to be aligned ferromagnetically. The front/back spins appear to preferentially align antiferromagnetically.

The relative orientations of the nearest neighbour spins, most closely resemble an A-type structure (ideal case shown in figure 4.12) which has ferromagnetic planes with antiferromagnetic coupling between the planes.

### 4.4.3 Spin orientations: second nearest neighbours

The second neighbour spins are those across the face diagonal of the cubic Mn network. The face diagonal Mn are identified based on the route to access them, therefore "Up-Right" is the manganese up and right of the central atom, and is the will give the same distribution as "Down-Left". The face diagonal neighbours therefore do not share a formate bridge.

Figure 4.13 is the normalised frequency distribution of the angle $\theta$ which is made between the second nearest neighbours. From this figure we see that the second nearest neighbours are more likely to align with ferromagnetically with one another. This observation is consistent with G-type antiferromagnetism.

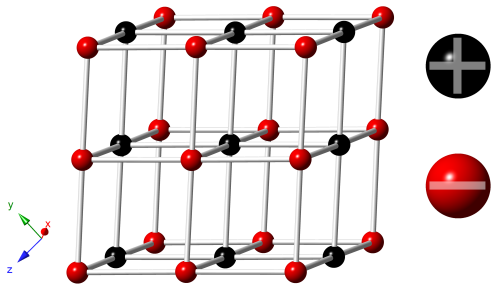

**Figure 4.12:** An ideal A-type structure where the spins on atoms in a cubic framework are shown pointing either + (black) or − (red) along an arbitrary direction. The distribution of spins observed for the nearest neigbour interactions most closely resembles the A-type structure with ferromagnetic planes (up/down and left/right) but neighbouring planes displaying antiferromagnetic coupling.

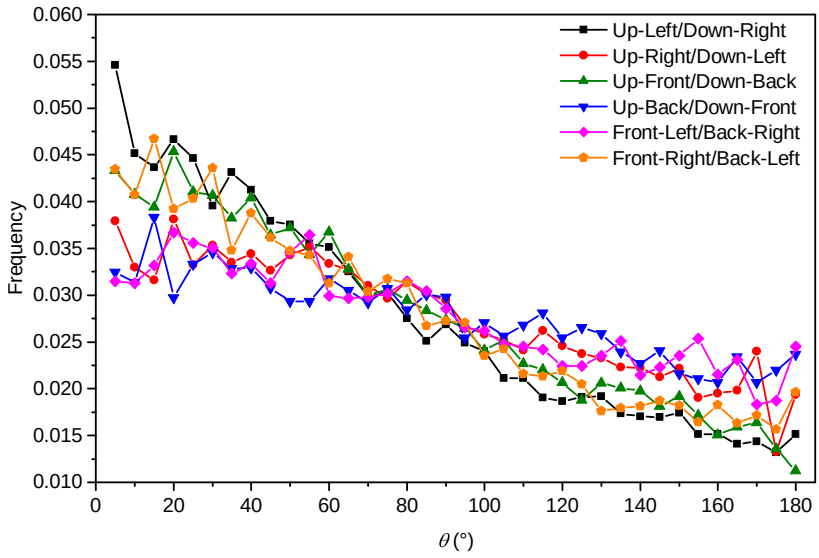


**Figure 4.13:** Analysis of the second neighbour spin orientations. Shows that the second neighbour spins are more likely to be aligned ferromagnetically

## 4.5 Conclusion

In this chapter neutron total scattering data were used to model the magnetic structure of the metal-organic framework DMMnF.

Rietveld refinement on the entire Bragg profile, and a "difference" profile found that the magnetic structure is best described as a G-type antiferromagnet, where there is antiferromagnetic coupling in all three directions of the cubic $Mn^{2+}$ network. DFT calculations also found that the lowest energy configuration of the spins in the unit cell corresponded to G-type antiferromagnetism.

Atomistic configurations were generated in a four-step process and the refined models were analysed for their N···O interactions and for the interactions between neighbouring and second-nearest neighbour magnetic moments.

The DMA cations did not significantly deviate from the initial orientation, and the framework did not distort in response to the orientation of the guest, therefore the DMA was

observed to bond to two adjacent formates as seen in the average unit cell. Due to the lack of DMA motion and the absence of framework distortion the N···O distances are comparable to those seen in the average unit cell.

The relative orientations of magnetic moments between the nearest neighbours were analysed; 4 of the 6 nearest neighbours displayed weak tendency towards ferromagnetic coupling and the other two neighbours displayed a more pronounced tendency towards antiferromagnetic coupling. When the relative orientations of the second nearest neighbours spins were analysed all 12 second nearest neighbours displayed tendency to align ferromagnetically.

The second-nearest neighbour spins are consistent with the G-type antiferromagnetic configuration seen in the average unit cell, but the nearest neighbours models suggest a different configuration. The difference between the apparent trends of the nearest and second nearest neighbour interactions could indicate canting of the spin, or it could be a function of having a less than ideal fit of the Bragg profile and $i(Q)$ during RMC refinement.

# Chapter 5

# Potassium Imidazolium Hexacyanoferrate

## 5.1 Introduction

As outlined in chapter 3, the interactions between a disordered cationic guest molecule within a charged framework through a phase transition are far from trivial and the average crystallographic representation of disorder of guest cations is sometimes insufficient to fully describe the change in local structure. With this in mind, this chapter outlines the total scattering study and subsequent atomistic models of a metal-organic framework with a double perovskite architecture.

## 5.2 The material

Potassium imidazolium hexacyanoferrate(III) – $(D_5C_3N_2)_2K[Fe(CN)_6]$ (herein referred to as PIH) can be described either as a MOF with a double perovskite structure where the B-site alternates, or as a Prussian Blue Analogue (PBA). Prussian Blue has formula $Fe_4^{III}[Fe^{II}(CN)_6]_3 \cdot nH_2O$ and is named after its dark blue colour. In PBAs two different metal sites, $M_A$ and $M_B$ are joined by cyanide linkers to form a 3D extended network with the form $M_A{-}NC{-}M_B{-}CN{-}$ where, for PIH, $M_A = K^+$ and $M_B = Fe^{3+}$.

Within the PBA family, the oxidation state of the metal sites dictates the number of filled and empty pores [103], for a PBA with general formula $AM_A[M_B(CN)_6]$ – where A is a guest cation – only half the pores of the framework would be filled. PIH, with general formula $A_2M_A[M_B(CN)_6]$, has all pores occupied. PBAs with fully occupied pores which have been previously investigated include $A_2Mn^{II(HS)}[Mn^{II(LS)}(CN)_6]$ (A = Na) where $Mn^{II}$ is in a high spin (HS) and low-spin (LS) state and the material orders magnetically below 58 K [104], and A = K and Rb [105].

The volume inside the pores of PBAs and the ready substitution of metal sites, with either different metals or larger ligand-type structures [106] mean that there are a range of interesting and potentially useful phenomena associated with the PBA architecture including negative thermal expansion in $M_3^{II}[Co^{II}(CN)_6]_2 \cdot n\ H_2O$ M = Mn, Fe, Zn, Co, Ni and Zn [107], and the possibility of PBAs as hydrogen-storage materials ($Cu_3[Co(CN)_6]_2$) [108]. The focus of this chapter is analysis on a PBA where long-range ordering of the guest cations is observed.

In PIH, first reported in 2010 [109] and shown in figure 5.1, $K^+$ and $Fe^{3+}$ form a framework of $KN_6$ and $FeC_6$ polyhedra which surround an imidazolium ring.

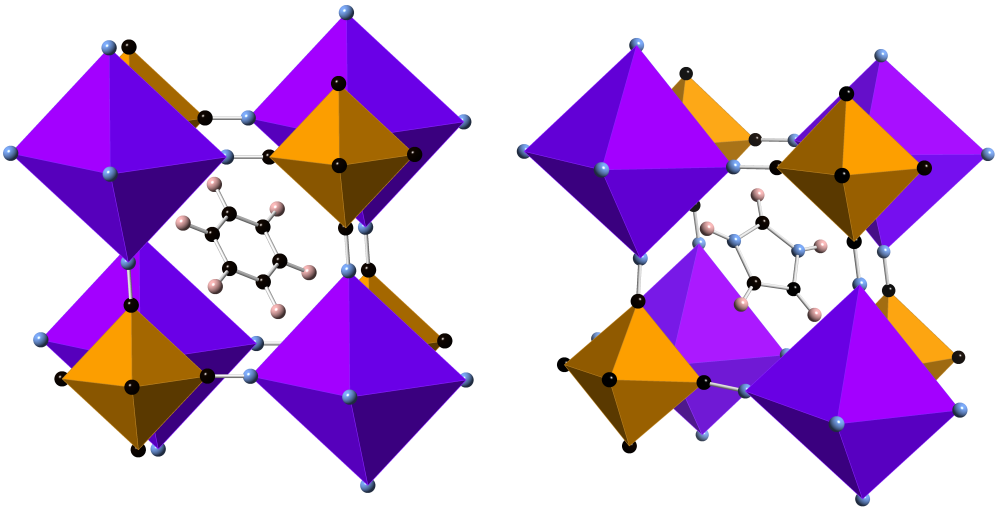

**Figure 5.1:** Pseudo-cubic cell of PIH, in the high (left) and low (right) temperature phases. The cyanide framework joins Fe (brown) and K (purple) sites forming ionic $KN_6$ and covalent $FeC_6$ octahedra. The imidazolium cation - modelled as a benzene ring in the high-temperature phase - rotates in plane within the centre of the cage.

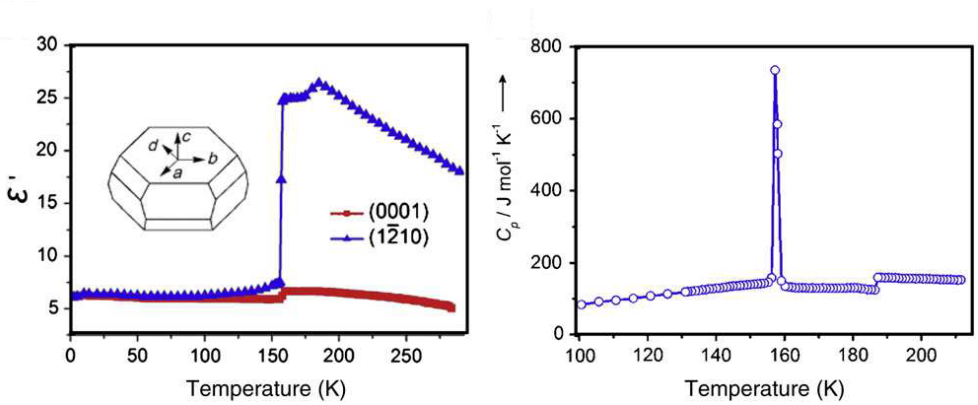


**Figure 5.2:** Left: The anisotropic dielectric permittivity of PIH crystals as a function of temperature where the most significant change in permittivity is along $1\bar{2}10$ in the plane of the imidazolium rings, there is little change perpendicular to the plane, along $0001$. Right: The molar heat capacity of PIH as a function of temperature. The large features at $158\,\mathrm{K}$ correspond to a first-order paraelectric to antiferroelectric transition and a change in crystal symmetry from $R\bar{3}m$ to $C2/c$. Small features at $187\,\mathrm{K}$ are proposed to correspond to a second-order phase transition. Data taken from [109], graphs adapted from [110].

PIH crystallises in the $R\bar{3}m$ space group at room temperature. The symmetry restrictions of the structure mean that the heteroatomic imidazolium ring which rotates perpendicular to its plane must be modelled as a benzene ring. At room temperature no ordering of neighbouring imidazolium rings is observed. However at $T_c = 158\,\mathrm{K}$ there is an abrupt anisotropic change in the dielectric constant (left figure 5.2) corresponding to a first-order phase transition ($R\bar{3}m$ to $C2/c$) and the onset of antiferroelectric ordering of the imidazole rings.

PIH is of particular interest for three reasons. Firstly due to the onset of antiferroelectric ordering of the imidazolium rings. The imidazolium ring of PIH exhibits a high degree of

rotational disorder at room temperature, but below $T_c$ is frozen into a single orientation, hydrogen-bonded to the framework [109]. As with DMMnF, it may be possible to observe the onset of electric ordering through preferred orientations of the imidazolium ring being observed before the phase transition.

The second feature of interest for PIH and total scattering studies is that two different metal coordination environments, $KN_6$ octahedra with weak, essentially ionic K−N bonds, and $FeC_6$ octahedra, with stronger, more covalent Fe−C bonds can be investigated simultaneously. Having two different bonding systems within the same environment allows the influence of bond strength on framework distortions to be directly compared.

Finally, in PIH, there are 2 possible phase transitions within one structure which can be investigated. Figure 5.2 shows the anisotropic dielectric permittivity and molar heat capacity for PIH crystals as a function of temperature [109]. At 158 K sharp changes in both are seen which correspond to a first order phase transition and a change in crystal structure from $R\bar{3}m$ to $C2/c$. In addition to the first-order transition at 158 K, small deviations in the anisotropic dielectric permittivity and the heat capacity are observed at 187 K. It has been proposed that these deviations correspond to a more subtle phase transition to an intermediate temperature phase where $T_i = 187$ K, with no accompanying change in crystal symmetry. [109]

In this chapter the high-temperature phase will refer to measurements taken above 187 K, the low-temperature phase to measurements taken below 158 K and the intermediate-temperature phase to measurements taken between 158 K and 187 K.

Throughout this chapter, PIH will be compared to three analogues shown in figure 5.3. Material **A**, $((CH_3)_2NH_2)_2K[Fe(CN)_6]$, [111] which has the same framework structure as PIH, but with the guest cation of dimethylammonium (DMA) as in DMMnF. Material **B**, $(H_5C_3N_2)_2K[Co(CN)_6]$, [112], where the guest cation is imidazolium, like PIH, but the framework is K/Co based rather than K/Fe based. Like PIH, **B** has a reported intermediate temperature phase, where the high to intermediate transition is observed through small features in its dielectric and DSC curves and no change in symmetry, and the intermediate to low-temperature phase transition has a large feature in both, and is accompanied by a change of symmetry. Material **C**, $((CH_3)_2NH_2)_2K[Co(CN)_6]$, [113] has the K/Co framework of **B** with the dimethylammonium cations of DMMnF and **A**. The key properties of **A** - **C** and PIH are provided in table 5.1.

| Parameter | **A** | **B** | **C** | PIH |
|---|---|---|---|---|
| Guest; Framework | DMA; K/Fe | Imid; K/Co | DMA; K/Co | Imid; K/Fe |
| $T_i$/K | - | 198 | - | 187 |
| $T_c$/K | 226 | 112 | 245 | 158 |
| HTP Space group | $P4/mnc$ | $R\bar{3}m$ | $P4/mnc$ | $R\bar{3}m$ |
| ITP Space group | - | $R\bar{3}m$ | - | $R\bar{3}m$ |
| LTP Space group | $P4/mnc$ | $C2/c$ | $P4/mnc$ | $C2/c$ |
| HTP K-metal distance /Å | 5.842 – 5.876 | 5.946 – 5.947 | 5.811 – 5.861 | 5.964 – 5.965 |
| ITP K-metal distance /Å | - | 5.930 – 5.931 | - | 5.952 – 5.953 |
| LTP K-metal distance /Å | 5.837 – 5.853 | 5.903 – 5.940 | 5.792 – 5.828 | 5.927 – 5.954 |
| HTP Guest disorder | 4-fold | 3-fold | 4-fold | 3-fold |
| ITP Guest disorder | - | 3-fold | - | 3-fold |
| LTP Guest disorder | 2-fold | 1-fold | 2-fold | 1-fold |

**Table 5.1:** Selected parameters for PIH and its three analogues, **A**: $((CH_3)_2NH_2)_2K[Fe(CN)_6]$, **B**: $(H_5C_3N_2)_2K[Co(CN)_6]$, and **C**: $((CH_3)_2NH_2)_2K[Co(CN)_6]$. Data for **A** from [111], **B**: [112], **C**: [113] and PIH [109]. All parameters given in this table correspond to data collected by x-ray diffraction on fully hydrogenated samples. Guest disorder values correspond to the average structure.

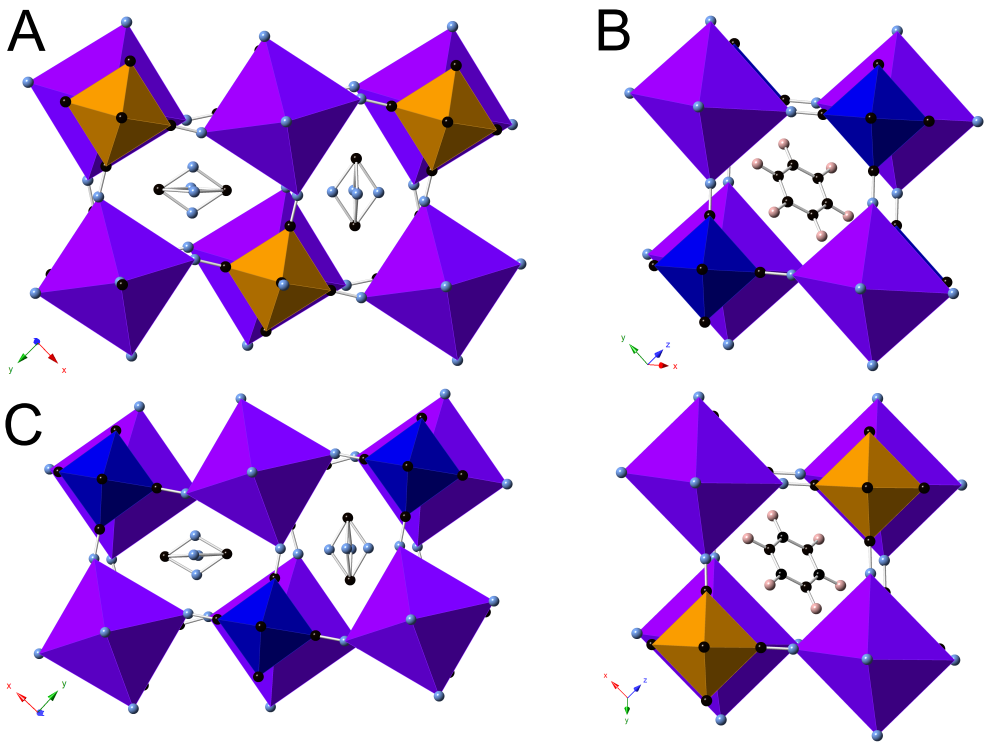


**Figure 5.3:** HTP representations of three PIH analogues and PIH. Top left: **A**, $((CH_3)_2NH_2)_2K[Fe(CN)_6]$, with 4-fold disorder on the DMA nitrogen. Top right: **B**, $(H_5C_3N_2)_2K[Co(CN)_6]$, where the Fe of PIH is replaced with a Co. Bottom left: **C**, $((CH_3)_2NH_2)_2K[Co(CN)_6]$, with 4-fold disorder on the DMA nitrogen and Fe replaced with Co. Bottom right: PIH. Hydrogen omitted from **A** and **C** for clarity.

## 5.3 Experimental

In this section the synthesis, data collection, and processing prior to application of the RMC algorithm will be discussed. Full details of collection run numbers and traceability for, and purity of the deuterated precursors are given in appendix A.2.

### 5.3.1 Synthesis

Synthesis of PIH was carried out according to the method outlined in [109]. Lot numbers for precursors that were used are given in appendix A.2.1. 5.72 g of $K_3[Fe(CN)_6]$ was added to 14 ml of $D_2O$ and heated until the solid was fully dissolved. Imidazolium chloride salt was obtained by dissolving 2.50 g of $D_5C_3N_2$ in 2.9 ml of DCl (35%) which was then added to the $K_3[Fe(CN)_6]$ solution. On addition of the acid some precipitation was immediately visible. The solution was slowly cooled to room temperature and left to crystallise for 1 hour 40 minutes, at which time orange crystals $\approx$ 1 mm were clearly visible. The crystals were recovered by filtration and dried under vacuum, producing a yield of 4.64 g - 67%. The recovered crystals are shown in figure 5.4.

The liquor from the filtration was retained and kept in a sealed container in a non-temperature controlled lab. Two crystals of PIH formed in the solution during the spring (left in figure 5.5), they dissolved back into solution during the summer, and then recrystallised to a large crystal in the winter (right in figure 5.5).

### 5.3.2 Data collection

Variable temperature neutron total scattering data were collected at the `ISIS` facility using the `POLARIS` diffractometer. An eight-hour total scattering measurement of the sample at 293 K in the sample changer was taken before the sample was transferred to a CCR and cooled to 10 K.

Total scattering measurements with a minimum collection time of eight hours were collected while heating at 10 K, 83 K, 150 K, 165 K, 180 K, 200 K, and 250 K. Shorter runs were collected on heating in 10 K increments between 10 K and 70 K for lattice parameter calculations only. Details of the run numbers along with the measured sample temperature can be found in table A.3.

### 5.3.3 Rietveld refinement

The reported high-temperature phase structure of PIH [109] is based on x-ray data, where the scattering signal from C and N of the imidazole ring would be indistinguishable and the benzene approximation – modelling a heteroatomic 5-membered ring as a benzene – is a sensible approximation. However C and N have significantly different neutron scattering lengths (6.646 fm and 9.36 fm respectively) and so when refining neutron scattering data of the high temperature phase, it is not suitable to use carbon atoms to represent the disordered imidazole ring as the scattering lengths will be incorrect. As the symmetry of the unit cell means that an imidazolium ring cannot be placed within the framework of the high temperature refinements, attempts were made to correct for the different scattering lengths, and are discussed later in this section.

**Figure 5.4:** Recovery of the orange crystals of PIH by vacuum filtration for use in the ISIS experiment.

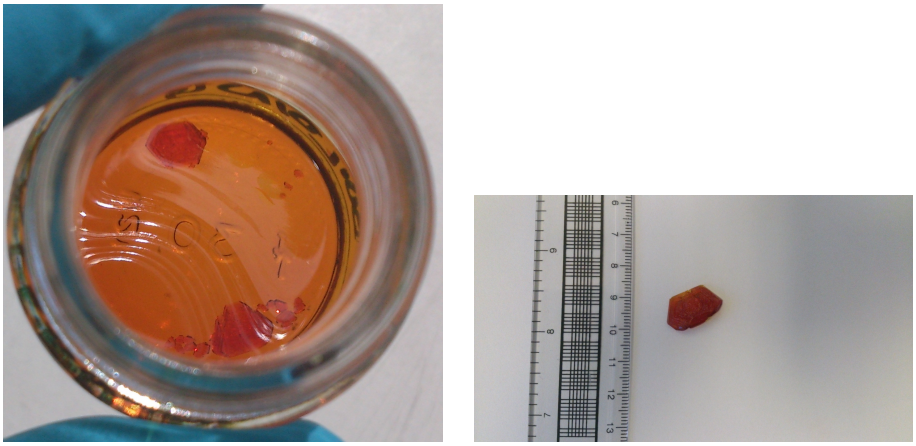

**Figure 5.5:** Left: Two PIH crystals in the mother liquor in spring 2013, they dissolved back into solution over the summer after being held in a non-temperature controlled lab but had reformed a large single crystal (Right) by December 2013.

Another problem with modelling a disordered ring as an ordered benzene ring is that any atomic displacement parameters of the benzene ring derived from the high-temperature phase refinement will not be meaningful as they will not correspond to a physical structure, and guest cation bond lengths (C−C and C−D) derived from these models would be equally meaningless.

As with DMMnF, the diffraction data were analysed by the Rietveld method [41], carried out using the GSAS program [42] and the EXPGUI interface [43]. Starting configurations for the $R\bar{3}m$ and $C2/c$ structures were taken from published x-ray structure determinations [109] (CSD identifiers *KAHKUB01* and *KAHKUB02* respectively). The $R\bar{3}m$ structure was modified to remove overlapping C atoms in the published structure.

During refinement, the model was refined against POLARIS detector banks 2–5 simultaneously. The bank 3 (scattering angle $2\theta = 40°$ to $61°$) profile was chosen to be used for

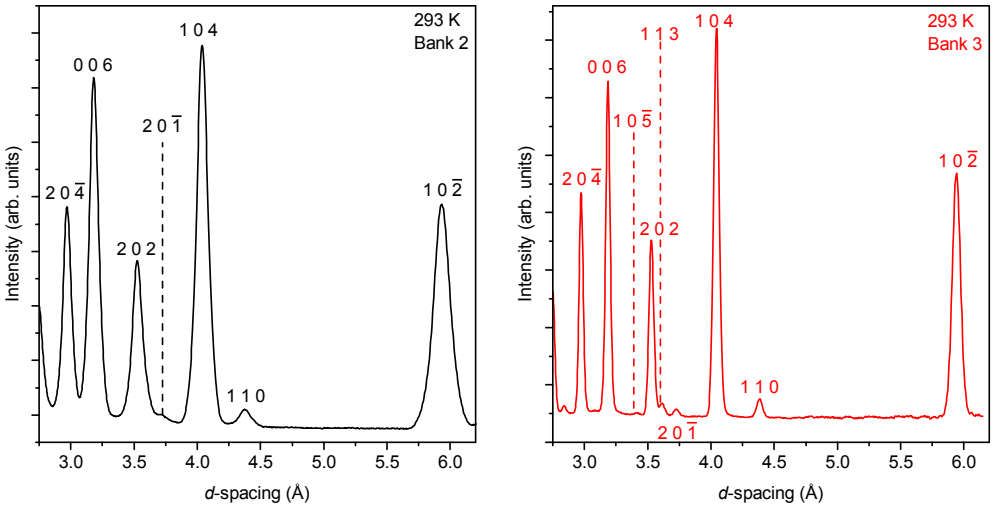


**Figure 5.6:** The observed Bragg profiles from POLARIS bank 2 (black) and 3 (red) for PIH at 293K. The greater resolution of Bank 3 allows the weaker $(113)$ and $(10\bar{5})$ peaks to be distinguished from the $(202)$ peak.

subsequent RMC modelling, due to the improved resolution compared to bank 2, particularly around $d$-spacing $= 3.5$ Å (figure 5.6) and despite the fact that the $d$-spacing range for bank 3 ($\approx 0.5$ Å to 6.2 Å) was smaller than that for bank 2.

The observed Bragg profiles for all temperatures where total scattering was recorded is shown in figure 5.7. Each profile in figure 5.7 is offset by the same value with the exception of the 293 K data, which had a stronger signal than the others due to the data being collected in an environment with less attenuation of the signal. From figure 5.7 we see no obvious difference in the Bragg profiles of the high and proposed-intermediate temperature phase, and only see the emergence of a small peak $(112)$ at 4.56 Å in the low-temperature phase.

While the previously published structures, and hence transition temperatures were based on data from hydrogenated samples the structures analysed in this thesis are from fully deuterated samples. The observed Bragg profile for deuterated PIH shown in figure 5.7 confirms the intermediate to low-temperature phase transition falls within the same temperature range (given the relatively few temperatures recorded over) as that of the hydrogenated sample, as the $(112)$ peak at 4.56 Å peak only appears below 158 K.

As with DMMnF, the background for each bank was described as a ten-term shifted Chebyshev polynomial, and the refinement was carried out using the least-squares method. The peak profiles were fit using `GSAS'` type 3 profile (described in section 2.4).

For the $R\bar{3}m$ structure (where ordered benzene was used as an analogue for disordered imidazolium - see left of figure 5.8) the occupancy of all atoms in the benzene ring was set to $\frac{5}{6}$ and the parameters were varied in the following order: background and scale, cell parameters, position of the benzene deuterium, diffractometer "constant" `DiffA` (section 2.4.1). Varying the peak shape parameters $\sigma_1, \sigma_2, \gamma_1$ and $\gamma_2$ did not improve agreement to the observed peaks.

No bond length or angle restraints were applied to the $KN_6$ and $FeC_6$ polyhedra.Due to the symmetry of the $R\bar{3}m$ unit cell – which required the disordered imidazolium ring be modelled as a benzene ring – no bond length or angle restraints were applied to the guest cation. The isotropic atomic displacement parameter $U_{\text{iso}}$ of the benzene carbon and the cyanide carbon

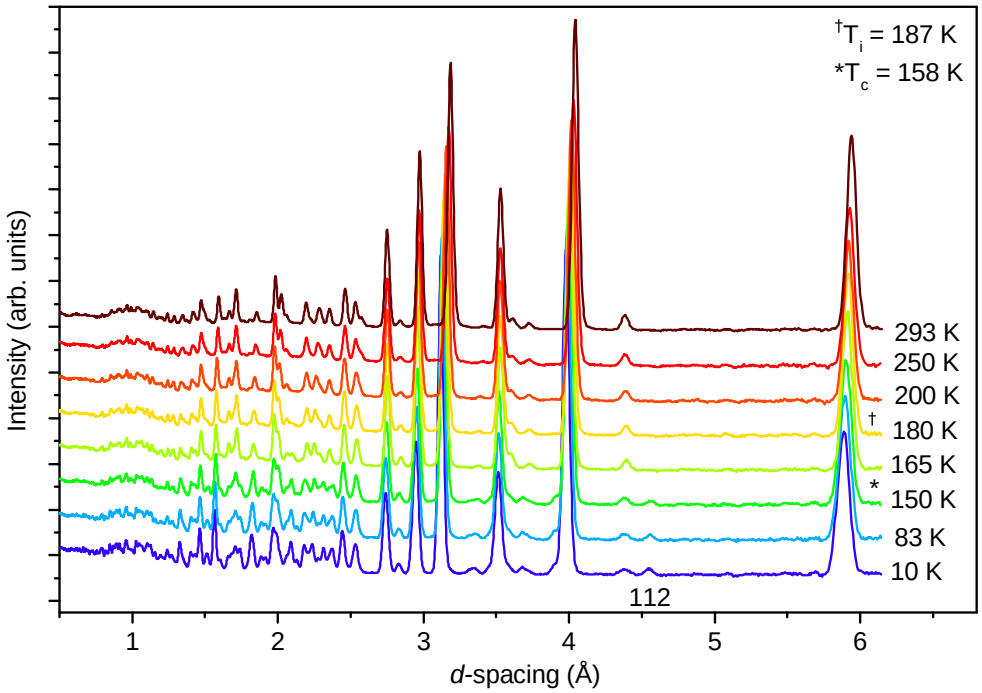


**Figure 5.7:** Observed Bragg profiles in the high and intermediate temperature ($R\bar{3}m$) and low temperature ($C2/c$) phases. A small peak at $4.56\,\text{Å}$ emerges in the at temperatures below $165\,\text{K}$.

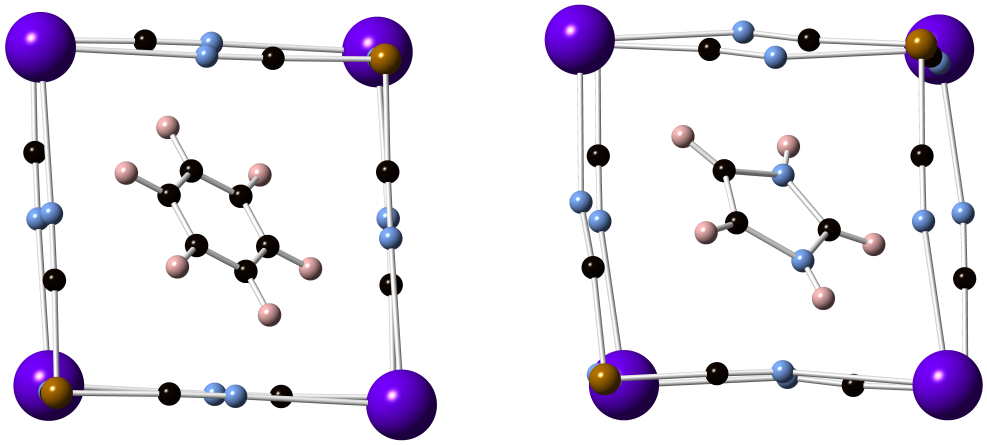

**Figure 5.8:** Initial configurations used for Rietveld refinement. Left: The $R\bar{3}m$ structure of PIH with benzene in place of the disordered imidazolium cations, Right: The $C2/c$ structure with imidazolium inside the cage. Both structures are derived from x-ray sources [109].

were treated separately due to the significantly different chemical environments.

A representative fit of the $R\bar{3}m$ refined profile is shown in figure 5.9. Most notable is the poor agreement in the $(10\bar{2})$ peak intensity at $5.94\,\text{Å}$ however several other peaks are very poorly fit. This poor agreement appears to be a function of using an ordered six-membered monatomic ring to simulate disorder in a five-membered diatomic ring.

In an attempt to more accurately describe the imidazolium cation in the $R\bar{3}m$ structure, the weighted average of the scattering length of the two nitrogen and three carbon in the

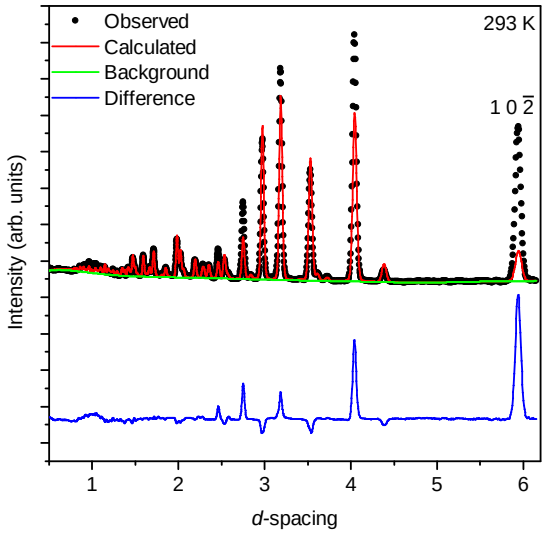


**Figure 5.9:** GSAS fit of 293 K data ($R\bar{3}m$) where disordered imidazolium rings are modelled as ordered benzene rings with $\frac{5}{6}$ occupancy. Poor agreement between the observed (black dots) and calculated (red line) profiles highlighted by the ($10\bar{2}$) peak at 5.94 Å is attributed to this disparity.

imidazole ring was calculated to be 6.443 fm. The atom with the closest scattering length, Gd – $b_{c,Gd} = 6.5$ – replaced the carbon atoms in the benzene ring. Replacement of the carbon atoms with Gd did not improve the agreement between the calculated and observed profiles for the high-temperature phase, and so it was decided to continue modelling the imidazolium as a benzene ring with $\frac{5}{6}$ occupancy on each site.

During refinement of the low-temperature phase $C2/c$ structure (right of figure 5.8) bond length restraints on the imidazolium ring, and the $KN_6$ and $FeC_6$ polyhedra and the cyanide linker were applied. The restraints are outlined in table 5.2. In addition to bond length restraints, bond angle restraints were initially applied to the imidazolium ring to keep the C/N-D-C/N angles at approximately 126°. These restraints were lifted later in the refinement. An additional constraint to ensure the imidazolium ring remained planar by keeping the $x$ component of the coordinates for all imidazolium C, N, and D was the same, was applied in the early stages of refinement and later relaxed.

| Bond type | Restraint length /Å |
|---|---|
| Fe−C | 1.940 |
| K−N | 2.860 |
| C−N (cyanide) | 1.150 |
| C−D | 1.030 |
| N−D | 1.030 |
| C−C | 1.270 |
| C−N (N−C−N) | 1.285 |
| C−N (C−C−N) | 1.370 |

**Table 5.2:** Bond length restraints applied during $C2/c$ GSAS refinement.

Least squares refinement was carried out on the $C2/c$ structure by allowing the following parameters to refine: background and scale, cell parameters, diffractometer constant `DiffA`,

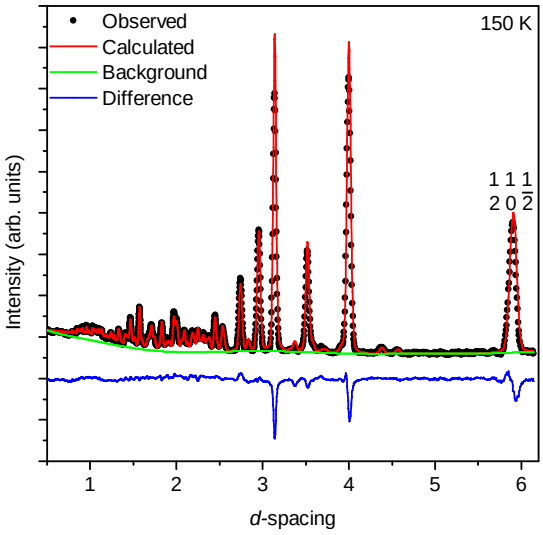


**Figure 5.10:** GSAS fit of 150 K data ($C2/c$). Better agreement is seen between the calculated and observed 111 and $20\bar{2}$ peak at 5.94 Å compared to the $R\bar{3}m$ refinement.

peak-shape parameters $\sigma_1$, $\sigma_2$, $\gamma_1$, and $\gamma_2$, deuterium coordinates and finally all imidazolium coordinates. A representative fit of a $C2/c$ refinement is shown in figure 5.10. The agreement between the $C2/c$ model and the observed data is significantly improved when compared to the $R\bar{3}m$ refinement. For both the $R\bar{3}m$, and $C2/c$ refined structures the ratio of deuterium:hydrogen (initially 1 : 0) was altered to see if the calculated profile showed better agreement with the observed. No improvement was seen, leading to the conclusion that any hydrogen exchange which may have occurred in the sample was negligible.

### 5.3.4 Pair distribution analysis

GUDRUN was used to extract the scattering function, $i(Q)$, correct for the sample environment and calculate the pair distribution functions. Details of the correction run numbers can be found in appendix A.2.3.

Detector bank 1 was not used to extract the PDF and scattering functions due to the small $Q$ range it covered. The $Q$-range used for banks 2 – 5 are given in table 5.3

| Bank # | $Q_{min}$ | $Q_{max}$ |
|---|---|---|
| 2 | 0.30 | 4.55 |
| 3 | 0.80 | 4.55 |
| 4 | 2.09 | 46.00 |
| 5 | 3.37 | 46.00 |

**Table 5.3:** Bank cut offs used in GUDRUN.

The decision as to where to place the $Q$ cut offs for all banks was based on how well the differential cross section for each individual bank merged to produce the final differential cross section, and the agreement between observed and expected PDFs. For all temperatures, the minimum and maximum radius for Fourier transform were 0.88 Å and 40 Å. After the bank cut-offs had been chosen the tweak factor was adjusted so the high $Q$ value of the merged

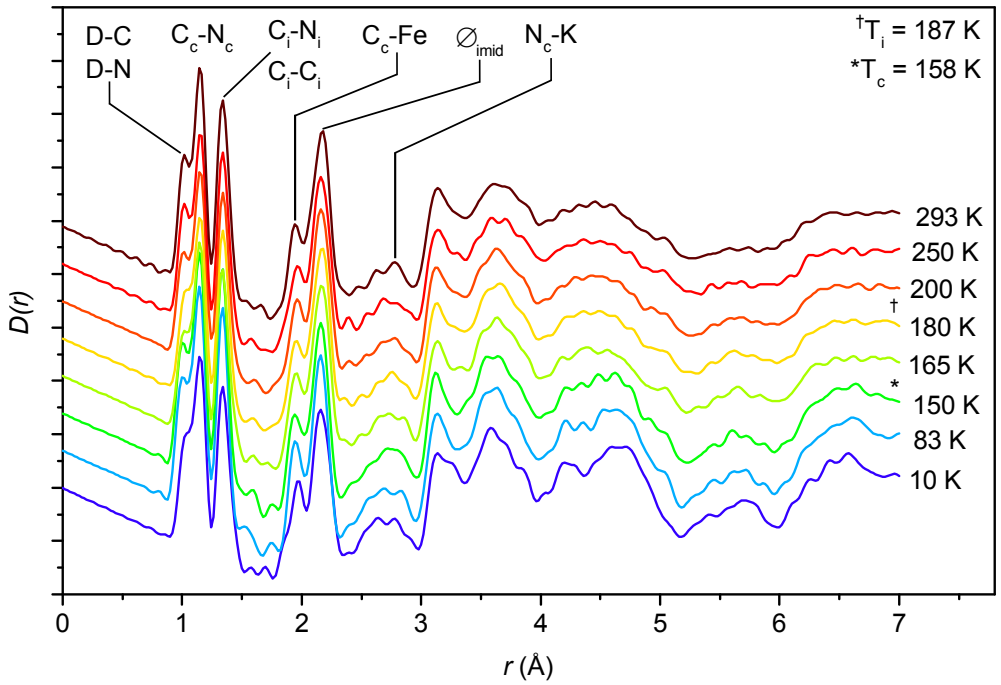


**Figure 5.11:** The $D(r)$ for PIH for $r < 7$ Å. Bonding peaks have been identified, peaks corresponding to the intramolecular distances in imidazole have been omitted for clarity. Bonding between carbon and nitrogen in cyanide and in imidazole have been differentiated with the subscripts $c$ and $i$ respectively.

differential cross section matched the expected ($i_{Q\to\infty} = \sum_i c_i b_i$) level. The data were then normalised to $\langle b \rangle^2$. The tweak factors for the data are given in table 5.4.

Termination ripples due to a finite $Q$ range were suppressed using equation (2.23b) with the broadening at 1.0 Å held constant at $\Delta_0 = 0.02$ Å, $\Delta(r)$ was extracted from each PDF separately, and the power of the broadening function, $\beta$ then calculated. The calculated $\beta$ is given in table 5.4.

| Temperature /K | Tweak Factor | $\beta$ |
|---|---|---|
| 293 | 2.4498 | 0.5345 |
| 250 | 2.9026 | 0.5320 |
| 200 | 2.9009 | 0.5592 |
| 180 | 2.8934 | 0.5229 |
| 165 | 2.8934 | 0.4878 |
| 150 | 2.8934 | 0.5170 |
| 83 | 2.5889 | 0.5195 |
| 10 | 2.6140 | 0.5434 |

**Table 5.4:** Parameters used in GUDRUN to extract the i(Q) and PDFs.

The GUDRUN-derived $D(r)$ for PIH up to 7 Å is shown in figure 5.11. The peaks at low $r$ have been identified, however when $r > 2.20$ Å identifying the peaks become difficult due to intramolecular separations within the imidazole ring. The diameter of the imidazole ring is approximately 2.20 Å. When the associated deuterium are also considered, bond separations between 2.20 Å and 4.50 Å are dominated by atomic pairs within the imidazolium ion.

Ripples in $D(r)$ at $r < 0.9$ Å are truncation ripples which have not been fully suppressed by

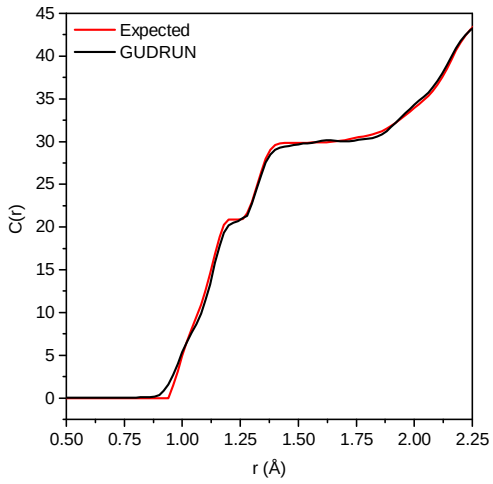


**Figure 5.12:** The expected and oberved $C(r)$ for $G'(r)$ up to $r$ =2.25 Å after optimisation of the individual bank cut offs in GUDRUN.

equation (2.23b), however a balance had to be made between minimisation of the termination ripples and blurring two peaks into one another. Unlike DMMnF, there are no features clearly indicative of either phase transition in $D(r)$ of PIH.

It was observed that the area under the 1.04 Å peak (corresponding to the C−D and N−D bonding pairs) was insufficient to account for the known coordination number. The integral $C(r) = \int_0^r G'(r)\mathrm{d}r$ was calculated for the system with the correct coordination number and for the experimental data for $r < 2.25$ Å and is shown in figure 5.12. The range of the low-angle banks was limited such that they only contributed to the low $Q$ region of the scattering data to minimise the errors associated with inelastic scattering, which in turn provided more accurate integrals at low $r$ in the PDF. After adjustment of the $Q$-range cut offs, good agreement is observed between the expected and GUDRUN-derived cumulative sum of this well-understood region.

### 5.3.5 Initial RMC configurations

There were three main features that had to be accounted for when generating the inital configurations for RMC refinement. Firstly, in the high-temperature phase Rietveld refinement; the disordered imidazolium rings had been modelled as benzene rings. The second feature was that in the structure there were two different C−N bonds, one for the framework cyanide and the other within the imidazole. These two bonds had different lengths ($\approx$ 1.14 Å and $\approx$ 1.35 Å, respectively) but when the distance windows and interatomic potential search distances were taken into account there could be some overlap where bonding in the imidazole ring was subject to the cyanide potentials, and vice versa. Finally, because the refinement contained planar rings, there needed to be some way to ensure the rings remained (largely) planar during refinement.

### 5.3.6 Disordered imidazolium

During the Rietveld refinement the benzene ring had been used to represent the disordered imidazolium ring. The imidazolium ring now needed to be introduced.

Figure 5.13 shows the steps that were carried out by my programs (in blue) to generate an `RMCProfile`-ready supercell with disordered imidazolium rings. Benzene rings were replaced with imidazole rings with the same centroid, rotated in their plane by a random angle. Figure 5.14 shows configurations before (left) and after (right) application of the imidazole disorder program.

The imidazolium disorder program was applied to all high and intermediate temperature phase initial configurations. The distribution of the rotation of the imidazole rings (between $\pm$ 180°) for all initial configurations is given in figure 5.15.

It was necessary to differentiate between the imidazole and cyanide C−N bonds for all refinements. The code of `RMCProfile` was edited to include two new atoms identified as Nx and Cx. Both Nx and Cx had the same scattering lengths as N and C respectively, but this allowed the program to treat them as two different atoms. A program was written to identify the cyanide atoms in the initial `RMCProfile` configurations and re-name the atoms.

Finally it was necessary to ensure the imidazole rings remained planar, this was achieved using bond bending and stretching potentials, and a planarity potential.

The planarity potential, implemented by E. O. R. Beake, is an additional interatomic potential restraint (section 2.5), a penalty term is added to the $\chi^2$ if the specified atoms deviate from a planar arrangement. A full discussion of the implementation of the planarity potential within `RMCProfile` is given in [53] with an abbreviated version presented here. The plane on which each imidazolium ring (with number of atoms, $i = 5$) lies is defined by $\mathbf{N} \cdot (\mathbf{X} - \mathbf{A}) = 0$ where $\mathbf{N}$ is the unit vector normal to the plane, $\mathbf{X}$ is the 3D position vector and $\mathbf{A}$ is the position vector of the point on the plane. For each atom, $i$, $\mathbf{Y}_i = \mathbf{X}_i - \mathbf{A}$, and $\mathbf{Y}_i$ expressed in terms of components perpendicular and parallel to the plane such that

$$\mathbf{Y}_i = \lambda_i \mathbf{N} + \mathbf{R}_i, \tag{5.1}$$

where $\lambda_i = \mathbf{N} \cdot \mathbf{Y}_i$. The error function which is then minimised is given by

$$E(\mathbf{A}, \mathbf{N}) = \sum_i \lambda^2 = \sum_i (\mathbf{N} \cdot \mathbf{Y}_i)^2 \tag{5.2}$$

The constant $L$ (from equation (2.37)) for the planarity term was set to $5000\,\mathrm{eV\AA}^{-2}$ for all refinements. Use of the planarity potential required that the atom numbers of the carbon and nitrogen of each imidazolium ring be given in order in a *.planarity* file. From this, `RMCProfile` would identify the imidazolium rings in the structure, calculate the deviation from a planar configuration, and apply the penalty term to the $\chi^2$ as needed.

### 5.3.7 RMC restraints

The standard MM3 potential set contains no potentials specifically for imidazole; the imidazole potentials from the protein set are inappropriate here as they are designed to model solution behaviour. Thus the potentials applied to the imidazolium cation were an average of the values for pyrrole and pyridine in the general MM3 potential set as shown in figure 5.16 with values given in tables 5.5 and 5.6.

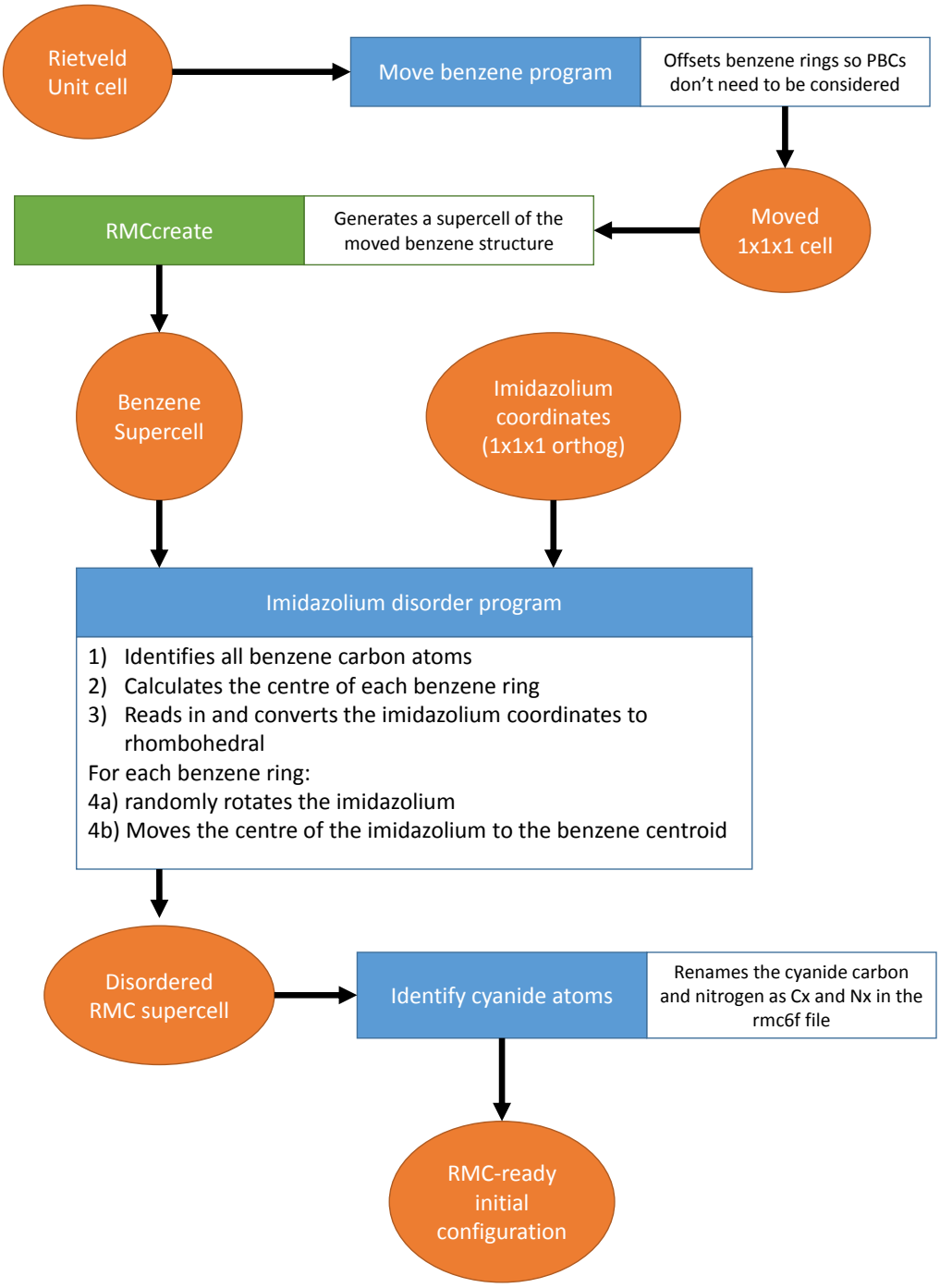


**Figure 5.13:** Flowchart of the steps taken to get from a HTP Rietveld refinement containing benzene rings to a RMC-ready supercell with disordered imidazolium rings.

No potentials were introduced for the NC−Fe or CN−K pairs, and the cyanide C−N potentials were taken from the standard MM3 set. A full list of stretching and bending potentials used for RMC refinement are given in tables 5.5 and 5.6.

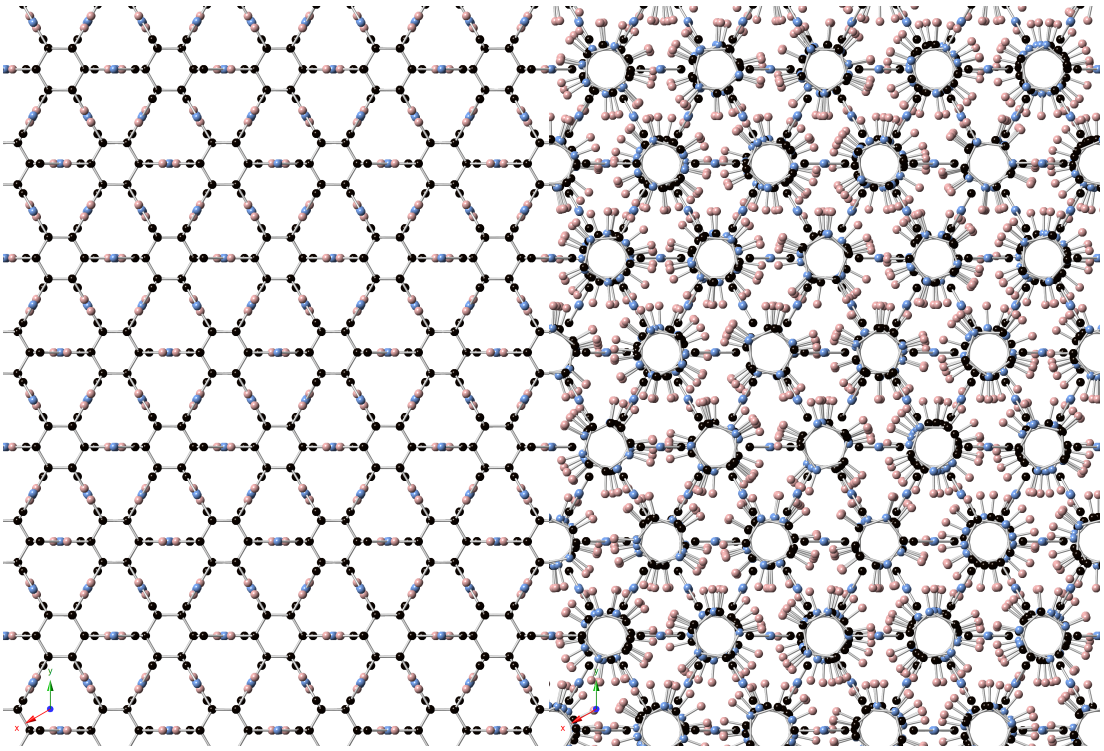

**Figure 5.14:** The RMC supercell with benzene rings (left) and the supercell after application of the disorder program (right). Fe and K ommitted for clarity.

As with DMMnF, distance window constraints were applied to all bonding pairs, and non-bonding metal-cyanide pairs. The values for the distance windows were based on a fraction of the maximum and minimum bond distances in the average structure.

Due to overlapping C−D and N−D peaks at $r \approx 1.04$ Å, two Gaussian artificial partial pair distribution functions were introduced, each with a weighting $\frac{1}{25}$ of that given to $D(r)$.

### 5.3.8 Completion criteria

The calculated $\chi^2$ was output after every 10 000 moves, the models were declared converged when continuing the refinement no longer improved the $\chi^2$. For the high and intermediate temperature configurations this corresponded to $\approx 4.5 \times 10^6$ accepted atomic moves, and for the low temperature configurations $\approx 6.4 \times 10^6$ accepted atomic moves. Graphs of the evolution of $D(r)$ for refinements at 293 K and 150 K are given in figure 5.17.

The PIH refinements took fewer atomic moves to reach convergence ($4 \times 10^6$ to $6 \times 10^6$ moves) than the DMMnF refinements ($15 \times 10^6$ to $18 \times 10^6$ moves), the reason behind this is unclear. The imidazole rings subject to the planarity potentials comprised of approximately 29% of the atoms in the cell.

### 5.3.9 Representative fits

Representative fits of $D(r)$ and $i(Q)$ for the 293 K, 180 K, and 150 K refinements (high, intermediate, and low-temperature phases) are given in figures 5.18 and 5.19. For $D(r)$ there is a difference between the observed and the calculated peak height at low $r$ however this fit

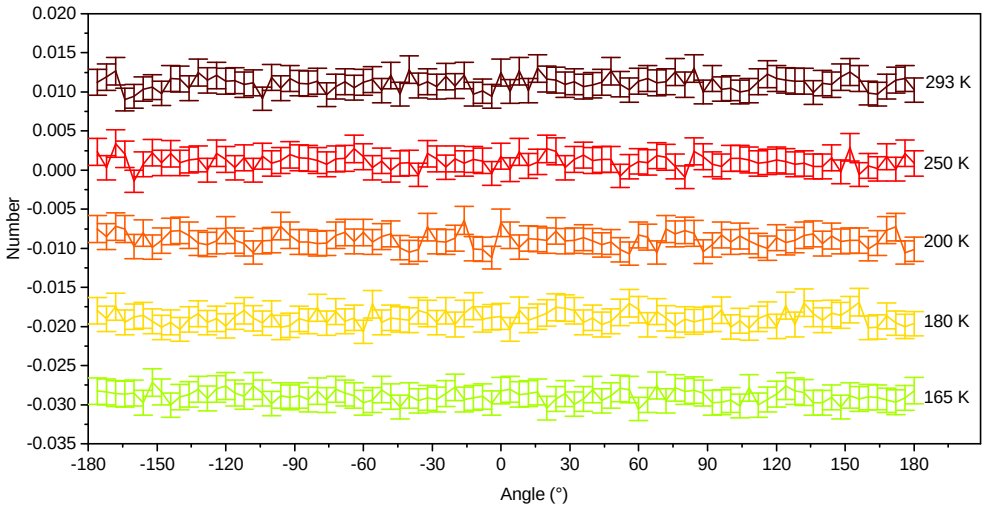


**Figure 5.15:** The initial orientation of the imidazole in the high and intermediate temperature phases offset for clarity. Each temperature displays 16 200 imidazole rings.

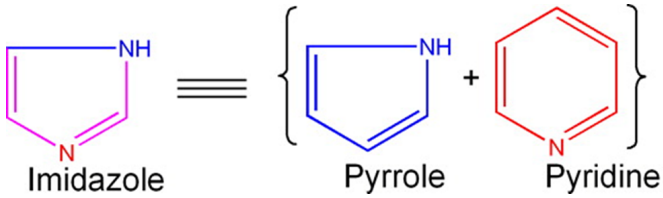


**Figure 5.16:** A potential way to describe the interatomic potentials of imidazolium in the absence of empirically-derived potentials in the MM3 data set. Figure is adapted from reference [114].

is the best which could be achieved (see section 5.3.4). There is good agreement in $D(r)$ for $r$ >3.0 Å and there is good agreement between the observed and calculated $i(Q)$ over the whole $Q$-range.

Figure 5.20 shows the improvement in the Bragg profile for the model of PIH at 293 K after the ordered benzene rings are replaced with (planar) disordered imidazolium and then refined. From this figure we see that the $(10\bar{2})$ peak shows better agreement with observed data when the benzene is replaced, however the $(21\bar{2})$, (006), and (104) peaks in the initial configuration show a much poorer agreement. Once the model is refined (bottom left in figure 5.20) the intensities of all 4 peaks are consistent with the observed data. For the refined model it appears that the peak position is not quite correct, implying that the Rietveld-refined lattice parameters are slightly incorrect. A Le Bail refinement was carried out in GSAS on a 200 K configuration to see if the peak positions could be improved by refinement of the lattice parameters, however no improvement to the peak position could be made and so the Rietveld-derived lattice parameters given in section 5.6.3 are assumed to give the best possible fit.

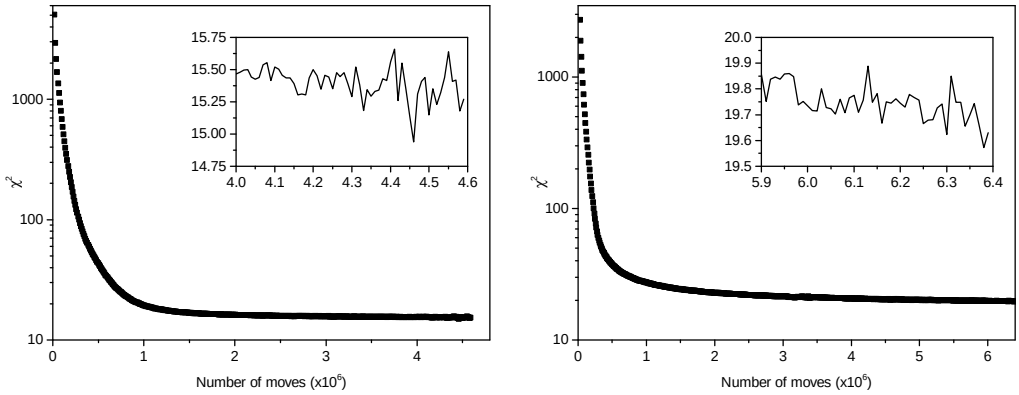


**Figure 5.17:** The goodness of fit, $\chi^2$, as a function of the number of atomic moves for $D(r)$ in the high (left) and low(right) temperature phase. The insets show the change in $\chi^2$ for the final half million moves of refinement.

| Atomic pair | $D$/eV | $r_0$/Å |
|---|---|---|
| C−C | 3.600 | 1.34 |
| C−D | 2.472 | 1.04 |
| C−N | 4.821 | 1.34 |
| N−D | 2.928 | 1.03 |
| Cx−Nx | 8.317 | 1.16 |

**Table 5.5:** Morse bond stretch potentials used to constrain RMC refinement.

| Atoms | $k$/eV | $\theta_0$/° |
|---|---|---|
| D−C−N | 6.429 | 126.000 |
| C−N−D | 7.2405 | 126.000 |
| N−C−N | 4.993 | 126.000 |
| C−N−C | 10.174 | 118.300 |
| C−C−N | 10.174 | 120.000 |
| C−C−D | 6.117 | 126.000 |

**Table 5.6:** Angle potentials used to constrain RMC refinement.

| $T$/K | D−C | D−N | C−C | C−N | Cx−Fe | Cx−Nx | K−Nx |
|---|---|---|---|---|---|---|---|
| 293 | 0.93-1.15 | 0.93-1.15 | 1.25-1.46 | 1.25-1.46 | 1.82-2.07 | 1.08-1.26 | 2.60-3.18 |
| 250 | 0.93-1.15 | 0.93-1.15 | 1.25-1.46 | 1.25-1.47 | 1.83-2.09 | 1.10-1.23 | 2.58-3.16 |
| 200 | 0.93-1.15 | 0.93-1.16 | 1.25-1.47 | 1.25-1.47 | 1.83-2.09 | 1.10-1.23 | 2.57-3.16 |
| 180 | 0.93-1.16 | 0.93-1.12 | 1.25-1.47 | 1.25-1.47 | 1.83-2.09 | 1.10-1.23 | 2.57-3.16 |
| 165 | 0.93-1.16 | 0.93-1.16 | 1.26-1.47 | 1.25-1.47 | 1.83-2.09 | 1.10-1.23 | 2.57-3.16 |
| 150 | 0.92-1.15 | 0.90-1.14 | 1.22-1.41 | 1.22-1.45 | 1.83-2.12 | 1.07-1.22 | 2.56-3.19 |
| 83 | 0.93-1.16 | 0.92-1.15 | 1.21-1.40 | 1.21-1.45 | 1.84-2.10 | 1.09-1.21 | 2.57-3.17 |
| 10 | 0.88-1.13 | 0.86-1.15 | 1.23-1.42 | 1.24-1.46 | 1.84-2.10 | 1.09-1.24 | 2.53-3.17 |

**Table 5.7:** Distance windows applied to RMC refinements.

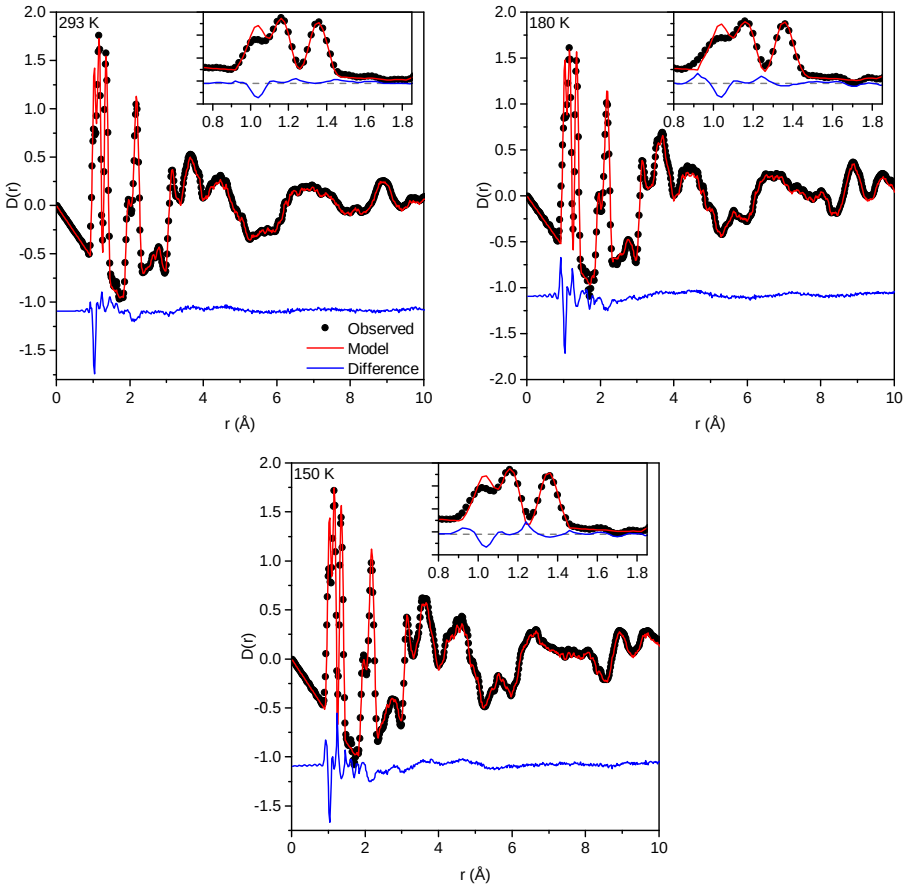


**Figure 5.18:** Top Left: The observed (black dots) and calculated (red line) $D(r)$ for a high-temperature phase refinement with the offset difference in blue for $r = 0\,\text{Å}$ to $10\,\text{Å}$. Insert shows agreement between the low-$r$ peaks. Top right, the corresponding plot for an intermediate temperature phase refinement. Bottom, low-temperature phase $D(r)$.

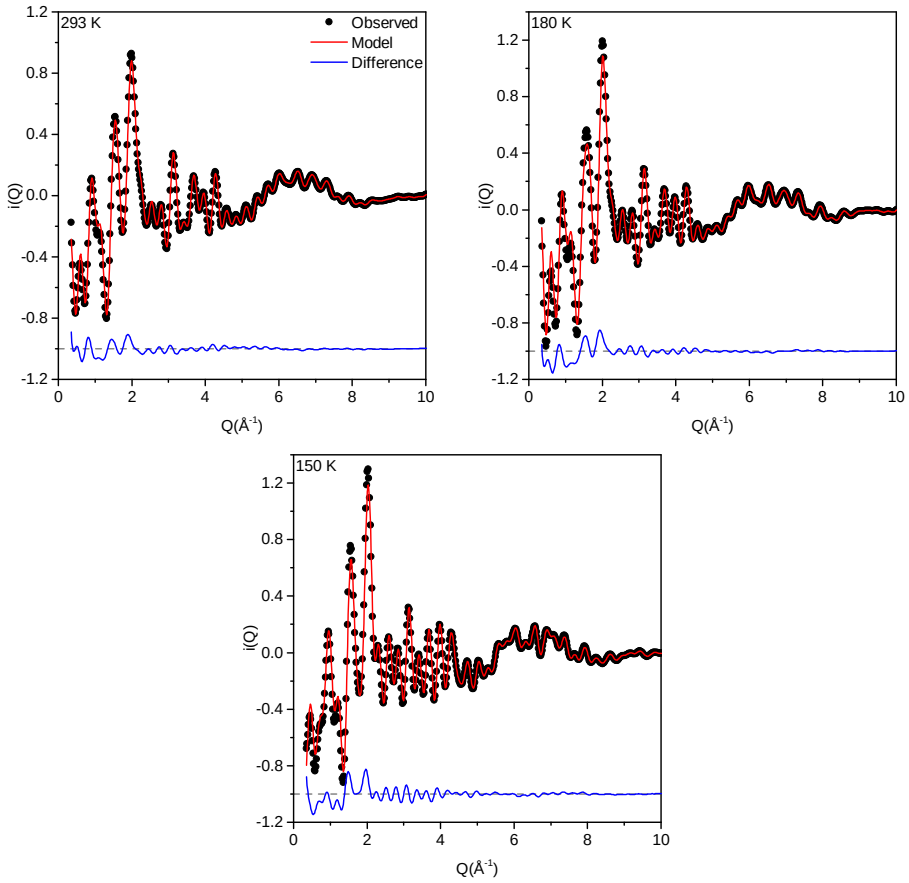


**Figure 5.19:** Top Left: The observed (black dots) and calculated (red line) $i(Q)$ for a high-temperature phase refinement with the offset difference in blue for $Q = 0\,\text{Å}^{-1}$ to $10\,\text{Å}^{-1}$. Top right, the corresponding plot for an intermediate temperature phase refinement. Bottom, low-temperature phase $i(Q)$.

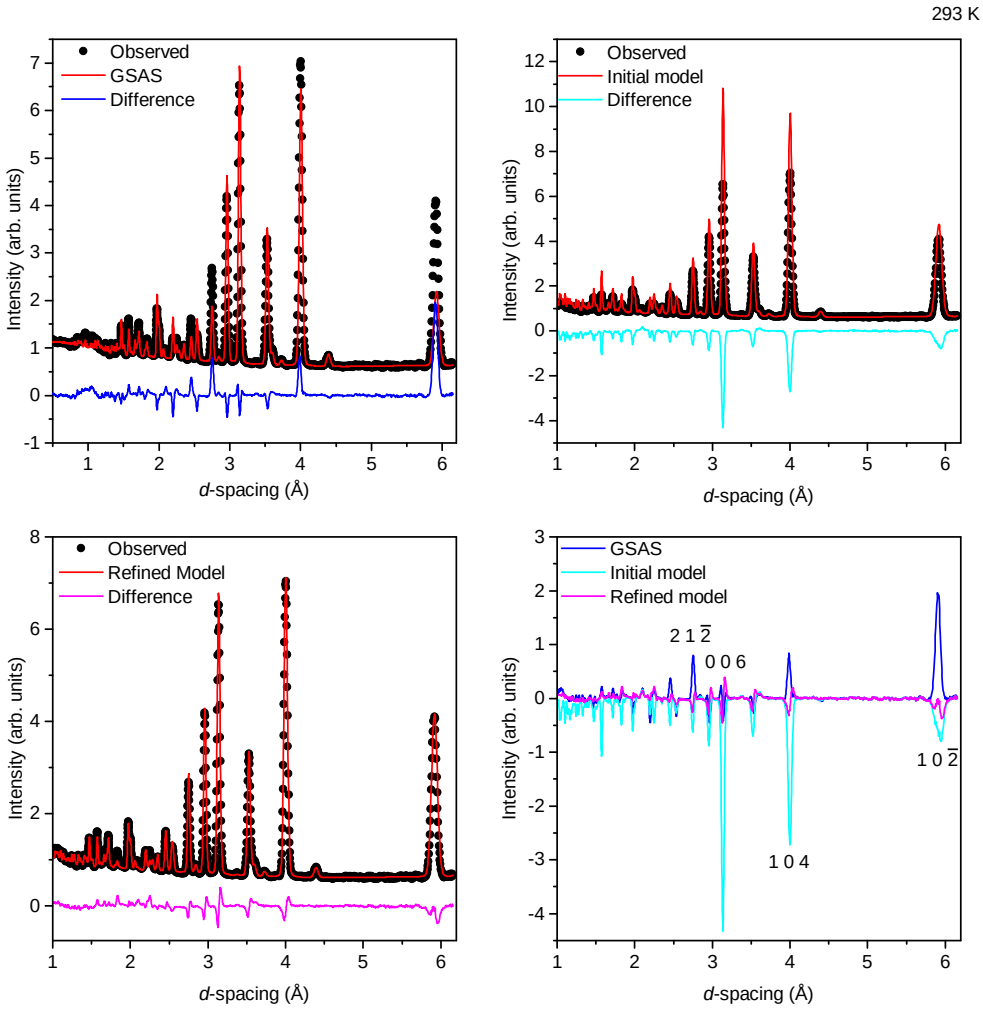


**Figure 5.20:** The Bragg profile of bank 3 for PIH at $293\,\mathrm{K}$ compared to three different models. Top left, the GSAS unit cell where disordered imidazolium are approximated by ordered benzene rings. Top right, the initial `RMCProfile` configuration for a $6 \times 6 \times 3$ supercell where disordered planar imidazole rings replace the benzene. Bottom left, the refined RMC model. Bottom right the differences between the three models and the observed profile with selected peaks identified. In this panel it can be seen that the difference between the refined model and the observed data (pink) is the smallest, showing the Bragg profile from the atomistic configurations – where symmetry restrictions are removed and the imidazole cations are free to move out of the plane of rotation – gives the best possible fit.

## 5.4 Analysis

The analysis section is divided into two sections, the first section discusses evidence for imidazole ordering about the dielectric transition. The second section discusses the observed differences between $FeC_6$ and $KN_6$ octahedra and discusses the evidence for the presence of an intermediate temperature phase in PIH, and places it in the context of the other PBAs.

## 5.5 Evidence of imidazole disorder

Below 158 K, the imidazolium rings of PIH order antiferroelectrically. With DMMnF, it was possible to observe preferred orientations of the guest cation in the high temperature phase. For PIH, two features of the imidazolium motion were investigated to see if there were signs that above 158 K, the imidazolium cation showed indications of ordering, the rotation of the ring, and its propensity to tilt about its centre of rotation. Comparison of the behaviour of the imidazolium were made between PIH and the K/Co analogue **B**.

### 5.5.1 Imidazole rotation

The rotation of the imidazolium cation was defined as the angle made between the vector from the centroid of the ring, to the N−C−N, and a reference vector parallel to the initial plane of the ring. The rotation angles ranged between $\pm 180°$.

Figure 5.21 shows the initial (grey) and final (colour) angles for imidazole rotation for selected refinements in the high and intermediate temperature phases, unlike DMMnF, there are no signs of preferred orientations above the transition temperature. The bin size was increased from 4° to 20° in 4° increments for the 293 K refinement, to see if the apparent lack of preferred orientation was a function of small increments. The change of bin sizes did not change the result that no preferred orientations were observed.

The change in rotation angles of the imidazolium between the initial to the final configurations were calculated. The change in angle was found to be independent of the temperature (no dependence was expected) with the change in rotation angle for most imidazole being less than $\pm$ 4° as shown in figure 5.22. There appears to be no correlation between the phase and the rotation of the imidazole ring during refinement.

Disordered imidazolium rings in the high and intermediate temperature phases of PIH are consistent with observations made of the K/Co analogue **B** [112] where $^2$H NMR measurements of a partially deuterated sample confirmed the onset of imidazole rotation only occurred above $T_i$ the absence of preffered orientations also consistent with a first-order transition.

### 5.5.2 Imidazole tilt

Application of the planarity potential in the `RMCProfile` refinements kept the imidazole largely planar; however the molecule on its own is free to tilt about its centre of rotation. The degree of this tilt was defined by calculating the plane of the refined imidazole ring (using a similar algorithm to that used in the planarity potentials) and the normal to that plane, and taking the difference between the initial and refined normals, as shown in figure 5.23. It should be noted that the crystallographic axis which were used as a reference vector were different in

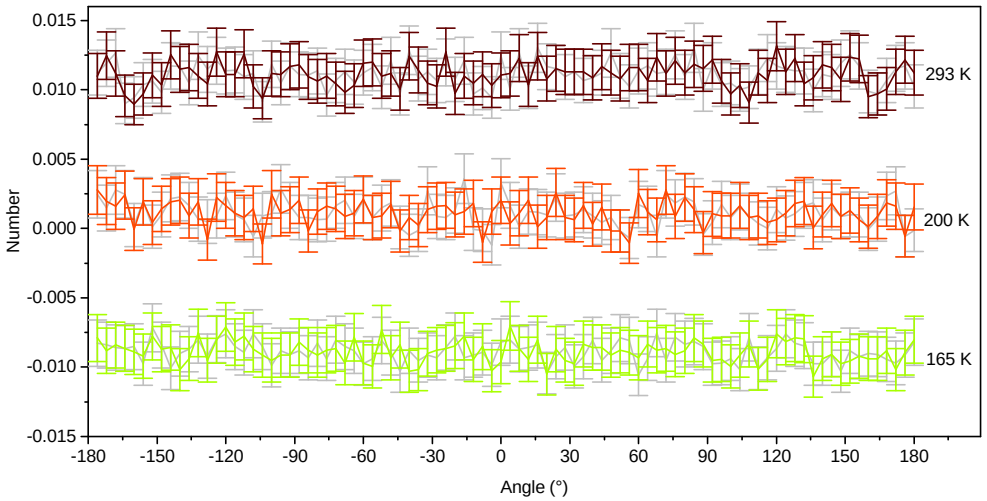


**Figure 5.21:** The initial (grey) and final (colour) orientations of the imidazole ring at 293 K, 200 K, and 165 K. Each data set corresponds to rotation angles calculated from 25 unique configurations

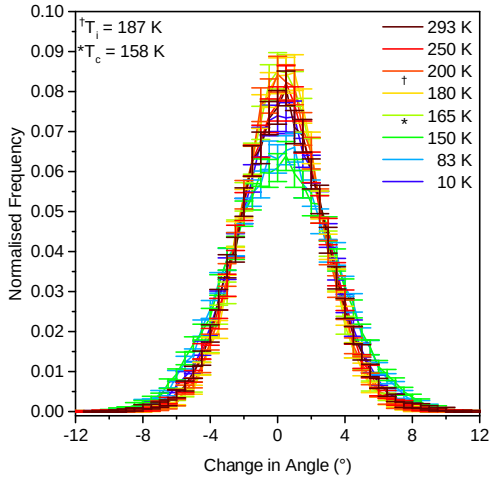


**Figure 5.22:** The change in imidazole rotation angle between initial and refined configurations as a function of temperature. The rotation of the imidazolium ring is independent of the phase of the structure.

the $R\bar{3}m$ and $C2/c$ unit cells, but both reference vectors are perpendicular to the plane of the imidazolium in the initial configuration.

A Gaussian of the form

$$y = \frac{1}{\sigma\sqrt{2\pi}} \exp\left(-\frac{(x-\mu)^2}{2\sigma^2}\right) \tag{5.3}$$

was used to fit the distribution of tilt angles, where $\mu = 0$. Figure 5.24 shows the distribution of the tilt angles over all temperatures, each from 25 unique refinements. The data were corrected by first dividing the frequency by $\sin\theta$, and then normalising so the area under each curve was 1. Division by $\sin\theta$ accounts for the fact that there are more possible configurations which produce larger angles than there are configurations producing smaller ones, by dividing my $\sin\theta$ the bias towards larger angles is removed. From figure 5.25 it can be seen that the imidazole in all temperature phase refinements tilt to some degree, with the higher

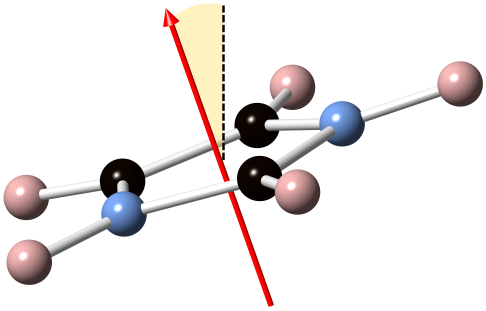

**Figure 5.23:** Definition of the imidazole tilt angle, where the normal to the imidazole cation plane is calculated and the angle that the normal made with the crystallographic axis perpendicular to the plane of the ring was calculated.

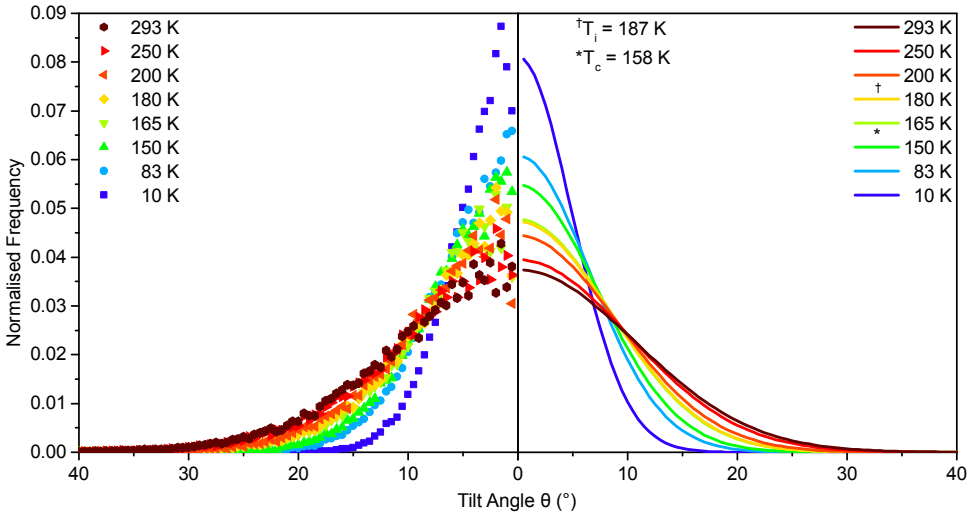


**Figure 5.24:** Left: The observed distribution of imidazole tilt angles. Right: Corresponding Gaussian fit

temperature imidazolium tilting more than the low temperature ones.

A graph of $\sigma$ vs. $T$ is given in figure 5.25. From figure 5.25 it can be seen that, upon heating, there is a steady increase in the width of the Gaussian fit with $\sigma$ increasing from 4.93° to 10.66°.

$^2$H NMR measurements on a partially deuterated K/Co analogue **B** found that the imidazole only tilted in the high temperature phase [112]. The PIH results show that there is tilting in all phases, and that the range of tilt angles increases with increasing temperature. As **B** has a different framework and is only partially deuterated, direct comparison between **B** and PIH is unwise, rather the results with PIH complement previous analysis performed on **B** and show how these apparently small structural changes can have substantial effects on the motion of the guest cation.

While it is seen that the tilting angle of the imidazolium changes as the material is cooled, no anomalous behaviour is observed at either the high to intermediate-temperature phase transtion or at the intermediate to low-temperature transition. The fact that the imidazole tilting angle is not correlated with the phase can be explained by the behaviour of the

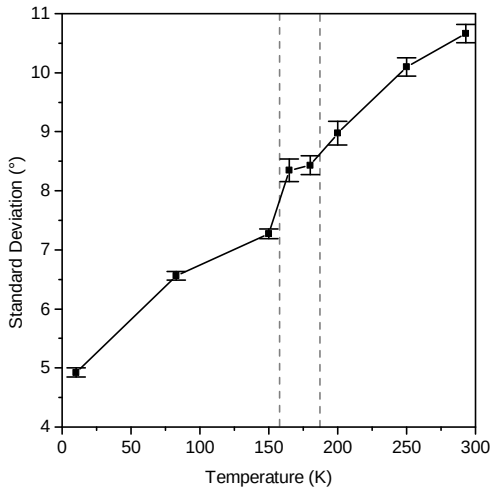


**Figure 5.25:** Standard deviation $\sigma$ used to fit the tilt-angle data in figure 5.24 where $\mu = 0$ $T_{\mathrm{i}}$ and $T_{\mathrm{c}}$ shown as dashed lines. Error bars show 95% confidence limit. Lines are a guide to the eye.

anisotropic dielectric permittivity shown in figure 5.2. In figure 5.2 there is very little change in the permittivity perpendicular to the plane of the imidazole rings (0001), shown in red, during the dielectric transition, and no discernible change between the high and intermediate temperature phases. Therefore it is expected that the bulk of the changes associated with the both phase transitions would occur within the plane of the imidazole rings, not perpendicular to it.

### 5.5.3 Imidazole to framework partial PDFs

In order to assess if the imidazolium ring moved away from the centre of the pore during the phase transition the partial PDFs from the centre of the imidazolium cation to the framework were calculated and are shown in figure 5.26. The distributions for the centroid···C in the high and intermediate temperature phase are indistinguishable from one another, and show one broad peak, however in the low temperature phase the peak is bimodal indicating that some of the imidazolium cations in the low temperature phase offset themselves. For the centroid···N correlations, the distribution of the pair density appears to shift continuously from a broad peak at 293 K to a bimodal distribution at 10 K. There is no anomalous behaviour in the intermediate temperature range.

This analysis cannot differentiate between the imdiazolium cation drifting in a static framework and the framework distorting around a static cation. However from this analysis it can be seen that the correlations between the centre of the guest and the linking atoms of the framework are different before and after the onset of electric ordering.

### 5.5.4 Imidazole disorder summary

For all configurations above 158 K, there are no indications of preferential imidazolium ordering, as the phase transition at 158 K is a first-order transition, where a discontinuous change in order parameters (such as cation orientation) is observed, it is not unusual. However the proposed high to intermediate temperature phase transition is a subtle one, and it was

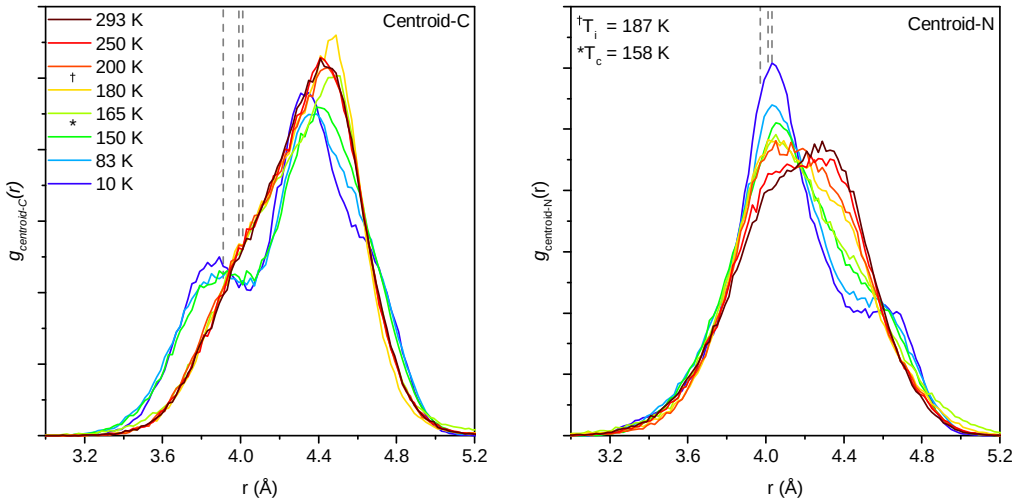


**Figure 5.26:** Partial pair distribution functions from the centre of the imidazolium to the cyanide atoms of the framework. Left: Centroid···C partials. Right: Centroid···N partials. Dashed lines indicate the Centroid···C and Centroid···N separations in the high- intermediate- and low-temperature phases, where the shorter distances correspond to lower temperatures.

possible that the presence of the intermediate-temperature phase could be inferred from the imidazole orientations. However the distribution of imidazolium cations of the high and proposed intermediate temperature phase are indistinguishable.

The imidazolium cation was observed to tilt about its centre of rotation, with the configurations of the higher temperature data displaying a broader distribution of angles. The sharp increase in the width of the distribution above $T_c$ could be evidence of the imidazolium responding to changes in the framework, such as a contraction about its plane of rotation.

## 5.6 Evidence for the intermediate-temperature phase

Indications that PIH undergoes a subtle phase transition above the dielectric transition are seen as small features in the anisotropic dielectric permittivity and DSC measurements at 187 K. However analysis of the imidazolium preferred orientations and tilting angles found no indication of anomalous behaviour corresponding to the proposed intermediate temperature phase. In this section, the framework dynamics, coordination polyhedra shape and spontaneous strain are investigated for signs of anomalous behaviour in the proposed intermediate temperature phase.

### 5.6.1 Polyhedra distortion

The level of distortion in the metal cyanide octahedra as PIH was cooled through the dielectric transition was characterised by the distribution of C−Fe−C and N−K−N angles. During RMC refinement, no interatomic restraints were applied to either the Fe−C or K−N bonds, yet when the distortion of the $KN_6$ and $FeC_6$ polyhedra were analysed by measuring the distribution of angles between C−Fe−C and N−K−N both were found to have a symmetrical distribution about 90°, as shown in figure 5.27. The distribution of angles confirms that there is no significant distortion of the polyhedra.

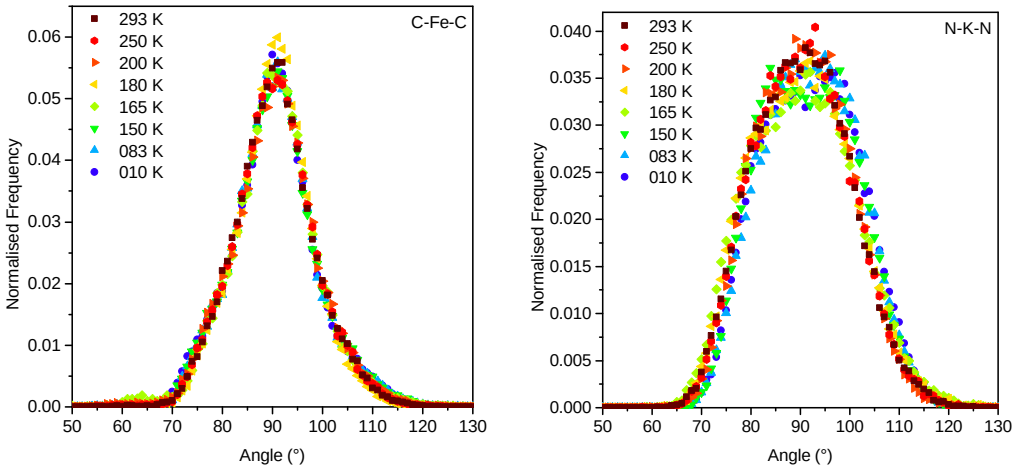


**Figure 5.27:** The distribution of C—Fe—C (left) and N—K—N (right) angles. The more ionic $KN_6$ polyhedra have a broader distribution of angles than the more covalent $FeC_6$ polyhedra.

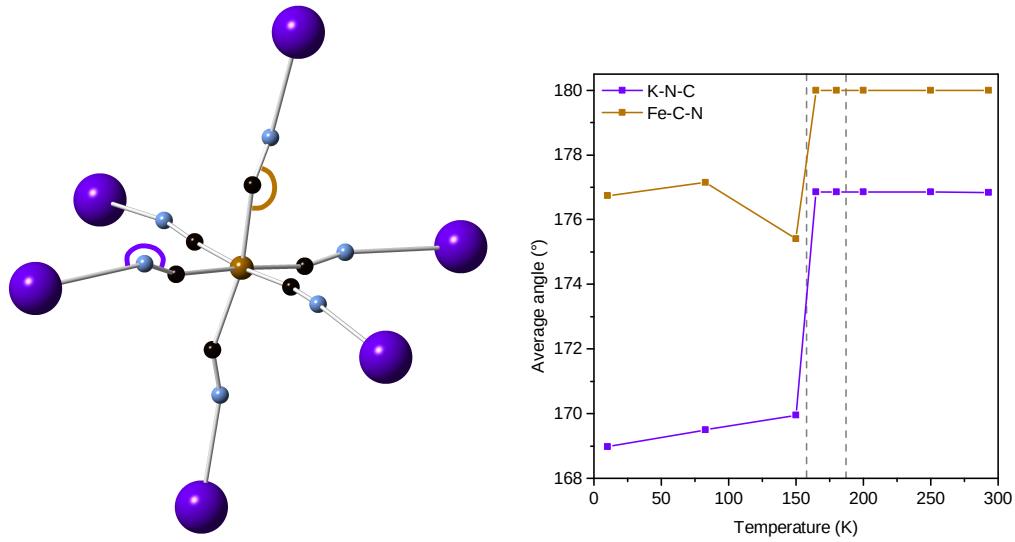


**Figure 5.28:** Left: Octahedral coordination for $Fe(CNK)_6$ from a 293 K refined atomistic configuration. The Fe—C—N angle is shown in brown, and the K—N—C in purple. Right: Rietveld-derived average angles made for Fe—C—N (brown) and K—N—C (purple) coordination polyhedra.

The $KN_6$ polyhedra have a wider distribution than $FeC_6$, this is attributed to the more ionic nature of the K—N bonds than the Fe—C bonds. The absence of a change in the distribution of angles in any temperature phase indicates that changes across the phase transition are independent of the coordination polyhedra shape.

### 5.6.2 Framework distortion

As the angles within the $FeC_6$ and $KN_6$ polyhedra remain regular, the next place to look for evidence of a distortion of the framework is through analysis of the distribution of the metal to cyanide angles, Fe—C—N and K—N—C shown on the left in figure 5.28 in brown and purple respectively. These angles can be thought of as a measure of linearity of the framework.

The average Fe−C−N and K−N−C angles as derived from Rietveld refinement were calculated and are shown on the right of figure 5.28. As the high and intermediate temperature phase have the same space group symmetry, the behaviour for both coordination polyhedra is similar in both phases. However, even from the average structure, we see a deviation from linearity below $T_c$ in Fe−C−N and in all phases for K−N−C.

From the average structure we observe that the K−N−C angles are consistently lower than their Fe−C−N counterparts. This is due to the presence of the more ionic K−N bonds, which can accommodate lower metal-cyanide angles.

The feature of the more ionic coordination polyhedra accommodating lower bond angles has been observed in other PBAs such as **B** and $Na_2Mn^{HS}[Mn^{LS}(CN)_6]$[104] (where Mn is in a high-spin, HS, and low-spin, LS, state). In the Mn analogue, the $Mn^{HS}$−N−C (analogus to K−N−C in PIH) was $142.4(4)°$, whereas the angle made by the more covalent $Mn^{LS}$−C−N was closer to linearity at $167.0(4)°$.

Analysis of the atomistic configurations allowed each individual Fe−C−N and K−N−C angle to be calculated and for the distributions of these angles in the high, intermediate and low temperature phases to be compared.

For each converged configuration, the Fe−C−N and K−N−C angles were calculated, binned in 1° increments, corrected by dividing by $\sin\theta$, before being normalised. Figure 5.29 shows the calculated distributions of the data as points, and their corresponding Gaussian fits as lines.

There are two features of particular interest in figure 5.29, firstly the distribution of angles of the K-centred octahedra is broader than the Fe-centred octahedra - consistent with the Rietveld results and the analysis of **b** and the Mn analogue - and secondly the distribution of metal cyanide angles in the intermediate temperature phase is noticeably narrower than the distribution of angles in either the high or low temperature phase.

The standard deviation, $\sigma$, of the fits, as a function of temperature for both K-centred and Fe-centred polyhedra given in figure 5.30, and shows the significant change in framework rigidity between the intermediate temperature phase and the high and low temperature phases.

Figure 5.29 shows that the distribution of both Fe−C−N and K−N−C angles narrows in the intermediate temperature phase, indicating the framework is more rigid in the intermediate temperature phase than it is in either the high or low temperature phase.

### 5.6.3 Lattice parameters

As the atomistic configurations had shown different behaviour of the framework in the intermediate temperature phase, it was decided to analyse the change in lattice parameters of PIH as it passed through both the high to intermediate and intermediate to low temperature phase transitions.

In order to directly compare lattice parameters across all temperatures, the $R\bar{3}m$ unit cells were expressed in terms of the $C2/c$ unit cell. The `STRUCTURE RELATIONS` program of the Bilbao crystallographic server [115] was used to calculate the transformation matrix between the $R\bar{3}m$ and $C2/c$ phases.

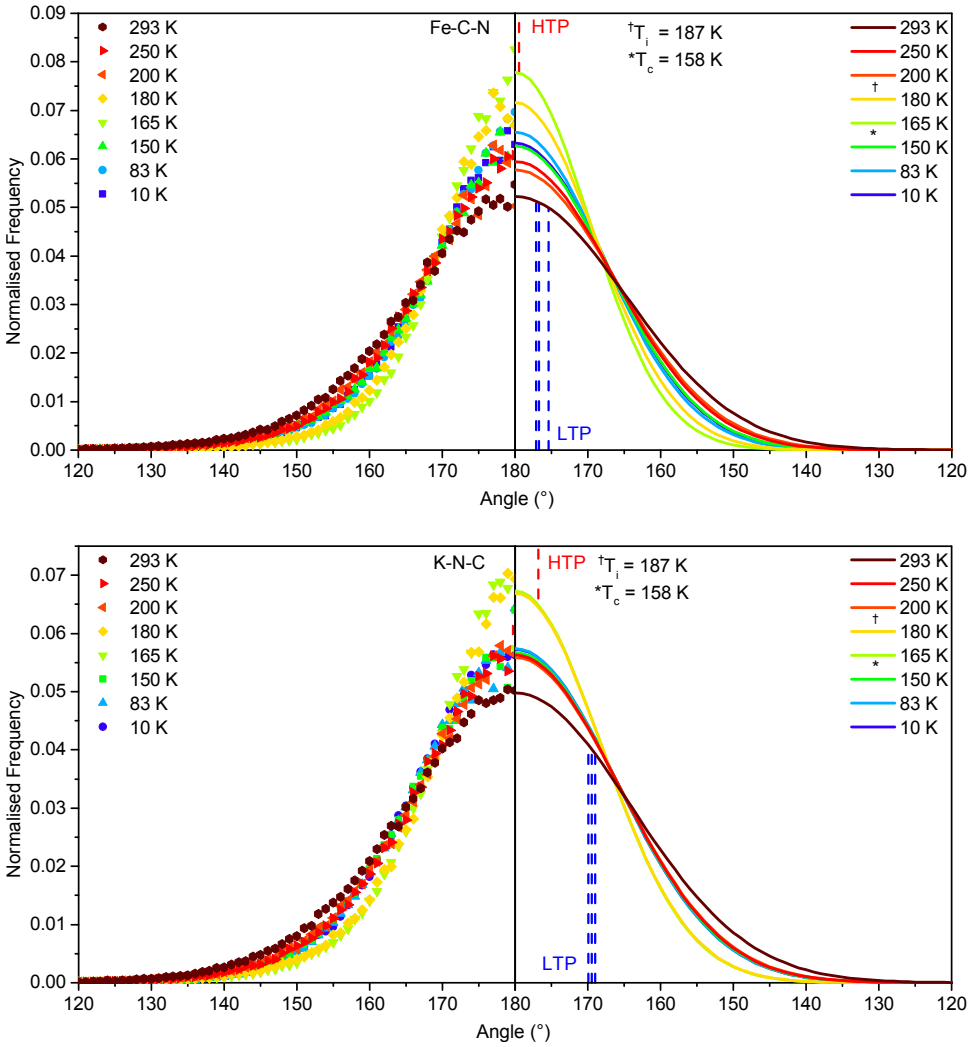


**Figure 5.29:** Distribution of angles around the Fe—Cx—Nx (top row) and K—Nx—Cx (bottom row). Left: Model data. Right: Gaussian fit. The disribution of angles appears to be much sharper for the two data sets in the intermediate temperature phase. Dashed lines indicate the corresponding angles from the average structure for the high and low temperature phases.

In the $R\bar{3}m$ phases, $\alpha = \beta = 90°$ and $\gamma = 120°$, therefore the lattice parameters for the $R\bar{3}m$ phases as expressed in terms of the $C2/c$ lattice are

$$[\mathbf{a}_m, \mathbf{b}_m, \mathbf{c}_m] = \begin{bmatrix} \frac{a+\frac{b}{2}}{3} & a - \frac{b}{2} & -a - \frac{b}{2} \\ \frac{-b\sqrt{3}}{6} & \frac{b\sqrt{3}}{2} & \frac{b\sqrt{3}}{2} \\ \frac{2c}{3} & 0 & 0 \end{bmatrix}, \tag{5.4}$$

and the angle $\beta$ calculated by

$$\sin\beta = \frac{|\mathbf{a}_m \times \mathbf{c}_m|}{|\mathbf{a}_m||\mathbf{c}_m|}. \tag{5.5}$$

Figure 5.31 shows the change in lattice parameters $a$, $b$, $c$, and $\beta$ with temperature, the values are given in table B.2. The grey dashed lines indicate $T_c$ and $T_i$. Upon heating, expansion is seen along the $a$ and $c$ axes, and contraction along the $b$. Sharp discontinuities in

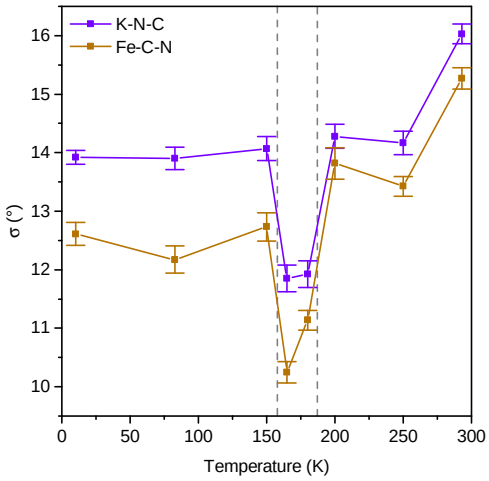


**Figure 5.30:** Standard deviation $\sigma$ for the metalbond1cyanide angle distribution of the K-centred (purple) and Fe-centred (brown) octahedra. Across all temperatures the distribution of angles is narrower in for the K—N—C angles, showing more deformation about the K site. For both sites, the distribution narrows in the intermediate temperature phase. Error bars show 95% confidence limit of $\sigma$.

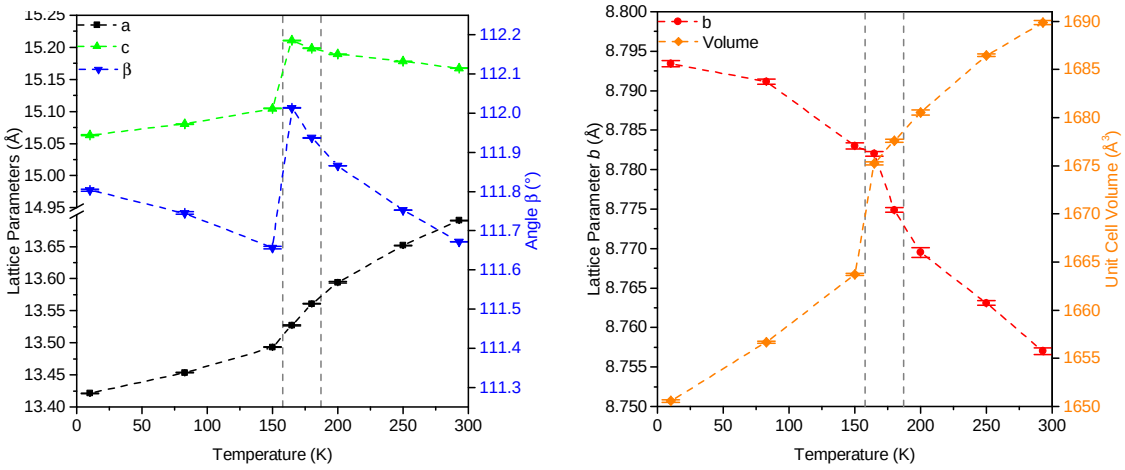


**Figure 5.31:** Left: Lattice parameters $a$, $c$, and $\beta$ through the high, intermediate, and low-temperature phases. Right: the $b$ lattice parameter and calculated unit cell volume. Unlike all the other parameters, there is a contraction along the $b$ axis on heating.

all parameters at temperatures below 165 K confirm the $R\bar{3}m$ to $C2/c$ transition is first-order in nature. The change in $\beta$ between 158 K and 187 K appears to differ from the change above 187 K which could be an indication of the intermediate to high temperature phase transition.

Observation of the change in lattice parameters, shows that there is a small change in the rate of contraction and expansion of the lattice between the high and intermediate temperature phases, with the largest indicator of an intermediate temperature phase being the change in angle $\beta$.

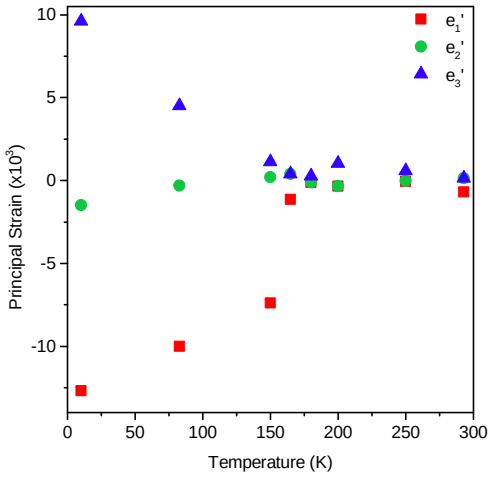


**Figure 5.32:** Principal components of the strain tensor based on the lattice parameters of PIH under the assumption that there is no intermediate temperature phase. Unlike DMMnF (figure 3.13) we see that above the single proposed transition temperature, the components are non-zero. This indicates that there may be an additional transition between 150 K and 293 K.

### 5.6.4 Spontaneous strain

From the lattice parameters, the spontaneous strain was calculated using the method outlined in 3.4.2. Strain analysis was performed to look for evidence of the proposed high to intermediate phase transition.

Linear extrapolation of the lattice parameters were performed under two assumptions. The first assumption was that there was no intermediate temperature phase, and that all data for $T > 150\,\mathrm{K}$ was from a single phase, the second assumption was that the intermediate temperature phase existed.

Figure 5.32 shows the principal components of the strain tensor under the first assumption when no intermediate-temperature phase is assumed. If there is no intermediate-temperature phase, then the principal components of the strain for $T > 150\,\mathrm{K}$ would be approximately zero, however figure 5.32 shows an unwanted discontinuity at 200 K.

The principal components were then re-calculated based on the assumption that there was an intermediate temperature phase, this meant that the analysis could be performed on the high to intermediate phase transition between 165 K and 293 K and the intermediate to low temperature phase transition between 10 K and 180 K. Figure 5.33 shows the principal components for the high to intermediate-temperature phase (left) and the intermediate to low-temperature phase (right). When the high to intermediate-temperature phase graph is observed we see that there is a definite deviation in all three parameters, with the strain along the high-temperature phase $e'_3$ decreasing, and the strain along the high-temperature phase $e'_1$ and $e'_2$ increasing. When the principal components of the high to intermediate phases are compared to those of the intermediate to low temperature phases we see how subtle the high to intermediate transition is, the magnitude of the components are $\approx \frac{1}{10}$ the magnitude of those for the phase change with associated symmetry change.

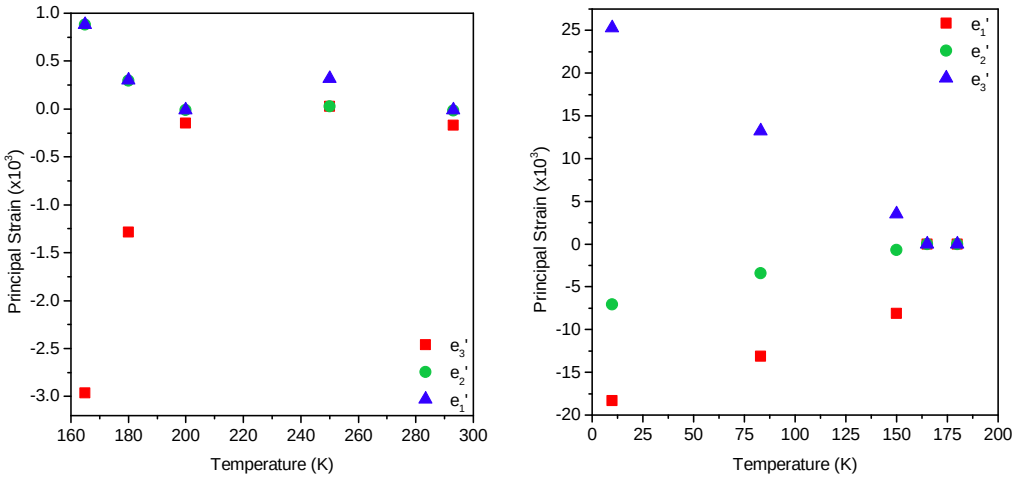


**Figure 5.33:** Left: Principal components of the strain tensor for the high to intermediate temperature phases. Right: Principal components of the strain tensor for the intermediate to low temperature phase. The phase change at 158 K with the accompanying change in symmetry shows significantly more change in the components than 187 K transition.

### 5.6.5 Strain with respect to the unit cell

The magnitude and direction of the spontaneous strain were then calculated and expressed as vectors on a structural representation of a pseudo-cubic PIH cell. Figure 5.34 is a representation of a PIH pseudo-cubic cell, with the imidazolium cation in the centre. For both the high to intermediate (left in figure 5.34) and the intermediate to low (right in figure 5.34) transitions, the spontaneous strain is shown. The blue arrows correspond to a contraction and the red to an expansion.

For the high to intermediate transition we see that there is a contraction perpendicular to the imidazole ring with no corresponding expansion. This is consistent with analysis of the distribution of metal cyanide angles which saw a stiffening of the framework during the intermediate temperature phase.

For the intermediate to low temperature phase transition, a contraction approximately parallel to the imidazole ring is observed, and a corresponding expansion approximately perpendicular to the ring. This suggests that the framework is somewhat rigid through this phase transition. The contraction parallel to the ring, corresponds to the framework contracting about the now static imidazolium cations.

### 5.6.6 Volume inside the pore

Systematic analysis of pore volume in frameworks with general formula $[(CH_3)_nNH_{4-n}]_2[KFe(CN)_6]$ [111] (where $n = 2$ is **A**) found that the volume inside the pore was dependent on the cation present. The larger the cation, the larger the pore. This is not unexpected as the synthesis route for MOFs such as DMMnF indicates that framework is templated by the cation, rather than a specific framework producing a set pore size [80].

However the pore size is also related to the metal centres, $Fe^{3+}$ is larger than $Co^{3+}$, therefore the K···Fe distances in both **A** and PIH are greater than the K···Co distances in **C** and **B** (see

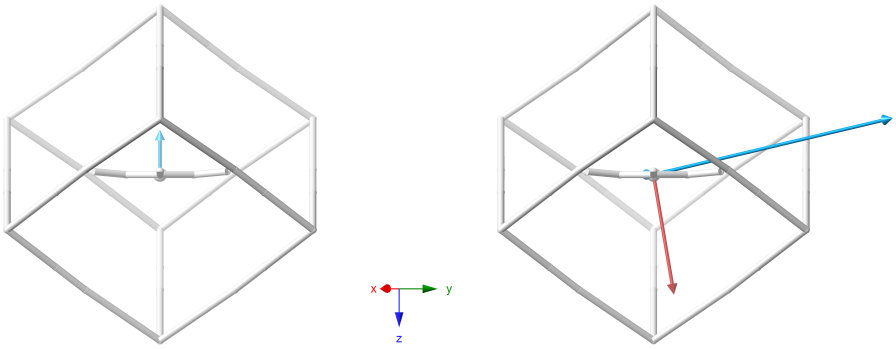


**Figure 5.34:** One pore of PIH in the high-temperature phase shown as a stick frame with the directions of the spontaneous strain shown. Blue arrows correspond to contraction along the specified vector, and red to expansion. Left: Spontaneous strain during the high to intermediate temperature phase transition. We can see that there is significant contraction of the cell perpendicular to the plane of the imidazole ring with no small associated expansion in the plane of the ring. Right: Spontaneous strain between the intermediate and low temperature phase transition. There is expansion of the framework approximately perpendicular to the plane of the imidazole ring, and a significant contraction in the plane of the ring, corresponding to the framework contracting around the now ordered cation.

table 5.1). The increased volume of the pore in the Fe analogues, when guest cations are held as the same, means that a weaker guest-framework interaction are expected, when compared to their equivalent K/Co frameworks. This weaker interaction means that $T_c$ for **A** is lower than $T_c$ for the Co equivalent, **C**.

A similar trend is observed with $T_i$ of PIH and **B** with the Fe-based framework having the lower transition temperature. However, the intermediate to low temperature phase transition, $T_c$, does not follow the same pattern. While the intermediate temperature phase of **B** spans 86 K, the intermediate temperature phase for PIH spans only 29 K. In order to understand this, the fractional change of the rhombohedral $c$ axis (the axis where there was a change in spontaneous strain) for PIH and **B**, shown in figure 5.35, were examined.

From figure 5.35 it can be seen that for PIH the contraction of the $c$ lattice parameter is slower in the high-temperature phase than it is in the low-temperature phase. However for **B** the contraction of the $c$ lattice parameter is faster in the high-temperature phase than it is in the low-temperature phase.This difference in contraction rates between PIH and **B** means that the strain along the $c$ axis between the high and intermediate temperature phase transition acts in opposite directions for each material.

In the intermediate temperature phase the PIH unit cell contracts quicker than **B**, therefore the volume available for the imidazolium cation in PIH to rotate in decreases quicker than it does for **B**. The faster the reduction in pore volume, the shorter the temperature range will be over which the imidazolium will be frozen into place by contraction of the framework. So while the temperature of $T_i$ follows the trend observed with **A** and **C**, the volume inside the pore, and hence the rate of cell contraction, dictates the $T_c$. Analysis presented earlier in this chapter on the distribution of imidazole rings in the unit cell has indicated that hydrogen bonding not does affect the dynamics of the guest cation, but it is worth noting that in this section the contraction rates of a hydrogenated Co analogue, **B**, are being compared to the contraction rates of fully deuterated PIH. The author believes though that this does not change

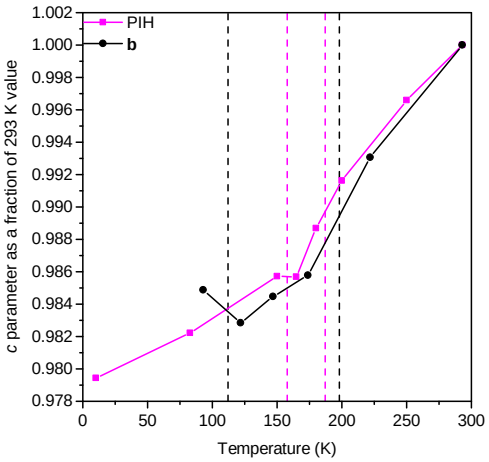


**Figure 5.35:** The change in the $c$ lattice parameter for PIH (pink) and b, Imid K/Co, as a fraction of their high temperature value expressed in terms of the $R\bar{3}m$ lattice. The two transition temperatures are highlighted as dashed lines.

the conclusion of this section. The change of the volume inside the pore indicates that $T_c$ depends on the pore volume while $T_i$ depends on the rate at which the pore volume changes with temperature.

## 5.7 Evidence for the intermediate-temperature phase summary

In this section lattice parameters, spontaneous strain and framework distortions from atomistic configurations and Rietveld refinements of PIH have been analysed and compared to other PBAs. Evidence of the intermediate phase was found in the form of the framework stiffening between 187 K to 158 K, which was corroborated by analysis of the spontaneous strain derived from the lattice parameters. The smaller temperature range for the PIH intermediate temperature phase, when compared to a K/Co analogue is proposed to be due to the increased rate of contraction of the $c$ lattice parameter of PIH.

## 5.8 Conclusion

In this chapter total scattering and RMC studies were performed on a Prussian blue analogue, PIH, to look for the onset of electric ordering of imidazolium rings at temperatures above the dielectric transition, and to look for evidence of and mechanisms behind the intermediate temperature phase.

In both the high and intermediate temperature phases, the disordered imidazolium cation shows no preference for any particular orientation during refinement indicating that the ordering process does not gradually set in. Unlike the K/Co analogue, **B**, the imidazolium in PIH are observed to tilt about their centre of rotation over all temperature phases, with the higher-temperature models reporting a wider range of tilt angles. There is no evidence that the guest cations behave differently in the intermediate temperature phase than they do in the high temperature phase.

In PIH the $KN_6$ octahedral units can better accommodate a wider range of internal angles than the $FeC_6$ units, due to the weaker K−N bond, however over all temperatures the polyhedra are not significantly distorted. This behaviour has been observed in PBA analogues **A**-**C**, but not by these methods. Comparisons between **A** and **C**, and **B** and PIH has shown how substitution within the framework can affect bulk properties.

Evidence for the presence and nature of the intermediate temperature phase was seen though analysis of the distribution of metal−cyanide angles, and via analysis of the spontaneous strain. The K−N−C−Fe framework is observed to distort, with the K−N−C and Fe−C−N angles deviating from 180°. The deformation of the framework is significantly less pronounced in the intermediate temperature phase. This indicates the mechanism for thermal expansion changes between in intermediate temperature phase and the high temperature phase. In the high temperature phase the framework is readily deformed around the imidazolium, however between 158 K to 187 K the framework becomes more rigid, but the imidazolium still rotates within the pore. In the low temperature phase, imidazolium cations are ordered the framework distorts around them.

The smaller temperature range of the intermediate temperature phase in PIH when compared to the K/Co analogue, **B**, is attributed to the faster rate of contraction of the cell along the rhombohedral *c* axis. This contraction effectively traps the PIH imidazolium quicker than the contraction along the same axis in **B**.

# Chapter 6

# Triglycine Sulfate

## 6.1 Introduction

The final material investigated was triglycine sulfate (TGS). Ferroelectricity in TGS was first reported by Matthias et al. in 1956 [116], and it is one of the most widely studied ferroelectrics. Despite this, the driving force behind the ferroelectric phase transition is still a contentious issue, with two possible mechanisms proposed which may be interconnected. Total neutron scattering measurements were taken of TGS above and below the phase transition, with the aim that the atomistic configurations generated could identify the dominant mechanism behind the onset of ferroelectricity. The analysis of TGS presented in this chapter has been performed to help understand how the atomic motions which govern each of the proposed mechanisms change as TGS approaches the phase transition, and to understand if one of these motions is the driving force behind the phase transition.

## 6.2 The material

TGS, $(NH_3CH_2CO_2)_3H_2SO_4$, is a room temperature organic ferroelectric [116], with applications including thermal imaging and detectors for IR spectroscopy. However TGS is also an interesting material in its own right due to it being one of the few room temperature ferroelectrics to undergo a second order phase transition [117]. Figure 6.1 shows the expected change in polarisation for first and second order phase transitions on the left, with the observed change in polarisation for TGS on the right. We see that for TGS there is a continuous change in polarisation as $T_c$ is approached.

TGS contains three glycine molecules, identified as GI, GII, and GIII (right in figure 6.2). Above $T_c$ TGS has $P2_1/m$ symmetry, with GII and GIII equivalent to each other due to the mirror plane (dashed line in figure 6.2). Between the COO groups of GII and GIII lies an "intermediate" hydrogen (beige in figure 6.2, right) which, in the high-temperature phase, has two equilibrium positions either side of the mirror plane, each with a 50% occupancy [120]. In addition to the intermediate hydrogen; the GI $NH_3^+$ head is dynamically disordered about the mirror plane [121–123], with a 50% occupancy on either side of the plane corresponding to the energy minima of the double-well potential of the $NH_3$ head displacement [124]. Figure 6.3 shows the motion of the disorder of the GI head and the intermediate hydrogen in the high-temperature phase.

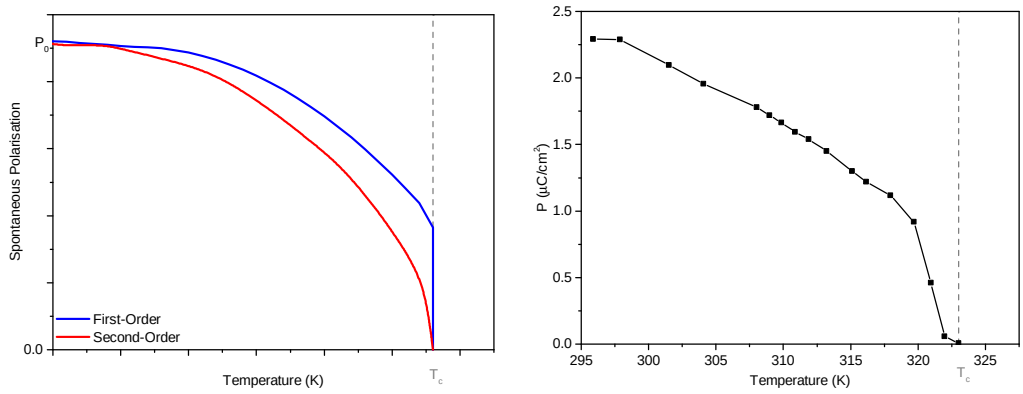


**Figure 6.1:** Left: Change of an order parameter, in this case the spontaneous polarisation, as a function of temperature for a typical first-order transition (blue) and a second-order transition (red). Right: Change in the spontaneous polarisation of (fully hydrogenated) TGS along the polar axis extracted from [118] using [119] with a reported $T_c$ of 323 K. We see that the phase transition for TGS is second order with a continuous change in order parameter as $T_c$ is approached from below.

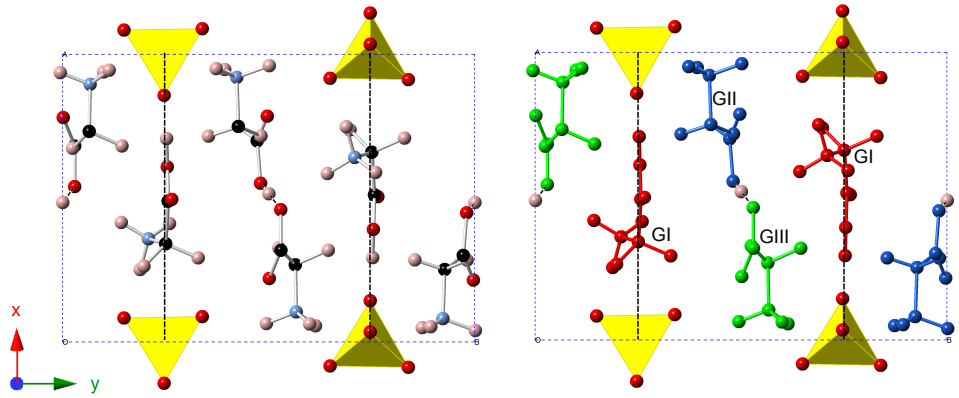


**Figure 6.2:** Triglycine sulfate at room temperature with space group $P2_1$ with unit cell shown as blue dashed lines, and approximate position of the mirror plane shown as black dashed lines. Left: TGS with blue nitrogen, black carbon, red oxygen and pale pink hydrogen/deuterium with $SO_4$ tetrahedra. Right: TGS with glycine molecules colour coded. Red: GI. Blue GII. Green GIII. Bonding between GII, the intermediate hydrogen, and GIII is shown by dashed lines between the atoms.

Below $T_c$ the mirror plane is lost, the intermediate hydrogen preferentially bonds to either GII or GIII and the disordered GI $NH_3$ head becomes ordered. It is the long range ordering of the GI $NH_3$ head which provides the spontaneous polarisation along the ferroelectric $b$ axis.

The interactions between the GI head and the intermediate deuterium as the phase transition is approached are not well understood. There are two proposed mechanisms for the driving force behind the phase transition. Firstly that the dipole-dipole interactions between neighbouring $NH_3^+$ heads drive the phase transition [125, 126], and that the intermediate hydrogen only plays a secondary role [127]. Or secondly, that the ordering of the intermediate hydrogen plays a crucial role in initiating the phase transition [128].

Total neutron scattering data were collected on a fully deuterated TGS sample. In section 1.1.4, the effect of substitution of hydrogen with deuterium on the transition temperature of a ferroelectric when proton transfer is the mechanism behind ordering was discussed. In the

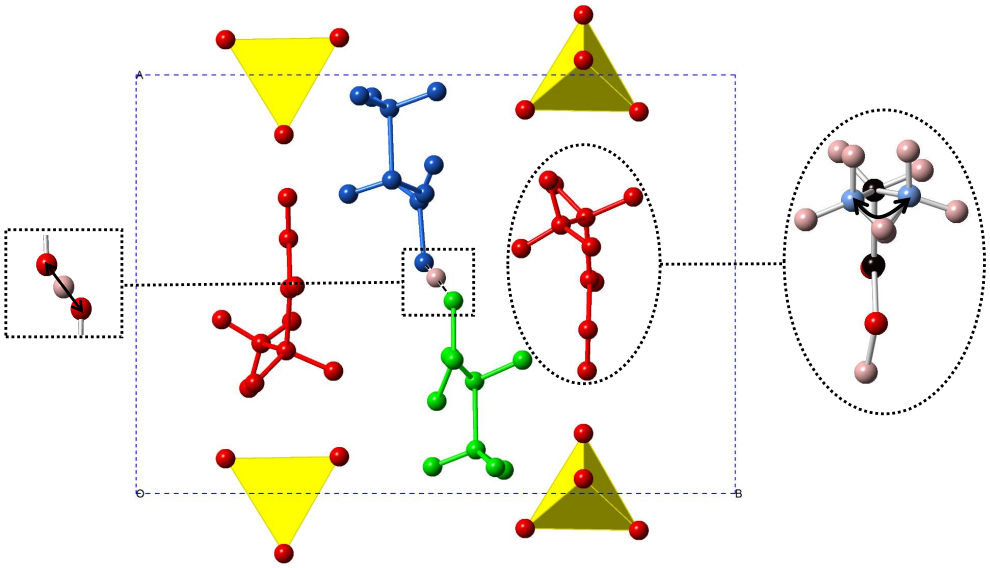

**Figure 6.3:** TGS with glycine GI is red, GII blue, and GIII green. The intermediate hydrogen in shown between the GII and GIII molecules. left insert: disorder of the intermediate hydrogen, right insert: disorder of the GI $NH_3$ group.

example given $T_c$ of KDP increased by approximately 90 K, but for TGS $T_c$ only increases by 12 K from 322 K to 334 K upon deuteration [129].

When the structure of TGS is analysed under applied electric fields, however, the position of the intermediate hydrogen is found to be correlated with the GI head orientation [130]. This observation does not tell us if the intermediate hydrogen bond ordering is driving the phase transition or simply responding to it.

A possible mechanism linking intermediate hydrogen bond ordering with GI $NH_3$ head motions has been proposed by Choudhury et al. [124]. In the low-temperature phase the GI $NH_3$ head will point in a specific direction (right in figure 6.4). The swing of the GI head brings it closer to the COO group of GIII ($N\cdots O = 2.8$ Å) shown as a long orange arrow in figure 6.4. The hydrogen bonding between the GI head and GIII means the GIII has less electron density to contribute to the hydrogen bond between GII and GIII, which in turn causes the intermediate hydrogen to form a shorter, stronger hydrogen bond with the COO group of GII (short orange arrow in 6.4). As the COO group of GII is now bonded to the intermediate deuterium, there is no electron density to contribute to forming a hydrogen bond with the next GI (pink dashed lines), and so the next GI $NH_3$ head points in the same direction as the first one. This trend propagates along the chain aligning the dipole moments of the GI head with each other via the intermediate hydrogen. For the structure shown in figure 6.4 this would correspond to all the GI heads pointing in the $-y$ direction and the intermediate hydrogen forming short hydrogen bonds with glycine GII.

Diffuse x-ray and neutron scattering studies on TGS [131, 132], have reported that between $T_c$ and $T_c - 40$ K, short range correlations between the GI heads are observed and at

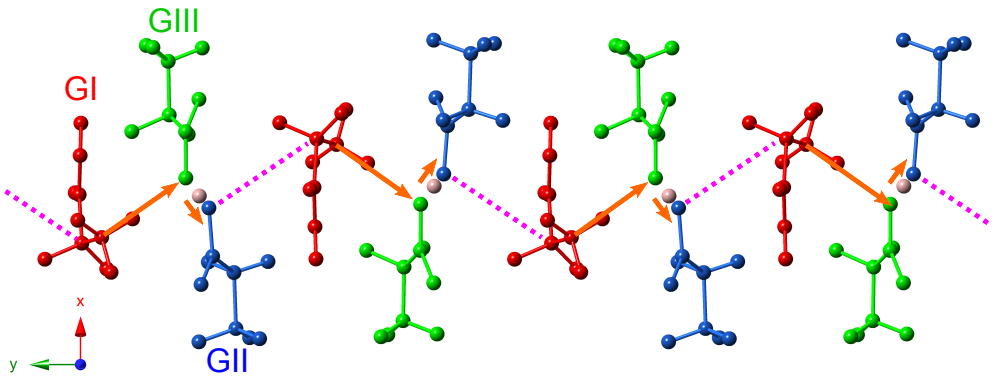


**Figure 6.4:** A proposed ordering for GI heads and the position of the intermediate hydrogen between GII and GIII. Orange arrows show the direction of the favoured hydrogen bonding and pink dashes the bonds which cannot form as a result of the GI head orientation/lack of electron density on the glycine COO tail.

temperatures below $T_c - 40\,\mathrm{K}$ the GI heads display long-range ordering. However scattering data presented in this thesis was only collected to $T_c - 40\,\mathrm{K}$. The structure of TGS has also been analysed using neutron diffraction methods [121, 127, 129, 132, 133], to the author's best knowledge, the work presented in this chapter is the first neutron total scattering study performed on TGS. The aim of performing total scattering experiments coupled with RMC modelling is to understand how the series of hydrogen bonds, which connect the molecules inside TGS, change as $T_c$ is approached, and to offer a mechanism behind the phase transition.

## 6.3 Experimental

In this section the synthesis, data collection, and processing prior to application of the RMC method will be discussed. Full details of collection run numbers are given in section A.3.

### 6.3.1 Synthesis

Fully deuterated TGS was synthesised following the first step of the procedure given in [118] and [134]. Reagent lot numbers and chemical purity results are given in A.3.1. 5.01 g of $C_2D_5NO_2$ was dissolved in 50 ml of $D_2O$ and the solution stirred continuously and held at 55 °C for 15 minutes before addition of 1.2 ml of sulfuric acid. The solution was held at 55 °C for an additional 10 minutes. The solution was taken off the heat and 15 g of deuterated ethanol immediately added. Small crystals were observed in the solution approximately ten minutes after addition of the ethanol. The solution was covered and left at room temperature for three days, after which 1.65 g of product was recovered by vacuum filtration. The mother liquor was retained, and 30 ml of deuterated methanol added to it. Immediately precipitate was visible. The methanol solution was left at room temperature for 5 hours, and 4.63 g of pale yellow crystals recovered by vacuum filtration. The methanol-extracted crystals were dried in a vacuum oven for 5 hours, the sample temperature did not exceed 50 °C during the drying procedure. 2.29 g of the product ($\approx 6.74$ mmol) was used during the scattering experiment.

### 6.3.2 Data collection

Variable temperature neutron total scattering data were collected at the ISIS facility using the POLARIS diffractometer. The experimental proposal outlined a collection run in the furnace to cover the 334 K phase transition. It was also possible to collect scattering data between 110 K and 150 K to investigate a possible low-temperature phase transition at 143 K [135] full analysis of the low-temperature scattering data has not been performed due to time restrictions.

Total scattering data were collected for a minimum total proton beam charge of 900 µA h upon heating, at 293 K, 303 K, 323 K, 343 K, 365 K, and 403 K. Short runs were collected in 5 K intervals between 323 K and 365 K in order to calculate the lattice parameters through the phase transition. Details of the run numbers along with the measured sample temperature are given in table A.6.

### 6.3.3 Rietveld refinement

GSAS [42] and the EXPGUI interface [43] was used to analyse the diffraction data and extract the cell parameters. The initial structure which was refined against the low-temperature phase data was taken from a room temperature neutron derived structure [136], and modified by addition of a mirror plane and small atomic movements to generate a $P2_1/m$ initial configuration. Bond length and angle restraints as outlined in tables 6.1 and 6.2 were applied at the beginning of the refinement and their weighting reduced in accordance with the reported $\chi^2$ from the detector banks.

| Bond type | Restraint length /Å |
|---|---|
| C−O | 1.248 |
| C−C | 1.519 |
| N−D | 1.046 |
| C−N | 1.480 |
| C−D | 1.046 |
| S−O | 1.470 |

**Table 6.1:** Bond length restraints applied during $P2_1/m$ and $P2_1$ GSAS refinement.

| Atoms | $\theta_0$/° |
|---|---|
| D−N−D | 109.5 |
| D−C−D | 112.5 |
| O−C−O | 126.0 |

**Table 6.2:** Bond angle restraints applied during $P2_1/m$ and $P2_1$ GSAS refinement

Figure 6.5 shows the observed Bragg profile for TGS over the phase transition. There are subtle changes in the intensity of the $(120)$ peak at 5.14 Å as TGS is cooled, but no sharp peaks emerge or disappear below $T_c$. However the lattice parameters, presented in section 6.4.1, show discontinuities at $T_c$, confirming the presence of a phase transition.

During refinement, detector banks 2–5 were refined simultaneously, the background for the scattering data were modelled as ten-term shifted Chebyshev polynomials, and the peak shapes were fit using the GSAS type 3 profile. For all detector banks, the high and low $d$-spacing

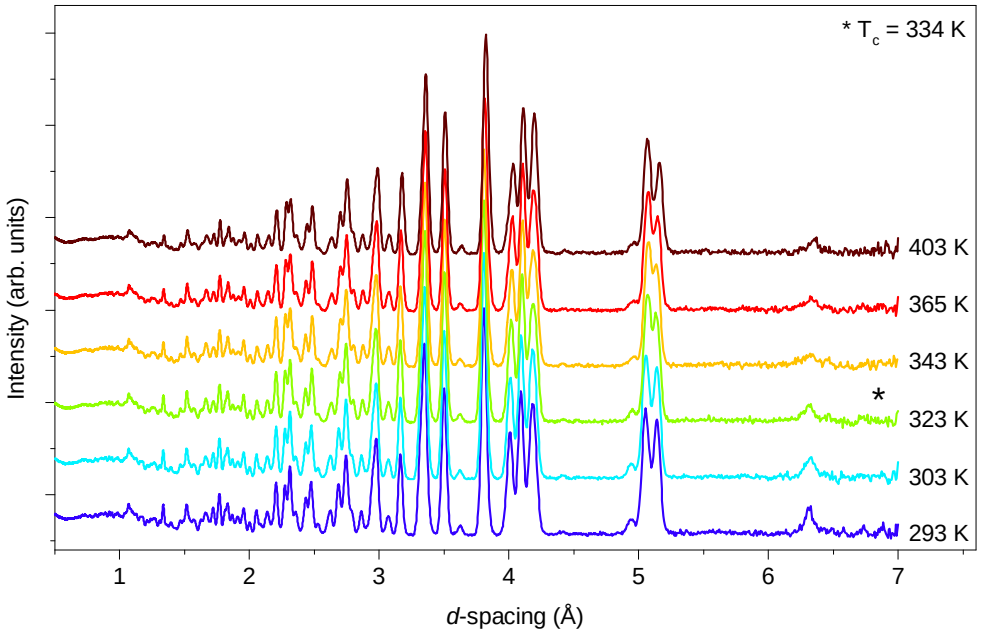


**Figure 6.5:** The observed Bragg profile for POLARIS bank 3 ($2\theta = 40°$ to $67°$) over all furnace-collected temperatures. Upon cooling the intensity of the $(120)$ peak at 5.14 Å appears to increase, however no peaks are observed to appear or disappear below the phase transition.

cut-offs were chosen so the profiles did not terminate mid-way though a peak, and to ensure the program was only fitting against peaks of interest, it was for this reason that bank 1 was not used during refinement.

Least squares refinement was carried out by varying the parameters in the following order; background and scale, followed by the unit cell parameters, DiffA, the atomic positions, $U_{\text{iso}}$, and finally the peak shape parameters $\sigma_1$ and $\sigma_2$.

Figure 6.6 shows a comparison of the observed Bragg profile for the 293 K data for POLARIS banks 2 and 3 over the $d$-spacing range 3.2 Å to 6.5 Å. Bank 3 was chosen to be used for RMCProfile refinement due to it having better resolution of peaks, most notably at approximately 4.2 Å where the large broad peak in the bank 2 profile has been resolved into three distinct peaks.

For the high-temperature phase, trials were run allowing the occupancy of the GI disordered $ND_3$ group to vary, and it was found that the models retained the 50 : 50 occupancy on both sites.

A representative Rietveld fit for the high and low-temperature data is shown in figure 6.7. A feature of particular interest is the $(220)$ peak at $\approx 3.61$ Å which is present (and allowed and expected) in the observed profiles of the high and low-temperature phase, but is absent in the fit of the high-temperature phase. It is interesting to note that the high-temperature phase, where the disorder in the GI head position is included, that the 220 peak intensity is not filled, but in the ordered configuration it is.

Analysis of the Rietveld-derived unit cell found that in the low-temperature phase the intermediate deuterium exclusively formed short bonds of 1.16 Å to 1.19 Å in length with glycine GII, and long bonds of 1.31 Å to 1.33 Å with glycine GIII.

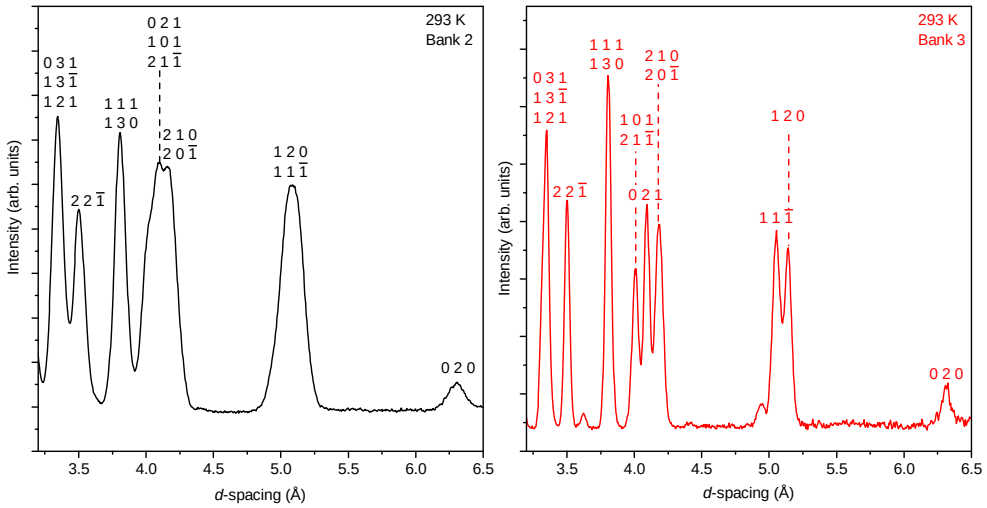


**Figure 6.6:** The observed Bragg profiles for TGS at 293K from POLARIS bank 2 ($2\theta = 19°$ to $34°$) shown in black, and bank 3 ($2\theta = 40°$ to $67°$) shown in red. The bank 3 profile shows better resolution than the bank 2, and is therefore used for RMC refinement.

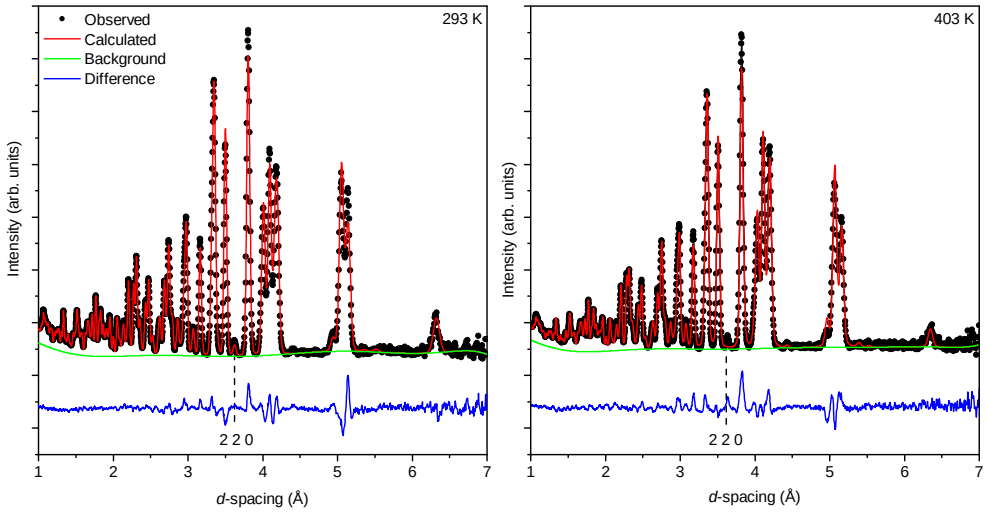


**Figure 6.7:** Representative GSAS fit for low (left) and high-temperature phase data. The $(220)$ peak in the high-temperature phase has not been fit by the model, however it is allowed and expected.

Rietveld refinement was performed on all total scattering data as well as on the shorter collection runs between 323 K and 365 K.

### 6.3.4 Pair distribution analysis

The scattering function and pair distribution functions were extracted from the raw data using GUDRUN. Run numbers for the data correction and individual temperature measurements are given in table A.6. The sample was assumed to be fully deuterated.

Detector bank 1 was not used to extract the PDF and scattering functions; the $Q$-range used for the other banks are given in table 6.3. Termination ripples in the real-space functions were suppressed though application of the broadening function (2.23b) where $\Delta_0$ was kept

constant at 0.02 Å. The shortest expected atomic bond was approximately 1.0 Å and so the minimum radius for Fourier transform was set just below it at 0.89 Å. The maximum radius was set to be 40 Å. The tweak factors and $\beta$ for the TGS refinements are given in table 6.4. The PDF was then normalised to $\langle b \rangle^2$.

| Bank # | $Q_{\text{min}}$ | $Q_{\text{max}}$ |
|---|---|---|
| 2 | 0.30 | 2.43 |
| 3 | 0.80 | 4.55 |
| 4 | 2.21 | 46.00 |
| 5 | 3.52 | 46.00 |

**Table 6.3:** Detector bank $Q$ ranges used for PDF and $i(Q)$ extraction in GUDRUN.

| Temperature /K | Tweak Factor | $\beta$ |
|---|---|---|
| 403 | 3.324 95 | 0.599 33 |
| 365 | 3.311 76 | 0.526 48 |
| 343 | 3.322 56 | 0.598 52 |
| 323 | 3.329 20 | 0.542 98 |
| 303 | 3.329 73 | 0.548 35 |
| 293 | 3.312 09 | 0.619 94 |

**Table 6.4:** Parameters used in GUDRUN to extract the $i(Q)$ and PDFs.

$D(r)$ for TGS up to 3.0 Å is shown in figure 6.8. Below 1.6 Å all peaks correspond to bonding within the glycine and $SO_4$ molecules. Between 1.6 Å and 3.0 Å the peaks correspond to distances between either neighbouring atoms within a single glycine molecule, neighbouring GII and GIII molecules, or the $ND_3^+$ head of GI and the $SO_4$.

No obvious systematic change in $D(r)$ as TGS passes through $T_c$ were observed. This is not unexpected as the transition is second-order. The magnitude of the D···O peak at 1.70 Å is of a similar size to the termination ripples present in the data. Therefore it is difficult to ascertain if there is any systematic loss or emergence of this peak upon heating. The peaks at low $r$ contain contributions from multiple atomic pairs. Attempts at increasing the power of the broadening function to minimise the noise at $\approx$ 1.70 Å led to the peak at $\approx$ 1.26 Å merging with that at $\approx$ 1.06 Å.

A list of the scattering power of each pair of atoms is given in table 6.5, where Oz is the O−H oxygen on GI, and Oh is oxygen in GII and GIII which can form hydrogen bonds with the intermediate deuterium. From table 6.5 we see that due to the number of deuterium atoms in TGS, the D, D correlations contribute most to the scattering, followed by D, O correlations, where the O is either on the $SO_4$ or the oxygen not involved in hydrogen bonding on GI, GII, and GIII.

### 6.3.5 Initial RMC configurations

The RMCProfile code was modified to include two artificial atoms, Oh and Oz (described in section 6.3.4). The addition of the two extra atoms allowed the partial pair distribution functions to be split, and the information pertinent to the GII/GIII interaction be readily

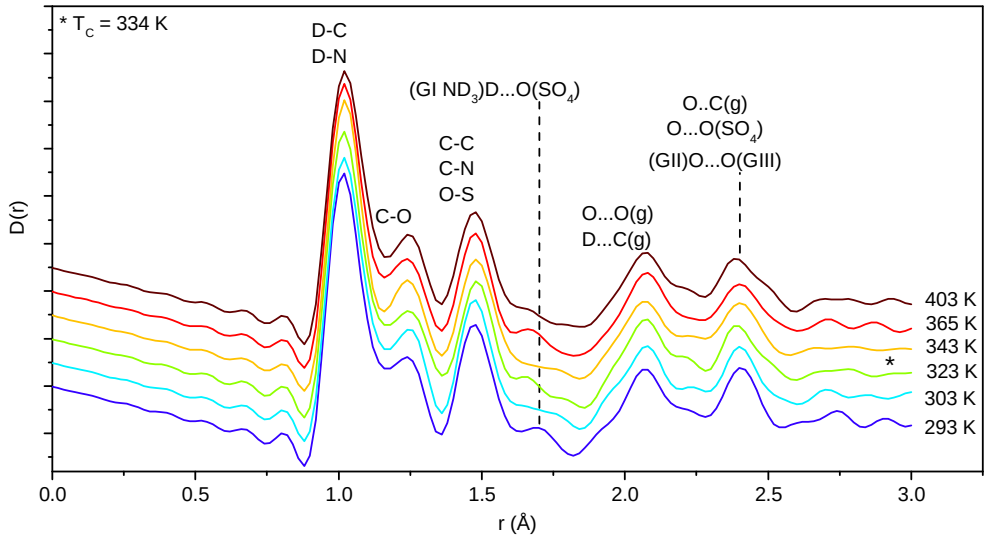


**Figure 6.8:** The experimentally derived D(r) for TGS with main peaks indexed. Brackets denote which molecule(s) each atom in the pair belong to with (g) referring to atomic pairs within the same glycine molecule.

| Atom pair $i$, $j$ | $b_i b_j c_i c_j$ (fm$^2$) | Atom pair $i$, $j$ | $b_i b_j c_i c_j$ (fm$^2$) |
|---|---|---|---|
| D, D | 9.395 | N, Oh | 0.238 |
| D, O | 3.365 | D, S | 0.236 |
| D, C | 3.303 | O, Oz | 0.172 |
| D, N | 2.326 | C, Oz | 0.169 |
| O, O | 1.205 | N, Oz | 0.119 |
| C, O | 1.183 | Oh, Oh | 0.098 |
| C, C | 1.162 | S, O | 0.084 |
| D, Oh | 0.961 | C, S | 0.083 |
| N, O | 0.833 | N, S | 0.058 |
| C, N | 0.818 | Oh, Oz | 0.049 |
| N, N | 0.576 | Oz, Oz | 0.025 |
| D, Oz | 0.481 | S, Oh | 0.024 |
| O, Oz | 0.344 | S, Oz | 0.012 |
| C, Oh | 0.338 | S, S | 0.006 |

**Table 6.5:** Faber-Ziman weighting factors for the partial pair distribution functions' contribution to the total PDF.

extracted. It also provided a way to apply different potentials to the two different C−O bonds in glycine.

The initial configuration was generated by replicating the Rietveld-derived unit cell along the $a$, $b$, and $c$ axes to produce a $5 \times 4 \times 9$ supercell (47 Å $\times$ 50 Å $\times$ 51 Å containing 13 320 atoms). The swinging motion of the GI $ND_3^+$ head in the high-temperature phase was approximated by randomly orienting the GI head either left or right along the $b$ axis relative to the glycine C/O "backbone" of the molecule. The partially occupied intermediate deuterium between GII and GIII were identified and replaced with one fully occupied deuterium mid-way between Oh···Oh of glycine GII and GIII.

Figure 6.9 describes the programs involved in producing the disordered high-temperature

phase initial configurations, and figure 6.10 shows the structures before and after application of the program.

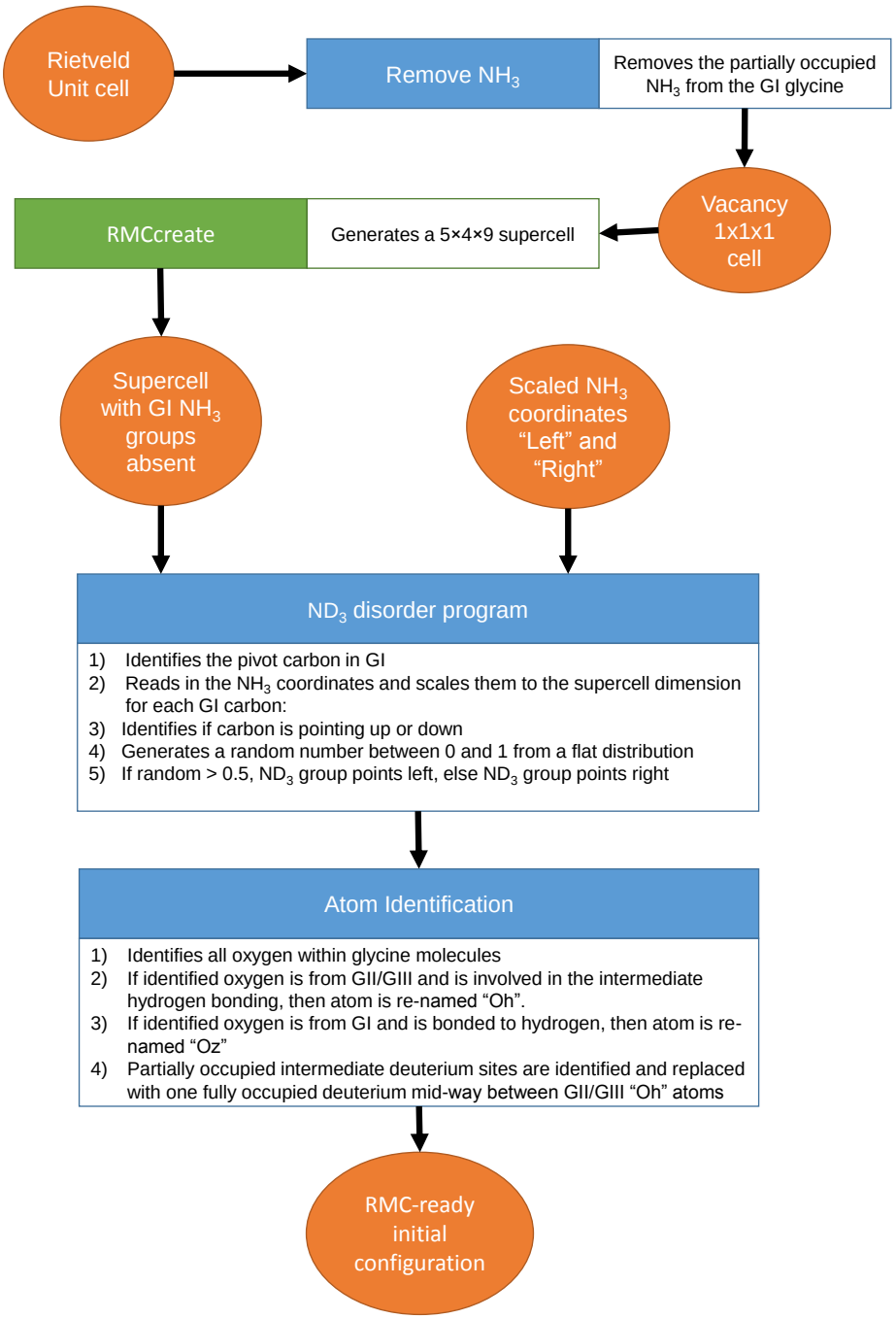


**Figure 6.9:** Process used to produce disordered high-temperature initial configurations, and to re-name specific atoms.

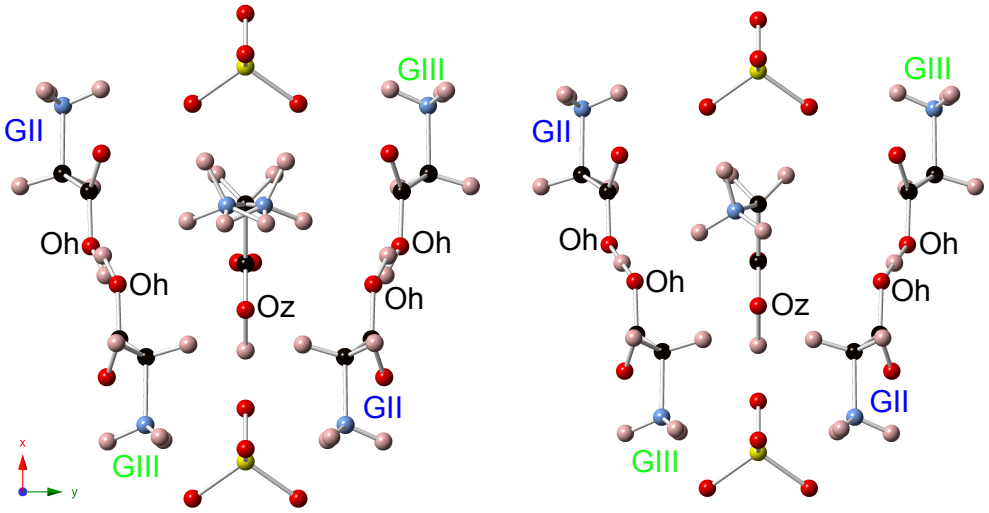


**Figure 6.10:** Left: A high-temperature phase configuration as produced by Rietveld refinement. The GI $ND_3$ head (centre) is disordered over two sites with $50\%$ occupancy of either site. The GII and GIII Oh atoms each have an intermediate deuterium (with $50\%$ occupancy) bonded to them. Right: Part of a configuration after application of the disorder program. The GI $ND_3$ atoms now have $100\%$ occupancy and are pointing in one of two directions. The two partially occupied intermediate deuterium between GII and GIII have been replaced with one, fully occupied deuterium mid-way between the two

### 6.3.6 RMC restraints

Bond bending and stretching potentials were selected from the MM3 set of potential parameters. As the motion of the intermediate deuterium was thought to be a significant feature in the onset of ferroelectric ordering, no Oh−D potential was applied. The values for the bond bending and stretching energies for $SO_4$ were not available and therefore were set to be as large as the strongest potentials used in the set.

| Atomic pair | $D$/eV | $r_0$/Å |
|---|---|---|
| D−C | 2.275 | 1.02 |
| D−N | 2.947 | 1.02 |
| D−Oz | 3.432 | 1.02 |
| C−C | 2.304 | 1.48 |
| C−N | 2.051 | 1.48 |
| C−O | 4.703 | 1.26 |
| C−Oh | 2.880 | 1.26 |
| C−Oz | 2.880 | 1.26 |
| S−O | 4.703 | 1.48 |

**Table 6.6:** Morse bond stretch potentials used to constrain RMC refinement.

In addition to the interatomic potentials, distance window constraints (outlined in table C.9) were applied. The maximum ($d_{\max}$) and minimum ($d_{\min}$) distances in the calculated unit cell were found, and the distance windows range was set between $d_{\min} - 10\%$ and $d_{\max} + 10\%$. No distance window restraints were applied to the Oh−D pair.

| Atoms | $k$/eV | $\theta_0$/° |
|---|---|---|
| D−N−D | 7.602 | 106.367 |
| D−N−C | 6.504 | 105.949 |
| N−C−D | 10.236 | 109.300 |
| N−C−C | 13.045 | 110.740 |
| D−C−D | 6.866 | 107.600 |
| D−C−C | 6.741 | 109.490 |
| C−C−O | 10.611 | 123.500 |
| C−C−Oh | 19.349 | 110.300 |
| C−C−Oz | 19.349 | 110.300 |
| O=C=Oh | 21.222 | 121.500 |
| O=C=Oz | 21.222 | 121.500 |
| O−S−O | 21.111 | 109.500 |

**Table 6.7:** Angle potentials used to constrain RMC refinement.

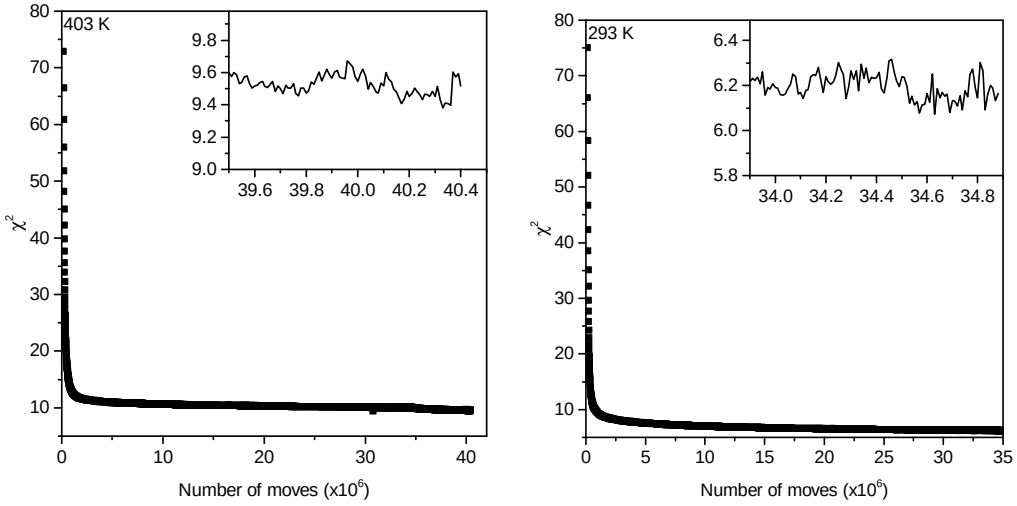


**Figure 6.11:** $\chi^2$ for $D(r)$ as a function of number of atomic moves for TGS in the high-temperature phase 403 K (left) and low-temperature phase 293 K (right)

### 6.3.7 Completion criteria

The high-temperature phase configurations were refined for approximately $45 \times 10^6$ atomic moves, and the low-temperature phase configurations refined for $35 \times 10^6$ atomic moves. This corresponded to 4 days of computing time, and 3000 moves per atom. $\chi^2$ as a function of number of atomic moves for $D(r)$ in the high and low-temperature phase is shown in figure 6.11.

### 6.3.8 Representative fits

Representative fits of $D(r)$ and the Bragg profile in the high and low-temperature phases are shown in figure 6.12. Unlike the GSAS fit in section 6.3.3, the high-temperature phase RMC configurations have filled some of the intensity of the $(220)$ peak at 3.61 Å.

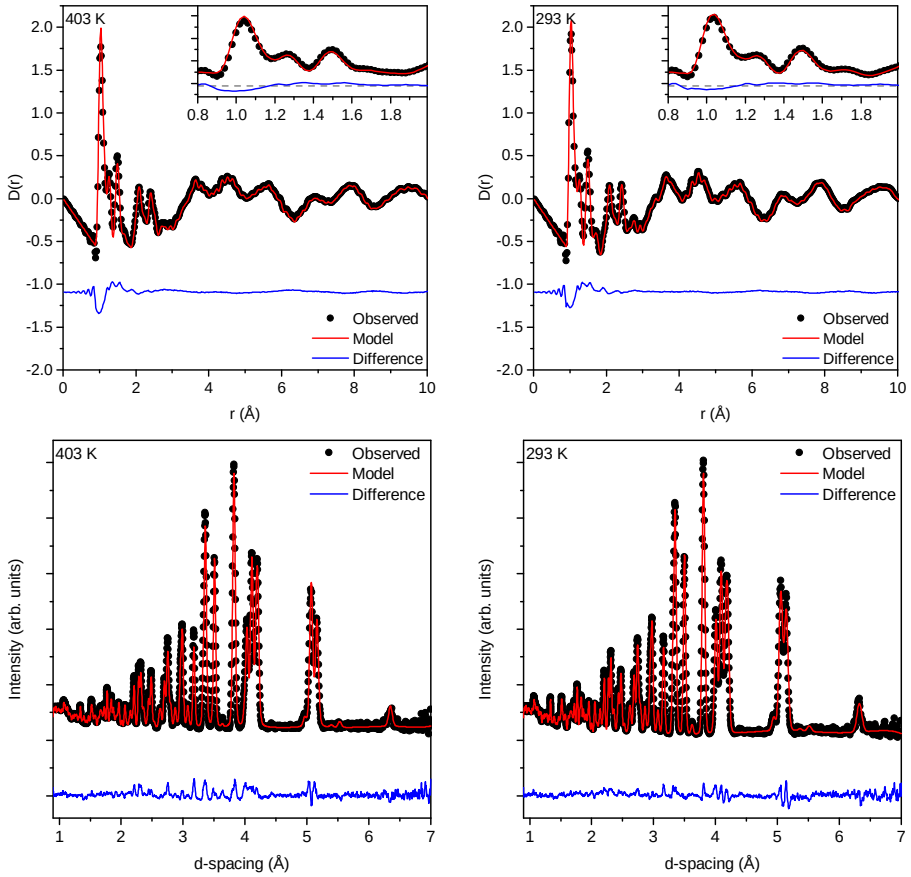


**Figure 6.12:** Top left: The observed (black dots) and calculated (red line) $D(r)$ for a high-temperature phase refinement with the offset difference in blue for $r \leq 10$ Å. Insert shows agreement between the low-$r$ peaks. Top right, the corresponding plot for a low-temperature phase refinement. Bottom row: The `RMCProfile` Bragg fit from converged configurations of TGS in the high (left) and low-temperature (right) phase. The high-temperature phase RMC Bragg fit has some intensity in the 220 peak unlike the corresponding Rietveld fit.

## 6.4 Analysis

When analysing TGS, I have focussed on looking for a correlation between the position of the intermediate deuterium, relative to GII and GIII, and the orientation of the GI $ND_3$ head.

### 6.4.1 Lattice parameters

While the Bragg profile and $D(r)$ show no obvious changes as TGS undergoes the dielectric transition, the lattice parameters do. As the only change in symmetry after the phase transition was the loss of the mirror plane, the lattice parameters of the $P2_1$ and $P2_1/m$ unit cells are directly compared.

Figure 6.13 shows comparable lattice parameters $a$, $b$, $c$, and $\beta$ as a function of temperature. We see that below $T_c$ there is a contraction along the $c$ axis and a small expansion along $a$. These values have been tabulated in B.4. As TGS cools towards $T_c$ there is significant contraction along the ferroelectric $b$ axis. Below $T_c$ TGS expands along the $b$ axis.

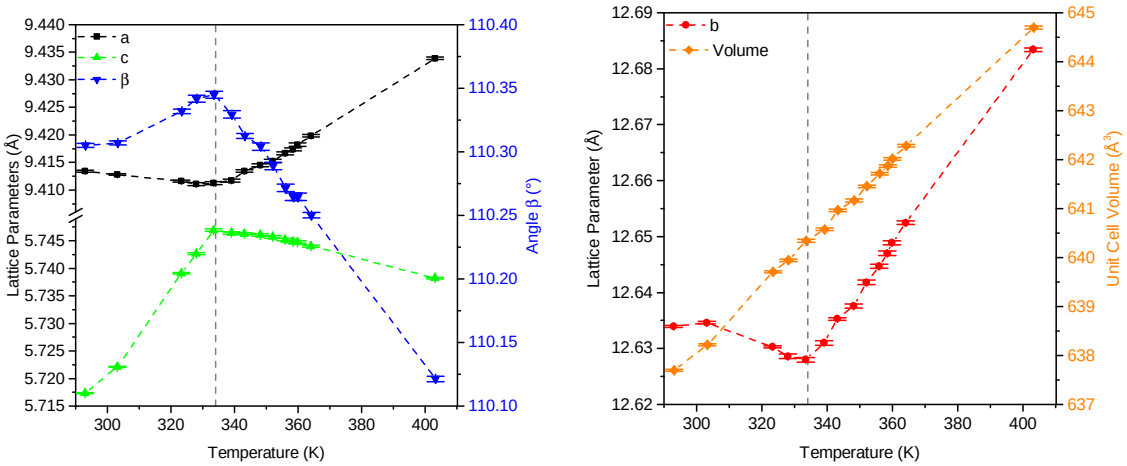


**Figure 6.13:** Left: Lattice parameters $a$, $c$, and $\beta$ in the high, and low-temperature phase from both total scattering data and short "diffraction only" runs. Right: The $b$ lattice parameter and calculated unit cell volume. Dashed line indicates the transition temperature $T_c$ = 334 K. Below $T_c$ there is a contraction along $c$ and of $\beta$ and an expansion along $a$ and $b$.

### 6.4.2 Strain tensor analysis

The three principal components of the strain $e'_1$, $e'_2$, and $e'_3$ for TGS were calculated using the method outlined in 3.4.2, and are shown in figure 6.14. Below $T_c$ all three principal components continue to change which indicates that just below $T_c$ TGS is not fully ordered. As with DMMnF, (3.7), if it is assumed that at 293 K TGS is fully ordered, then the values of $e'_1$ can be used to estimate the disorder just below $T_c$. This assumes that at room temperature ($T_c - 40$ K) TGS is fully ordered, but previous studies [131, 132], have found that long-range ordering of $NH_3^+$ continues at temperatures well below $T_c - 40$ K, so while we can be confident that TGS continues to order below $T_c$, we cannot use the assumption that it is fully ordered at 293 K to quantify the disorder.

### 6.4.3 Order parameter

Another method for calculating the order parameter was performed by measuring how far the fractional $y$ coordinates (along the ferroelectric $b$ axis) of intermediate deuterium and $ND_3^+$ in the low-temperature phase deviate from the position of the mirror plane (at $\frac{1}{4}$ and $\frac{3}{4}$) in the $P2_1/m$ cell . $\Delta y$ for the intermediate deuterium was multiplied by $-1$ and $\Delta y$ for the the nitrogen of the GI head multiplied by 1. The order parameter $\eta$ for each temperature was the sum of these two values for every intermediate deuterium and GI N in the unit cell. Figure 6.14 shows $\eta$ as a function of temperature and the projection of the order parameter to $\eta = 0$ which would correspond to $T_c$. This analysis predicts $T_c = 339$ K, 5 K above the reported value. This calculation assumes that the motion of the intermediate deuterium and the relative displacement of the GI head are equally important, and has only been performed for temperatures where for which total scattering data were recorded. Due to the few data points, and approximations made, this method can only be used to conclude that this method predicts that the spontaneous polarisation decreases as TGS approaches $T_c$.

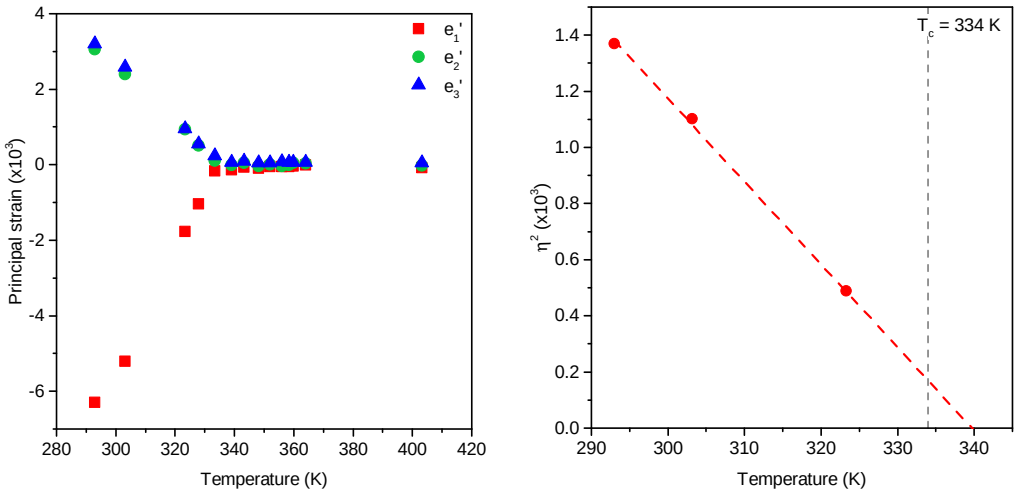


**Figure 6.14:** Left: Change in the principal components of TGS below the phase transition. Right: Order parameter $\eta^2$ as estimated by the offset of GI heads and intermediate deuterium in the low-temperature phase. Dashed line is line of best fit which predicts $T_c$ of 339 K.

### 6.4.4 Intermediate deuterium

The partial PDF $g_{\mathrm{OhD}}(r)$ was analysed to look for changes in the distribution of intermediate deuterium with respect to the Oh of both GII and GIII as TGS passed through the phase transition. In the high-temperature phase the intermediate deuterium has two equivalent positions - one closer to GII, and one closer to GIII both on the Oh···Oh vector shown in figure 6.15a. If the intermediate deuterium occupied one of the two position, then it is expected that $g_{\mathrm{OhD}}(r)$ would show a bimodal distribution corresponding to the deuterium forming one short and one long bond between the two neighbouring Oh. Figure 6.15b shows $g_{\mathrm{OhD}}(r)$ where only the intermediate deuterium are considered. It shows that in the converged models the intermediate deuterium has moved off the mid-point (dashed line), however there are three peaks at 1.21 Å, 1.33 Å, and 1.55 Å.

When $g_{\mathrm{OhD}}(r)$ was split into GII Oh−D and GIII Oh−D contributions (6.15c and 6.15d) similar distributions are observed. This indicates there is no preference for the intermediate deuterium to form short hydrogen bonds with either GII or GIII even in the low temperature phase where according to the average unit cell it would preferentially form short bonds with GII.

As the Oh···Oh distance is approximately 2.50 Å, then if the intermediate deuterium were oscillating along the Oh···Oh vector, the 1.55 Å peak would have a corresponding peak at 0.95 Å. As this is not seen it can be concluded that the intermediate deuterium moves away from this vector.

### 6.4.5 Deviation from the GII GIII Oh· · · Oh vector

As the intermediate deuterium atoms deviate from the Oh···Oh vector, the sum of the distances between any intermediate deuterium and Oh on GII and GIII will exceed the GII GIII separation distance. For each GII GIII pair, the vector between the two Oh was identified and the position of the intermediate deuterium projected onto it, the corresponding distance along

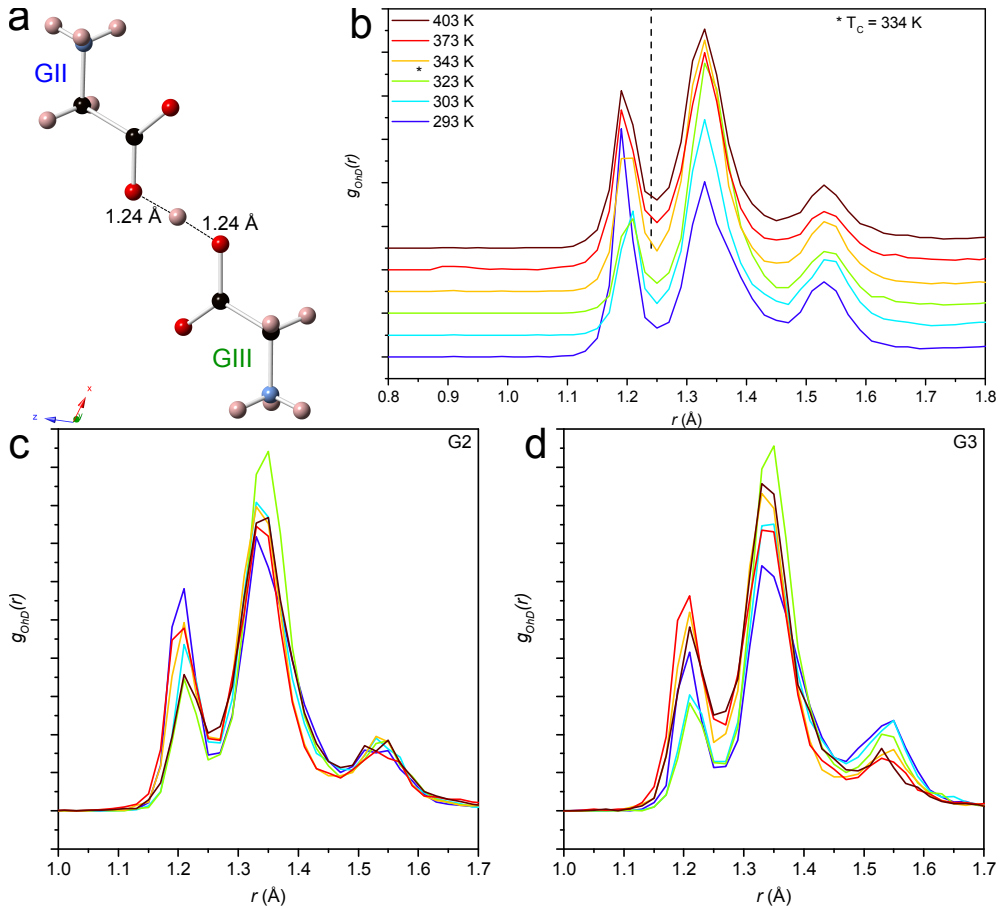


**Figure 6.15:** a: GII and GIII with the intermediate deuterium mid-way between the Oh···Oh vector. b: The partial pair distribution for Oh···D where only the intermediate deuterium are considered. The dashed line shows the initial Oh···D distance for the initial configuration. There are three peaks at $\approx 1.21$ Å, 1.33 Å, and 1.55 Å. Bottom row: $g_{\mathrm{OhD}}(r)$ for Oh from GII (c) and GIII (d).

that vector, $\lambda$, was calculated and is shown in figure 6.16.

As with the partial PDFs we see a trimodal distribution of distances. Some negative values of $\lambda$ were calculated, these corresponded to the intermediate deuterium forming a very short hydrogen bond to one glycine, and deviating away from the Oh···Oh vector entirely. Upon examination of the structures it is seen that the short, 1.21 Å, Oh−D separations in $g_{OhD}(r)$ are due to the intermediate deuterium deviation from the Oh···Oh vector (figure 6.16b).

In addition to the intermediate deuterium deviating from Oh···Oh, GII and GIII are also observed to move apart from one another. This increase in GII GIII distance is visible in $g_{\mathrm{OhD}}(r)$ as the longer Oh···D distances of 1.55 Å. Figure 6.16c and 6.16d show representative configurations for $\lambda = 1.33$ Å where the intermediate deuterium lies along Oh···D and GII and GIII have not drifted apart, and for $\lambda = 1.52$ Å with the intermediate deuterium still along Oh···D but where GII and GIII have drifted.

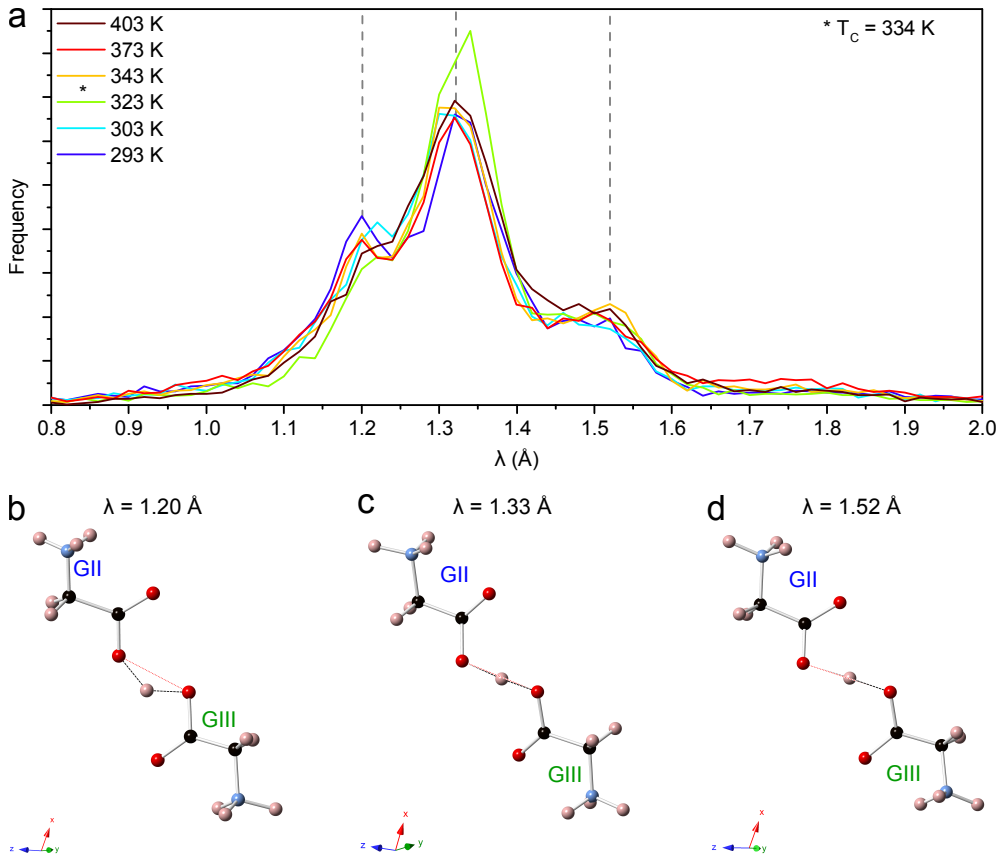


**Figure 6.16:** a: The projection of the intermediate deuterium position onto the GII GIII Oh···Oh, $\lambda$, for all converged refinements. The positions of the three peaks, at 1.20 Å, 1.32 Å and 1.52 Å are indicated. Bottom row: Representative structures from converged refinements at 403 K where Oh···Oh is shown as red dots, and Oh···D as black dashes for $\lambda = 1.20$ Å (b), $\lambda = 1.33$ Å (c), and $\lambda = 152$ Å (d).

### 6.4.6 GII GIII correlations

The scatter plot in figure 6.17 shows the D−Oh distance for GIII against the D−Oh distance for GIII for the same D atom. It has been split into 9 sections, corresponding to the three separate peaks in $g_{\mathrm{OhD}}(r)$. Next to the axes of the scatter plot are $g_{\mathrm{OhD}}(r)$ for the corresponding glycine. Figure 6.17 was generated in order to identify the correlations in the distances between D···$\mathrm{Oh_{GII}}$ and D···$\mathrm{Oh_{GIII}}$.

The central, most populated grid, shows that the the intermediate deuterium will largely form two "medium length" bonds with Oh of GII and GIII, within the range 1.25 Å to 1.48 Å. We also see that the two short or two long bonds are unlikely to be formed. If there was a correlation between the GII $g_{\mathrm{OhD}}(r)$ and GIII $g_{\mathrm{OhD}}(r)$ then it would be expected that short GII D···Oh distances would be accompanied by long GIII D···Oh distances. This is not seen, therefore the main result from this analysis is that the distance between Oh from GII and the intermediate deuterium is independent from the distance between the same intermediate deuterium and the Oh from GIII.

Although the 403 K data are shown in figure 6.17, the same trend is observed in all temperature refinements. Which means that as far as correlations between the intermediate deuterium and the Oh of glycine GII and GIII, the high- and low-temperature phases are

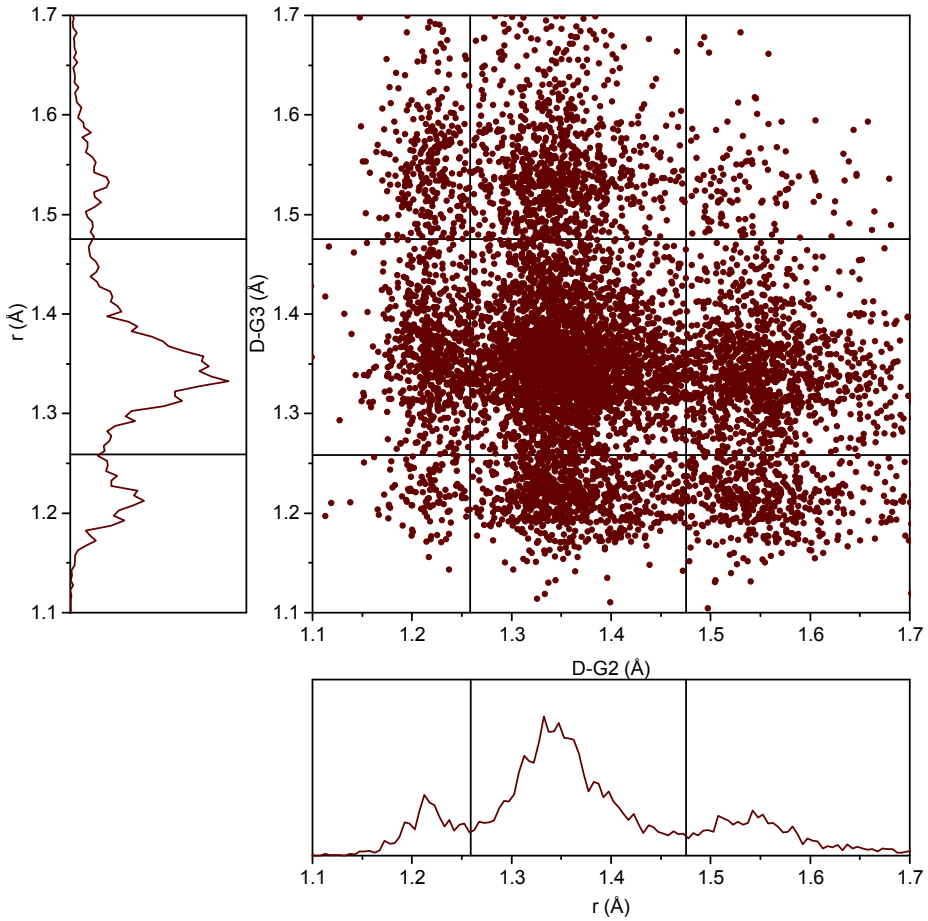


**Figure 6.17:** Centre: intermediate D to G2 distance (x axis) same intermediate D to G3 distance (y axis). Left: Partial PDF for the intermediate D to G3 distance. Bottom: Partial PDF for the intermediate D to G2 distance.

indistinguishable.

### 6.4.7 Chains

The initial `RMCProfile` supercell contained 4 repeating units of the unit cell along the ferroelectric $b$ axis, which corresponds to a length of approximately 50 Å. Therefore in each configuration there were chains of 8 repeating units of a GI head with its neighbouring GII/GIII and intermediate deuterium. Each configuration contained 13 320 atoms which corresponds to 45 unique chains.

A proposed mechanism behind the phase transition was shown in figure 6.4, where the orientation of the GI heads would move electron density away from GIII, causing the intermediate deuterium to preferentially bond with GII. This mechanism relies on the assumption that in the high-temperature phase there would be enough thermal motion to move the GI heads between their two positions either side of the mirror plane, and that the intermediate deuterium would respond to this motion.

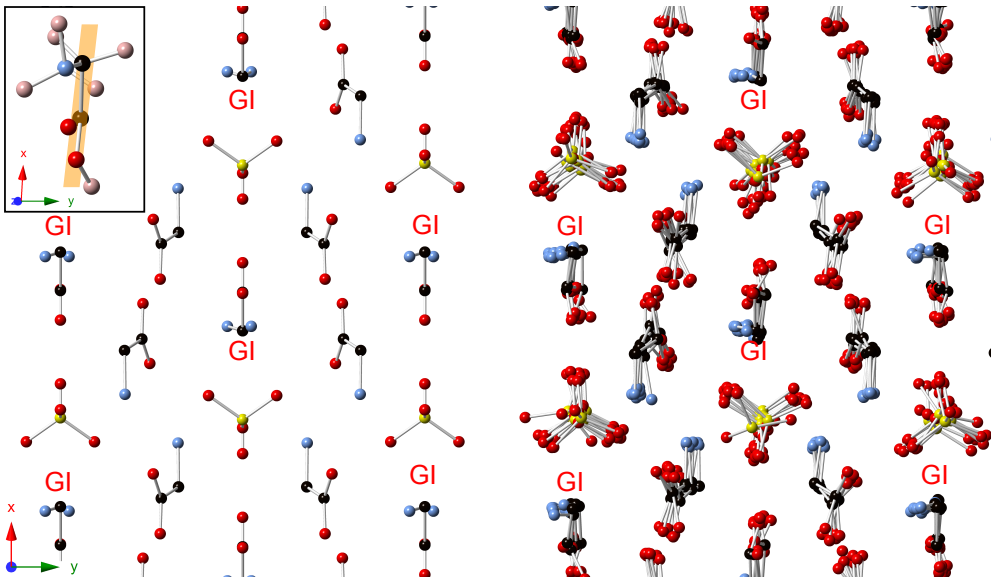


**Figure 6.18:** Inset: Plane of GI carbon/oxygen backbone shown in orange, with the $ND_3^+$ head in the $-y$ direction. Main picture: One high-temperature phase configuration of TGS in a $5 \times 4 \times 9$ supercell. Deuterium has been removed for clarity and GI molecules have been highlighted. Left: Initial configuration where the disorder of the $ND_3^+$ head (blue atoms) is visible as they are present on either side of the GI backbone. Right: Same configuration and view after model has converged. We see that the GI heads are now uniformly on one side of the molecule, despite this being the high-temperature phase.

The correlation between GI head orientation and the intermediate deuterium that forms short bonds with either GII or GIII can be extracted from the converged configurations. While in the initial configurations for the high-temperature phase, the GI heads were randomly oriented, the converged structures show the overwhelming majority of the GI heads pointing in the same direction.

Figure 6.18 shows a section from an initial and converged high-temperature phase refinement where the GI have been identified. In the initial configuration the $ND_3^+$ heads are randomly oriented either side of the glycine carbon/oxygen "backbone" (see the insert in figure 6.18). In the converged structure, all the GI heads point in the $-y$ direction, despite the fact that in the high-temperature phase the GI $ND_3^+$ head is expected to be disordered either side of the GI backbone.

To see if this ordering of the high-temperature phase was observed in all converged configurations; for every configuration all GI molecules were identified, and their plane defined based on the glycine carbon/oxygen "backbone" (insert figure 6.18). The position of the nitrogen relative to the plane was then calculated, and the number of GI heads oriented in either the $+y$ or $-y$ direction collected.

In addition to measuring the orientation of the GI heads, the length of the intermediate deuterium bond with respect to GII and GIII was calculated. For each chain the orientation of the GI head and the bonding between the neighbouring intermediate deuterium was visualised using coloured blocks. An example of the output and how it corresponds to the structure is given in figure 6.19.

Figure 6.19 shows a section of one chain from a high-temperature phase configuration

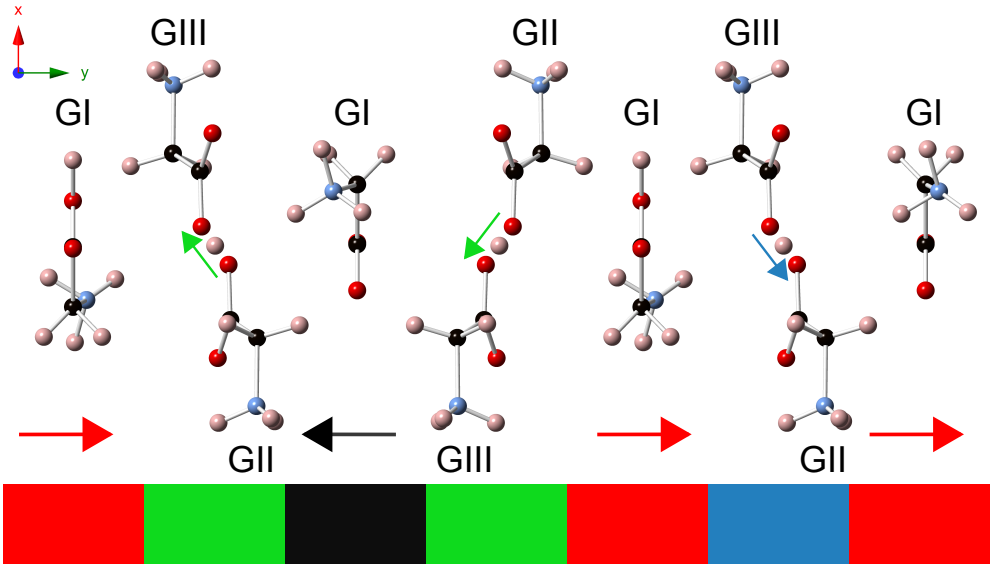


**Figure 6.19:** A section of a "chain" in TGS with three GI heads pointing in the $+y$ direction, and one pointing in the $-y$ direction, identified in the coloured boxes below as three red blocks and one black block. The intermediate deuterium forms a short bond with either GII (blue arrow and block) or GIII (green arrow and block).

showing 4 GI and 3 GII/GIII pairs in between them. On the structure, the direction of the GI head has been shown with red and black arrows pointing along the $y$ direction, where red corresponds to the GI pointing in the $+y$ direction and black to the head pointing in the $-y$ direction. Inbetween neighbouring GI molecules, the short bond formed by the intermediate deuterium is shown as an arrow pointing along the GII/GIII Oh···Oh vector. If the intermediate deuterium forms a short bond with GII then the arrow is blue, if it forms a short bond with GIII, the arrow is green. Underneath the structure is the corresponding output from the analysis program.

The analysis program was applied to the initial configurations of the high and low-temperature phases. Figure 6.20 shows the distribution of GI head positions and intermediate deuterium for 5 individual configurations. From this we see the random orientation of the GI heads in the initial high-temperature phase configurations and the ordered nature of the low-temperature phase initial configurations.

Examining converged configurations both by eye (figure 6.18) and by formal analysis (figure 6.21) shows that there is overwhelming alignment of the GI $ND_3$ groups and no correlation between the direction of the GI heads and the formation of a short hydrogen bond between either GII or GIII.A summary of the distribution of the GI head orientations and short hydrogen bonding is given in table 6.21. The fraction of intermediate deuterium forming short bonds with GIII decreases with temperature, from 56.2% at 403 K to 43.3% at 293 K.

As the origin of the electric ordering in TGS is the alignment of the polar GI heads, then this analysis suggests that even at $T_c+$ 70 K, TGS would display spontaneous polarisation, which it does not. As the Rietveld results found that the GI heads were distributed equally between the two sites either side of the mirror plane, the analysis of the atomistic configurations is, at first, quite puzzling. Therefore it is proposed that the models which have been produced

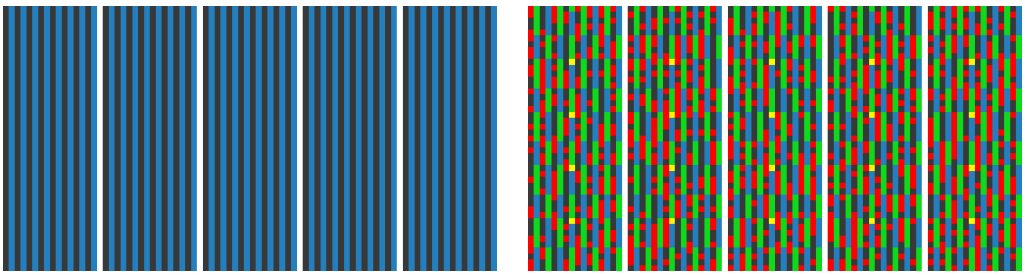

**Figure 6.20:** Chains from the initial configurations of 5 low-temperature phase models (left) and 5 high-temperature phase models (right). Each block contains 45 chains, each containing the relative orientations of 8 GI heads and the short bond formed by 8 intermediate deuterium. In the low-temperature phase the initial configuration is fully ordered with the GI heads aligned and the intermediate deuterium forming short bonds exclusively with GII. In the high-temperature phase the GI heads are randomly oriented and the intermediate deuterium forms short bonds with both GII and GIII. The yellow squares correspond to the intermediate deuterium being precisely mid-way between GII and GIII. In the high-temperature phase initial configurations this is true for all intermediate deuterium, however rounding errors lead to a small preference in one direction or the other.

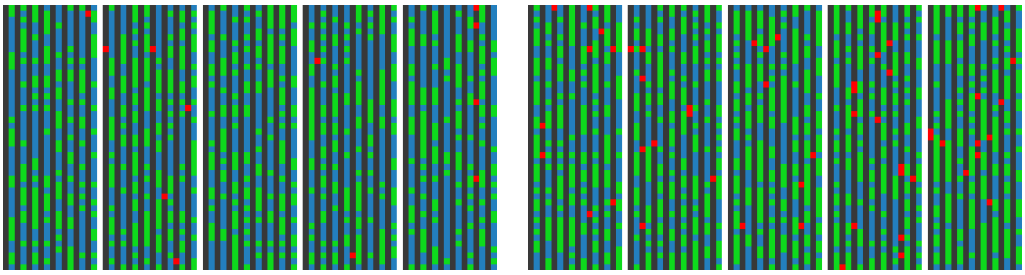

**Figure 6.21:** Chains from 5 converged configurations in the low-temperature phase (left) and the high-temperature phase (right). Black and red blocks correspond the the relative orientations of the GI heads, and blue and green blocks correspond to the intermediate deuterium forming short hydrogen bonds with either GII or GIII. For both the high and low-temperature phase refinements we see that most GI heads point in the $-y$ direction (black blocks), despite the fact that in the high-temperature phase, it is expected that half of the GI heads would point in the $+y$ direction.

| Temperature/K | % GI pointing $-y$ | % GIII short hydrogen bonds |
|---|---|---|
| 403 | 99.6 | 56.2 |
| 365 | 97.1 | 52.8 |
| 343 | 94.0 | 51.8 |
| 323 | 99.5 | 48.8 |
| 303 | 99.1 | 45.0 |
| 293 | 99.5 | 43.3 |

**Table 6.8:** GI head orientation and corresponding % of intermediate deuterium which form short hydrogen bonds with GIII

are of a single domain within TGS, and that the size of the simulation box is smaller than the domain size. This would mean that while the bulk sample would show no spontaneous polarisation, there would be domains with differently oriented GI heads.

This proposal is supported by the fit of the high-temperature Bragg profile from Rietveld analysis and from the RMC refinements. The Rietveld model, which incorporates disorder of

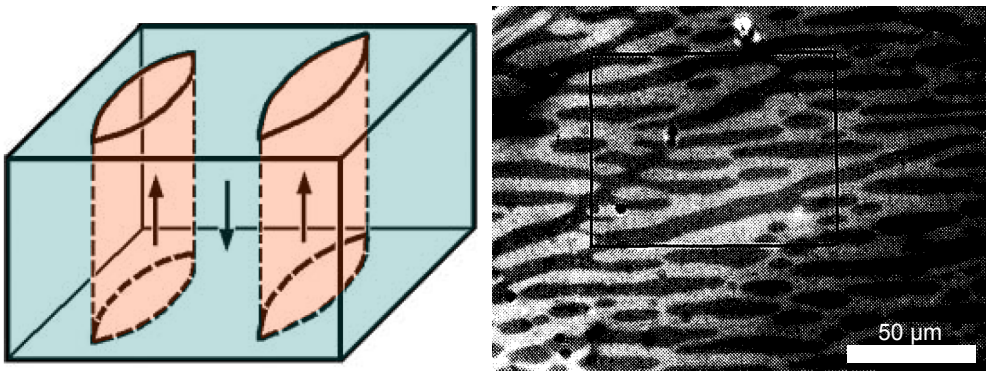


**Figure 6.22:** Left: Diagram showing the shape of the domain structure of TGS with walls parallel to the ferroelectric $b$ axis [139]. Right: Micrograph of TGS at $T_c - 0.39\,\mathrm{K}$ after heat treatment, adapted from [137] showing large domains. It would require $\approx 10^9$ atomistic configurations to cover the surface area shown.

the GI head about the mirror plane, did not fill the intensity of the $(220)$ Bragg peak (figure 6.7), despite the fact that the peak was allowed based on the symmetry of the unit cell. The RMC refinements of the high-temperature phase configurations (figure 6.12) did fill some of this peak intensity.

The contraction and expansion of the lattice parameters shown in figure 6.13 confirms TGS went through the phase transition at the expected temperature, so the origin for the $(220)$ peak intensity in the converged configurations is not due to a higher than expected phase transition temperature. It is suggested that this peak intensity is filled by the configurations generating domains, and that on the scale of the configurations (approximately 50 Å), TGS does not display this short range disorder which the Rietveld model suggests.

Domains have been observed in single crystal TGS just below $T_c$. These domains are rod shaped and lie along the ferroelectric $b$ axis [137, 138] (left in figure 6.22). The domains become coarser with both time and decreasing temperature [139], that is to say the domain structure of TGS is dependent on both the temperature of the sample, and how long it has been below $T_c$. During synthesis, the sample was not heated above 55 °C, but it was held at 50 °C (323 K, 12 K below $T_c$ for the deuterated sample) for 5 hours before the experiment when it was dried. It is unknown if this could have had an effect on the sample produced.

While no domains were observed in TGS above $T_c$ [137] the difference in scale as to what would be called domains in [137] when compared to our atomistic configurations are significant. The right of figure 6.22 shows the domain structure for (non-deuterated) TGS just below $T_c$. It would take $1 \times 10^9$ atomistic configurations to cover the surface of the micrograph shown in figure 6.22.

## 6.5 Summary

Total neutron scattering experiments were performed on fully deuterated triglycine sulfate in the temperature range $T_c + 70\,\mathrm{K}$ to $T_c - 50\,\mathrm{K}$. The second order nature of the phase transition meant that any changes in the Bragg profile or PDFs were subtle. Atomistic configurations were generated of TGS above and below the phase transition and the converged models analysed. Even in the high-temperature phase, the GI head was observed to preferentially point in one

direction, a feature which is attributed to domains within the sample. No correlation was observed between the GI head orientation and the propensity of the intermediate deuterium to form short hydrogen bonds with either GII or GIII. However the fraction of intermediate deuterium forming short bonds with GIII decreases with temperature.

There were three peaks in $g_{\mathrm{OhD}}(r)$ partial PDF, the shortest of which is attributed to the intermediate deuterium moving away from the Oh···Oh vector, the mid-length peak is attributed to the deuterium being positioned approximately mid-way along the Oh···Oh vector when GII and GIII are separated by the amount seen in the average structure. Contributions to the peak at high $r$ come from the glycine opposite the intermediate deuterium which form the low r peak, and also from GII GIII pairs which have drifted apart.

Analysis of the principal components of the strain as well as literature reports indicate that TGS continues to order as it is cooled. This is not seen in the RMC configurations below $T_{\mathrm{c}}$ as the overwhelming majority of GI heads are already aligned in one direction above the phase transition. Therefore it is suggested that the `RMCProfile` simulation box is too small to model the extent of the breakdown of cooperative behaviour between GI heads in the low-temperature phase or the disorder in the high-temperature phase explicitly.

# Chapter 7

# Conclusions

The reverse Monte Carlo method has been successfully applied to three organic ferroic materials in order to model the behaviour of polar molecules as the dielectric transition is approached. The work presented in this thesis has shown that analysis of atomistic configurations above and below their phase transitions can give significant insight into the behaviour of polar species.

In addition to modelling the electric ordering, neutron total scattering performed on multiferroic DMMnF, and the subsequent magnetic RMC configurations allowed us to probe the magnetic interactions of 432 different $Mn^{2+}$ in each simulation box rather than the 4 $Mn^{2+}$ from Rietveld refinement.

For these three structures the disorder within crystals has been explored, something that is not easy to do using standard crystallographic techniques, but something that is well suited to the RMC method. That being said, these three materials have some of the most complex structures which have been studied using the RMC method, and their successful analysis has confirmed that it is possible to extend the method to larger and more flexible unit cells.

## 7.1 Summary

### 7.1.1 DMMnF

RMC models of DMMnF found that the dimethylammonium cation interacts with the framework via two different formate groups. The DMA cation either forms shorter N···O hydrogen bonds with the framework than the average structure would indicate but with the same topology of the average structure, or the dimethylammonium cation forms slightly longer bonds with the framework but bonds with only one formate group instead of two forming a "pincer-like" arrangement. This arrangement cannot be observed via standard crystallographic analysis. The change in entropy for DMMnF between the high and low-temperature phases, was higher than would be expected for a simple 3-fold order-disorder model, and indicated that correlations between the dimethylammonium cation and the framework are important.

Atomistic configurations of the high-temperature phase showed that the DMA cation has preferred orientations that are consistent with the crystal symmetry.

Rietveld refinement of the magnetic phase of DMMnF found that the system is best described as a G-type antiferromagnet. However the RMC configurations, which included

contributions from $i(Q)$, found that the magnetic moments on 4 of the 6 nearest neighbour $Mn^{2+}$ are likely to align ferromagnetically, and the other 2 spins align antiferromagnetically the target spin.

### 7.1.2 PIH

Analysis of the lattice parameters of PIH confirmed the existence of an intermediate-temperature phase, and that it causes a contraction of the unit cell perpendicular to the imidazolium ring, with no corresponding expansion. Analysis of the RMC models found that in this intermediate temperature phase the distribution of metal cyanide angles in the framework contracted, leading to a stiffening of the framework. Analysis of the imidazolium dynamics found that even just below the dielectric transition, there was no preferred imidazole orientation, and that the imidazolium tilted relative to the crystallographic axes in the high, intermediate and low-temperature phases.

### 7.1.3 TGS

Analysis of PIH and DMMnF had found indications of structural changes during the phase transitions, however the same was not seen in TGS. There was no correlation between the bonding of the intermediate deuterium and the orientation of the GI head. Indeed for TGS domains of unidirectional GI heads at least the size of the RMC configurations were observed. TGS could be an example of a situation where the `RMCProfile` simulation box is too small to model the extent of the cooperative behaviour between GI heads, and if computer modelling of TGS around its phase transition is to be used, a slightly larger scale method is perhaps needed.

## 7.2 Comments about RMC in general

A comment that is often made about the RMC method is that it will tend to generate the most disordered models that are consistent with the scattering data. But both DMMnF and TGS produced ordered configurations out of disordered initial configurations. In the case of TGS the resultant high-temperature phase configurations were more ordered than were expected. Clearly for these models this is not the case.

The work presented in this thesis has shown that the RMC algorithm is well suited to model systems such as MOFs with unit cells the size of DMMnF or PIH. The configuration box is large enough to model polar interactions, but not so large that computing time is prohibitively long. As was seen with TGS, there are systems where the simulation box is perhaps too small to model the polar interactions, but I believe this work has highlighted the suitability of the RMC method to model MOFs with two and three atom bridges. It could be argued that the failure of the TGS models to generate discernibly different configurations above and below the phase transition is due to TGS having a second-order phase transition, with longer correlation lengths than the two MOFs. But indications of the subtle high to intermediate-temperature phase transition were observed in PIH, so it could be that the suitability of application of the RMC method to different materials needs to be made on a case-by-case basis.

The magnetic analysis of DMMnF highlighted, even if atomistic configurations are successfully converged, they may not give a definitive answer. This was observed when trying to fit a small amount of information, such as one or two Bragg peaks, using a method where there are tens of thousands of variables which can be varied. However as seen with the high-temperature phase of TGS, even when we start with a disordered configuration for a phase which is allowed to be disordered, RMC still consistently produces order. So the many variables issue which has perhaps blighted the magnetic DMMnF analysis is not as straightforward as it initially seems.

As with many analysis techniques, it is difficult to know if the conclusions drawn from the configurations are really correct. There is a focus on how complementary RMC is when compared to other methods, (eg Raman/NMR) but few results between RMC and other methods are directly compared, and these checks have not been performed on complex structures such as the MOFs presented in this thesis. A good test of the robustness of the RMC program would be to compare specific results from specific materials to those derived from other methods, perhaps this work, where MOFs have been investigated is the place to start?

Two recent and quite public failures in the scientific method have highlighted the need for "sanity checks". A bug in an fMRI code which has been used for 15 years has lead to clusters of activity being reported within brains when there was no activity [140], potentially putting the results of analysis performed using this code into question. In a recent attempt to reproduce a cancer study, it was found that there is significant variation in "stock" antibodies which are routinely used, and that these antibodies have been found to attach to the wrong sites [141]. These incidents have shown how often it is easy to get caught up in pushing boundaries that we forget to check the basics. I believe a good sanity check would be to perform neutron total scattering experiments on the cobalt analogue of PIH specifically to see if it is possible to attribute the difference in the imidazolium tilting angle in PIH and the analogue to them being different materials, or different analysis techniques.

## 7.3 Future work

**Metal formates:** Preliminary analysis of magnetic DMMnF prompted a collaboration between the research group and `MERLIN` instrument scientists. Preliminary analysis on `MERLIN` data found that better resolution was needed for analysis of the magnetic structure of DMMnF, than could be offered by `MERLIN`. Inelastic neutron scattering was then performed on DMMnF in `LET`, where sharp excitations were observed below the magnetic transition temperature which disappear as the DMMnF is heated. Figure 7.1 shows the energy transfer as a function of scattering vector for DMMnF above and below the magnetic ordering temperature. At 5 K we see sharp features which are broadened at 8 K (just below the ordering temperature). The features continue to broaden as DMMnF is heated above the transition temperature. Beam-time to characterise the spin excitations of DMMnF with respect to temperature has recently been awarded.

**Prussian blue analogues:** I think that the sensible next step for analysis on the Prussian blue analogues, and to verify that the RMC method is consistent with other analysis techniques, is to perform total neutron scattering on the Co analogue. The same analysis should be performed on the analogue as was on PIH to allow not only comparison between previously

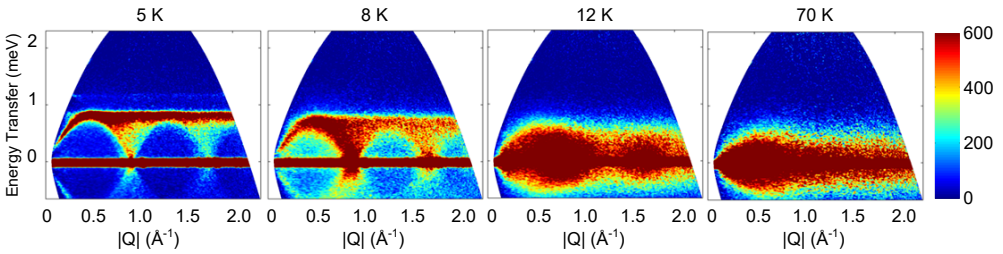


**Figure 7.1:** The energy transfer vs $|Q|$ for DMMnF below the magnetic transition 5 K and 8 K and above the magnetic transition, 12 K and 70 K. We see that upon heating the sharp features broaden.

published Raman studies on the analogue and RMC analysis, but also to directly compare cation motion between two very similar systems using the same technique. Being able to compare the rate of pore contraction (as was done in section 5.6.6) of the fully deuterated Co analogue to PIH will be particularly useful to confirm that the isotope effect is not a contributing factor to the different rates of contraction.

**Triglycine sulfate:** The analysis of TGS found that even at $T_c + 70$ K the domain sizes were larger than the simulation box. If we are going to see the break down of long-range order in TGS it is necessary to collect to higher temperatures that we already have. I propose a total scattering experiment of TGS where data are collected up to $T_c + 150$ K (or until the sample degrades). The same analysis technique can be performed on the newly collected data and so there will be a rapid turn around from data collection to analysis.

**More complex materials:** The work presented in this thesis has shown that the RMC method can readily be applied to MOFs with two and three atom linkers, and this is a very large group to investigate, and different cation framework dynamics will be present in the different permutations. It would also be interesting to see if these techniques can be applied to larger MOFs such as MOF-5 (figure 7.2). MOF-5 is a low density material, and as such a much larger simulation box would be produced to accommodate the size of the pore, while still having a comparable number of atoms to the DMMnF and PIH models. The constituent elements of the MOF-5 structure have already been successfully analysed using `RMCProfile` and planarity potentials could be applied to the carbon rings, as they were to the imidazole rings of PIH. The potential limiting factor in generating these configurations is how long it would take to collect neutron scattering data. However a one-day trial run in either `GEM` or `POLARIS` could lead the decisions on the viability of larger scale studies on these materials.

**RMCProfile:** For the three materials presented in this thesis, the number of atomic moves for the system to converge have varied between $4 \times 10^6$ to $40 \times 10^6$ moves. Currently when running `RMCProfile` the user specifies a length of time for the program to run, not a specific number of moves, or the stability of $\chi^2$. I think a very useful addition to the `RMCProfile` code would be a termination condition specified by the user that if $\chi^2$ hasn't changed by a set amount (say $\pm 1\%$) for a set number of moves, then the model is considered converged.

**Final remarks:** In this thesis I have shown that it is possible to analyse complex structures such as MOFs with perovskite-like architecture using the RMC method. The analysis of these complex structures is more involved than it is for their inorganic equivalents, but there is a wealth of information that can be extracted from these configurations and, through further extension of this method, I believe there are some very interesting things still to discover.

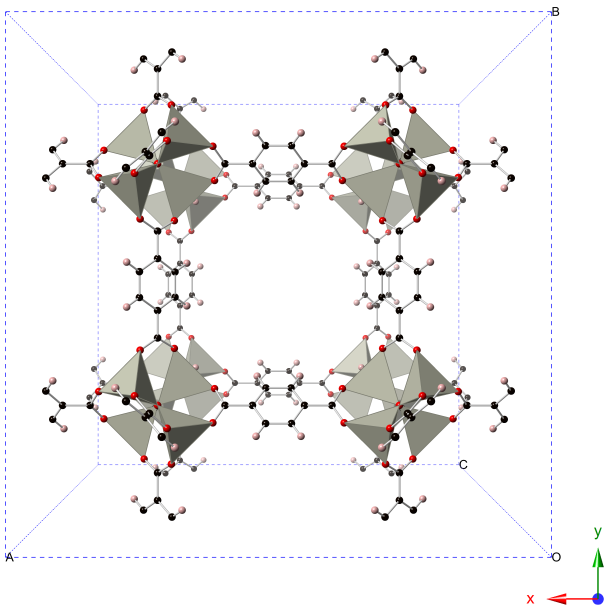


**Figure 7.2:** The low-density metal-organic framework MOF-5 [142] with the unit cell shown as dashed lines. Unit cell dimensions are $25\,\text{Å} \times 25\,\text{Å} \times 25\,\text{Å}$.

# Appendix A

# Run Numbers

## A.1 DMMnF

### A.1.1 Data collection

| $T_{\text{nominal}}$ / K | $T_{\text{CCR}}$ / K | $T_{\text{sample}}$ / K | Run numbers | Total proton beam charge / µA h |
|---|---|---|---|---|
| 293 | – | 300.9(5) | GEM60010–GEM60018 | 1288 |
| 250 | 250 | 243(3) | GEM60024–GEM60031 | 1200 |
| 225 | 225 | 218.3(1) | GEM60133–GEM60136 | 508 |
| 200 | 200 | 194.2(1) | GEM60037–GEM60044 | 1200 |
| 190 | 190 | 184.5(5) | GEM60050 | 150 |
| 180 | 180 | 175.0(5) | GEM60056 | 150 |
| 170 | 170 | 165.5(5) | GEM60062 | 150 |
| 160 | | | GEM60068 | 150 |
| 150 | 150 | 145.6(1) | GEM60074–GEM60081 | 1200 |
| 100 | 100 | 97.4(1) | GEM60087–GEM60094 | 1200 |
| 20 | 20.2(1) | 21.5(1) | GEM60100–GEM60106 | 1050 |
| 3 | 4.75(3) | 6.81(3) | GEM60117–GEM60122 | 900 |

**Table A.1:** Collection run numbers for data sets $> 150\,\mu\text{A h}$ for DMMnF

### A.1.2 `GUDRUN` corrections

| Description | Run number | Description | Total proton beam charge / µA h |
|---|---|---|---|
| Normalisation | GEM60002 | 8mm V rod | 500 |
| Normalisation background | GEM60003 | Empty GEM | 150 |
| Sample background | GEM60004 | Empty CCR | 200 |
| Container | GEM60005–GEM60008 | Empty vanadium can | 600 |

**Table A.2:** Run numbers required for normalisation and background corrections

## A.2 PIH

### A.2.1 Synthesis

For the synthesis of perdueterated PIH, the following reagents were used:
Imidazole-$d_4$: Lot number X247P2; NMR result 99.4 atom % D; G.C. result 99.5 % chemical purity
Potassium hexacyanoferrate (III) ACS reagent; $\geq$ 99.0%.

### A.2.2 Data collection

| $T_{\text{nominal}}$/K | $T_{\text{sample}}$/K | Run numbers | Total proton beam charge /µA h |
|---|---|---|---|
| 293 | – | POL62836–POL62843 | 1200 |
| 250 | 248(2) | POL62917–POL62925 | 1185 |
| 200 | 194(3) | POL62905–POL62912 | 1200 |
| 180 | 175(2) | POL62897–POL62904 | 1200 |
| 165 | 161(3) | POL62889–POL62896 | 1200 |
| 150 | 146(3) | POL62881–POL62888 | 1200 |
| 83 | 86(10) | POL62873–POL62880 | 1200 |
| 70 | 66(3) | POL62872 | 25 |
| 60 | 59(5) | POL62871 | 25 |
| 50 | 48(4) | POL62870 | 25 |
| 40 | 40(5) | POL62869 | 25 |
| 30 | 31(4) | POL62868 | 25 |
| 20 | 23(1) | POL62867 | 25 |
| 10 | 16(7) | POL62859–POL62866 | 1200 |

**Table A.3:** Collection run numbers for PIH

### A.2.3 GUDRUN corrections

| Process | Run number | Description | Total proton beam charge /µA h |
|---|---|---|---|
| Normalisation | POL62806–POL62809 | 8mm V rod | 600 |
| Normalisation background | POL62804 POL62805 | Empty POLARIS changer | 300 |
| Sample background | POL62852 | Empty POLARIS cryostat | 600 |
| Container | POL62853, POL62926–POL62928 | Empty vanadium can in cryostat | 650 |

**Table A.4:** Run numbers required for normalisation and background corrections for the CCR measurements

| Process | Run number | Description | Total proton beam charge /µA h |
|---|---|---|---|
| Normalisation | POL62806–POL62809 | 8mm V rod | 600 |
| Normalisation background | POL62804 POL62805 | Empty POLARIS changer | 300 |
| Sample background | POL62804–POL62805 | Empty POLARIS changer | 300 |
| Container | POL62810–POL62813 | Empty vanadium can in changer | 600 |

**Table A.5:** Run numbers required for normalisation and background corrections for the ambient total scattering measurement

## A.3 TGS

### A.3.1 Synthesis

For the synthesis of perdueterated PIH, the following reagents were used:
**Glycine-$d_5$**
Lot number W549P28
NMR result 98.4 atom % D
HPLC result $>$ 99% chemical purity
**Sulfuric Acid-$d_2$ (96%w/w in $D_2O$)**
Lot number I135AP2
NMR result 99.8 atom % D
Titration 96.5% chemical purity
**Ethyl Alcohol-$d_6$**
Lot number X298P1
NMR result 99.69 atom % D
GC result 99.85 % chemical purity

### A.3.2 Data collection

| $T_{\text{nominal}}$/K | $T_{\text{sample}}$/K | Run numbers | Total proton beam charge /µA h |
|---|---|---|---|
| 403 | 403.2(2) | POL64783–POL64791 | 925 |
| 373 | 364(2) | POL64759–POL64767 | 925 |
| 368 | 359.9(7) | POL64758 | 25 |
| 363 | 358.4(4) | POL64757 | 25 |
| 358 | 356(1) | POL64756 | 25 |
| 353 | 352(1) | POL64755 | 25 |
| 348 | 348.2(9) | POL64754 | 25 |
| 343 | 343.2(1) | POL64745–POL64753 | 925 |
| 338 | 339(1) | POL64744 | 25 |
| 333 | 333.5(4) | POL64743 | 25 |
| 328 | 328(1) | POL64742 | 25 |
| 323 | 323.3(4) | POL64734–POL64741 | 900 |
| 303 | 303.2(0) | POL64728–POL64733 | 900 |
| 293 | – | POL64717–POL64724 | 900 |

**Table A.6:** Collection run numbers for TGS in furnace and sample changer (293 K).

### A.3.3 GUDRUN corrections

| Process | Run number | Description | Total proton beam charge /µA h |
|---|---|---|---|
| Normalisation | POL64586 | 8mm V rod | 600 |
| Normalisation background | POL64585 | Empty POLARIS | 257 |
| Sample background | POL64712–POL64713 | Empty furnace | 299 |
| Container | POL64714–POL64716 | Empty 8 mm V can in furnace | 500 |

**Table A.7:** Run numbers required for normalisation and background corrections for the furnace measurements. The furnace background colllection time is significantly smaller than that for the crysostat (table A.8) due to the furnace having a much lower background

| Process | Run number | Description | Total proton beam charge /µA h |
|---|---|---|---|
| Normalisation | POL64586 | 8mm V rod | 600 |
| Normalisation background | POL64585 | Empty POLARIS | 257 |
| Sample background | POL64588–POL64589, POL64635 | Empty cryostat | 532 |
| Container | POL64590, POL64636–POL64639 | Empty 8 mm V can in cryostat | 748 |

**Table A.8:** Run numbers required for normalisation and background corrections for the cryostat measurements.

# Appendix B

# Lattice Parameters

## B.1 DMMnF

| Temperature /K | a /Å | b /Å | c /Å | $\beta$ /° | V /Å$^3$ |
|---|---|---|---|---|---|
| 300 | 14.4347(4) | 8.3339(2) | 9.0141(3) | 122.261(9) | 916.99(10) |
| 243 | 14.4314(4) | 8.3332(2) | 8.8907(3) | 122.388(9) | 911.87(10) |
| 218 | 14.4351(4) | 8.3341(2) | 8.9722(3) | 122.431(9) | 911.03(10) |
| 194 | 14.4316(4) | 8.3321(2) | 8.9612(3) | 122.467(9) | 909.12(10) |
| 184 | 14.4340(4) | 8.3335(2) | 8.9602(3) | 122.478(9) | 909.23(10) |
| 175 | 14.3746(3) | 8.3208(2) | 8.8852(2) | 120.831(1) | 912.55(3) |
| 166 | 14.3707(3) | 8.3207(2) | 8.8815(2) | 120.810(1) | 912.12(3) |
| 160 | 14.3675(3) | 8.3209(2) | 8.8778(2) | 120.798(1) | 911.69(3) |
| 146 | 14.3628(3) | 8.3214(2) | 8.8734(1) | 120.784(1) | 911.10(3) |
| 97 | 14.3530(3) | 8.3214(2) | 8.8582(2) | 120.781(1) | 908.96(3) |
| 21 | 14.3477(3) | 8.3231(2) | 8.8454(2) | 120.802(1) | 907.30(4) |
| 7 | 14.3460(4) | 8.3222(2) | 8.8446(2) | 120.799(2) | 907.03(4) |

**Table B.1:** Lattice parameters for DMMnF in the high and low temperature phase, expressed in terms of the monoclinic $Cc$ lattice

## B.2 PIH

| Temperature /K | a /Å | b /Å | c /Å | $\beta$ /° | V /Å$^3$ |
|---|---|---|---|---|---|
| 293 | 13.6906(7) | 8.7570(4) | 15.1675(4) | 111.6720(2) | 1689.8692(1933) |
| 250 | 13.6518(5) | 8.7631(3) | 15.1782(3) | 111.7528(2) | 1686.4894(1421) |
| 200 | 13.5944(9) | 8.7695(6) | 15.1892(6) | 111.8661(3) | 1680.5182(2729) |
| 180 | 13.5610(6) | 8.7749(3) | 15.1985(3) | 111.9369(2) | 1677.6143(1532) |
| 165 | 13.5271(6) | 8.7820(3) | 15.2109(3) | 112.0135(2) | 1675.2388(1532) |
| 150 | 13.4932(4) | 8.7830(4) | 15.1048(6) | 111.6565(35) | 1663.7251(1200) |
| 83 | 13.4535(4) | 8.7911(3) | 15.0805(5) | 111.7453(30) | 1656.6666(1000) |
| 10 | 13.4212(6) | 8.7934(4) | 15.0633(8) | 111.8038(27) | 1650.5628(1400) |

**Table B.2:** Lattice parameters for PIH in the high, intermediate, and low temperature phase, expressed in terms of the monoclinic $C2/c$ lattice.

| Temperature /K | Space Group | Fe−C−N angle /° | K−N−C angle /° |
|---|---|---|---|
| 293 | $R\bar{3}m$ | 178.25–179.08 | 177.32–177.99 |
| 250 | $R\bar{3}m$ | 179.29–179.96 | 176.36–177.15 |
| 200 | $R\bar{3}m$ | 179.29–179.96 | 176.37–177.16 |
| 180 | $R\bar{3}m$ | 179.29–179.96 | 176.37–177.16 |
| 165 | $R\bar{3}m$ | 179.29–179.96 | 176.38–177.17 |
| 150 | $C2/c$ | 172.56–178.35 | 163.33–173.90 |
| 83 | $C2/c$ | 175.54–177.40 | 166.72–169.34 |
| 10 | $C2/c$ | 175.44–179.05 | 165.32–171.77 |

**Table B.3:** Range of Fe−C−N and K−N−C from Rietveld-derived strucutres.

## B.3 TGS

| Temperature /K | a /Å | b /Å | c /Å | $\beta$ /° | V /Å$^3$ |
|---|---|---|---|---|---|
| 403 | 9.4339(2) | 12.6834(3) | 5.7382(2) | 110.121(2) | 644.69(3) |
| 373 | 9.4198(2) | 12.6525(3) | 5.7441(2) | 110.250(2) | 642.29(3) |
| 368 | 9.4182(3) | 12.6489(4) | 5.7448(2) | 110.265(3) | 642.02(3) |
| 363 | 9.4174(3) | 12.6470(4) | 5.7449(2) | 110.265(3) | 641.87(3) |
| 358 | 9.4167(3) | 12.6447(4) | 5.7452(2) | 110.272(3) | 641.71(3) |
| 353 | 9.4153(3) | 12.6418(4) | 5.7457(2) | 110.289(3) | 641.45(3) |
| 343 | 9.4135(2) | 12.6353(3) | 5.7463(2) | 110.312(2) | 640.97(3) |
| 348 | 9.4145(3) | 12.6376(4) | 5.7460(2) | 110.304(2) | 641.17(3) |
| 338 | 9.4117(3) | 12.6310(4) | 5.7464(2) | 110.329(3) | 640.58(3) |
| 333 | 9.4113(3) | 12.6280(4) | 5.7469(2) | 110.345(3) | 640.34(3) |
| 328 | 9.4111(3) | 12.6286(4) | 5.7427(2) | 110.342(3) | 639.95(3) |
| 323 | 9.4116(2) | 12.6303(2) | 5.7391(1) | 110.332(2) | 639.71(2) |
| 303 | 9.4128(2) | 12.6346(2) | 5.7221(1) | 110.307(2) | 638.22(2) |
| 293 | 9.4134(2) | 12.6340(2) | 5.7173(1) | 110.305(2) | 637.70(2) |

**Table B.4:** Lattice parameters for TGS in the high and low temperature phase.

# Appendix C

# RMC Restraints

The bond bending and stretching potentials, and distance window restraints applied to the RMC configurations are given here. With the exception of TGS distance windows, these values have been reported in the main body of the thesis.

## C.1 DMMnF

### C.1.1 Bond Bending and Stretching Potentials

| Atomic pair | $D$/eV | $r_0$/Å |
|---|---|---|
| C−N | 2.051 | 1.50 |
| C=O | 3.376 | 1.24 |
| C−D | 2.275 | 1.06 |
| N−D | 2.947 | 1.06 |

**Table C.1:** Morse bond stretch potentials used to constrain RMC refinement.

| Atoms | $k$/eV | $\theta_0$/° |
|---|---|---|
| O=C=O | 17.876 | 129.800 |
| C−N−C | 7.864 | 108.600 |
| D−C−D | 8.976 | 107.114 |
| C−N−D | 7.602 | 106.376 |
| D−C−O | 7.403 | 114.900 |
| N−C−D | 11.235 | 104.700 |
| C−N−D | 6.504 | 105.949 |

**Table C.2:** Angle potentials used to constrain RMC refinement.

### C.1.2 Distance Windows

| $T$/K | D−C | D−N | C−O | C−N | O−Mn |
|---|---|---|---|---|---|
| 293 | 0.9091 - 1.1288 | 0.9482 - 1.1726 | 1.1179 - 1.3783 | 1.3311 - 1.6420 | 2.0751 - 2.3625 |
| 250 | 0.9207 - 1.1403 | 0.9484 - 1.1732 | 1.1161 - 1.3761 | 1.3261 - 1.6361 | 2.0713 - 2.3582 |
| 200 | 0.9478 - 1.1713 | 0.9485 - 1.1736 | 1.1152 - 1.3750 | 1.3229 - 1.6326 | 2.0693 - 2.3560 |
| 150 | 0.9229 - 1.2262 | 0.9310 - 1.2100 | 1.1431 - 1.3483 | 1.3657 - 1.7030 | 2.0156 - 2.3755 |
| 100 | 0.9268 - 1.2436 | 0.9300 - 1.2174 | 1.1632 - 1.3570 | 1.3606 - 1.7179 | 2.0206 - 2.3184 |
| 20 | 0.9290 - 1.2640 | 0.9338 - 1.2340 | 1.1638 - 1.3642 | 1.3682 - 1.7350 | 2.0312 - 2.3154 |
| 7 | 0.9257 - 1.2446 | 0.9272 - 1.2256 | 1.1637 - 1.3762 | 1.3677 - 1.7227 | 1.9984 - 2.3529 |

**Table C.3:** Distance windows applied to RMC refinements

## C.2 PIH

### C.2.1 Bond Bending and Stretching Potentials

| Atomic pair | $D$/eV | $r_0$/Å |
|---|---|---|
| C−C | 3.600 | 1.34 |
| C−D | 2.472 | 1.04 |
| C−N | 4.821 | 1.34 |
| N−D | 2.928 | 1.03 |
| Cx−Nx | 8.317 | 1.16 |

**Table C.4:** Morse bond stretch potentials used to constrain RMC refinement.

| Atoms | $k$/eV | $\theta_0$/° |
|---|---|---|
| D−C−N | 6.429 | 126.000 |
| C−N−D | 7.2405 | 126.000 |
| N−C−N | 4.993 | 126.000 |
| C−N−C | 10.174 | 118.300 |
| C−C−N | 10.174 | 120.000 |
| C−C−D | 6.117 | 126.000 |

**Table C.5:** Angle potentials used to constrain RMC refinement.

### C.2.2 Distance Windows

| $T$/K | D−C | D−N | C−C | C−N | Cx−Fe | Cx−Nx | K−Nx |
|---|---|---|---|---|---|---|---|
| 293 | 0.93-1.15 | 0.93-1.15 | 1.25-1.46 | 1.25-1.46 | 1.82-2.07 | 1.08-1.26 | 2.60-3.18 |
| 250 | 0.93-1.15 | 0.93-1.15 | 1.25-1.46 | 1.25-1.47 | 1.83-2.09 | 1.10-1.23 | 2.58-3.16 |
| 200 | 0.93-1.15 | 0.93-1.16 | 1.25-1.47 | 1.25-1.47 | 1.83-2.09 | 1.10-1.23 | 2.57-3.16 |
| 180 | 0.93-1.16 | 0.93-1.12 | 1.25-1.47 | 1.25-1.47 | 1.83-2.09 | 1.10-1.23 | 2.57-3.16 |
| 165 | 0.93-1.16 | 0.93-1.16 | 1.26-1.47 | 1.25-1.47 | 1.83-2.09 | 1.10-1.23 | 2.57-3.16 |
| 150 | 0.92-1.15 | 0.90-1.14 | 1.22-1.41 | 1.22-1.45 | 1.83-2.12 | 1.07-1.22 | 2.56-3.19 |
| 83 | 0.93-1.16 | 0.92-1.15 | 1.21-1.40 | 1.21-1.45 | 1.84-2.10 | 1.09-1.21 | 2.57-3.17 |
| 10 | 0.88-1.13 | 0.86-1.15 | 1.23-1.42 | 1.24-1.46 | 1.84-2.10 | 1.09-1.24 | 2.53-3.17 |

**Table C.6:** Distance windows applied to RMC refinements.

## C.3 TGS

### C.3.1 Bond Bending and Stretching Potentials

| Atomic pair | $D$/eV | $r_0$/Å |
|---|---|---|
| D−C | 2.275 | 1.02 |
| D−N | 2.947 | 1.02 |
| D−Oz | 3.432 | 1.02 |
| C−C | 2.304 | 1.48 |
| C−N | 2.051 | 1.48 |
| C−O | 4.703 | 1.26 |
| C−Oh | 2.880 | 1.26 |
| C−Oz | 2.880 | 1.26 |
| S−O | 4.703 | 1.48 |

**Table C.7:** Morse bond stretch potentials used to constrain RMC refinement.

| Atoms | $k$/eV | $\theta_0$/° |
|---|---|---|
| D−N−D | 7.602 | 106.367 |
| D−N−C | 6.504 | 105.949 |
| N−C−D | 10.236 | 109.300 |
| N−C−C | 13.045 | 110.740 |
| D−C−D | 6.866 | 107.600 |
| D−C−C | 6.741 | 109.490 |
| C−C−O | 10.611 | 123.500 |
| C−C−Oh | 19.349 | 110.300 |
| C−C−Oz | 19.349 | 110.300 |
| O=C=Oh | 21.222 | 121.500 |
| O=C=Oz | 21.222 | 121.500 |
| O−S−O | 21.111 | 109.500 |

**Table C.8:** Angle potentials used to constrain RMC refinement.

### C.3.2 Distance Windows

| $T$/K | D−C | D−N | D−Oz | C−C | C−N | C−O | C−Oh | C−Oz | S−O |
|---|---|---|---|---|---|---|---|---|---|
| 403 | 0.89 - 1.16 | 0.82 - 1.17 | 0.99 - 1.21 | 1.36 - 1.67 | 1.26 - 1.68 | 1.06 - 1.39 | 1.12 - 1.36 | 1.12 - 1.36 | 1.33 - 1.64 |
| 365 | 0.88 - 1.15 | 0.77 - 1.23 | 1.00 - 1.31 | 1.33 - 1.67 | 1.25 - 1.68 | 1.06 - 1.46 | 1.12 - 1.36 | 1.15 - 1.41 | 1.29 - 1.69 |
| 343 | 0.89 - 1.15 | 0.80 - 1.32 | 1.01 - 1.24 | 1.34 - 1.69 | 1.25 - 1.66 | 1.05 - 1.43 | 1.14 - 1.46 | 1.15 - 1.41 | 1.27 - 1.69 |
| 323 | 0.89 - 1.26 | 0.88 - 1.34 | 0.92 - 1.12 | 1.33 - 1.71 | 1.32 - 1.66 | 1.11 - 1.41 | 1.18 - 1.47 | 1.12 - 1.38 | 1.32 - 1.64 |
| 303 | 0.90 - 1.26 | 0.85 - 1.31 | 0.97 - 1.19 | 1.28 - 1.70 | 1.31 - 1.66 | 1.12 - 1.42 | 1.16 - 1.46 | 1.14 - 1.39 | 1.31 - 1.63 |
| 293 | 0.91 - 1.26 | 0.85 - 1.20 | 0.96 - 1.18 | 1.28 - 1.72 | 1.32 - 1.66 | 1.13 - 1.38 | 1.15 - 1.45 | 1.14 - 1.40 | 1.31 - 1.63 |

**Table C.9:** Distance windows applied to RMC refinements

# Bibliography


[1] H. D. Duncan, M. T. Dove, D. A. Keen, A. E. Phillips, *Dalton Trans. Camb. Engl. 2003* **2016**, *45*, 4380.

[2] J. Valasek, *Phys. Rev.* **1921**, *17*, 475.

[3] E. Suzuki, Y. Shiozaki, *Phys. Rev. B* **1996**, *53*, 5217.

[4] S. Horiuchi, Y. Tokura, *Nat Mater* **2008**, *7*, 357.

[5] M. E. Lines, A. M. Glass, *Principles and Applications of Ferroelectrics and Related Materials*, Clarendon Press, Oxford, **1977**.

[6] W. Zhang, H.-Y. Ye, R.-G. Xiong, *Coordination Chemistry Reviews*, Functional Hybrid Nanomaterials:Design, Synthesis, Structure, Properties and Applications **2009**, *253*, 2980.

[7] Z.-M. Wang, S. Gao, *Natl. Sci. Rev.* **2014**, *1*, 25.

[8] S.-W. Cheong, M. Mostovoy, *Nat. Mater.* **2007**, *6*, 13.

[9] W. Zhang, R.-G. Xiong, *Chem. Rev.* **2012**, *112*, 1163.

[10] N. A. Hill, *J. Phys. Chem. B* **2000**, *104*, 6694.

[11] M. Dawber, K. M. Rabe, J. F. Scott, *Rev. Mod. Phys.* **2005**, *77*, 1083.

[12] N. A. Spaldin, M. Fiebig, *Science* **2005**, *309*, 391.

[13] D. Khomskii, *Physics* **2009**, *2*, 20.

[14] G. Rogez, N. Viart, M. Drillon, *Angew. Chem.-Int. Ed.* **2010**, *49*, 1921.

[15] W. Eerenstein, N. D. Mathur, J. F. Scott, *Nature* **2006**, *442*, 759.

[16] D.-W. Fu, W. Zhang, H.-L. Cai, Y. Zhang, J.-Z. Ge, R.-G. Xiong, S. D. Huang, T. Nakamura, *Angew. Chem.-Int. Edit.* **2011**, *50*, 11947.

[17] T. Hang, W. Zhang, H.-Y. Ye, R.-G. Xiong, *Chem. Soc. Rev.* **2011**, *40*, 3577.

[18] M. T. Dove, *Am. Miner.* **MAR-APR 1997**, *82*, 213.

[19] M. T. Dove, Key Equations for Neutron Total Scattering, **2015**.

[20] M. T. Dove, G. Rigg, *J. Phys.: Condens. Matter* **2013**, *25*, 454222.

[21] T. R. Welberry, B. D. Butler, *J. Appl. Crystallogr.* **1994**, *27*, 205.

[22] V. M. Nield, D. A. Keen, *Diffuse Neutron Scattering from Crystalline Materials*, Clarendon Press, **2001**.

[23] T. Proffen, *Jom* **2012**, *64*, 112.

[24] T. Proffen, S. J. L. Billinge, *J. Appl. Crystallogr.* **1999**, *32*, 572.

[25] T. Proffen, K. L. Page, S. E. McLain, B. Clausen, T. W. Darling, J. A. TenCate, S. Y. Lee, E. Ustundag, *Z. Kristall.* **2005**, *220*, 1002.

[26] C. L. Farrow, P. Juhas, J. W. Liu, D. Bryndin, E. S. Božin, J. Bloch, T. Proffen, S. J. L. Billinge, *J. Phys.: Condens. Matter* **2007**, *19*, 335219.

[27] M. G. Tucker, M. P. Squires, M. T. Dove, D. A. Keen, *J. Phys.-Condes. Matter* **2001**, *13*, 403.

[28] M. T. Dove, M. G. Tucker, D. A. Keen, *Eur. J. Mineral.* **2002**, *14*, 331.

[29] V. Sears, F, *Neutron News* **1992**, *3*, 26.

[30] X. Y. Wang, L. Gan, S. W. Zhang, S. Gao, *Inorg. Chem.* **2004**, *43*, 4615.

[31] L. Pusztai, R. McGreevy, *Phys. B Condens. Matter* **1997**, *234–236*, 357.

[32] P. Chater, XPDF The New XPDF Beamline Hardware, **02/SEPT/2015**.

[33] D. A. Keen, *J. Appl. Crystallogr.* **2001**, *34*, 172.

[34] P. King, ISIS Muon Training School: ISIS and Its Muon Facility, **2012**.

[35] A. C. Hannon, *Nucl. Instrum. Methods Phys. Res. Sect. A-Accel. Spectrom. Dect. Assoc. Equip.* **2005**, *551*, 88.

[36] STFC, ISIS - Polaris Technical Information, **2015**, `http://www.isis.stfc.ac.uk/instruments/polaris/technical/polaris-technical-information7277.html`.

[37] S. T. Norberg, I. Ahmed, R. Smith, S. G. Eriksson, L. C. Chapon, S. Hull, The Polaris Diffractometer at ISIS: Planned Upgrade and New Facilities, Poster, ISIS Facility, Rutherford Appleton Laboratory, Harwell Science and Innovation Campus, Didcot, OX11 0QX, Target Station 1, **2009**, p. 1.

[38] P. F. Peterson, M. Gutmann, T. Proffen, S. J. L. Billinge, *J. Appl. Crystallogr.* **2000**, *33*, 1192.

[39] A. K. Soper, GudrunN and GudrunX : Programs for Correcting Raw Neutron and X-Ray Diffraction Data to Differential Scattering Cross Section, Report RAL-TR-2011-013, **2011**.

[40] A. K. Soper, *GudrunN and GudrunX: Programs for Correcting Raw Neutron and X-Ray Total Scattering Data to Differential Cross Section*, *Vol. 5*, **2012**.

[41] H. M. Rietveld, *J. Appl. Crystallogr.* **1969**, *2*, 65.

[42] A. C. Larson, R. B. Von Dreele, General Structure Analysis System (GSAS), LAUR 86-748, Los Alamos National Laboratory, **2004**.

[43] B. H. Toby, *J. Appl. Crystallogr.* **2001**, *34*, 210.

[44] R. B. Von Dreele, *J. Appl. Crystallogr.* **1999**, *32*, 1084.

[45] R. Smith, *Refinement of Profile Parameters with Polaris Data*, **2014**.

[46] R. Vondreele, J. Jorgensen, C. Windsor, *J. Appl. Crystallogr.* **1982**, *15*, 581.

[47] R. L. McGreevy, L. Pusztai, *Mol. Simul.* **1988**, *1*, 359.

[48] R. L. McGreevy, *J. Phys.-Condens. Matter* **2001**, *13*, R877.

[49] M. Pasciak, R. Welberry, *Z. Kristall.* **2011**, *226*, 113.

[50] M. G. Tucker, D. A. Keen, M. T. Dove, A. L. Goodwin, Q. Hui, *J. Phys.-Condens. Matter* **2007**, *19*, DOI 10.1088/0953-8984/19/33/335218.

[51] N. L. Allinger, Y. H. Yuh, J. H. Lii, *J. Am. Chem. Soc.* **1989**, *111*, 8551.

[52] M. G. Tucker, M. T. Dove, A. L. Goodwin, D. A. Keen, *RMCProfile User Manual: Code Version 6.5.0*, **18/April/2012**, 145 pp.

[53] E. Beake, M. T. Dove, H. D. Duncan, A. E. Phillips, *To be sumbmitted* **2016**.

[54] B.-Q. Wang, H.-B. Yan, Z.-Q. Huang, Z. Zhang, *Acta Crystallogr. Sect. C-Cryst. Struct. Commun.* **2013**, *69*, 616.

[55] W. Li, Z. Zhang, E. G. Bithell, A. S. Batsanov, P. T. Barton, P. J. Saines, P. Jain, C. J. Howard, M. A. Carpenter, A. K. Cheetham, *Acta Mater.* **2013**, *61*, 4928.

[56] M. Maczka, A. Ciupa, A. Gagor, A. Sieradzki, A. Pikul, B. Macalik, M. Drozd, *Inorg. Chem.* **2014**, *53*, 5260.

[57] M. Kurmoo, K.-L. Hu, Z. Wang, S. Gao, *Chem.- Eur. J.* **2009**, *15*, 12050.

[58] Y. Tian, A. Stroppa, Y.-S. Chai, P. Barone, M. Perez-Mato, S. Picozzi, Y. Sun, *Phys. Status Solidi RRL* **2015**, *9*, 62.

[59] A. Stroppa, P. Jain, P. Barone, M. Marsman, J. Manuel Perez-Mato, A. K. Cheetham, H. W. Kroto, S. Picozzi, *Angew. Chem.-Int. Edit.* **2011**, *50*, 5847.

[60] A. Stroppa, P. Barone, P. Jain, J. M. Perez-Mato, S. Picozzi, *Adv. Mater.* **2013**, *25*, 2284.

[61] G.-C. Xu, W. Zhang, X.-M. Ma, Y.-H. Chen, L. Zhang, H.-L. Cai, Z.-M. Wang, R.-G. Xiong, S. Gao, *J. Am. Chem. Soc.* **2011**, *133*, 14948.

[62] Z. Wang, B. Zhang, K. Inoue, H. Fujiwara, T. Otsuka, H. Kobayashi, M. Kurmoo, *Inorg. Chem.* **2007**, *46*, 437.

[63] Z. Zhang, W. Li, M. A. Carpenter, C. J. Howard, A. K. Cheetham, *Crystengcomm* **2015**, *17*, 370.

[64] X.-Y. Wang, Z.-M. Wang, S. Gao, *Chem. Commun.* **2008**, 281.

[65] L. C. Gómez-Aguirre, B. Pato-Doldán, J. Mira, S. Castro-García, M. A. Señarís-Rodríguez, M. Sánchez-Andújar, J. Singleton, V. S. Zapf, *J. Am. Chem. Soc.* **2016**, *138*, 1122.

[66] D. Di Sante, A. Stroppa, P. Jain, S. Picozzi, *J. Am. Chem. Soc.* **2013**, *135*, 18126.

[67] E. Sletten, L. Jensen, *Acta Crystallogr. Sect. B-Struct. Sci.* **1973**, *29*, 1752.

[68] T. Besara, P. Jain, N. S. Dalal, P. L. Kuhns, A. P. Reyes, H. W. Kroto, A. K. Cheetham, *Proc. Natl. Acad. Sci. U. S. A.* **2011**, *108*, 6828.

[69] P. Jain, N. S. Dalal, B. H. Toby, H. W. Kroto, A. K. Cheetham, *J. Am. Chem. Soc.* **2008**, *130*, 10450.

[70] Y. Tian, J. Cong, S. Shen, Y. Chai, L. Yan, S. Wang, Y. Sun, *Phys. Status Solidi RRL* **2014**, *8*, 91.

[71] Y. Tian, S. Shen, J. Cong, L. Yan, Y. Chai, Y. Sun, *Chinese Phys. B* **2016**, *25*, 017601.

[72] M. Maczka, W. Zierkiewicz, D. Michalska, J. Hanuza, *Spectrochim. Acta Part -Mol. Biomol. Spectrosc.* **2014**, *128*, 674.

[73] T. Asaji, S. Yoshitake, Y. Ito, H. Fujimori, *J. Mol. Struct.* **2014**, *1076*, 719.

[74] B. Pato-Doldan, M. Sanchez-Andujar, L. C. Gomez-Aguirre, S. Yanez-Vilar, J. Lopez-Beceiro, C. Gracia-Fernandez, A. A. Haghighirad, F. Ritter, S. Castro-Garcia, M. A. Senaris-Rodriguez, *Phys. Chem. Chem. Phys.* **2012**, *14*, 8498.

[75] K. Vinod, C. S. Deepak, S. Sharma, D. Sornadurai, A. T. Satya, T. R. Ravindran, C. S. Sundar, A. Bharathi, *RSC Adv.* **2015**, *5*, 37818.

[76] Z. Wang, P. Jain, K.-Y. Choi, J. van Tol, A. K. Cheetham, H. W. Kroto, H.-J. Koo, H. Zhou, J. Hwang, E. S. Choi, M.-H. Whangbo, N. S. Dalal, *Phys. Rev. B* **2013**, *87*, 224406.

[77] J.-P. Zhao, B.-W. Hu, F. Lloret, J. Tao, Q. Yang, X.-F. Zhang, X.-H. Bu, *Inorg. Chem.* **2010**, *49*, 10390.

[78] L. Canadillas-Delgado, O. Fabelo, J. Alberto Rodriguez-Velamazan, M.-H. Lemee-Cailleau, S. A. Mason, E. Pardo, F. Lloret, J.-P. Zhao, X.-H. Bu, V. Simonet, C. V. Colin, J. Rodriguez-Carvajal, *J. Am. Chem. Soc.* **2012**, *134*, 19772.

[79] M. Mączka, A. Gągor, K. Hermanowicz, A. Sieradzki, L. Macalik, A. Pikul, *Journal of Solid State Chemistry* **2016**, *237*, 150.

[80] M. Maczka, A. Pietraszko, L. Macalik, A. Sieradzki, J. Trzmiel, A. Pikul, *Dalton Trans. Camb. Engl. 2003* **2014**, *43*, 17075.

[81] I. E. Collings, J. A. Hill, A. B. Cairns, R. I. Cooper, A. L. Thompson, J. E. Parker, C. C. Tang, A. L. Goodwin, *Dalton Trans.* **2016**, *45*, 4169.

[82] G. P. Nagabhushana, R. Shivaramaiah, A. Navrotsky, *J. Am. Chem. Soc.* **2015**, *137*, 10351.

[83] M. Kosa, D. T. Major, *Cryst Eng Comm* **2015**, *17*, 295.

[84] J.-C. Tan, P. Jain, A. K. Cheetham, *Dalton Trans.* **2012**, *41*, 3949.

[85] R. I. Thomson, P. Jain, A. K. Cheetham, M. A. Carpenter, *Phys. Rev. B* **2012**, *86*, 214304.

[86] P. Jain, V. Ramachandran, R. J. Clark, H. D. Zhou, B. H. Toby, N. S. Dalal, H. W. Kroto, A. K. Cheetham, *J. Am. Chem. Soc.* **2009**, *131*, 13625.

[87] P. Baker, T. Lancaster, I. Franke, S. Blundell, F. Pratt, P. Jain, Z. Wang, M. Kurmoo, *Phys. Rev. B* **2010**, *82*, 012407.

[88] Z. M. Wang, B. Zhang, T. Otsuka, K. Inoue, H. Kobayashi, M. Kurmoo, *Dalton Trans.* **2004**, 2209.

[89] M. Maczka, A. Gagor, B. Macalik, A. Pikul, M. Ptak, J. Hanuza, *Inorg. Chem.* **2014**, *53*, 457.

[90] N. Abhyankar, S. Bertaina, N. S. Dalal, *J. Phys. Chem. C* **2015**, *119*, 28143.

[91] M. Sanchez-Andujar, S. Presedo, S. Yanez-Vilar, S. Castro-Garcia, J. Shamir, M. A. Senaris-Rodriguez, *Inorg. Chem.* **2010**, *49*, 1510.

[92] M. Sanchez-Andujar, L. C. Gomez-Aguirre, B. P. Doldan, S. Yanez-Vilar, R. Artiaga, A. L. Llamas-Saiz, R. S. Manna, F. Schnelle, M. Lang, F. Ritter, A. A. Haghighirad, M. A. Senaris-Rodriguez, *Crystengcomm* **2014**, *16*, 3558.

[93] W. Wang, L.-Q. Yan, J.-Z. Cong, Y.-L. Zhao, F. Wang, S.-P. Shen, T. Zou, D. Zhang, S.-G. Wang, X.-F. Han, Y. Sun, *Sci Rep* **2013**, *3*, 2024.

[94] J. Schlenker, G. Gibbs, M. Boisen, *Acta Crystallogr. Sect. A* **1978**, *34*, 52.

[95] J.-C. Tolédano, P. Tolédano, *The Landau Theory of Phase Transitions : Application to Structural, Incommensurate, Magnetic, and Liquid Crystal Systems*, **1987**.

[96] W. Brixel, J. Rivera, A. Steiner, H. Schmid, *Ferroelectrics* **1988**, *79*, 495.

[97] M. Kurmoo, *Chem. Soc. Rev.* **2009**, *38*, 1353.

[98] E. Colacio, M. Ghazi, R. Kivekäs, J. M. Moreno, *Inorg. Chem.* **2000**, *39*, 2882.

[99] C. Ruiz-Pérez, J. Sanchiz, M. H. Molina, F. Lloret, M. Julve, *Inorg. Chem.* **2000**, *39*, 1363.

[100] P. Jain, Florida State University, Florida, **2010**.

[101] H. Stokes, B. Campbell, Magnetic Space Groups Help, **2016**, `http://stokes.byu.edu/iso/magneticspacegroupshelp.php` (visited on 06/01/2016).

[102] M. Rotter, Magnetic Form Factors for Neutrons, **2013**, `http://www2.cpfs.mpg.de/~rotter/homepage_mcphase/manual/node137.html#ffacts` (visited on 01/15/2015).

[103] T. Matsuda, J. Kim, Y. Moritomo, *Dalton Trans.* **2012**, *41*, 7620.

[104] C. M. Kareis, S. H. Lapidus, J.-H. Her, P. W. Stephens, J. S. Miller, *J. Am. Chem. Soc.* **2012**, *134*, 2246.

[105] J.-H. Her, P. W. Stephens, C. M. Kareis, J. G. Moore, K. S. Min, J.-W. Park, G. Bali, B. S. Kennon, J. S. Miller, *Inorg. Chem.* **2010**, *49*, 1524.

[106] M. Ohba, H. Okawa, *Coord. Chem. Rev.* **2000**, *198*, 313.

[107] S. Adak, L. L. Daemen, M. Hartl, D. Williams, J. Summerhill, H. Nakotte, *J. Solid State Chem.* **2011**, *184*, 2854.

[108] L. J. Murray, M. Dinca, J. R. Long, *Chem. Soc. Rev.* **2009**, *38*, 1294.

[109] W. Zhang, Y. Cai, R.-G. Xiong, H. Yoshikawa, K. Awaga, *Angew. Chem.-Int. Ed.* **2010**, *49*, 6608.

[110] M. Guo, H.-L. Cai, R.-G. Xiong, *Inorg. Chem. Commun.* **2010**, *13*, 1590.

[111] W.-J. Xu, S.-L. Chen, Z.-T. Hu, R.-B. Lin, Y.-J. Su, W.-X. Zhang, X.-M. Chen, *Dalton Trans.* **2016**, *45*, 4224.

[112] X. Zhang, X.-D. Shao, S.-C. Li, Y. Cai, Y.-F. Yao, R.-G. Xiong, W. Zhang, *Chem. Commun.* **2015**, *51*, 4568.

[113] W. Zhang, H.-Y. Ye, R. Graf, H. W. Spiess, Y.-F. Yao, R.-Q. Zhu, R.-G. Xiong, *J. Am. Chem. Soc.* **2013**, *135*, 5230.

[114] A. Richaud, N. Barba-Behrens, F. Mendez, *Org. Lett.* **2011**, *13*, 972.

[115] University of the Basque Country, Bilbao Crystallograpic Server, **2016**, `http://www.cryst.ehu.es/`.

[116] B. T. Matthias, C. E. Miller, J. P. Remeika, *Phys Rev* **1956**, *104*, 849.

[117] R. R. Choudhury, R. Chitra, P. U. Sastry, A. Das, M. Ramanadham, *Pramana-J. Phys.* **2004**, *63*, 107.

[118] C. J. Raj, S. Kundu, K. B. R. Varma, *Appl. Phys. -Mater. Sci. Process.* **2011**, *105*, 1025.

[119] A. Rohatgi, *WebPlotDigitizer*, **2016**.

[120] K. Itoh, A. Nishikori, H. Yokomizo, E. Nakamura, *Jpn. J. Appl. Phys.* **1985**, *24*, 594.

[121] V. Tripadus, D. Aranghel, M. Statescu, A. Buchsteine, *Chem. Phys.* **2008**, *353*, 59.

[122] R. Blinc, M. Mali, R. Osredkar, A. Prelesnik, I. Zupančič, L. Ehrenberg, *J. Chem. Phys.* **1971**, *55*, 4843.

[123] G. Slosarek, A. Heuer, H. Zimmermann, U. Haeberlen, *J. Phys.: Condens. Matter* **1989**, *1*, 5931.

[124] R. R. Choudhury, R. Chitra, M. Ramanadham, *J. Phys.-Condens. Matter* **2003**, *15*, 4641.

[125] S. R. Fletcher, E. T. Keve, A. C. Skapski, *Ferroelectrics* **1976**, *14*, 775.

[126] S. R. Fletcher, E. T. Keve, A. C. Skapski, *Ferroelectrics* **1976**, *14*, 789.

[127] R. R. Choudhury, R. Chitra, *J. Phys.-Condens. Matter* **2009**, *21*, DOI `10.1088/0953-8984/21/33/335901`.

[128] A. R. Lim, S.-Y. Jeong, *Journal of Molecular Structure* **2013**, *1048*, 471.

[129] J. M. Hudspeth, D. J. Goossens, M. J. Gutmann, A. J. Studer, *Cryst. Res. Technol.* **2013**, *48*, 169.

[130] T. Kikuta, D. Hamatake, T. Yamazaki, N. Nakatani, *Ferroelectrics* **2007**, *347*, 65.

[131] Y. Fujii, Y. Yamada, *J. Phys. Soc. Jpn.* **1971**, *30*, 1676.

[132] J. M. Hudspeth, D. J. Goossens, T. R. Welberry, M. J. Gutmann, *J. Mater. Sci.* **2013**, *48*, 6605.

[133] R. R. Choudhury, R. Chitra, *Pramana-J. Phys.* **2008**, *71*, 911.

[134] S. Aravazhi, R. Jayavel, C. Subramanian, *Mater. Chem. Phys.* **1997**, *50*, 233.

[135] F. Eleithan, A. Bates, W. Gough, D. Somerford, *J. Phys.-Condens. Matter* **1992**, *4*, L249.

[136] M. Kay, Kleinber.r, *Ferroelectrics* **1973**, *5*, 45.

[137] N. Nakatani, *Jpn. J. Appl. Phys.* **1985**, *24*, L528.

[138] N. Nakatani, *Jpn. J. Appl. Phys.* **1973**, *12*, 1723.

[139] N. Nakatani, *Ferroelectrics* **2011**, *413*, 238.

[140] A. Eklund, T. E. Nichols, H. Knutsson, *PNAS* **2016**, *113*, 7900.

[141] M. Baker, *Nature* **2015**, *521*, 274.

[142] H. Li, M. Eddaoudi, M. O'Keeffe, O. M. Yaghi, *Nature* **1999**, *402*, 276.